Universidade de Aveiro Departamento de Engenharia de Materiais e Cerâmica
Ano 2016

ISABEL ALEXANDRA GONÇALVES ANTUNES

MECANOQUÍMICA DE MATERIAIS DE PILHAS DE COMBUSTÍVEL DE ALTA TEMPERATURA

MECHANOCHEMISTRY OF HIGH TEMPERATURE FUEL CELL MATERIALS

Universidade de Aveiro
Ano 2016
Departamento de Engenharia de Materiais e Cerâmica

ISABEL ALEXANDRA GONÇALVES ANTUNES

MECANOQUÍMICA DE MATERIAIS DE PILHAS DE COMBUSTÍVEL DE ALTA TEMPERATURA

MECHANOCHEMISTRY OF HIGH TEMPERATURE FUEL CELL MATERIALS

Tese apresentada à Universidade de Aveiro para cumprimento dos requisitos necessários à obtenção do grau de Doutor em Ciência e Engenharia de Materiais, realizada sob a orientação científica do Doutor Duncan Paul Fagg, Equiparado a Investigador Principal do Departamento de Engenharia Mecânica da Universidade de Aveiro, e do Doutor Jorge Ribeiro Frade, Professor Catedrático do Departamento de Engenharia de Materiais e Cerâmica da Universidade de Aveiro.

Apoio Financeiro da Fundação para a Ciência e Tecnologia (FCT) com a bolsa de doutoramento SFRH/BD/76738/2011 e com os projetos MatSILC (FP6-STRP033410), ULCOS (P515960) e IERO (RFSR-CT-2010-00002)

Dedico este trabalho aos meus Pais.

o júri

presidente

Doutor Amadeu Mortágua Velho da Maia Soares
Professor Catedrático, Universidade de Aveiro

Doutor Adélio Miguel Magalhães Mendes
Professor Catedrático, Faculdade de Engenharia, Universidade do Porto

Doutor Fernando Manuel Bico Marques
Professor Catedrático, Universidade de Aveiro

Doutor Bruno Miguel Quelhas de Sacadura Cabral Trindade
Professor Associado, Faculdade de Ciências e Engenharia, Universidade de Coimbra

Doutor João Carlos Bentes Waerenborgh
Investigador Principal, Centro de Ciências e Tecnologias Nucleares (C2TN), Instituto Superior Técnico, Universidade de Lisboa

Doutor Duncan Paul Fagg
Equiparado a Investigador Principal, Universidade de Aveiro (orientador)

agradecimentos

Aos meus orientadores Professor Jorge Frade e Doutor Duncan Fagg, pela partilha de conhecimento, pela disponibilidade e compreensão. Serei sempre grata pela oportunidade que me deram em iniciar um percurso na Investigação.

Ao Doutor Glenn Mather, do ICV, Madrid, pela sua colaboração na análise estrutural por refinamento de Rietveld, à Doutora Maria do Rosário Correia e à Mestre Adriana Alves, do Departamento de Física, I3N, da Universidade de Aveiro pela sua colaboração na caracterização dos materiais por espetroscopia de Raman.

Aos colaboradores do Departamento de Materiais e Cerâmica pela ajuda e disponibilidade.

Aos colegas de laboratório do Departamento de Engenharia de Materiais e Cerâmica e do Departamento de Engenharia Mecânica. Pela troca de ideias, sugestões, pelo apoio no trabalho e pelo convívio. Em especial quero agradecer ao Eddy, ao Vlad, à Ana, à Sofia, à Teresa e ao Javi, pela vossa Amizade.

Ao meu irmão, pelos conselhos, sugestões, apoio e incentivo.

Aos meus Pais, pelo Amor e Apoio incondicional. Por estarem ao meu lado em todos os momentos. Tudo o que consegui e sou devo-o a vocês.

palavras-chave

Mecanoquímica, pilha de combustível de óxido sólido, moagem de alta energia, mecanossíntese, ativação mecânica, condutores protónicos, condutores mistos, perovesquite.

resumo

Nos últimos anos, a mecanoquímica tem sido uma temática muito abordada na formação de materiais, motivada pelo grande interesse na preparação de nanopós. A sobressaturação estrutural de lacunas e a heterogeneidade química dos pós preparados por via mecanoquímica permitem melhoria na sinterabilidade, enquanto a elevada densidade dos agregados e a reduzido tamanho de cristalite produzem densidade em verde elevada. Estes fatores são extremamente atrativos na preparação de materiais cerâmicos óxidos densos, como é requerido na preparação de membranas eletroquímicas. Além disso, o processamento cerâmico por via mecanoquímica possibilita a síntese de novos materiais, que não conseguem ser sintetizados por outros métodos.

Esta tese apresenta um estudo detalhado do processamento por via mecanoquímica de potenciais materiais de eletrólito e elétrodo para pilhas de combustível de óxido sólido de alta temperatura, e sua caracterização estrutural e eletroquímica. Por manipulação das variáveis do processo mecanoquímico pretende-se melhorar a capacidade de processamento e desenvolver novos materiais para aplicação em tecnologias de pilhas de combustível.

A investigação foca-se, especificamente, no desenvolvimento de materiais de estrutura perovesquite à base de $BaZrO_3$ e $BaPrO_3$, com possíveis aplicações como condutores protónicos e condutores mistos, eletrónicos e protónicos, respetivamente.

keywords

Mechanochemistry, solid oxide fuel cells, high energy milling, mechanosynthesis, mechanical activation, proton conductors, mixed conductors, perovskite

abstract

In recent years, mechanochemistry has become an increasingly hot topic for the formation of materials, motivated by an explosion of interest in the preparation of nanopowders. The structural supersaturation by vacancies and chemical non-uniformity of mechanochemical powders promote enhanced sinterability, while the high density of aggregates and reduced crystallite density produce high green-densities. Such factors are highly attractive for preparation of dense ceramic oxide materials, as required for the formation of electrochemical-membranes. Additionally, mechanochemical ceramic processing may allow the synthesis of novel materials, which cannot be synthesized by other methods.

In this thesis one offers a detailed study of mechanochemical processing for important potential electrolyte and electrode materials for high temperature solid oxide fuel cells and their subsequent structural and electrochemical characterisation. By mechanochemical manipulation one aims to improve the processing ability and to develop novel materials for fuel cell technologies. The research work is focused specifically on the development of perovskite materials based on $BaZrO_3$ and $BaPrO_3$, with potential applications as proton and mixed proton-electron conductors, respectively.

SUMMARY

Developed in a research group devoted to the development of "Materials for Energy" the starting point of the present thesis was to overcome the processing difficulties of the foremost proton conducting material, yttrium–doped barium zirconate, by adoption of mechanochemical processing.

Barium zirconate materials have created immense interest due to high levels of proton conductivity coupled with superior stability in steam or CO_2 containing atmospheres. However, the refractory nature of these materials leads to processing difficulties, with formation of segregation phases, alteration of stoichiometry or formation of carbonate phase as impurity, in addition to the requirement of extreme temperatures for the formation of dense ceramics (> 1973 K). These limitations cause phase inhomogeneities that have been shown to be detrimental to the electrical performance of these materials. In this context, mechanochemical processing was assumed as a possible option of powder production, since it has been shown to be an efficient method to achieve reactive, homogeneous nanopowders with enhanced sinterability. The thesis is, therefore, devoted to the mechanosynthesis of nanopowders of various potential solid oxide fuel cell components, at room temperature, with focus on their phase formation, microstructural analysis, assessment of carbonate formation, densification levels and subsequent electrical properties.

The mechanochemical processing of $Ba(Zr,Y)O_{3-\delta}$ ceramics and its impact on the resultant phase purity and microstructure of dense ceramics and subsequent electrical properties was analysed by comparison with literature data of the reference compositions $BaZr_{0.80}Y_{0.20}O_{3-\delta}$ and $BaZr_{0.85}Y_{0.15}O_{3-\delta}$. Modelling of electrical properties was also performed to separate the contributions of different charge carriers to the total electrical conductivity. In these materials, Ba-losses caused by sintering at high sintering temperatures has been commonly associated with the presence of inhomogeneities and high grain-boundaries resistances of

$Ba(Zr,Y)O_{3-\delta}$ materials. Thus, the $Ba(Zr,Y)O_{3-\delta}$ nanopowders prepared by mechanosynthesis were also utilized as homogenous base materials for analysis of the impact of non-stoichiometry on materials properties. For that purpose, typical Ba-losses during sintering were simulated by the formation of controlled Ba-deficiency in powders formed by mechanosynthesis.

In addition to the adoption of mechanochemical processing for electrolyte materials, such as $Ba(Zr,Y)O_{3-\delta}$, the research also extended to the development of novel mixed conducting materials by mechanochemical processing. Potential mixed electron-proton conductors based on $BaPrO_3$ were prepared by such methods.

The research focused on the development of novel materials of $Ba(Pr,Zr,Y)O_{3-\delta}$ and $Ba(Pr,Zr)O_{3-\delta}$, involving detailed structural characterization, chemical stability experiments and electrical properties with the aim to stablish interrelations between composition, crystallographic structures and the properties exhibited.

TABLE OF CONTENTS

List of Figures ..... *i*

List of Tables ..... *ix*

List of Symbols ..... *xi*

List of Acronyms ..... *xii*

1. Introduction *1*

1.1. Historical Background and Overview of Fuel Cells 1
1.2. Solid Oxide Fuel Cells: Designs, Operating Principles and Materials 5
1.2.1. Oxide-Ion Conducting SOFC (O-SOFC) 7
1.2.2. Proton-Conducting SOFC (H-SOFC) 10
1.3. Perovskite-Proton Conductors 14
1.3.1. Perovskite-Type Structure 14
1.3.2. Formation of Protonic Defects 17
1.3.3. Proton Transport Mechanisms 20
1.4. Y-Doped $BaZrO_3$: A Model System for Processing Difficulties 22
1.5. Mechanochemical Processing 24
1.5.1. Mechanism of Mechanical Alloying 26
1.5.2. Mechanochemical Processing of Ceramics 28
1.6. Aim of the Thesis 30

2. Experimental: Materials Processing and Characterization Techniques *31*

2.1. Materials Processing 31
2.1.1. Precursors 31
2.1.2. Mechanochemical Ceramic Processing 34
2.2. Characterization of Materials 35
2.2.1. X-Ray Diffraction 35
2.2.1.1. Size-Strain Plots 35
2.2.1.2. Rietveld Refinement 36
2.2.2. Raman Spectroscopy 37
2.2.3. ICP-AES and FT-IR Analysis 37
2.2.4. Chemical Stability Studies 38
2.2.5. Electron Microscopy Studies 38
2.2.6. Electrochemical Measurements 39
2.2.6.1. Fundamentals 40
2.2.6.2. Preparation of Samples 45
2.2.6.1. Equipment and Measurements Conditions 46

3. Mechanosynthesis of $Ba(Zr,Y)O_{3-\delta}$ Nanopowders 49

3.1. Thermodynamic Guidelines for the Selection of Ba- Precursors 49
3.2. Phase Formation 52
3.3. Effect of Milling Conditions 57
3.4. Microstructure 58
3.5. Carbonate Formation 61
3.6. Densification 63
3.7. Enhanced $BaZrO_3$ Mechanosynthesis by the Use of Metastable ZrO_2 Precursors 67
3.7.1. Synthesis of Zirconia Polymorphous 67
3.7.2. Transformation of Zirconia Polymorphs under High-Energy Milling 70
3.7.3. Mechanosynthesis of $BaZrO_3$ 76
3.8. Concluding Remarks 80

4. Phase Purity, Microstructure and Electrical Properties of $BaZr_{1-y}Y_yO_{3-\delta}$ ($y = 0.15, 0.20$) Prepared by Mechanochemical Processing 83

4.1. Phase Formation and Compositional Analysis 83
4.2. Microstructure 87
4.3. Electrical Conductivity 89
4.3.1. Comparison of Total Electrical Conductivity with Literature Data 89
4.3.2. Electrochemical Characterization 91
4.3.3. Modelling of Electrical Conductivity 94
4.3.3.1. Methodology 94
4.3.3.2. Results of Modelling 96
4.4. Concluding Remarks 106

5. Effect of Ba-Deficiency on $Ba(Zr,Y)O_{3-\delta}$ Properties 107

5.1. Introduction 107
5.2. Phase Formation and Compositional Analysis 111
5.3. Structural Characterisation 115
5.4. Grain Growth and Densification 117
5.5. Electrical Characterisation 123
5.6. Concluding Remarks 127

6. Mechanochemical Preparation and Stability Studies of $Ba(Pr,Zr,Y)O_{3-\delta}$ Materials as Potential Electrodes for Protonic SOFC 129

6.1. Phase Formation 130
6.2. Structural Characterization 133
6.3. Stability Studies 135
6.3.1. Dry and Wet O_2 136
6.3.2. 10% H_2/N_2 137
6.3.3. Pure CO_2 140
6.3.4. Stability in Wet Compared to Dry Conditions 144
6.4. Concluding Remarks 145

7. Phase Formation, Structural and Electrical Properties of $BaPr_{1-x}Zr_xO_{3-\delta}$ Materials *147*

7.1. Phase Formation 148
7.2. Structural Characterization 150
7.3. Electrical Properties 157
7.4. Concluding Remarks 161

8. Further Considerations *163*

9. References *177*

Appendix 1: Chemical-Potential Diagrams *201*

LIST OF FIGURES

Fig. 1.1. Schematic of planar (left) [15] and tubular (Siemens-Westinghouse) [16] (right) SOFC designs. 6

Fig. 1.2. Basic operating principle of oxide-ion conducting solid oxidefuel cell (O-SOFC) considering that the fuel is hydrogen and air the supplier of oxygen [18]. 8

Fig. 1.3. Basic operating principle of oxide-ion conducting solid oxidefuel cell (O SOFC) considering that the fuel is hydrogen and air the supplier of oxygen [18].....11

Fig. 1.4. Proton conductivity of various oxides as calculated from data on proton concentrations and mobilities, according to Norby & Larring [71]. 13

Fig. 1.5. Two schematic representations of cubic perovskite structure ABO_3 with the origin centered at (a) B-site ion and (b) A-site ion (polyhedron representation) [73]. 14

Fig. 1.6. Schematic diagram indicating the relation between tilt system and space group. The dashed lines indicate first-order phase transitions and the filled lines correspond to the second-order phase transitions [80,81]. 16

Fig. 1.7. The trace of a proton in a perovskite showing the two main features of proton transport: rotational diffusion and proton transfer (data obtained by quantum-MD simulation of a proton in $BaCeO_3$) [18,93]. 20

Fig. 1.8. Scheme of the proton transfer mechanism between two adjacent oxide ions in perovskite oxides (from [79]). 21

Fig. 1.9. Two-dimensional scheme illustrating the primary event of the mechanical alloying mechanism (a) initial state; (b) roll growth until collision, accompanied by emission processes, and (c) relaxation of $(A_xB)^*$ to the primary product [131]. 27

Fig. 1.10. Dynamics of mechanochemical synthesis in systems with intermediate primary products. (1) primary product, (2) secondary product, (3) starting reactants [131]. 28

Fig. 1.11. Mechanically produced barium titanate-based powders. 29

Fig. 2.1. Schematic impedance plot in the Nyquist representation of an ideal crystalline material. 41

Fig. 2.2. Brick-layer model of a polycrystalline material (from [142]). 43

Fig. 2.3. Experimental setup and a cell holder used in the impedance experiments. 48

Fig. 3.1. Free energy change (ΔG_R) of formation of barium zirconate starting from zirconium oxide and different barium precursors.....51

Fig. 3.2. Evolution of powder X-ray diffraction patterns with milling time for $BaZr_{1-y}Y_yO_{3-\delta}$ compositions (a) $y = 0$, (b) $y = 0.06$, (c) $y = 0.15$ for $BaO_2 + ZrO_2$, $(ZrO_2)_{0.97}(Y_2O_3)_{0.03}$ or $(ZrO_2)_{0.92}(Y_2O_3)_{0.08}$ precursors, respectively. The markers identify (○) barium peroxide; (▣, ■) yttria doped zirconia (3 and 8 mol%, respectively; (□) monoclinic zirconia; and (◆) perovskite phase. Partial X-ray patterns of $BaZr_{1-y}Y_yO_{3-\delta}$, $y = 0$, in (a) highlights the presence of *m*-ZrO2 impurity. 53

Fig. 3.3. X-ray diffraction pattern after calcination at 1250 ºC of the mechanosynthesised powder of composition $BaZr_{1-y}YyO_{3-\delta}$, $y = 0$. The marker (◆) identifies the perovskite phase. 54

Fig. 3.4. Evolution of powder X-ray diffraction patterns with milling time for $BaZr_{1-y}Y_yO_{3-\delta}$ composition $y = 0$ for $BaCO_3 + ZrO_2$ precursors. The markers identify: (⦿) barium carbonate and (□) monoclinic zirconia. 55

Fig. 3.5. X-ray diffraction patterns highlighting the impaired rate of perovskite phase formation when the formed oxygen is prevented from being released by keeping the vial closed. Composition $BaZr_{1-y}Y_yO_{3-\delta}$, $y = 0.15$. The markers identify: (○) barium peroxide; (■) yttria doped zirconia (8 mol%) and (◆) perovskite phase.. 58

Fig. 3.6. (a) Size-strain plots shown for compositions, $y = 0$, 0.06 and 0.15 with 420, 300 and 420 minutes of milling time, respectively. (b) Average crystallite size determined from XRD plotted as a function of milling time. 59

Fig. 3.7. TEM image collected for samples $y = 0$, $y = 0.06$ and $y = 0.15$, milled for 420, 300 and 420 minutes, respectively. 61

Fig. 3.8. Comparison between infrared transmission spectra of undried $BaCO_3$ commercial powder with mechanosynthesised $BaZr_{0.85}Y_{0.15}O_{3-\delta}$ powder after exposure to atmospheric conditions for 1 month, and fresh mechanosynthesised $BaZr_{0.85}Y_{0.15}O_{3-\delta}$ powder. 62

Fig. 3.9. Grain size (a) and relative density (b) for $BaZr_{1-y}Y_yO_{3-\delta}$ ceramics as a function of sintering temperature. Dwell time at each temperature is 5 hours. 64

Fig. 3.10. Polymorphic transformation of ZrO_2: changes in lattice and crystal system view (adapted from [166]). 67

Fig. 3.11. X-ray diffraction patterns of the synthesized zirconia powders. The markers identify: (△) *m*-ZrO_2 and (○) *t*-ZrO_2. 69

Fig. 3.12. SEM images of (a) monoclinic zirconia and (b) tetragonal zirconia powders mounted on carbon tapes. 70

Fig. 3.13. X-ray diffraction patterns of (a) *t*-ZrO_2, and (b) *m*-ZrO_2 powders after different milling times. The markers identify: (□) *m*-ZrO_2; (∗) *t*-ZrO_2. 71

Fig. 3.14. Weight fractions of *t*-ZrO_2 as a function of milling time starting from: (□) *m*-ZrO_2, and (∗) *t*-ZrO_2. 72

Fig. 3.15. Size-strain plots of (a) *m*-ZrO_2 and (b) *t*-ZrO_2 before milling and after 60, 120 and 180 min of high energy milling 74

Fig. 3.16. Average crystallite size (■) and root mean square strain, e_{rms}, (○) determined from the size-strain plot as a function of milling time for: (a) *m*-ZrO_2, and (b) *t*-ZrO_2. 75

Fig. 3.17. X-ray diffraction patterns of $BaZrO_3$ after different milling time using BaO_2 and *t*-ZrO_2 as precursors. The markers identify: (○) BaO_2, (∗) *t*-ZrO_2, and (⦿) $BaCO_3$ and (◆) perovskite phase. 76

Fig. 3.18. X-ray diffraction patterns of $BaZrO_3$ after different milling time using BaO_2 and *m*-ZrO_2 as precursors. The markers identify: (○) BaO_2, (□) *m*-ZrO_2, (⦿) $BaCO_3$ and (◆) perovskite phase. 77

Fig. 3.19. Weight fraction of $BaZrO_3$ as a function of milling time for mixtures of barium peroxide with different zirconia precursor polymorphs. 78

Fig. 3.20. TGA plot of $BaZrO_3$ powders obtained from *t*-ZrO_2-BaO_2 and *m*-ZrO_2-BaO_2 powder mixtures, heated and cooled under dry Ar atmosphere, at a rate of 5 ºC·min^{-1}. 80

Fig. 4.1. X-ray diffraction patterns of: (a) $BaZr_{0.85}Y_{0.15}O_{3-\delta}$ (BZY15) and (b) $BaZr_{0.80}Y_{0.20}O_{3-\delta}$ (BZY20) prepared by sintering of nanopowders formed by mechanosynthesis, at 1250 ºC and 1600 ºC, for 1 and 5 hours, respectively; and the correspondent partial X-ray diffraction patterns in the vicinity of major $BaZrO_3$ (110), (200) and (211) peaks. …… 84

Fig. 4.2. Partial powders X-ray diffraction patterns in the vicinity of major $BaZrO_3$ (211) peak of: (a) $BaZr_{0.85}Y_{0.15}O_{3-\delta}$ (BZY15) and $BaZr_{0.80}Y_{0.20}O_{3-\delta}$ (BZY20) compositions prepared by mechanochemical processing using the sintering conditions adopted by Oyama et al. [173]; (b) obtained by Oyama et al. [173] for $BaZr_{1-y}Y_yO_{3-\delta}$, with $0 \leq y \leq 0.50$, prepared by solid-state reaction. 86

Fig. 4.3. SEM micrographs of fractured $BaZr_{0.85}Y_{0.15}O_{3-\delta}$ (BZY15) and $BaZr_{0.80}Y_{0.20}O_{3-\delta}$ (BZY20) pellets after sintering in air at 1600 ºC, for 5 hours. 87

Fig. 4.4. Total electrical conductivity of (a) $BaZr_{0.85}Y_{0.15}O_{3-\delta}$ (BZY15) and (b) $BaZr_{0.80}Y_{0.20}O_{3-\delta}$ (BZY20) obtained in this work and reported in the literature, in wet atmospheres (H_2, N_2, Ar or air). The number of each curve corresponds to the samples and testing conditions described in Table 4.1. 90

Fig. 4.5. Typical electrochemical impedance spectroscopy spectra measured in composition $BaZr_{0.85}Y_{0.15}O_{3-\delta}$, at 100 ºC and 430 ºC, in wet 10 % H_2/N_2 atmosphere and correspondent equivalent circuits. 91

Fig. 4.6. The temperature dependence of total, bulk, grain boundary conductivities (primary axis), and area specific grain boundary condutance (secondary axis), in wet 10 % H_2/N_2 atmosphere of compositions $BaZr_{0.85}Y_{0.15}O_{3-\delta}$ (BZY15) and $BaZr_{0.80}Y_{0.20}O_{3-\delta}$ (BZY20). 92

Fig. 4.7. Total conductivity of $BaZr_{0.85}Y_{0.15}O_{3-\delta}$ vs $P_{O_2}^{1/4}$, under constant P_{H_2O} at various temperatures (a) dry, (b) $P_{H_2O} = 0.0018$ atm, and (c) $P_{H_2O} = 0.036$ atm. 97

Fig. 4.8. The equilibrium constant of hydration as a function of inverse temperature for the compositions $BaZr_{0.85}Y_{0.15}O_{3-\delta}$ (BZY15) and $BaZr_{0.80}Y_{0.20}O_{3-\delta}$ (BZY20). 100

Fig. 4.9. Calculated total and partial conductivities in $P_{O_2} = 0.01$ atm at 600 ºC, as a function of water vapour partial pressure. 101

Fig. 4.10. Total and partial conductivities at $P_{O_2} = 1$atm and $P_{O_2} = 0.01$ atm, with $P_{H_2O} = 0.036$ atm, for: (a) BZY15 and (b) BZY20. 103

Fig. 4.11. Transference number vs 1000/T at $P_{H_2O} = 0.036$ atm for BZY15 and BZY20 (a) t_{ionic} and t_p at $P_{O_2} = 1$ atm, (b) t_{ionic} and t_p at $P_{O_2} = 0.01$ atm, and (c) $t_{V_O^{\cdot\cdot}} / t_{ionic}$ and $t_{OH_O^{\cdot}} / t_{ionic}$,where $t_{ionic} = t_{V_O^{\cdot\cdot}} + t_{OH_O^{\cdot}}$ . .. .105

Fig. 5.1. Phase diagram of $BaO–YO_{1.5}–ZrO_2$ adapted from ref. [143] showing the location of non-stoichiometric compositions of $Ba_{1-x}Zr_{1-y}Y_yO_{3-\delta}$, with $y = 0.20$ (Y20) and $y = 0.15$ (Y15), and $x = 0$, 0.02, 0.04, 0.06, 0.08, 0.10, 0.20 and 0.30. Area around $BaZrO_3$ expanded in inset. 108

Fig. 5.2. X-ray diffraction patterns of Ba1-$x$$Zr_{0.85}Y_{0.15}O_{3-\delta}$ compositions, $0 \le x \le 0.10$, 420 minutes after high energy milling, and the corresponding

expanded profile for 2-theta range 25º - 50º. (♦) identifies perovskite phase, and (□) identifies yttrium-doped zirconia. 112

Fig. 5.3. X-ray diffraction patterns of $Ba_{1-x}Zr_{0.85}Y_{0.15}O_{3-\delta}$ compositions, $0 \leq x \leq 0.1$, after annealing the mechanosynthesized powders, at 1250 ºC, for 5 hours, and the corresponding expanded profile for 2-theta range of 25º - 35º. (♦) identifies perovskite phase, (△) identifies Y_2O_3, and (+) identifies Ni used as internal standard. 113

Fig. 5.4. X-ray diffraction patterns of $Ba_{1-x}Zr_{0.85}Y_{0.15}O_{3-\delta}$ compositions, $0 \leq x \leq 0.1$, after annealing the mechanosynthesized powders, at 1600 ºC, for 5 hours and the corresponding extended profile for 2-theta range of 25º - 35º. (♦) identifies perovskite phase, (△) identifies Y_2O_3, and (+) identifies Ni used as internal standard. 114

Fig. 5.5. Nominal and actual Ba-deficiency of $Ba_{1-x}Zr_{0.85}Y_{0.15}O_{3-\delta}$ pellets sintered at 1250, 1500 and 1600 ºC, assessed by EPMA, $0 \leq x \leq 0.1$. 115

Fig. 5.6. Lattice parameter of $Ba_{1-x}Zr_{0.85}Y_{0.15}O_{3-\delta}$ compositions ($0 \leq x \leq 0.10$) sintered at 1500 and 1600 ºC. Open symbols correspond to multiphase-samples. 116

Fig. 5.7. SEM images of $Ba_{1-x}Zr_{0.85}Y_{0.15}O_{3-\delta}$, sintered at 1600 ºC: (a) $x = 0.02$ and (b) $x = 0.08$. 117

Fig. 5. 8. Grain size of $Ba_{1-x}Zr_{0.85}Y_{0.15}O_{3-\delta}$, after sintering at 1300, 1400, 1500 and 1600 ºC, as a function of Ba-deficiency, x. Open symbols correspond to multiphase-samples. 118

Fig. 5. 9. Ratio between yttrium concentration in grain boundary (C_{gb}) and yttrium concentration in grain interior (C_b) in $Ba_{1-x}Zr_{0.85}Y_{0.15}O_{3-\delta}$ ($x = 0$, 0.02, 0.04 and 0.06), measure by EDS-TEM analysis, and corresponding error bars. 120

Fig. 5.10. Densification (%) in function of Ba-deficiency, x, for $Ba_{1-x}Zr_{0.85}Y_{0.15}O_{3-\delta}$, sintered at 1300, 1400, 1500 and 1600 ºC, for 5 hours. Open symbols correspond to multiphase-samples. 121

Fig. 5.11. Final density in function of green density of compositions for $Ba_{1-x}Zr_{0.85}Y_{0.15}O_{3-\delta}$, $0 \leq x \leq 0.10$, sintered at 1300, 1400, 1500 and 1600 ºC, for 5 hours. 122

Fig. 5.12. Nyquist plots collected at 190 ºC for Ba-deficient samples of $x = 0.02$ and $x = 0.10$, under wet 10 % H_2/N_2 atmosphere, and respective equivalent circuits models. 123

Fig. 5.13. Arrhenius plot of total and bulk electrical conductivity, under wet 10 % H_2/N_2, of $Ba_{1-x}Zr_{0.85}Y_{0.15}O_{3-\delta}$ samples, $0 \leq x \leq 0.10$, sintered at 1600 ºC. The inset shows a comparison of the bulk conductivity of the series at 230 ºC as a function of Ba-deficiency. 124

Fig. 5.14. Impact of Ba-deficiency on grain boundary conductivity, under wet 10 % H_2/N_2, in $Ba_{1-x}Zr_{0.85}Y_{0.15}O_{3-\delta}$ samples, $0 \leq x \leq 0.10$, sintered at 1600 ºC. (a) Arrhenius plot of area specific grain boundary conductance; (b) grain boundary conductivity and (c) area specific grain boundary conductance, determined at 230 ºC, as a function of *x*. 126

Fig. 6.1. X-ray diffraction pattern of the $Ba(Pr_{1-x}Zr_x)_{0.8}Y_{0.2}O_{3-\delta}$ system prepared by solid-state synthesis, after a second sintering at 1500 ºC, highlighting broad asymmetric peak shapes suggesting the presence of inhomogenities. Arrow indicates secondary phase in composition $x = 0.75$. The marker (◆) identifies the perovskite phase. 130

Fig. 6.2.(a) X-ray diffraction patterns demonstrating the evolution of mechanical activation with milling time and formation of single-phase $Ba(Pr_{0.4}Zr_{0.6})_{0.8}Y_{0.2}O_{3-\delta}$ perovskite after annealing at 1250 ºC for 5 hours; (b) X-ray diffraction patterns of the $Ba(Pr_{1-x}Zr_x)_{0.8}Y_{0.2}O_{3-\delta}$ system prepared by a combination of high energy milling and annealing at 1250 ºC for 5 hours. Phase purity is obtained for all values of *x*. The markers identify (○) barium peroxide; (▣) yttria doped zirconia (3 mol %); (△) yttria oxide; (⊗) Pr_6O_{11}; (+) PrO_2; and (◆) perovskite phase. 132

Fig. 6.3. Reduced unit-cell parameter as a function of composition, superimposed with stability information under different atmospheres for: (a) $Ba(Pr_{1-x}Zr_x)_{0.9}Y_{0.1}O_{3-\delta}$ and (b) $Ba(Pr_{1-x}Zr_x)_{0.8}Y_{0.2}O_{3-\delta}$. Stability was analysed by X-ray diffraction analysis after heat treatment at 600 ºC. Bullet points signify stable compositions for each atmosphere. 134

Fig. 6.4. X-ray diffraction patterns of $Ba(Pr_{0.4}Zr_{0.6})_{0.9}Y_{0.1}O_{3-\delta}$, after annealing at 600 ºC in dry and wet O_2 atmospheres, highlighting instability in dry O_2. Filled and open stars indicate perovskite phases of differing lattice parameter. 137

Fig. 6.5. X-ray diffraction patterns of compositions from the systems $Ba(Pr_{1-x}Zr_x)_{0.9}Y_{0.1}O_{3-\delta}$ and $Ba(Pr_{1-x}Zr_x)_{0.8}Y_{0.2}O_{3-\delta}$ with $x = 0.2$, after annealing at 600 ºC in wet and dry H_2 atmospheres, highlighting greater stability in the system with higher Y-content and greater stabilities on dry atmospheres. 139

Fig. 6.6. Expected trends in tolerance factor with respect to the ionic size of praseodymium in different oxidation states for the $Ba(Pr_{1-x}Zr_x)_{0.9}Y_{0.1}O_{3-\delta}$ and $Ba(Pr_{1-x}Zr_x)_{0.8}Y_{0.2}O_{3-\delta}$ systems. 140

Fig. 6.7. TGA plot for the $Ba(Pr_{1-x}Zr_x)_{0.9}Y_{0.1}O_{3-\delta}$ and $Ba(Pr_{1-x}Zr_x)_{0.8}Y_{0.2}O_{3-\delta}$ systems heated under dry, flowing 100 % CO_2 at a rate of1 1 ºC·min^{-1}. 141

Fig. 6.8. Comparison of the maximum CO_2 uptake on second stage carbonation in dry flowing CO_2 with the theoretical value calculated for the stoichiometric formation of $BaCO_3$ for each composition for the systems $Ba(Pr_{1-x}Zr_x)_{0.9}Y_{0.1}O_{3-\delta}$ and $Ba(Pr_{1-x}Zr_x)_{0.8}Y_{0.2}O_{3-\delta}$. 142

Fig. 6.9. The X-ray diffraction intensity ratio between the most intense (111) reflection of the $BaCO_3$ phase and the most intense (110) reflection in the perovskite phase for samples carbonated at 600 ºC for 12 hours in wet and dry atmospheres for the systems $Ba(Pr_{1-x}Zr_x)_{0.9}Y_{0.1}O_{3-\delta}$ and $Ba(Pr_{1-x}Zr_x)_{0.8}Y_{0.2}O_{3-\delta}$, corresponding to the first stage carbonation. 144

Fig. 7.1. X-ray diffraction patterns of $Ba(Pr_{1-x}Zr_x)_{0.8}Y_{0.2}O_{3-\delta}$ ($0.20 \le x \le 0.80$) after high energy milling. The markers identify: (+) PrO_2; and (◆) perovskite phase. 148

Fig. 7.2. Evolution of powder X-ray diffraction patterns with milling time for composition $BaPr_{0.20}Zr_{0.80}O_{3-\delta}$. The markers identify: (○) barium peroxide; (□) zirconia oxide; (⊗) Pr_6O_{11}; (+) PrO_2; and (◆) perovskite phase. 149

Fig. 7.3. X-ray diffraction patterns of mechanically produced powders of compositions $BaPr_{1-x}Zr_xO_{3-\delta}$ ($0.2 \le x \le 0.8$), after annealing 1250 ºC in air. (◆) identifies perovskite phase. 150

Fig. 7.4. Room temperature Raman spectra of polycrystalline $BaPr_{1-x}Zr_xO_{3-\delta}$ samples ($0 \le x \le 1$). 151

Fig. 7.5. (a) Raman shift and **(b)** FWHM of bands A, B, C, marked at Fig. 7.4, as function of Zr content for $BaPr_{1-x}Zr_xO_{3-\delta}$. 153

Fig.7.6. Reduced (pseudo-cubic) unit-cell parameter as a function of x for $BaPr_{1-x}Zr_xO_{3-\delta}$. Data for the end-member phase $BaPrO_3$ (*Pnma*) are taken from ref. [85]. 156

Fig. 7.7. The temperature dependence of total conductivity in dry O_2 (△) and dry N_2 (□) atmospheres of compositions $BaPr_{1-x}Zr_xO_{3-\delta}$, with $x = 0.20$, 0.40, 0.60 and 0.80. 158

Fig. 7.8. The temperature dependence of total conductivity of compositions $BaPr_{1-x}Zr_xO_{3-\delta}$ in (a) dry and wet O_2 atmosphere; and (b) dry and wet N_2

atmosphere. Open symbols correspond to dry conditions, and filled symbol to wet conditions. 159

Fig. 8.1. Structure maps plotted by the tolerance and octahedral factors. Circles represent the perovskite structure and crosses the non-perovskite structure of $A^{2+}B^{4+}O_3$-type compounds, according to the collected data on the literature [225-228]. 165

Fig. 8.2. Structure maps plotted by the tolerance and octahedral factors with data of $Ba(Pr,M)O_3$ compositions, with x = 0, 0.20, 0.40, 0.60 and 0.80, zoom image on the righ. 166

Fig. 8.3. Evolution of powder X-ray diffraction patterns with milling time for composition $BaPr_{0.20}Ti_{0.80}O_{3-\delta}$. The markers identify: (○) barium peroxide; (×) TiO_2; (⊗) Pr_6O_{11}; and (◆) perovskite phase. 167

Fig. 8.4. X-ray diffraction pattern of the $BaPr_{1-x}Ti_xO_{3-\delta}$ ($0.20 \leq x \leq 0.80$) after high energy milling. The markers identify: (+) PrO_2; and (◆) perovskite phase. 167

Fig. 8.5. X-ray diffraction patterns of the $BaPr_{1-x}Ce_xO_{3-\delta}$ ($0.20 \leq x \leq 0.80$) after high energy milling. The markers identify: (○) barium peroxide; (∗) cerium oxide; (+) PrO_2; and (◆) perovskite phase. 168

Fig. 8.6. Chemical potential diagrams describing conditions for synthesis of (a) barium zirconate; (b) barium titanate; and (c) barium cerate from precursors oxides BaO_2 and m-ZrO_2, TiO_2 (anatase) and CeO_2, respectively, at 323 K and versus oxygen partial pressure. 170

Fig. 8.7. TEM images collected for powder samples of $BaPr_{0.20}Ti_{0.80}O_{3-\delta}$ after high energy milling, revealing the presence of amorphous phase. 171

Fig. 8.8. X-ray diffractions patterns of $BaPr_{1-x}Ce_xO_{3-\delta}$, x = 0.20, 0.40, 0.60 and 0.80, prepared by high energy milling with further annealing in air at 1250 ºC, and after annealing in air at 1250 ºC. The marker (◆) identify the main peaks of $BaCeO_3$ 172

Fig. 8.9. X-ray diffraction patterns of high-milled powders corresponding to $BaPr_{1-x}Ti_xO_{3-\delta}$ compositions (x = 0.20, 0.40, 0.60 and 0.80), after annealing in air, at 1250 ºC. The markers identify: (⊗) Pr_6O_{11}; (■) Ba_2TiO_4; (◇) $BaPrO_3$; and (◆) $BaTiO_3$. 173

Fig. 8.10. X-ray diffraction powder patterns of $BaPr_{0.20}Ti_{0.80}O_{3-\delta}$ samples at room temperature and after annealing at 200, 600 and 1250 ºC, in air. The markers identify: (■) Ba_2TiO_4; (⦿) $BaCO_3$; and (◆) perovskite phase. 174

LIST OF TABLES

Table 1.1. Total conductivity of selected oxide-ion conducting electrolytes. 10

Table 2.1. Precursors mixtures used in the preparation of perovskite compositions..... 32

Table 2.2. Thermal cycles and relative density of samples used in impedance measurements. The dwell time is 5 hours for all the samples. 46

Table 3.1. Summary of chemical analysis by ICP-AES of $BaZr_{1-y}Y_yO_{3-\delta}$ powders prepared by mechanosynthesis, including analysis of the initial mixture of precursors respecting to the composition $BaZr_{0.85}Y_{0.15}O_{3-\delta}$ precursor for comparative purposes. 56

Table 3.2. Crystallite size and root-mean-square strain calculated from size-strain plot for $y = 0$, $y = 0.06$ and $y = 0.15$ compositions, with 420, 300 and 420 minutes of milling time respectively, and comparison with particle size observed by TEM. Table also includes lattice parameters of compositions sintered at 1250 ºC for 5 hours. 60

Table 3.3. Relative density (% ThD) of mechanosynthesised composition $y = 0.15$, with 420 minutes of milling time, compared with literature values for $BaZr_{1-y}Y_yO_{3-\delta}$ prepared by a wide range of synthesis routes. 66

Table 3.4. Weight percentages of $BaZrO_3$, $BaCO_3$ and amorphous phase after room temperature mechanosynthesis for each set of precursors..... 79

Table 4.1. Processing methods, sintering profile and characteristics of compositions of $BaZr_{0.85}Y_{0.15}O_{3-\delta}$ (BZY15) and $BaZr_{0.80}Y_{0.20}O_{3-\delta}$ (BZY20) obtained in this study, and reported in the literature. 88

Table 4.2. Comparison of the activation energy (E_a) of bulk, grain boundary, and total conductivity of $BaZr_{0.85}Y_{0.15}O_{3-\delta}$ (BZY15) and $BaZr_{0.80}Y_{0.20}O_{3-\delta}$ (BZY20), in wet 10 % H_2/N_2. 92

Table 4.3. The slopes, intercepts and linear correlation coefficients, *r*, obtained by linear fitting of σ_{tot} vs $P_{O_2}^{1/4}$ plots for the compositions $BaZr_{0.85}Y_{0.15}O_{3-\delta}$ and $BaZr_{0.80}Y_{0.20}O_{3-\delta}$. 98

Table 4.4. Calculated parameters α, $K_w \sigma^*_{OH_O^\bullet}$, $\sigma^*_{V_O^{\bullet\bullet}}$, and σ^*_p at different temperatures for the compositions $BaZr_{0.85}Y_{0.15}O_{3-\delta}$ and $BaZr_{0.80}Y_{0.20}O_{3-\delta}$. 99

Table 4.5. Activation energy (E_a) of proton, oxide-ion and p-type conductivity for compositions BZY15 and BZY20. 104

Table 5.1. Average grain size and activation energy values of bulk and grain boundary conductivities of $Ba_{1-x}Zr_{0.85}Y_{0.15}O_{3-\delta}$, $0 \leq x \leq 0.10$, in the temperature range of 140 – 280ºC. 125

Table 7.1. Structural parameters, agreement factors and additional structural information for $BaPr_{1-x}Zr_xO_{3-\delta}$ obtained from Rietveld refinement of XRD data[a]. 155

Table 7.2. Activation energy of electrical conductivity in $BaPr_{1-x}Zr_xO_{3-\delta}$ as a function of Zr concentration, in O_2 and N_2 atmospheres, at 500 - 1000 ºC..... 160

Table 8.1. Size mismatch, denoted as $(r_M - r_{Pr})/r_{Pr}$ between the dopant Pr and M cations in $BaPr_{1-x}M_xO_{3-\delta}$ sytems (M = Zr^{4+}, Ce^{4+} and Ti^{4+}). 175

Table A.1. Two-phase equilibria in the ZrO_2-BaO-O_2 system. 203

LIST OF SYMBOLS

A	Area
A_0	Pre-exponential factor for conductivity
C	Capacitance
Cp	Heat capacity
d	Interplanar distance
e_{rms}	Root-mean-square strain
E_a	Activation energy
i	Current
I_0	Amplitude of current
K	Equilibrium constant
L	Length
P_{H_2O}	Water partial pressure
P_{O_2}	Oxygen partial pressure
Q	pseudo-capacitance
r_A	Ionic radius of the A-site cation
r_B	Ionic radius of the B-site cation
R	Ideal gas constant
R_b	Bulk (grain interior) resistance
R_{gb}	Grain boundary resistance
t	Tolerance factor
t_i	Transport number of “i” species
T	Temperature
v	voltage
V_0	Amplitude of voltage
Z	Impedance
β	Integral breadth
ΔG	Free energy change
ΔH	Enthalpy change
ΔS	Entropy change
ε	Average apparent diameter
ε_0	Vacuum permeability
ε_r	Relative permeability
η	Mean value of the strain
σ	Electrical Conductivity
ϕ	Phase shift
ω	Angular frequency

LIST OF ACRONYMS

AC	Alternating Current
AFC	Alkaline Fuel Cell
BET	Brunauer-Emmet-Teller
BIMEVOX	Bismuth Metal (dopant) Vanadium Oxide
CPE	Constant Phase Element
DC	Direct Current
DAFC	Direct Alcohol Fuel Cells
DCFC	Direct Carbon Fuel Cells
EDS	Energy Dispersive X-ray Spectroscopy
EIS	Electrochemical Impedance Spectroscopy
EPMA	Electron-Probe Micro-Analysis
FT-IR	Fourier Transform InfraRed Spectroscopy
FWHM	Full Width at Half Maximum
H-SOFC	Proton-Conducting SOFC
HTPC	High Temperature Proton Conductors
ICP-AES	Inductively Coupled Plasma Atomic EmissionSpectroscopy
LAMOX	La_2Mo2O_9 -based materials
MCFC	Molten Carbonate Fuel Cells
MEA	Membrane-Electrode Assembly
ODS	Oxide Dispersion Strengthening
O-SOFC	Oxide-Ion Conducting SOFC
PEMFC	Polymer Electrolyte Membrane Fuel Cell
PAFC	Phosphoric Acid Fuel Cells
PCFC	Proton Ceramic Fuel Cells
RE	Rare-Earth
SEM	Scanning Electron Microscopy
SOFC	Solid Oxide Fuel Cells
TEM	Transmission Electron Microscopy
TGA	Thermal Gravimetric Analysis
UPS	Uninterruptible Power Supply
XRD	X-Ray Diffraction

1. INTRODUCTION

1.1. HISTORICAL BACKGROUND AND OVERVIEW OF FUEL CELLS

A fuel cell is an electrochemical device that converts chemical energy, via redox reactions, directly in electrical energy (and heat). The operating principles of fuel cells are similar to those of batteries, where the energy-generation processes occur through two electrodes in contact with an ion-conducting electrolyte and the electron and ion transport are separated. However, contrary to that of batteries, in which the electrodes, besides being a charge-transfer medium, are also "active masses" in the electrochemical reactions, being consumed during operation, fuel cells are open systems where the fuel and oxidant are provided to the electrodes outside the cells and the electrodes are not consumed. Hence, fuel cells continue to operate as long as reactants are supplied to the electrodes and without requiring periodic component replacement or recharging [1–6].

The best known early fuel cells experiments were performed in the middle of 19th century and were attributed to Sir William R. Grove (1811-1896) and Christian Friedrich Schoenbein (1799-1868). Grove built the first fuel cell in the 1840´s, which he named a "gaseous voltaic battery", consisting of platinum electrodes in two small upturned glass vessels, one containing oxygen and the another hydrogen, and both immersed in a sulphuric acid solution (electrolyte). Grove observed that voltage was generated between the two electrodes and that higher voltages could be obtained by linking several cells together [3,6].

However, it was Christian Friedrich Schoenbein (1799-1868), in 1839, who firstly reported the "fuel cell effect", as the generation of current flow from the reaction of the gaseous fuels hydrogen and oxygen, though the inverse electrolysis process [6].

Despite the early introduction of fuel cells, their development was notably slow during the first century of their discovery. This is mainly due to the existence of easily accessible primary energy sources that were unrestricted and inexpensive and the success of the internal

combustion engine that overshadowed the potentialities of fuel cell technology at that time [3,7].

The resurgence of interest in fuel cell technology in the 20th century is attributed mainly to its use in the U.S. Space Program [7]. The first polymer membrane fuel cells were used in the Gemini program in the early 1960s [4]. Subsequently, in 1969, the Apollo missions also used fuel cells to supply the electric power for life support, guidance, and communications, as well as to provide water for the crew throughout missions on the moon [6]. Although the use of fuel cells for aerospace applications has been successfully implemented and continues until today, its development for terrestrial applications did not become significant until the 1990s [4]. Over the last three decades, increasing concern about the environmental consequences of fossil fuels used in the production of electricity and for the propulsion of vehicles coupled with economic, politic and social problems that can arise from extensive dependence of industrialized countries on oil, a factor that became tangibly apparent during the oil crisis, led to renewed interest by governments and industry on the development of alternatives for the generation and/or conversion power systems that could be more efficient and environmental friendly [3].

In this context, fuel cell technologies have experienced an exponential increase in attention in the drive to lower the dependence on fossil fuels and diminish poisonous emissions into the atmosphere [3]. Fuel cells present higher efficiencies compared with common internal combustion engines due to the fact that they are not subject to the Carnot limitation. The possibility of co-generation of electricity and heat in fuel cell systems allows further improvements in their overall efficiency. In addition, fuel cells are quiet, can operate with a wide variety of fuels and, as a modular technology, allow the existence of different power-scale plants, while being ideal for remote site locations and applications where an Uninterruptible Power Supply (UPS) is required and/or need independence from the utility grid [1,8].

The integration of fuel cells in renewable energy systems, enabling the generation of energy in a truly clean, efficient and sustainable way, offers the most relevant added value potential for fuel cell technology [8]. At the present time, the main barrier for the widespread use of many

renewable energy sources, such as photovoltaic, hydroelectric and wind power, is their intermittent nature. The electricity is highly variable at different time-scales, from hour to hour, daily and/or seasonally, which leads to serious problems to assure grid stability solely from renewable energy generation. In this context, the use of integrated systems with the production of hydrogen by water electrolysis using renewable generated electrical energy, the storage of hydrogen, and finally fuel cells to regenerate electricity from the stored fuel, can both circumvent the inherent intermittency problem of renewable energy sources, and also offer an efficient and environmental friendly closed process to produce energy. Indeed, using pure hydrogen, fuel cells only produce water, without formation of any other emissions, contrary to that which occurs when other hydrocarbon power generation systems are used [8]. Despite these potentialities, fuel cells are currently not adopted on a full commercial scale and still require several technical advances to become a more reliable and competitive technology [7]. Indeed, many fuel cell power systems are still complex chemical plants that need sophisticated manufacturing techniques and control circuitry [1]. Their performance and durability may be negatively affected by the presence of impurities in the gas stream and pulse demands and the cost of fuel cell power systems is still too high [1]. Simplification of fuel cell design, e.g. reduction in the number of parts, lowered material costs and cost of manufacture units, without compromising fuel cell performance, are the main challenges to make fuel cells technical and economically competitive to a wider range of stationary, transport and portable applications.

Currently, several different types of fuel cells are under development [9]. Fuel cells are commonly classified by the type of electrolyte used in five main groups: Alkaline Fuel Cell (AFC), Polymer Electrolyte Membrane Fuel Cell (PEMFC), Phosphoric Acid Fuel Cells (PAFC), Molten Carbonate Fuel Cells (MCFC), or Solid Oxide Fuel Cells (SOFC). Correspongingly, an aqueous solution of potassium hydroxide, a hydrated polymeric ion exchange membrane, a phosphoric acid immobilized in a SiC-based matrix, LiK or LiNa-based molten alkaline carbonates salts in a porous ceramic matrix, and solid oxide ceramic materials, are the electrolytes in AFC, PEMFC, PAFC, MCFC and SOFC's fuel cells, respectively [1,3,4]. In parallel to this classification some fuel cells are classified by the type

of fuel used, such as Direct Alcohol Fuel Cells (DAFC), that use alcohol without reforming, and Direct Carbon Fuel Cells (DCFC), that use directly carbon rich material such as biomass or coal [5]. In turn, the choice of electrolyte dictates the operating temperature range of fuel cell, which determines the type of materials used and the degree of fuel processing. According to the operating temperature fuel cells are commonly grouped as the so called low-temperature and high-temperature fuel cells. Low-temperature fuel cells typically have operating temperatures of about 220 ºC or lower, and include alkaline fuel cells (< 100 ºC), polymeric exchange membrane fuel cells (60 – 120 ºC), and phosphoric acid fuel cells (120 – 220 ºC) [3,4]. The aqueous electrolyte present in these cells requires low operating temperatures, due to their high vapour pressure and rapid degradation at higher temperatures [4]. High-temperature fuel cells include molten carbonate fuel cells (400 – 800 ºC) and solid oxide fuel cells (500 – 1000 ºC) [3].

Low-temperature fuel cells require high fuel purity (all the fuel must be converted in hydrogen prior entering the fuel cell) due to the inability to internally reform hydrocarbon fuels at these temperatures and the potential to poison precious-metal catalysts (usually platinum), which are required to enhance electrode kinetics, by CO and CO_2 [7]. Conversely, high-temperature fuel cells may operate with different hydrocarbon fuels and are not prone to CO and CO_2 contamination [3], as the use of high operating temperature improves the kinetics of electrode reactions eliminating the need of noble catalysts. The applicability of high temperature fuel cells for internal reforming, using the waste heat in a combined cycle power plants, offers a consequent improvement on maximum levels of total efficiency [3]. However, higher operating temperatures also require long start-up times, large energy inputs to heat the cell to the operating temperature, and severe restrictions on the choice of materials.

According to their features, fuel cells are, therefore, devoted to different type of applications, namely, stationary power, electronic portable and automotive. For example, alkaline fuel cells are preferred for aerospace applications; phosphoric acid fuel cells for small stationary power plants (< 10 MW); polymer electrolyte fuel cells for automotive, micro, portable, and small stationary power plants; molten carbonate fuel cells for small power plants; and solid oxide

fuel cells for small and large stationary power plants, portable power and auxiliary power in automobiles [3,4].

1.2. SOLID OXIDE FUEL CELLS: DESIGNS, OPERATING PRINCIPLES AND MATERIALS

High energy-conversion efficiency, environmental safety, fuel flexibility, possibility of complete internal reforming and recovery of exhaust heat for co-generation in bottoming cycles, are the primary attractions to use solid oxide fuel cells as energy conversion devices [1–6].

A single-cell of a solid oxide fuel cell, also named a Membrane-Electrode Assembly (MEA), is an all solid-state system composed by a non-porous metal oxide electrolyte sandwiched between two porous metal, ceramic or composite ceramic-metal (cermet) electrodes. The fuel is supplied to the anode and the oxidant, usually oxygen, to the cathode. Half-cell reactions occur on the electrodes, producing ions, which can traverse the electrolyte, together with electrons, heat and oxidised products (water and/or carbon dioxide). Direct chemical combustion is prevented by the electrolyte, which acts as a barrier to gas diffusion, but which allows ions to migrate across it. The electrons transported through an external circuit provide electrical energy [5,9–14]. In real applications, single-cells are connected in series to form stacks, in order to achieve commercially useful output. The connection between the cells is done via an interconnect, a component of high stability and electronic conductivity that may be ceramic or metallic in nature. At present, different SOFC designs have been developed, which mainly differ in the shape of each cell, the method of connecting between each cell, or the flow of fuel and oxidant through their channels [1–3,5,9,11,12]. However, the two most common stack designs of SOFC are the tubular and planar designs, illustrated in Fig. 1.1.

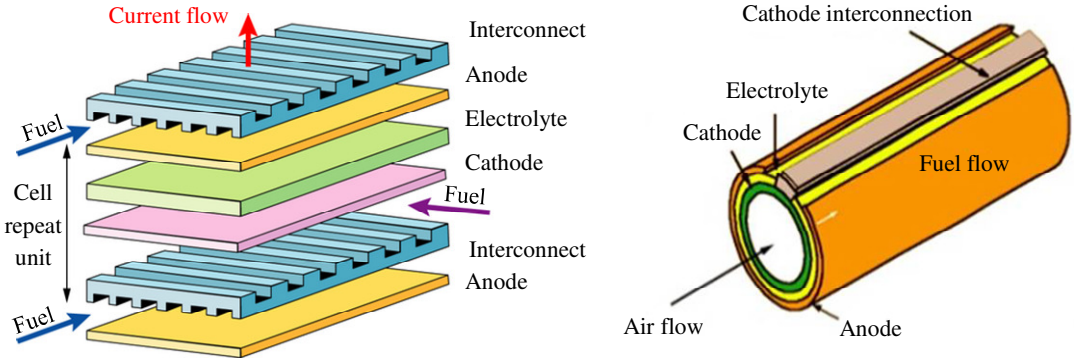

Fig. 1.1. Schematic of planar (left) [15] and tubular (Siemens-Westinghouse) [16] (right) SOFC designs.

The choice of SOFC materials should fulfil several criteria in order to assure their maximum performance in own function and its use with the other cell components, as well as its use at operating temperatures and during several years. Common requirements of SOFC electrode materials are [9,11,17]:

- mixed electronic-ionic or electronic conductivity. Typically electrode conductivity should be higher than 10 $S \cdot cm^{-1}$. The presence of ionic conductivity in electrode materials is found to be preferable due to allowing the electrochemical reactions to occur over an enlarged active volume, enhancing reaction rates;
- sufficient porosity, to facilitate the transport of the oxidant/fuel to the electrocatalytic sites of cathode/anode;
- good catalytic activity (for oxygen dissociation and reduction in cathode, and fuel oxidation in anode);
- chemical and mechanical compatibility with other cell materials (the electrodes should be chemically stable, and with minimum thermal expansion mismatch in respect to other cell components);
- reasonable tensile strength, fracture toughness and thermal shock resistance, for ease handling and to withstand thermal and mechanical stresses during fabrication and cell operation;
- low vapour pressure to avoid loss of material.

The SOFC electrolyte material should possess [9,13]:

- high density, with no open porosity, to avoid cross diffusion of fuel and oxidant;
- high ionic conductivity (0.01 - 0.1 $S \cdot cm^{-1}$) and negligible electronic conductivity, at the operating temperatures and in oxidising and reducing conditions, to provide a fast ionic transport and to reduce the leakage current.

The interconnects should be [3,9,11]:

- stable in both operating oxidizing and reducing atmospheres, since they are in contact with both electrodes;
- high electronically conductivity, to provide the electronic contact between the electrodes;
- impervious to fuel and oxidant gases, to provide fuel and oxidant separation between the adjacent cells.

In addition, the desired components of SOFCs should possess competitive cost for both of raw materials and the processing. Depending on the ion species conducted by electrolyte, one can considered two different types of SOFC's: Oxide-ion conducting Solid Oxide Fuel Cell (O-SOFC), and Proton-conducting Solid Oxide Fuel Cell (H-SOFC).

1.2.1. OXIDE-ION CONDUCTING SOFC (O-SOFC)

Oxide-ion conducting Solid Oxide Fuel Cells (O-SOFCs) were the first ceramic fuel cell to be developed and are the most widely used and studied. Transport of oxide-ions from the cathode to the anode is done through the medium of an oxide-ion conducting electrolyte (Fig. 1.2).

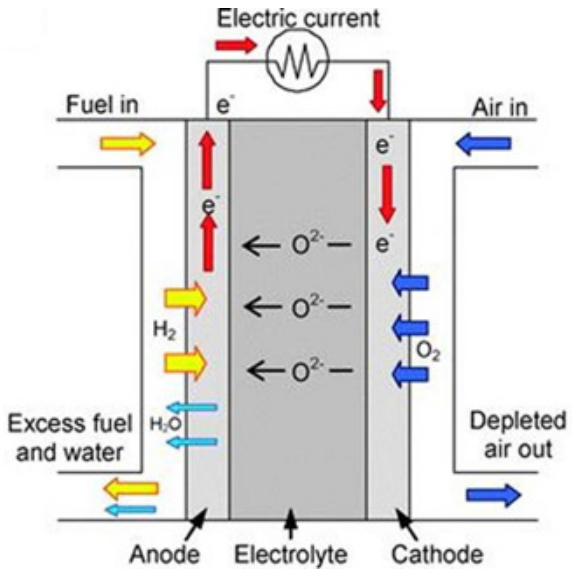

Fig. 1.2. Basic operating principle of oxide-ion conducting solid oxidefuel cell (O-SOFC) considering that the fuel is hydrogen and air the supplier of oxygen [18].

At the cathode, oxide-ions are formed by the dissociation and reduction of oxygen, with the consumption of electrons,

$$O_2 + 4e^- \rightarrow 2O^{2-} \quad (1.1)$$

These oxide-ions are conducted through the electrolyte and combined with fuel (H_2 and/or CO, CH_4) at the anode forming water and/or CO_2 and heat:

$$2H_2 + 2O^{2-} \rightarrow 2H_2O + 4e^- \quad (1.2)$$

$$2CO + 2O^{2-} \rightarrow 2CO_2 + 4e^- \quad (1.3)$$

$$½\ CH_4 + 2O^{2-} \rightarrow H_2O + ½\ CO_2 + 4e^- \quad (1.4)$$

The movement of oxide-ions through the electrolyte is usually dominated by oxide-ion vacancies in the crystal structure, and their thermally-activated hopping through the crystalline lattice, with a superimposed drift due to the electric field [14,19]. Accordingly,

the ion conductivity is strongly temperature dependent, but at high temperatures can reach values comparable to those presented by liquid electrolytes (~1 $S \cdot cm^{-1}$) [14,19].

The lattice crystal of an oxide-ion conducting electrolyte material should ensure that the unoccupied sites are energetically similar to those occupied by the lattice oxide-ions, to minimise the energy involved in the migration of oxide-ions (less than about 1 eV), with a low concentration of electronic carriers [19]. The most conventional oxide-ion conducting electrolytes materials comprise: fluorite-structured oxides ($A_{1-x}B_xO_{2-\delta}$) such as, fully or partially stabilised zirconia (e.g. 3 - 10 mol% Y_2O_3-ZrO_2, 9 mol% Sc_2O_3-ZrO_2), doped ceria (e.g. $Ce_{1-x}Gd_xO_{2-\delta}$, $Ce_{1-x}Sm_xO_{2-\delta}$) or δ-Bi_2O_3 related structures (e.g. 20 mol% Er_2O_3-Bi_2O_3, 15 mol% Ni_2O_5-Bi_2O_3), and perovskite-type structures such as (Sr,Mg)-doped $LaGaO_3$ ($La_{1-x}Sr_xGa_{1-y}Mg_yO_{3-\delta}$) [18–20].

Apart from conventional materials, novel oxide-ion conducting materials, with alternative structures and ionic conducting mechanisms, have been developed, in view of applications as O-SOFC electrolytes. The more promising examples include: $La_2Mo_2O_9$-based materials (LAMOX)[21–23], based Si- and Ge-lanthanum apatites, $La_{9.33}(MO_4)_6O_2$ (M = Si, Ge) [24-29], tetrahedrally-coordinated gallium oxides, such as $La_{1-x}Ba_{1+x}GaO_{4-x/2}$ and $La_{1-x}Sr_{1+x}GaO_{4x/2}$ [30–35], $Ca_{12}Al_{14}O_{33}$ (maynite structure) [36], or the Bi_2O_3 related system, based on parent oxide $Bi_4V_2O_{11}$, named as BIMEVOX (e.g. $Bi_2Mg_xV_{1-x}O_{5.5-3x/2}$) [37,38]. Electrical conductivity of selected oxide-ion conducting electrolyte are presented in Table 1.1.

Table 1.1. Total conductivity of selected oxide-ion conducting electrolytes.

Material	σ, $S \cdot cm^{-1}$ (*T*, ºC)	σ, $S \cdot cm^{-1}$ (*T*, ºC)	Reference
3 mol% Y_2O_3-ZrO_2	0.058 (1000)	0.018 (800)	[39]
8 mol% Y_2O_3-ZrO_2	0.178 (1000)	0.052 (800)	[20]
10 mol% Y_2O_3-ZrO_2	0.136 (1000)	0.037 (800)	[20]
8 mol% Sc_2O_3-ZrO_2	0.31 (1000)	0.12 (800)	[40]
9 mol% Sc_2O_3-ZrO_2	0.34 (1000)	0.109 (800)	[40]
$Ce_{0.7}Gd_{0.3}O_{1.85}$	0.25 (1000)	0.093 (800)	[41]
$Ce_{0.8}Sm_{0.2}O_{1.9}$	0.25 (1000)	0.096 (800)	[20]
$La_{0.9}Sr_{0.1}Ga_{0.8}Mg_{0.2}O_{3-\delta}$	0.316 (1000)	0.121 (800)	[42]
$La_{0.8}Sr_{0.2}Ga_{0.83}Mg_{0.17}O_{3-\delta}$	-	0.17 (800)	[43]
20 mol% Er_2O_3- Bi_2O_3	-	0.37 (700)	[44]
β-$La_2Mo_2O_9$	-	0.082 (800)	[21]
$La_{10}(SiO_4)_6O_3$	-	0.0014 (700)	[29]

1.2.2. PROTON-CONDUCTING SOFC (H-SOFC)

In the 1980's, work conducted by Iwahara and co-workers [45] noted appreciable protonic conduction under hydrogen-containing atmospheres at high temperatures in ceramic oxides of doped strontium and barium cerates. Since this time the search for similar ceramic proton conductors has been an active line of research for the development of H-SOFCs and other electrochemical devices, such as, steam electrolysers, hydrogen pumps and sensors [45,46][20]. Application of high temperature proton conductors (HTPC) in SOFC technology enables the reduction of the operating temperature in comparison to the conventional O-SOFCs, due to the lower activation energy of protonic transport which allows suitable levels of ionic conductivity to be exhibited in the intermediate temperature range

(400 ºC - 700 ºC) [10,47,48]. Such reduction of operating temperatures can alleviate degradation of materials and extend component lifetimes. An additional advantage of the H-SOFCs is that the formation of steam on the cathode side avoids the dilution of fuel, thereby potentially improving the overall fuel cell efficiency [49]. In proton conducting solid oxide fuel cells oxygen and protons are introduced at the cathode and anode, respectively (Fig. 1.3).

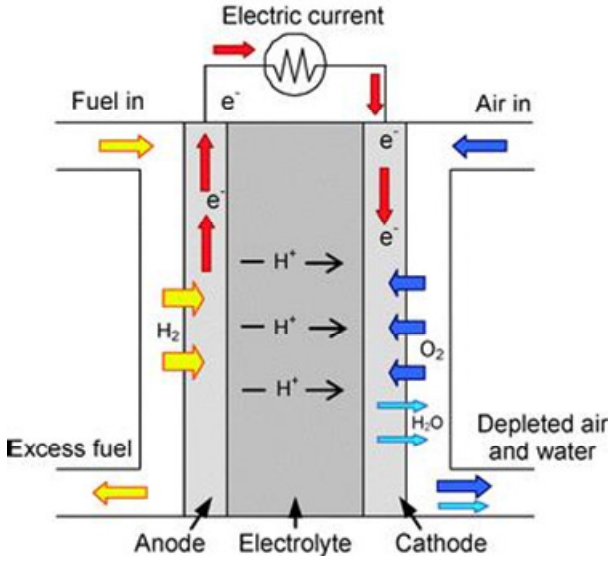

Fig. 1.3. Basic operating principle on proton-conducting solid oxide fuel cell (H-SOFC) considering that the fuel is hydrogen and air the supplier of oxygen [18]

In its simplest form, at the cathode side, the oxygen reduction produces water, while at the anode hydrogen oxidation produces protons, able to migrate through the electrolyte, according to the following general cathode and anode reactions (1.5) and (1.6), respectively.

$$\tfrac{1}{2}\, O_2 + 2H^+ + 2e^- \rightarrow H_2O \qquad (1.5)$$

$$H_2 \rightarrow 2H^+ + 2e^- \qquad (1.6)$$

Perovskites-type oxides based on acceptor-doped cerates and zirconates $BaZr_{1-x}M_xO_{3-\delta}$ and $BaCe_{1-x}M_xO_{3-\delta}$, with M a trivalent cation (e.g. Y^{3+}, Gd^{3+},Sc^{3+}, In^{3+}), have been the most

widely studied proton conducting systems, and continue, nowadays to dominate the research on proton conductors SOFCs [18,45,50–55].

Nonetheless, high proton conductivity has also been achieved for complex perovskites structures of the type $A_2(B'B'')O_6$ and $A_3(B'B'')O_9$, where A is a divalent cation, B′ is a divalent or trivalent cation, and B″ is a pentavalent cation. Some examples include $Sr_2Sc_{1+x}Nb_{1-x}O_{6-\delta}$ (with $x = 0.05$ and 0.1) [56] $Sr_3Ca_{1.18}Nb_{1.82}O_{9-\delta}$ [57], or $Sr_3CaZr_{0.5}Ta_{1.5}O_{8.75}$ [58].

Firstly proposed as oxide-ion conductors, brownmillerite-type $Ba_2In_2O_5$ materials have attracted considerable interest due to their ability to also conduct protons [59–64]. Evidence of proton conductivity has also been found in $Ba_2In_2O_5$ at low temperature (< 400 ºC) [59], in Sn- doped $Ba_2In_2O_5$ [64], $(Ba_{1-x}La_x)_2In_2O_{5+x}$ [65], and in $Ba_2(In_{1-x}Ti)_2O_{5+x}$ systems [66]. Other high temperature proton conductors include phosphates, such as Ca- and Sr- $LaPO_4$ [67,68], and polyphosphates, such as Sr- doped LaP_3O_9 and $La_7P_3O_{18}$)[69,70]. For comparison, Fig. 1.4 illustrates the proton conductivity behaviour of the most known proton conductors [47].

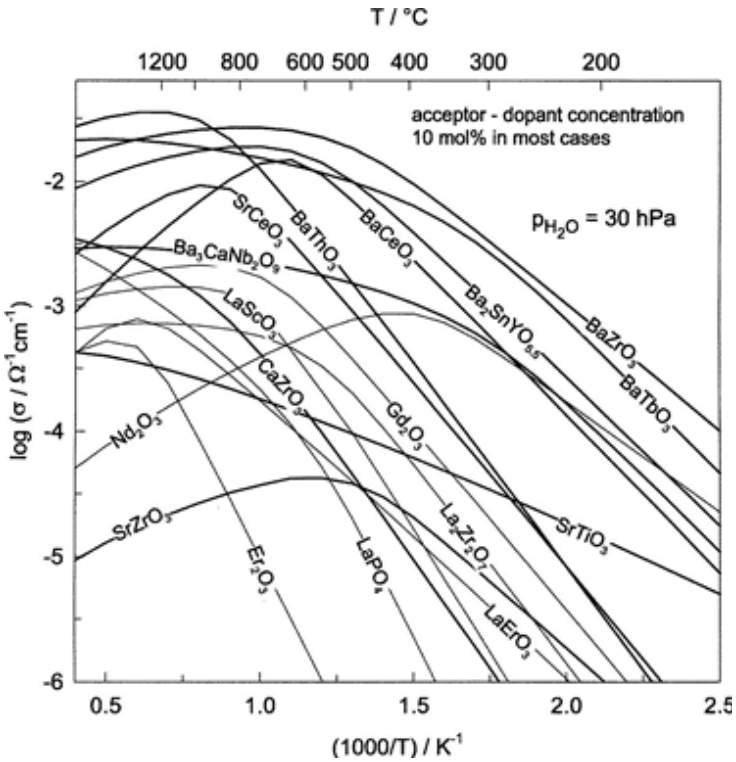

Fig. 1.4. Proton conductivity of various oxides as calculated from data on proton concentrations and mobilities, according to Norby & Larring [71].

More recently, in research conducted by Norby et al. [72], novel proton conducting materials have also been suggested based on niobates and tantalates, of general formula $RE_{1-x}A_xMO_4$, where RE = La; M = Ta or Nb; A = Ca, Sr or Ba. As in the other systems, acceptor doping is required for formation of oxygen vacancies, however, in the $RE_{1-x}A_xMO_4$ compounds, the conductivity enhancement is observed for comparatively very low doping levels (~1%). Although the protonic conductivity of these materials is lower in respect to the benchmark perovskite-type cerates (for optimally doped niobates is in order of 10^{-3} S·cm^{-1}), they show much higher stability in CO_2 containing atmospheres [72]. Similar proton conductivities have also been reported in similar structures of gallium-based oxides, with general formula $La_{1-x}Ba_{1+x}GaO_{4-x/2}$ [30–32].

Due to the aforementioned possibility to obtain proton conductivity also in ceramic materials that are not oxides, e.g. the phosphates materials, proton conducting solid oxide fuel cells have

been attributed with a more generic acronym in the recent literature of PCFC, standing for Proton Ceramic Fuel Cell.

1.3. PEROVSKITE-PROTON CONDUCTORS

1.3.1. PEROVSKITE-TYPE STRUCTURE

The general formula of perovskite-type oxides can be written as ABO_3, where, generally, the A-site cation with +2 valence, has a larger ionic radius than the tetravalent, commonly transition metal, B-site cation.

The perovskite structure comprises a network of corner-sharing BO_6 octahedra, with the larger A-cation occupying the interstices between these units (Fig. 1.5). The coordination numbers of A and B- cations are 12 and 6, respectively.

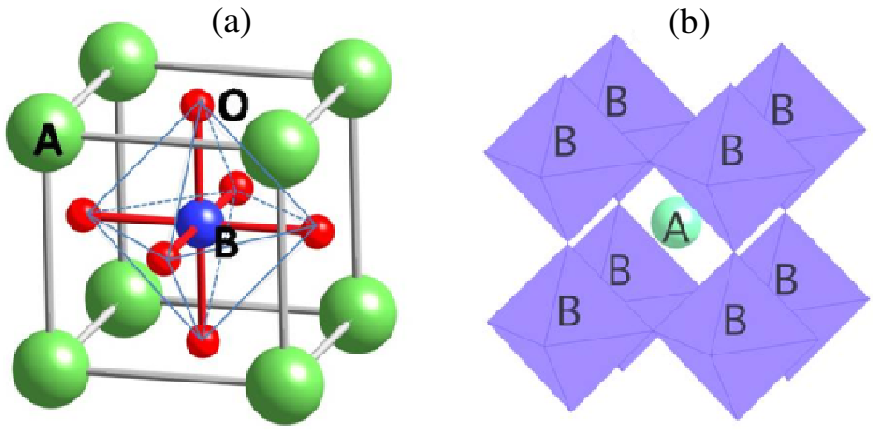

Fig. 1.5. Two schematic representations of cubic perovskite structure ABO_3 with the origin centered at **(a)** B-site ion and **(b)** A-site ion (polyhedron representation) [73].

In an ideal cubic perovskite structure, the octahedra are aligned along their axes, however, most of perovskites present deviations from cubic symmetry, caused by different mechanisms [74,75], namely:

a) distortions of BO_6 octahedra;

b) displacement of the B-site cation within the octahedron;

c) displacement of the A-site cation;

d) tilting of the octahedra relative to one another.

The first mechanism, distortions of BO_6 octahedra, is associated with the presence of Jan-Teller effects, the second and third mechanisms are typical of ferroelectric distortion, while tilting of the octahedra, forth mechanism, arises from the need to optimize the coordination of the A cation, when the A-site cation is too small for the dodecahedral site [74,76].

The transitions occur on the progressive loss of tilting of layers of the BO_6 octahedra around the four-fold axes of the cubic aristotype [75]. In order to describe the octahedral tilting in perovskites the notation introduced by Glazer [77] is commonly used, in which different tilting systems are identified in terms of the rotations of layers of successive octahedral along an axis. Then, one uses $a^{\#}b^{\#}c^{\#}$ to denote different tilting systems where # can be "*0*", "+", or "- ". "*0*" means no rotation around the corresponding axes, "+" means that the tilting of layers of successive octahedra along an axis are equal (in-phase), and "-" means that the tilting is in the opposite sense to the adjacent layers of octahedral (anti-phase). Repeated letters among $a^{\#}b^{\#}c^{\#}$ means that the corresponding rotations have the same magnitude.

The distortions result in systems with lower symmetry and extended unit cells, such as orthorhombic, rhombohedral or tetragonal structures [78,79].

The relations between tilt system and space group have been outlined by Howard and Stokes [80] (Fig. 1.6).

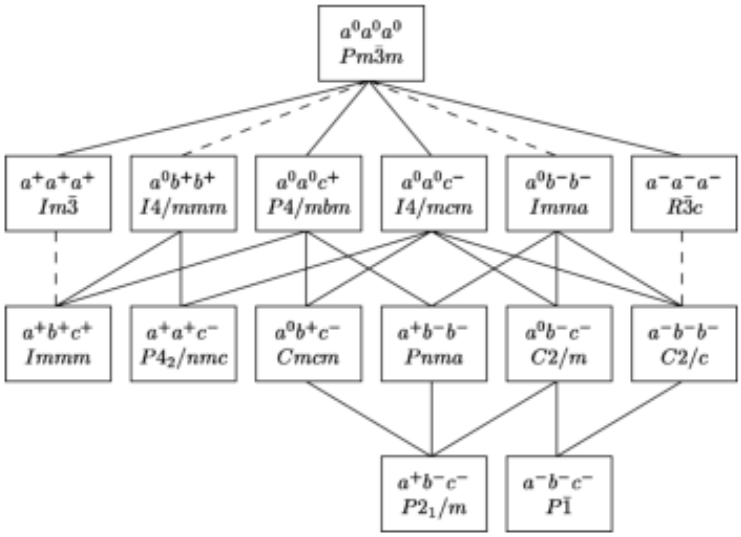

Fig. 1.6. Schematic diagram indicating the relation between tilt system and space group. The dashed lines indicate first-order phase transitions and the filled lines correspond to the second-order phase transitions [80,81].

In this respect, Goldshmidt quantified the extent of distortion of the perovskite from the ideal cubic structure, with a factor, known as the Goldschmidt tolerance factor (*t*) [82], which takes into account the ionic radii of A- and B- site cations:

$$t = \frac{(r_A + r_O)}{\sqrt{2}(r_B + r_O)} \tag{1.7}$$

where r_A, r_B and r_O are the ionic radii of A- and B-site cations and oxide-ions, respectively. In complex perovskites, where more than one ion occupies the A- and/or B-site, one considers the average radius of the ions on each site for the calculation of r_A and r_B.

Perovskites very often exhibit a number of symmetry changes with an increase in tolerance factor that can occur on increasing temperature or with changes in composition. $A^{2+}B^{4+}O_3$ perovskites commonly display the space group sequence $Pbnm \rightarrow Ibmm \rightarrow I4/mcm \rightarrow Pm\bar{3}m$ on the pathway from orthorhombic to cubic symmetry

[83,84]. Other similar sequences have also been reported, with $R\bar{3}c$ observed prior to cubic symmetry for $BaCeO_3$, $BaPrO_3$, and $BaPr_{0.9}Y_{0.1}O_{3-\delta}$ [85,86].

Reaney and coworkers [87,88] have shown a correlation between the tilting characteristics and the tolerance factor. At room temperature, perovskites with tolerance factor in the range $0.985 < t < 1.06$ are associated with untilted cubic structures $Pm\bar{3}m$. In the range $0.964 < t < 0.985$, anti-phase tilting only Ibmm (orthorrombic), $R\bar{3}c$ (rhombohedral), or *I4/mcm* (tetragonal) are usually exhibited, whereas for $t < 0.964$, both in-phase and anti-phase tilting occur, with structures in this regime most commonly crystallising in the *Pbnm* (orthorrombic) space group (alternative setting of *Pnma*). Close relations between physical properties and the tolerance factor are frequently reported, showing that tolerance factor largely controls the thermodynamic of perovskites [89].

1.3.2. FORMATION OF PROTONIC DEFECTS

The presence of proton conductivity in perovskites oxides involves the formation of protonic defects, $OH_O^{\bullet}$, in hydration conditions, which in turn requires the presence of oxygen vacancies, $V_O^{\bullet\bullet}$, in the perovskite structure [47]. Oxygen vacancies are typically formed to compensate the addition of acceptor dopant cations. In this way, when $BaZrO_3$ or $BaCeO_3$ are doped on the B-site by lower valence elements, typically Y^{3+} or other rare earth metals (e.g. Gd, Yb, Sc, In), the substitution is charge-compensated by the formation of an oxygen vacancy.

In the $BaZrO_3$ system, for example, the replacement of Zr^{4+} ions with Y^{3+} cations is charge-compensated by formation of oxygen vacancies, according to the defect reaction:

$$2\,Zr_{Zr}^{\times} + Y_2O_3 + O_O^{\times} \longrightarrow 2\,Y_{Zr}^{/} + V_O^{\bullet\bullet} + 2\,ZrO_2 \qquad (1.8)$$

The protonic defects are formed when the oxide, with oxygen vacancies, absorbs water vapour from the surrounding gas phase, which dissociates into an hydroxide ion and a proton. The

hydroxide ion fills an oxygen vacancy, and the proton forms a covalent bond with a lattice oxygen [18,47]. The process of hydration can be written in Kröger-Vink notation, as:

$$H_2O(g) + V_O^{\bullet\bullet} + O_O^{\times} \rightleftarrows 2\,OH_O^{\bullet} \tag{1.9}$$

Dissociative absorption of water has been found, both experimentally and theoretically, to be an exothermic reaction for cerates and zirconates materials, which explains the increase of proton uptake with decreasing temperature observed in these materials [18,47].

The equilibrium constant, K_w, for water incorporation, assuming an ideal solution behaviour can be written as [47]:

$$K_W = \frac{\left[OH_O^{\bullet}\right]^2}{P_{H_2O}\left[V_O^{\bullet\bullet}\right]\left[O_O^{\times}\right]} \tag{1.10}$$

Where $\left[OH_O^{\bullet}\right]$ and $\left[V_O^{\bullet\bullet}\right]$ are the concentrations of protonic defects and oxygen vacancies, respectively, $\left[O_O^{\times}\right]$ is the concentration of oxygen atoms on normal oxygen sites, and P_{H_2O} is the water vapour partial pressure.

The equilibrium constant, K_W, can also be expressed in terms of entropy, ΔS_W, and enthalpy, ΔH_W, of the water incorporation reaction, in the Arrhenius form:

$$\ln(K_W) = \frac{\Delta H_W}{RT} - \frac{\Delta S_W}{R} \tag{1.11}$$

where T is the temperature and R is the universal gas constant.

Apart from the formation of protonic defects, $OH_O^{\bullet}$, other charge defects may be formed by reaction with surrounding gas. For example, the generation of electron holes is favourable under moderately to highly oxidizing conditions [47,90,91]:

$$\frac{1}{2}O_2 + V_O^{\bullet\bullet} \rightleftarrows O_O^{\times} + 2h^{\bullet} \tag{1.12}$$

while the generation of electrons and oxygen vacancies can occur at low oxygen partial pressures:

$$O_O^{\times} \rightleftarrows V_O^{\bullet\bullet} + 2e' + \frac{1}{2} O_2 \tag{1.13}$$

However, at intermediate temperatures (< 750 ºC) and moderately oxidizing conditions, the concentration of electronic defects can be neglected [47,92,93] and the overall electroneutrality equation can be written as:

$$2\left[V_O^{\bullet\bullet}\right] + \left[OH_O^{\bullet}\right] = \left[Y_{Zr}'\right] \tag{1.14}$$

Furthermore, the number of oxygen sites per formula unit is restricted to 3, implying the site restriction condition:

$$\left[V_O^{\bullet\bullet}\right] + \left[O_O^{\times}\right] + \left[OH_O^{\bullet}\right] = 3 \tag{1.15}$$

Then, from equations (1.14) and (1.15) the equilibrium constant for water incorporation reaction can also be written as:

$$K_W = \frac{4\left[OH_O^{\bullet}\right]^2}{P_{H_2O}\left(6 - \left[Y_{Zr}'\right] - \left[OH_O^{\bullet}\right]\right)\left(\left[Y_{Zr}'\right] - \left[OH_O^{\bullet}\right]\right)} \tag{1.16}$$

Determination of the concentration of protonic defects, $\left[OH_O^{\bullet}\right]$, from Thermal Gravimetric Analysis (TGA) and further comparison with calculated values from equation (1.16), using thermodynamic data for determination of hydration constant (equation ((1.11)); showed that for cubic and slightly distorted Y-doped $BaZrO_3$ perovskites, the hydration behaviour is well described by the equation (1.16). A similar hydration behaviour is also observed in Y-doped $BaCeO_3$ perovskites. However, for structures that deviate strongly from the ideal cubic perovskite the hydration process cannot be fitted by equation (1.16), as the presence of different oxygen sites makes the hydration behaviour more complex and reduces the saturation

limit [47]. Also at high temperature, equation (1.16) becomes invalid as the temperature dependence of the entropies and enthalpies of water incorporation, and the influence of hole and oxygen vacancies concentrations at high temperatures, cannot be neglected.

1.3.3. PROTON TRANSPORT MECHANISMS

The proton transport mechanism in perovskites involves proton hopping between adjacent oxide-ions at normal lattice sites (the so-called Grotthuss mechanism), and the rotational motion (molecular reorientation) of the proton around an oxide-ion [47] (Fig. 1.7).

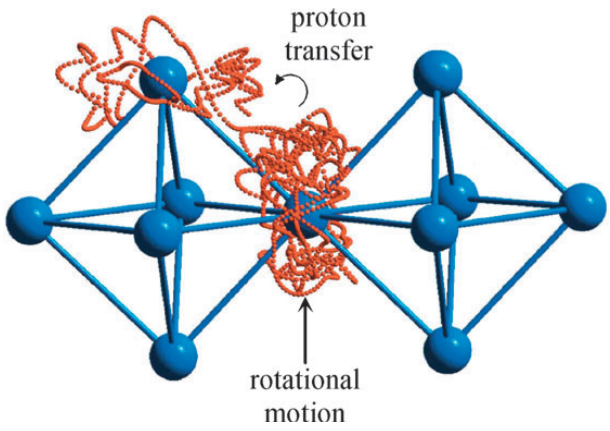

Fig. 1.7. The trace of a proton in a perovskite showing the two main features of proton transport: rotational diffusion and proton transfer (data obtained by quantum-MD simulation of a proton in $BaCeO_3$) [18,94].

Fig. 1.8 shows a scheme for a possible proton conduction mechanism in perovskites. The bond between the B-site cation (red sphere) and the oxide-ions A and B should bend, shortening the bond distance between the oxyde ions, and consequently reducing the energetic barrier for proton transfer from position 1 to position 2. In this more favourable position, a new O-H bond is formed with the adjacent oxide-ion B. The rotation motion around the oxide-ion B from position 2 to position 3, allows the repetition of the conduction mechanism in the material [79,95].

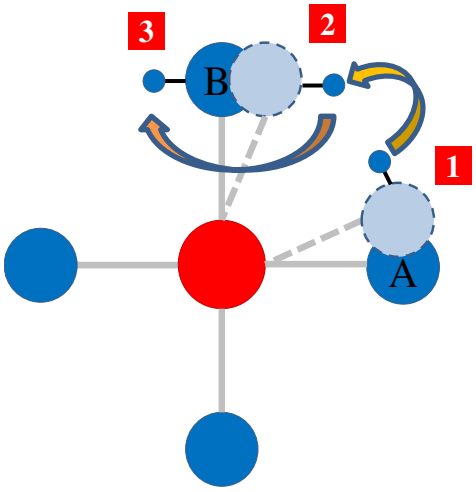

Fig. 1.8. Scheme of the proton transfer mechanism between two adjacent oxide-ions in perovskite oxides (from [79]).

Any reduction in symmetry relative to the cubic structure was shown to be detrimental to the defect mobility. This effect has been related with the different chemical interactions between the cations and oxide-ion which results in different electron densities on oxygen sites and therefore, different binding energies for the proton. The resultant biased rotational diffusion to certain directions (defect orientation) is thought to increase the activation energy of proton mobility [18,96].

Besides the reduction of crystallographic symmetry, the local and chemical perturbation induced by cation dopants can also influence the protonic defect mobility. Traditionally, on tailoring of oxide-ion conductors, aliovalent dopants are chosen on the basis of the best ionic radius match. However, this approach commonly fails when used for proton conductors due to the effect of dopant electronic structure on the host matrix. For instance, the ionic radii of six-coordinated Sc^{3+} (0.745 Å [97]) and In^{3+} (0.8 Å [97]) match very well with the ionic radius of Zr^{4+} (0.72 Å[97]), while the ionic radius of Y^{3+} (0.9 Å [97]) is significantly larger. Nonetheless, $BaZrO_3$ shows significantly lower proton mobility when doped with Sc or In than with Y, and only for Y the activation energy of proton mobility appear to be independent of dopant concentration [47]. Although the presence of Y on the Zr-site locally expands the $BaZrO_3$ lattice and results in distortions of the perovskite structure at Y contents above

5% (mol), it does not modify the atomic and electronic structure of the host matrix (Y^{3+} isoelectronic with Zr^{4+} and presents similar electronegativity), leaving the acid/base properties of the coordinating oxygens almost unchanged [18,96].

1.4. Y-DOPED $BaZrO_3$: A MODEL SYSTEM FOR PROCESSING DIFFICULTIES

Among the well-known proton conducting oxides, Y-doped $BaZrO_3$ is particularly attractive as it combines high levels of proton conductivity with superior stability in steam and CO_2 containing atmospheres, conditions required for application in a variety of electrochemical devices, such as intermediate temperature fuel cells, electrolysis cells, sensors or hydrogen pumps. Although $BaCeO_3$-based materials generally show higher total protonic conductivity they exhibit poor chemical stability against CO_2-containing atmosphere. Conversely, less basic oxides, such as In-doped $CaZrO_3$, show very low conductivity.

Despite its promising properties for use as high-temperature proton conductors, commercial implementation of Y-doped $BaZrO_3$ materials in fuel cells and other electrochemical devices has been constrained by the processing difficulties exhibited by these materials that may also compromise their electrochemical performance.

The classical solid state processing method of $Ba(Zr,Y)O_{3-\delta}$ ceramics, starting from $BaCO_3$, ZrO_2 and Y_2O_3, requires high sintering temperatures (1700 – 1800 ºC). Powders prepared by this approach have repeatedly shown lack of reproducibility, producing large and varied grain sizes, strong agglomeration and no guarantee of compositional homogeneity [98,99]. Authors using this technique are typically forced to repeated calcinations and re-grindings to achieve pure phases. The extreme temperature required on processing hampers the ready implementation of these materials in fuel cells due to the impossibility of fabrication of co-sintered structures under these conditions (e.g. electrolyte film for anode-supported SOFC). Moreover, these temperatures also have a detrimental effect on both bulk and grain boundary conductivity caused by barium evaporation, poor and abnormal grain growth and phase inhomogeneities [98–102].

To overcome the drawbacks resulting from high temperature processing of barium zirconate materials, soft chemical routes have taken an ever increasing importance. In general, these methods offer the benefits of lower synthesis temperatures and the possibility to produce ultrafine powders. A wide range of soft chemistry techniques have been employed to form barium zirconate based materials such as co-precipitation [103–105], hydrothermal synthesis [106,107], sol–gel techniques [108–111], thermal decomposition of nitrate [112], spray pyrolysis [113,114] and combustion synthesis [101,109].

However, several disadvantages have been noted with many of these techniques such as the evaporation of solvents due to non-homogeneity causing the formation of segregation phases or changes of stoichiometry due to incomplete precipitation processes [115]. Furthermore, the formation of $BaCO_3$ as an impurity phase on decomposition of organics, a common occurrence in many soft chemical processes, requires additional calcinations steps to remove, which may also contribute to compositional inhomogeneity, negating the potential advantage of the soft chemical route. In addition, soft chemistry techniques often require expensive chemicals, have time consuming processes [108,109,111,116] and involve discharge of pollutant gases [101,103,109,112]. As such, $Ba(Zr,Y)O_{3-\delta}$ can be considered an ideal study material as it presents the worst case scenario of many of the typical processing difficulties, for example, poor sinterability, Ba-loss, phase inhomogeneities and poor reproducibility on reported conductivities, that are closely related to synthetic history.

In this context, the use of mechanochemical processing in these ceramic materials may offer additional benefits, once it can lead to the formation of reactive, single phase powders at room temperature [117–125] that can be sintered to dense pellets at relatively low temperatures and can be prepared without the formation of significant quantities of $BaCO_3$ [118,119]. Furthermore, it is a cheap, simple, quick and environmental friendly processing route.

1.5. MECHANOCHEMICAL PROCESSING

The effect of mechanical energy in the activation of chemical reactions has been observed since pre-historical times, when primitive man used flints to initiate fire [126]. The first written document which refers to a mechanochemical reaction has been attributed to the Theophrastus of Efesus (371–286 BC), a student of Aristotle, who described mercury recovery from cinnabar by a mechanical treatment [127]. Other examples of mechanochemical reactions were documented between 300 B.C. until the end of 1800's in Agricola's *De Natura Fossilicum* [128]. However, the experimental work carried out by Carey Lea is frequently referred to as the first systematic study on the chemical effects of mechanical action [129]. Indeed, on the basis of his research on endothermic decomposition of a wide range of materials by the application of mechanical force (e.g. silver and mercury halides), and using different techniques to deliver the mechanical energy [129], he attributed the application of mechanical force as the direct cause of the chemical changes observed. Although, the term "mechanochemistry" was introduced by Ostwald, it was the ground-breaking work of Carey Lea which explicitly discussed the possibility that mechanical force could induce chemical reactions, and which established mechanochemistry as a separate branch of chemistry [129,130]. In the first half of the 20^{th} century an increasing development occurred in the study of the effect of mechanical energy in chemical reactions and in physical-chemical changes on different types of materials.

The extensive accumulation of knowledge in this area resulted from [126]:

- studies on reactions occurring upon mechanical treatment of solid mixtures;
- investigations of the influence of high pressure and combined action of pressure and shift on the phase transition in crystals and on the rate of chemical solid-state reactions;
- experimental works on the explosion excitation under mechanical action in both initiating and highly explosive materials;
- experimental works on the effect of energy milling on the reactivity of organic macromolecules (e.g. cellulose);
- investigations on phase transformations in minerals during milling.

Advances in knowledge on the mechanism of mechanical energy conversion to chemical energy during the second half of last century, have contributed to the development of novel technological procedures in different areas, such as, mineral raw processing or in the preparation of new construction materials, mineral fertilizers and functional ceramics [126]. The mechanical processing of materials also showed relevance in the preparation of alloys by ball milling, with emphasis on oxide dispersion strengthening (ODS) of nickel and iron supperalloys for aerospace applications, developed at the end of the 1960s [126,131]. In the 1980s, the emergence of nanotechnology motivated a growing interest in the formation of materials under mechanical action for preparation of nanopowders.

Nowadays, mechanical processing remains a matter of interest in the field of materials science with an increasing number of publications. Terms like mechanical alloying, mechanochemical processing, mechanical activation, mechanosynthesis, high energy milling or mechanochemical ceramic processing have been intensely used in literature in different areas such as physics, chemistry, metallurgy, mineral processing, biology, pharmacology, environmental protection or materials science to describe different processing techniques associated with the use of mechanical energy [132]. The proliferation of publications and the wide scope of this topic have led to some inconsistences among authors in respect to the meaning attributed to some of these terms. Thus, an explanation of its significance in the scope of this work becomes necessary.

Mechanical alloying and mechanochemical processing are both powder processing techniques which use mechanical milling to prepare a wide variety of materials. The main difference between these two techniques is that, while chemical reactions occur in mechanochemical processing, mechanical alloying does not assume the occurrence of chemical reaction during the processing, i.e., the chemical reaction need not occur [131].

In respect to mechanochemical processing, it may comprise processes of mechanical activation or mechanosynthesis. Mechanical activation, originally defined by Smekal in 1952, is nowadays usually referred to a process where the reaction ability of a material increases by milling, inducing chemical reactions in the subsequent heat treatment after milling [127]. The

increase in reactivity has been attributed mainly to the physicochemical changes that occur during milling, such as the increase of the internal and specific surface energy, or the emergence of different types of structural and electronic defects [127], which allows synthesis at lower temperatures than is required by conventional synthesis methods. If the application of mechanical energy leads to an increase in the reactivity of materials with consequent occurrence of chemical reaction at room temperature, the process is called mechanosynthesis or mechanochemical synthesis.

The expression "high energy milling" is usually employed in the literature to emphasize the character of the applied milling equipment in the processing of materials, and may include all the processing techniques aforementioned [133]. Indeed, mechanical allowing, mechanical activation and mechanosynthesis processes occur, most times, concurrently during the high energy milling.

In a more restricted field, namely related with the development of ceramic materials, the expression mechanochemical ceramic method is frequently used when referring to ceramic processing of materials prepared by mechanochemical methods [132], and will be approached further in this work.

1.5.1. MECHANISM OF MECHANICAL ALLOYING

On the basis of experimental data of the preparation of a variety of systems, Zyryanov [132] proposed a theory to explain the mechanism of mechanochemical processing of mixed oxides, supported by independent structural studies and by statistical analysis of dynamic results. The main problem in the study of mechanochemical processing is the irreproducibility of results obtained even in very similar operating conditions (the so-called mechanical "black-box"). Thus, the theoretical description of mechanical alloying mechanism has been developed from the use of a quantitative comparison of the chemical response with relative mechanical loading under similar and suitable experimental conditions, which ensure macro-homogeneity, lower contamination and approximately constant hollowness [132]. The mechanism of mechanical alloying considers a primary mechanochemical event represented by the general equation [132]:

$$A + B \rightarrow (A_x B)^* \rightarrow A_{1-\delta}B^* + B^* \quad (1.17)$$

where $(A_xB)^*$ defines a dynamic state, in the form of a layer grown due to a rolling mass transfer mechanism (Fig. 1.9), A and B represent the hard and soft reactants, respectively, B* is a particular form of reactant B, with amorphous or turbostratic structure, resulting from the relaxation of dynamic state, and $A_{1-\delta}B^*$ represents the primary product, deficient in the hardest reagent [132]. The composition of the dynamic state and the primary reaction product is determined by the difference in the Mohs' hardness of the oxide precursors.

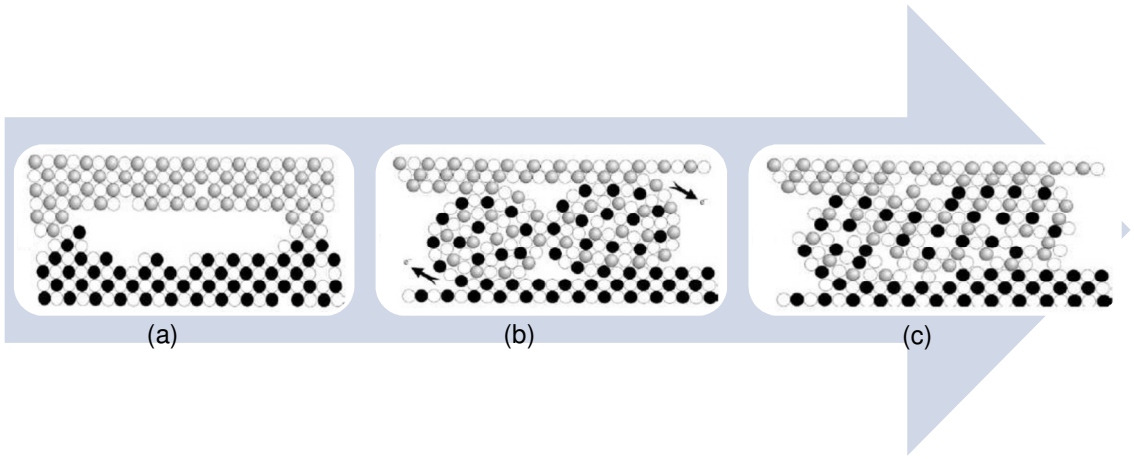

Fig. 1.9. Two-dimensional scheme illustrating the primary event of the mechanical alloying mechanism **(a)** initial state; **(b)** roll growth until collision, accompanied by emission processes, and **(c)** relaxation of $(A_xB)^*$ to the primary product [132].

During the secondary event of the mechanical alloying mechanism, there is a slow conversion of the primary product towards the final equilibrium composition by a deformation mixing regime, with the formation of rotation zones, and further mass transfer during stoppage and unloading [132]. Fig. 1.10 describes graphically the dynamics of the process, highlighting the gradual change between reagent consumption, primary product formation and conversion to final product.

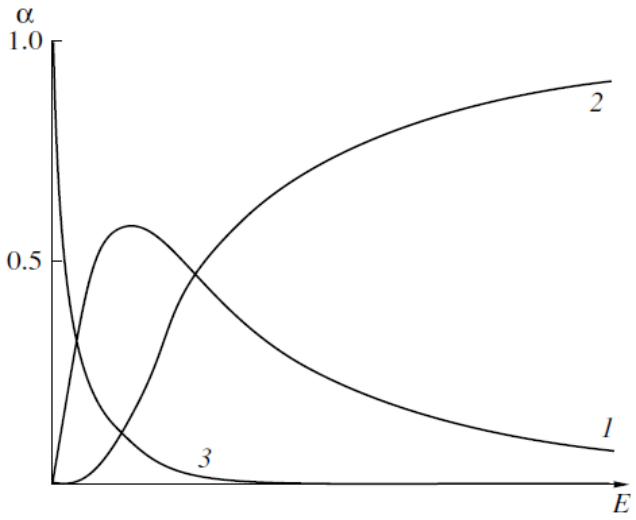

Fig. 1.10. Dynamics of mechanochemical synthesis in systems with intermediate primary products. (1) primary product, (2) secondary product, (3) starting reactants [132].

1.5.2. MECHANOCHEMICAL PROCESSING OF CERAMICS

The processing of nanocrystalline materials using mechanical milling has evoked a particular interest, namely in the preparation of functional ceramic materials such as complex oxides with perovskite and spinel structures, layered structures, magnetic materials or ceramic nanocomposites [134].

In comparison with other processing routes usually used in ceramic processing, namely conventional solid-state reactions or the soft chemistry-based processing routes, mechanochemical ceramic processing shows some relevant advantages in respect to the cheap, rapid, non-polluting, formation of nanostructured powders that can exhibit high compatibility and improved sinterability to allow the formation of ceramics materials at lower temperature.

Mechanochemically produced powders often show agglomerates up to 100 μm with low densities (65 - 70 %), consisting of aggregates with densities up to 80 % in the range

0.2 - 2 μm [132]. These aggregates are comprised of composites of nanosized crystallites in an amorphous matrix (Fig. 1.11).

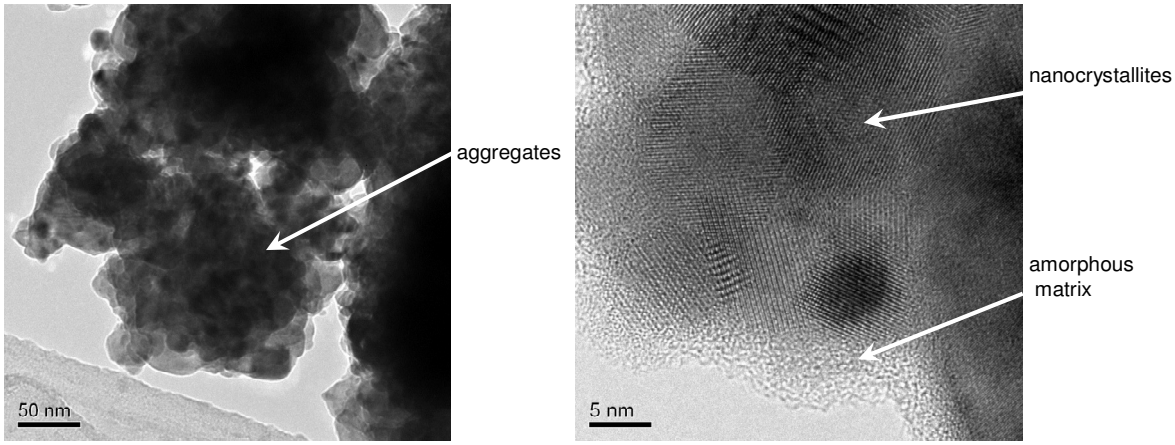

Fig. 1.11. Mechanically produced barium titanate-based powders.

Phase formation and subsequent ceramic processing at comparatively much lower temperatures and in a controlled atmospheres (closed vial) can allow improved control of the chemical and compositional stoichiometry of the prepared materials avoiding loss of volatile precursors during the preparation. Moreover, the obtained ceramic materials often exhibit favourable and unique features such as structural stability, extended solid solubility and surface and structural defects, which have been associated to improvements in their electrical, electronic, magnetic or functional properties [134]. Indeed, alternative phase forming mechanisms in the mechanochemical methods often circumvent the formation of transitional or impurity phases, formed during conventional solid state processing, contributing to superior properties shown by mechanochemical processed ceramics. Furthermore, mechanochemical ceramic processing allows the synthesis of novel materials, that cannot be synthesized by other methods [134].

In the current project the strategy followed will be focused on the adoption of different types of mechanochemical processing, to improve functional properties or to process novel ceramic materials for high temperature fuel cells technologies.

1.6. AIM OF THE THESIS

The present thesis aims to create a knowledge platform in view of the improvement of properties of well-known and promising PC-SOFC materials, and the tailoring of properties of novel materials, by manipulation of mechanochemical processes and composition. By such manipulation one aims to improve the processing ability of fuel cell components and to develop novel materials with superior properties, with emphasis on transport properties and chemical stability. The research is focused on the study of potential proton and mixed conductors for application in H-SOFCs components, based on $BaZrO_3$. However, one also expects the formed know-how to be transferable to other related materials.

2. EXPERIMENTAL: MATERIALS PROCESSING AND CHARACTERIZATION TECHNIQUES

2.1. MATERIALS PROCESSING

As a general rule, a standard high energy milling procedure was adopted for all systems studied, with the aim to facilitate comparison between the different perovskite systems. However, conventional solid state synthesis was also occasionally used for comparison with the mechanochemical processing method.

2.1.1. PRECURSORS

The mechanochemical processing of $BaZrO_3$ and $BaPrO_3$ based compositions was performed from stoichiometric mixtures of suitable dry commercial metal oxides: barium peroxide (Riedel-de-Häen or Acros, 95 % purity), $(ZrO_2)_{0.92}Y_2O_3)_{0.08}$ (TOSOH Co.), $(ZrO_2)_{0.92}(Y_2O_3)_{0.08}$ (TOSOH Co.), zirconium (IV) oxide, *m*-ZrO_2 (Riedel-de-Häen, 99 % purity), yttrium oxide (Hermann C.Stark, calcined at 950 ºC, 1 hour), praseodymium oxide (Aldrich > 99.9 %), anatase titanium oxide (Aldrich, 99.8 %), and cerium (IV) oxide (Aldrich, 99.8 %). The commercial powder of barium peroxide was found to be a mixture of BaO_2 and carbonate impurities, the exact quantities of which were confirmed by thermogravimetric analysis using a SETARAM TG-DTA/DSC Labsys Intrument with a 1600 ºC Rod by complete carbonation of a sample in flowing CO_2. Table 2.1 presents the precursors used in the preparation of the compositions studied.

Table 2.1. Precursors mixtures used in the preparation of perovskite compositions.

System	Composition	Precursors
$BaZr_{1-y}Y_yO_{3-\delta}$	$y = 0$	$BaO_2 + ZrO_2$
	$y = 0.06$	$BaO_2 + (ZrO_2)_{0.97}(Y_2O_3)_{0.03}$
	$y = 0.15$	$BaO_2 + (ZrO_2)_{0.92}(Y_2O_3)_{0.08}$
	$y = 0.20$	$BaO_2 + ZrO_2 + Y_2O_3$
$Ba_{1-x}Zr_{0.852}Y_{0.148}O_{3-\delta}$	$x = 0.02$	$BaO_2 + (ZrO_2)_{0.92}(Y_2O_3)_{0.08}$
	$x = 0.04$	
	$x = 0.06$	
	$x = 0.08$	
$Ba(Pr_{1-x}Zr_x)_{1-y}Y_yO_{3-\delta}$	$x = 0$; $y = 0.8$ or 0.9	$BaO_2 + (ZrO_2)_{0.97}(Y_2O_3)_{0.03} +$ $+ Pr_6O_{11} + Y_2O_3$
	$x = 0.20$; $y = 0.8$ or 0.9	
	$x = 0.40$; $y = 0.8$ or 0.9	
	$x = 0.60$; $y = 0.8$ or 0.9	
	$x = 0.80$; $y = 0.8$ or 0.9	
	$x = 1$; $y = 0.8$ or 0.9	
$BaPr_{1-x}Zr_xO_{3-\delta}$	$x = 0$	$BaO_2 + ZrO_2 + Pr_6O_{11}$
	$x = 0.20$	
	$x = 0.40$	
	$x = 0.60$	
	$x = 0.80$	
	$x = 0.85$	
	$x = 0.90$	
	$x = 0.95$	
	$x = 1$	
$BaPr_{1-x}M_xO_{3-\delta}$ (M = Ti or Ce)	$x = 0.20$	$BaO_2 + Pr_6O_{11} + TiO_2$ (or CeO_2)
	$x = 0.40$	
	$x = 0.60$	
	$x = 0.80$	

Additionally, tetragonal zirconia (*t*-ZrO_2) and monoclinic zirconia (*m*-ZrO_2) were prepared and used as precursors for the mechanosynthesis of $BaZrO_3$. The tetragonal phase of pure undoped zirconia is thermodynamically stable only at temperatures higher than 1170 ºC, although this phase can be retained in metastable form at room temperature. Nonetheless, this metastable material is not commercially available. Several preparation routes have been documented [135–137] that can produce the tetragonal phase of pure ZrO_2 in metastable form, such as the slow alkaline precipitation procedure used in this work.

For the preparation of tetragonal zirconia, H_2O_2 (Sigma-Aldrich, 30 wt.% in H_2O) was added to the aqueous zirconyl solution, $ZrOCl_2 \cdot 8H_2O$ (Sigma-Aldrich, 95 % purity) to give a molar ratio of ZrO_2 to H_2O_2 equal to 1:4. For the precipitation of gels, ammonia solution (Fluka) was added until the pH reached a value of 9. The gels were subsequently aged for 30 minutes, then filtered and washed with distilled water until no Cl^- ions were detected in the filtered water ($AgNO_3$ test). The powder was then dried at 110 °C for 12 hours. The dried powder was sulphated by adding 3 ml of 1 N H_2SO_4 (Sigma-Aldrich) per gram of powder and stirring at room temperature. The sulphated powder was dried at 110 °C for 12 hours and then calcined at 600 °C for 4 hours.

Monoclinic zirconia is also prepared in order obtain powders with nanometric particle size range comparable with the particle size of t-ZrO_2 powders. For the preparation of *m*-ZrO_2, a stock solution of $ZrOCl_2 \cdot 8H_2O$ with a concentration of 0.1 M was used. Ammonia solution (Fluka) was added to the salt solution until the pH value of 10 was reached. The precipitate formed was filtered and washed with distilled water and subsequently dried at 90 °C for 24 hours. Finally calcination treatment was carried out at 550 °C for 5 hours.

2.1.2. MECHANOCHEMICAL CERAMIC PROCESSING

High energy milling experiments were conducted in a planetary ball mill (Retsch PM200 or PM100), with constant planetary rotation of 650 rpm, using 125 cm^3 tetragonal zirconia vials (Retsch) and balls (Tosoh Co.) with diameters of 10 and 15 mm, in the proportion 2 to 1, with 5.5 g of the stoichiometric mixture of precursors, resulting in the powder weight ratio ~10:1. Excess heating was avoided by milling for periods of 5 minutes with a subsequent pause for the same period of time. After each interruption the direction of rotation was reversed. No special atmospheres were used during milling. Progression of mechanochemical reaction was monitored by X-ray diffraction (XRD) analysis of powder samples collected at regular periods of time, using a Rigaku Geigerflex diffractometer (Cu$K\alpha$ radiation, scan rate $1^{o} \cdot min^{-1}$). The milling was stopped when no relevant crystallographic changes were observed.

In some cases an annealing step was necessary for phase formation of mechanically activated powders and was performed in air at 1000 – 1250 ºC. Such a calcination step was also necessary to increase crystallinity for structural characterization of mechanochemically produced powders.

Ceramic samples were prepared by uniaxial pressure at ~65 MPa, followed by isostatic pressure of 200 or 300 MPa, of the mechanically obtained powders with subsequent heat treatment in air for complete synthesis and sintering between 1300 and 1600 ºC. Samples were covered with sacrificial powder of the same composition to minimize Ba-evaporation. The formation of single phase materials was confirmed by XRD analysis. The density was measured by geometric measurements and/or by Archimedes method by immersion in diethyl phthalate.

The level of densification on sintering was determined by the equation:

$$\text{Densification}\,(\%) = \frac{\text{Final Density} - \text{Green Density}}{\text{Green Density}} \times 100 \qquad (2.1)$$

where the green density is the density before sintering and the relative density is calculated by the following equation:

$$\text{Relative Density}\,(\%) = \frac{\text{Final Density}}{\text{Crystallographic Density}} \times 100 \qquad (2.2)$$

where crystallographic density is determined from the formula mass of the chemical composition and the unit-cell volume obtained by Rietveld refinement.

2.2. CHARACTERIZATION OF MATERIALS

2.2.1. X-RAY DIFFRACTION

X-ray diffraction (XRD) of powder samples, was performed using a Rigaku Geigerflex diffractometer (CuKα radiation), over the angular range 10 - 115º (2θ), in a continuous scan mode with a scan rate of 1 - 3º·min^{-1}, or in step scan mode at 6 s·step^{-1}, with a step width of 0.02º. The collected data were used for phase identification, estimation of crystallite size and lattice strain, quantification of weight fractions of crystalline phases, and/or determination of structural parameters using Rietveld refinement, such as the lattice parameters and average bond-length.

2.2.1.1. SIZE-STRAIN PLOTS

A significant peak broadening is typical of X-ray diffraction patterns of powders prepared by high energy milling, which may be attributed to a combined effect of crystallite size in the nanometric range, lattice strain and significant residual micro-strain resultant of high energy milling.

The crystallite size and lattice strain of nanopowders prepared by high energy milling were estimated from the size-strain plot, based on the integral-breadth method [138,139]. The X-ray diffraction line profiles were modelled by a Pearson VII distribution function (program Winfit 1.2.1 [140]), in order to determine the profile parameters. The instrumental contribution to line broadening was determined using LaB_6 as standard reference.

The contributions to integral-breadth of crystallite size and the strains can be evaluated by the adoption of an integral-breadth method relating the crystallite size, expressed as the average apparent diameter, ε, with the mean value of the strain, η [138].

$$\left(\frac{\beta^*}{d^*}\right)^2 \approx \frac{1}{\varepsilon}\frac{\beta^*}{\left(d^*\right)^2} + \left(\frac{\eta}{2}\right)^2 \tag{2.3}$$

where $\beta^* = \frac{\beta\cos(\theta)}{\lambda}$ and $d^* = \frac{2\sin(\theta)}{\lambda}$. β and d are the integral breadth and the interplanar distance, respectively. η is related with the root-mean-square strain (e_{rms}) by the relation:

$$e_{\text{rms}} \cong \frac{\eta}{5} \tag{2.4}$$

Therefore, the crystallite size and the mean value of the strain were estimated from the fitted linear data of the graphic representation of equation (2.3), based on the slope and *y*-intercept values, respectively.

2.2.1.2. RIETVELD REFINEMENT

Rietveld refinement of XRD data was performed to obtain both lattice parameters of phase-pure material and weight fractions of crystallised phases in mechanochemical activated powders, using the Fullprof program [141] according to the a method documented in reference [142].

The XRD samples were prepared using Ni (Merck) as internal weight and lattice parameter standard. This standard was chosen since it meets the requirements of not having overlapping XRD peaks with the sample and has a small particle size (~0.4 μm) which limits differences in microabsorption between the two phases on performing quantitative analysis. The powders for analysis were mixed in an agate mortar with Ni powder, of known weight, in a quantity so that the intensity of its strongest Ni peak would be similar to that of the strongest peak of the sample.

The weight fraction of crystallized phase, $(W_{cryst})_{XRD}$ was corrected for the presence of the amorphous phase, from the X-ray and real weight fractions of internal standard, $(W_{Ni})_{XRD}$ and $(W_{Ni})_{real}$ respectively, according to a method documented in [142], using the relation:

$$\left(W_{cryst}\right)_{real} = \frac{\left(W_{cryst}\right)_{XRD} \cdot \left(W_{Ni}\right)_{real}}{\left(W_{Ni}\right)_{XRD}} \tag{2.5}$$

2.2.2. RAMAN SPECTROSCOPY

Raman spectroscopy studies were used to complement X-ray diffraction and Rietveld refinement, once they present higher sensibility to identify possible local changes of symmetry, e.g. offering resolution of crystallographic changes often at lower doping concentrations with respect to X-ray diffraction. For example, its use became necessary to obtain a detailed structural characterization of the system $BaPr_{1-x}Zr_xO_{3-\delta}$.

The Raman spectra were acquired, at room temperature, in backscattering configuration with a Jobin-Yvon LabRam HR equipped with a Multichannel air cooled (70 °C) CCD detector. An objective of 50x magnification was used to focus the sample surface when excited with 532 nm laser line. As a rule, the incident laser power was kept at 2 μW to avoid structural transformations due to the overheating. For each sample were recorded different spectra corresponding to different regions of the ceramic sample. For the analysis were considered the spectra that presented better relation signal/noise.

2.2.3. ICP-AES AND FT-IR ANALYSIS

Inductively coupled plasma atomic emission spectroscopy (ICP-AES) allows the identification and quantification of elements in residual concentrations. In this context, ICP-AES studies have been performed on $Ba(Zr,Y)O_{3-\delta}$ materials in order to detect the occurrence of deviation of stoichiometry of the compositions prepared by mechanochemical processing, and possible zirconia milling contaminations. The spectroscopy analysis is performed in a

Jobin-Yvon 70 Plus spectrometer, with solutions of the milled powders that had been dissolved in acid mixtures in an ultrasonic bath.

Fourier Transform Infrared Spectroscopy (FT-IR) offers higher sensitivity on the detection of lower concentration of materials (detection limit of ~ ppm), respecting to the X-ray diffraction technique (detection limit of ~1 wt.%). In this context, FT-IR is used to investigate the presence of traces of barium carbonate nanopowders prepared by high energy ball milling. Room temperature infrared absorption spectra were collected, in the range of 300 – 2000 cm^{-1} using a KBr pellet, using a Spectrum-1000 Fourier transform infrared instrument (Perkin-Elmer).

2.2.4. CHEMICAL STABILITY STUDIES

The chemical stability was assessed by post-operation examination by XRD of samples annealed under different temperatures and atmospheres, such as dry and wet air, O_2, N_2, CO_2 and 10% H_2/N_2. Additionally, stability in flowing dry CO_2 was also studied by TGA using the SETARAM instrument with a heating rate of 1 ºC·min^{-1}, up to the maximum temperature 1300 ºC. For this, samples were preliminary heated at 5 ºC·min^{-1} in dry argon to 1300 ºC to remove residual hydration and any minor initial traces of $BaCO_3$, and cooled under the same atmosphere before exposure to CO_2. Subsequent analysis by XRD of powder samples was performed after TGA experiments were completed.

2.2.5. ELECTRON MICROSCOPY STUDIES

The submicron-sized powders obtained by mechanochemical preparation were characterized by Transmission Electron Microscopy (TEM) coupled with Energy Dispersive X-ray spectroscopy (EDS) in a Hitachi H-9000 microscope operated at 300 kV and equipped with an Röntec EDS detector. Samples were prepared by dispersing in ethanol and supporting on perforated copper grid holders. The microstructural inspections of fractured ceramics were

performed by Scanning Electron Microscopy (SEM) using a Hitachi S4100 microscope. Average particle size and grain size were estimated from equivalent circular diameters measured on TEM and SEM digital micrographs upon suitable processing and analysed with ImageJ 1.37v software of Wayne Rasband (National Institutes of Health, USA).

Electron-Probe MicroAnalysis (EPMA) was used for chemical analysis of ceramic samples to assess composition accuracy using a Jeol Superprobe JXA-890M electron probe microanalyser.

Ceramic samples were also studied using electronic transmission microscopy, coupled with a system of energy-dispersive X-ray spectroscopy, TEM/EDS (JEOL 2200FS), to assess the local chemical composition in grain interior and triple points.

2.2.6. ELECTROCHEMICAL MEASUREMENTS

The electrical characterization of materials was performed by Electrochemical Impedance Spectroscopy (EIS). AC impedance spectroscopy measures the electrical response of the material by the application of a sinusoidal field over a large frequency range. It has the benefit over DC measurements that the various phenomena can be separated, allowing processes of the material with different times constants to be characterized. Additionally, with continuous variation of applied potential on the sample, the electric field changes periodically its direction, avoiding polarization phenomena that commonly occur by application of constant voltage on the ionic materials.

2.2.6.1. FUNDAMENTALS [143]

In AC impedance spectroscopy measurements, one measures the complex impedance of a sample as a function of frequency. A single frequency voltage, v, is applied across the sample:

$$v(t) = V_0 . \sin(\omega t) \tag{2.6}$$

and the resultant current is measured, according to:

$$i(t) = I_0 . \sin(\omega t + \phi) \tag{2.7}$$

where ω represents the angular frequency (2π times the frequency), V_0 and I_0 the amplitude of signal and current, respectively; and ϕ the phase shift.

For a pure resistor, the voltage, v, and the resultant current, i, are in phase ($\phi = 0$); while for in a pure capacitor i leads v by a phase angle of 90º (i.e. ϕ = 90º). In a real system can be considered both capacity and resistive terms can be considered, once voltage always lags behind the current by a phase angle less than 90º, and thus, can be modelled by combination of resistive and capacitive elements.

By definition, impedance is defined by the opposition to the flow of charge in a system and is given by:

$$Z(\omega) = \frac{v(t)}{i(t)} \tag{2.8}$$

As a vector quantity can also be defined as a complex number, whose magnitude and direction can be expressed by the combination of a real Z' and imaginary Z'' components:

$$Z(\omega) = |Z| \cos(\phi) + j \ |Z| \sin(\phi) = Z' + j \ Z'' \tag{2.9}$$

where the imaginary number $j = \sqrt{-1} = \exp(j \pi/2)$ indicates an anticlockwise rotation by $\pi/2$ relative to the real axis.

Experimental impedance data are plotted by the Nyquist representation, which plots the imaginary component, Z'', against the real component, Z', of the sample impedance, at

different frequencies. Typically, the Nyquist representation of ceramic ionic conducting materials exhibit distinct arcs corresponding to different phenomena from the intragranular bulk and intergranular grain boundary transport on the electrolyte and to the electrode response. Due to their characteristic relaxation frequencies, the arc at high frequencies is normally attributed to conduction in grain interior (bulk), the intermediate frequency arc is attributed to conduction in grain boundary, and that at low frequencies is attributed to the electrode response. The analysis of the electrolyte and electrode responses can be represented by series combinations of resistive (R) and capacitive (C) elements in parallel, stated to be the equivalent circuit.

In ideal polycrystalline materials, the arcs correspondent to the bulk, grain boundary and electrode response can be conveniently modelled by three subcircuits in series, composed by parallel connection of a resistor and capacitor (RC element), Fig. 2.1.

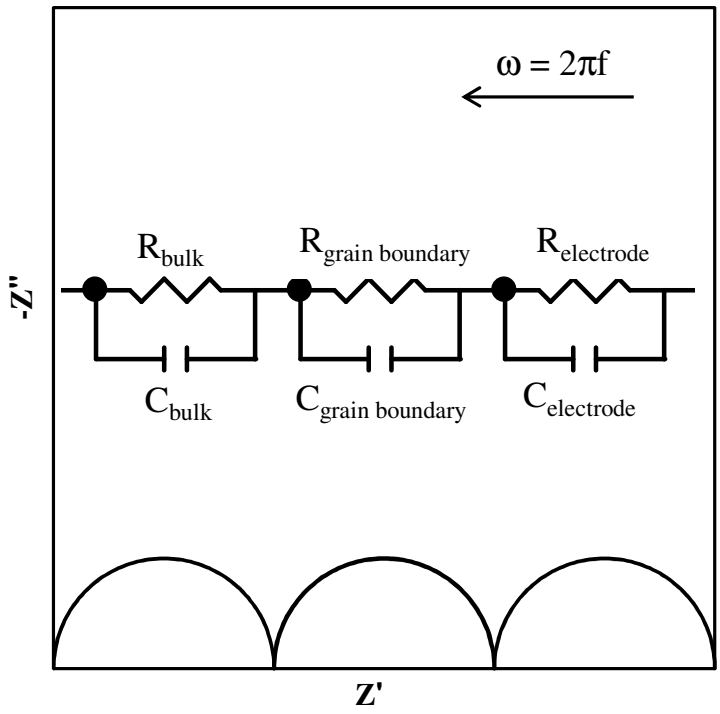

Fig. 2.1. Schematic impedance plot in the Nyquist representation of an ideal crystalline material.

Nonetheless, many materials are found to give non-ideal responses. The semi-circles produced in the impedance plot are often depressed, and have centres which are located below the real axis, which can be attributed to the relaxation processes with a distribution of relation times or other relaxation processes with different time constants, caused by e.g. inhomogeneous samples. In this situation, the simple combination of RC elements with a single time constant is insufficient to model this type of behaviour, and the capacitor should be replaced by a Constant Phase Element (CPE) in order to model conveniently the electrochemical processes. The CPE describes the behaviour of an element whose nature deviates from that of a pure resistor or capacitor and can be characterized from pseudo-capacitance, Q, and the parameter n, related with depression of the semicircle obtained in a non-linear response.

The relation between capacitance, C, and pseudo capacitance, Q, can be stablished by equating the characteristic relaxation frequency, ω_0:

$$\omega_0 = \frac{1}{RC} = \left(\frac{1}{RQ}\right)^{1/n} \tag{2.10}$$

and consequently:

$$C = Q^{1/n}.R^{(1-n)/n} \tag{2.11}$$

From the value of capacitance, one may estimate the relative permittivity of materials as:

$$\varepsilon_r = \frac{C.L}{\varepsilon_0.A} \tag{2.12}$$

ε_r is the relative permeability of material, ε_0 is the vacuum permeability, and A e L is the cross sectional area and the length of the sample, respectively.

From the knowledge of the resistance and capacitance extracted from impedance data analysis and the sample geometry (cross sectional area and length), the conductivity of bulk (grain interior) and grain boundary can be estimated considering the “brick layer” model.

According to the "brick layer" model a polycrystalline material consists of identical cubic grains whose size is D and with the same conductivity, and the grain-boundaries whose thickness is δ, which possess a different resistivity to the grains interior.

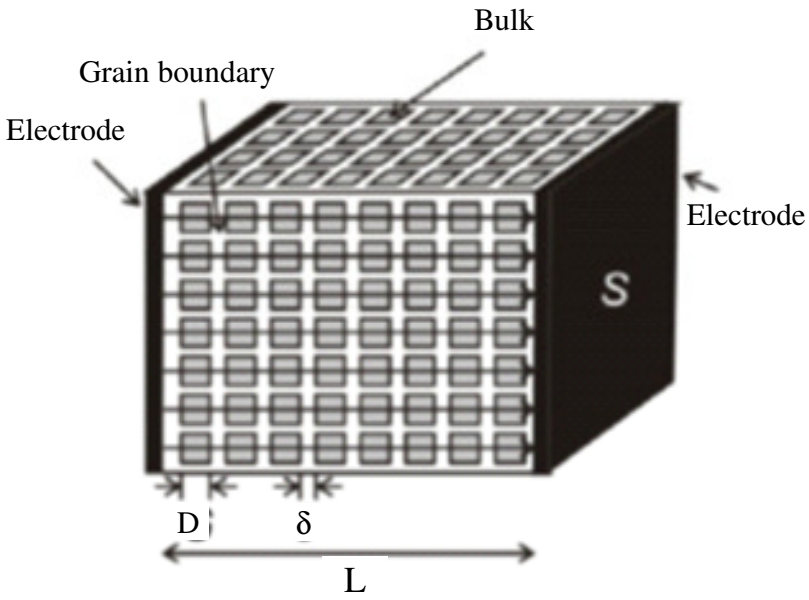

Fig. 2.2. Brick-layer model of a polycrystalline material (from [144]).

The total conductivity of a polycrystalline material can be obtained by the relation:

$$\sigma = \frac{L}{(R_b + R_{gb}) \cdot A} \tag{2.13}$$

where R_b and R_{gb} are the resistances of bulk (grain interior) and grain boundary respectively, that can be obtained from impedance spectroscopy measurements.

The bulk conductivity can be obtained from:

$$\sigma_b = \frac{D.N}{R_b.A} \tag{2.14}$$

where N is the number of grains.

Attending that the grain is much larger than the grain boundary, $D >> \delta$, one can be consider that:

$$L \approx N \cdot D \tag{2.15}$$

and the bulk conductivity can be determined from the knowledge of the overall sample geometry:

$$\sigma_b = \frac{L}{R_b \cdot A} \tag{2.16}$$

Also, on the assumption that the bulk conductivity is much larger than specific grain boundary, current will flow primarily through the grains, and will traverse the grains boundaries perpendicular to the grains, as indicated in Fig. 2.2, and the specific grain boundary conductivity can be determined as:

$$\sigma_{gb,sp} = \frac{\delta . N}{R_{gb} \cdot A} \cong \frac{L}{R_{gb} . A} \cdot \frac{\delta}{D} \tag{2.17}$$

If one further assumes that the dielectric constant of the grain boundaries is approximately equal to the bulk ($\varepsilon_{gb} \approx \varepsilon_b$) [102,144]:

$$\frac{\delta}{D} = \frac{C_b}{C_{gb}} \tag{2.18}$$

The specific grain boundary conductivity can be measured solely from impedance data, in the absence of microstructural information, combining by equations (2.14) and (2.15):

$$\sigma_{gb,sp} = \frac{L}{R_{gb} \cdot A} \cdot \frac{C_b}{C_{gb}} \tag{2.19}$$

where the total or effective grain boundary conductivity is defined as:

$$\sigma_{gb} = \frac{L}{R_{gb} \cdot A} \tag{2.20}$$

In the case that the capacitances of the bulk and grain boundary responses cannot be resolved, an estimation of the inherent grain-boundary properties independent of microstructure can be provided on the assumption that the proportionality factor of the grain-boundary thickness remains effectively constant. In this case the following relation can be adopted [145]:

$$\sigma^{*}_{gb,sp} = \frac{\sigma_{gb}}{D} \tag{2.21}$$

where $\sigma^{*}_{gb,sp}$ is the area specific grain-boundary conductance.

2.2.6.2. PREPARATION OF SAMPLES

On the preparation of ceramic samples for electrical characterization, a threshold of relative density of > 85 % was enforced, in order to minimise possible deviations of true conductivity caused by porosity [146–148]. Table 2.2 presents the thermal cycles adopted on the preparation of dense samples used in electrical measurements, and the corresponding relative density.

Table 2.2. Thermal cycles and relative density of samples used in impedance measurements. The dwell time is 5 hours for all the samples.

System	Composition	Temperature (ºC)	Heating and cooling rate (ºC·min^{-1})	Relative density (%)
$BaZr_{1-x}Y_xO_{3-\delta}$	$x = 0.15$	1600	5	86-91
	$x = 0.20$		2	
$Ba_{1-x}Zr_{0.85}Y_{0.15}O_{3-\delta}$	$x = 0$ - 0.10	1600	5	
$BaPr_{1-x}Zr_xO_{3-\delta}$	0.20	1400	1	85-94
	0.40	1500	2	
	0.60			
	0.80	1600	5	

2.2.6.3. EQUIPMENT AND MEASUREMENTS CONDITIONS

Impedance spectroscopy measurements were performed using an Electrochemie-Autolab PGSTAT302N analyser (frequency range of 1MHz - 0.01 Hz, amplitude 50 mV) or a Novocontrol Alpha-ATB analyser (frequency range of 40 MHz - 0.1 Hz, amplitude 100 mV). Measurements were made on bar (~$14 \times 4 \times 3$ mm) or circular (~7 mm diameter and ~2 mm thickness) shaped samples, with two porous platinum electrodes, obtained by painting the sample with a platinum paste with further calcination at 900 ºC, for 10 minutes. The studies were carried out in an isolated alumina sample holder, and platinum wires were used as contacts using a pseudo 4-electrode geometry to avoid lead resistances.

The sample is placed on the top of an alumina tube, supported by an alumina pellet, and pressed with the Pt electrodes by a spring-loaded alumina rod attached to a metallic wire of Ni-Cr alloy, resistant to high temperatures. This arrangement is then inserted into a vertical tube furnace (Fig. 2.3).

Impedance measurements were taken at 50 ºC intervals in the direction of decreasing temperature in the temperature range 900 – 100 ºC, under dry and wet oxygen, nitrogen or 10 % H_2 – 90 % N_2 mixtures.

Isothermal impedance measurements were also performed as a function of the oxygen partial pressure, P_{O_2}, by mixing various amount N_2 and O_2 gases, under different water partial pressure, P_{H_2O}, conditions (dry, wet and intermediate water vapour partial pressure), with a total flowrates of 50 $ml \cdot min^{-1}$. Equilibrium was verified by performing repeated impedance measurements with one hour stabilization, for each atmosphere and temperature condition. Drying was carried out by passing gases through Varian gas clean filter moisture. Gases were humidified by bubbling through water followed by a saturated KCl solution in contact with solid KCl, producing approximately 83.5 % relative humidity at room temperature. Different pressure of water vapour was achieved by mixing fractions of wet and dry gases. For all the experiments, oxygen partial pressure was measured by an inbuilt oxygen sensor, while the humidity was recorded using an external humidity sensor.

Fig. 2.3 presents a schematic representation of the experimental setup used in the impedance experiments and an electrical measurement cell.

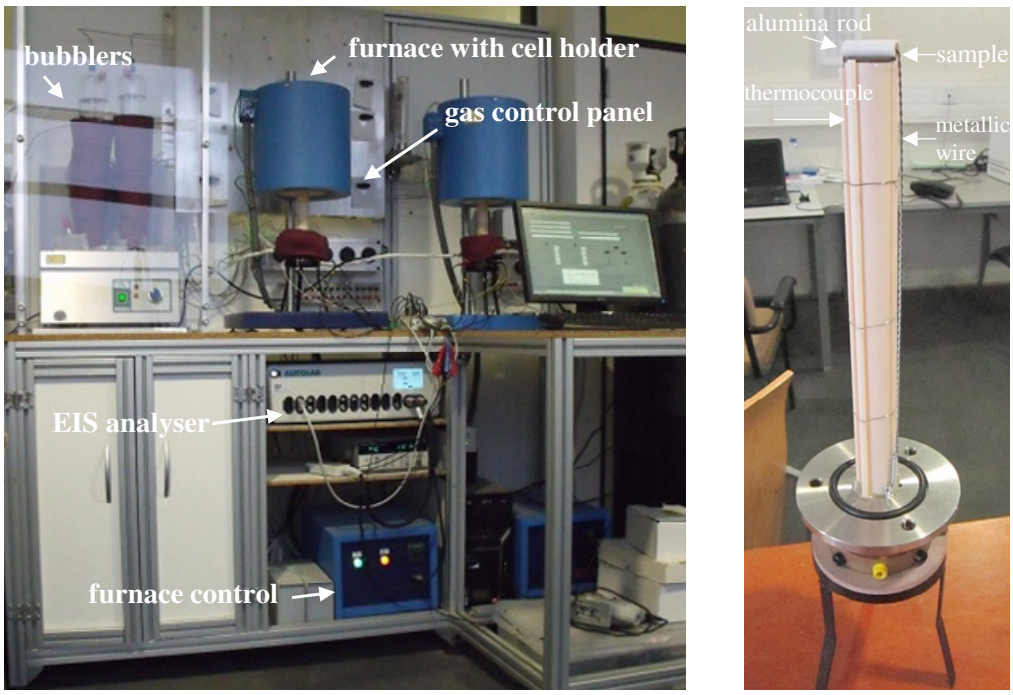

Fig. 2.3. Experimental setup and a cell holder used in the impedance experiments.

The impedance data were deconvoluted using the ZView program (Scribner Associates, Inc.) to obtain contributions ascribed to bulk, grain boundaries and external interfaces, as suggested by typical capacitance values in the ranges of 10 - 20 pF·cm^{-2}, ~ 1 - 10 nF·cm^{-2}, and ~1 - 10 μF·cm^{-2}, respectively [149]. The total, bulk and grain boundary conductivities were determined according to the aforementioned equations (2.13), (2.16) and (2.18-2.20).

The activation energy, E_a, for the bulk and grain boundary conductivities was calculated from the Arrehnius equation, given by:

$$\sigma = \frac{A_0}{T}\exp\left[-\frac{E_a}{R \cdot T}\right] \tag{2.22}$$

where A_0 is the pre-exponential factor.

3. MECHANOSYNTHESIS OF $Ba(Zr,Y)O_{3-\delta}$ NANOPOWDERS

Previous works have demonstrated room temperature mechanosynthesis of the comparable perovskite material $BaTiO_3$ by use of a standard planetary mill at 200 rpm for BaO_2 and TiO_2 precursors [150]. Other authors have shown that $BaCO_3$ and TiO_2 precursors can be reacted by use of a very high energy steel mill operating at 4000 rpm [151]. For the barium zirconate system a two step process of mechanical activation with an additional annealing step has been suggested to produce the perovskite phase [152]. In contrast, the current chapter documents the one step mechanosynthesis of $BaZr_{1-y}Y_yO_{3-\delta}$ materials for compositions $y = 0$, 0.06 and $y = 0.15$, outlining the influence of the choice of thermodynamic favourable precursors, the effect of milling conditions and how this technique may solve many of the limitations presently suffered by alternative synthesis techniques.

3.1. THERMODYNAMIC GUIDELINES FOR THE SELECTION OF Ba-PRECURSORS

Mechanochemical experiments were preceded by thermodynamic analysis as a guide to select the most favourable Ba-precursors for one step mechanosynthesis of $BaZr_{1-y}Y_yO_{3-\delta}$ materials. The free energy change (ΔG) of formation of barium zirconate, from zirconium oxide (ZrO_2) and different barium precursors were determined from the fundamental thermodynamic relation:

$$\Delta G_R = \Delta H_R - T\Delta S_R \tag{3.1}$$

where the enthalpy change (ΔH_R) and entropy change (ΔS_R) of chemical reactions were computed according to the relations:

$$\Delta H_R = \Delta H_R^0 + \int_{298}^{T} \left[\sum_p n_p Cp_p - \sum_r n_r Cp_r \right] dT \tag{3.2}$$

$$\Delta S_{\mathrm{R}} = \Delta S_{\mathrm{R}}^{0} + \int_{298}^{T} \left[\sum_{\mathrm{p}} n_{\mathrm{p}} \frac{C\mathrm{p}_{\mathrm{p}}}{T} - \sum_{\mathrm{r}} n_{\mathrm{r}} \frac{C\mathrm{p}_{\mathrm{r}}}{T} \right] \mathrm{d}T \tag{3.3}$$

where Cp is the heat capacity, n_{p} and n_{r} are the stoichiometric coefficients of products and reactants, respectively, and $\Delta H_{\mathrm{R}}^{0}$ and $\Delta S_{\mathrm{R}}^{0}$ are the enthalpy change and entropy change of chemical reaction, at standard conditions (298 K, 1 atm).

In these equations, the temperature dependence of heat capacity (*C*p) was described as a series of power law terms:

$$C\mathrm{p} = a + bT + cT^{2} + dT^{-2} + \ \ldots \tag{3.4}$$

where *a*, *b*, *c* and *d* are constants. The standard enthalpy ($\Delta H_{\mathrm{R}}^{0}$) and standard entropy ($\Delta S_{\mathrm{R}}^{0}$) of chemical reaction, in reference state (298 K, 1 atm) were calculated from:

$$\Delta H_{\mathrm{R}}^{0} = \sum_{\mathrm{p}} n_{\mathrm{p}} \Delta H_{\mathrm{f,\,p}}^{0} - \sum_{\mathrm{r}} n_{\mathrm{r}} \Delta H_{\mathrm{f,\,r}}^{0} \tag{3.5}$$

$$\Delta S_{\mathrm{R}}^{0} = \sum_{\mathrm{p}} n_{\mathrm{p}} S_{\mathrm{p}}^{0} - \sum_{\mathrm{r}} n_{\mathrm{r}} S_{\mathrm{r}}^{0} \tag{3.6}$$

Thermodynamic data of the standard enthalpy of formation ($\Delta H_{\mathrm{f}}^{0}$), standard entropy ($S^{0}$) and heat capacity terms of the products and reactants were provided by a suitable database (FactSage, GTT Technologies) [153].

The free energy change of formation of barium zirconate from monoclinic zirconium oxide and different barium precursors is shown in Fig. 3.1.

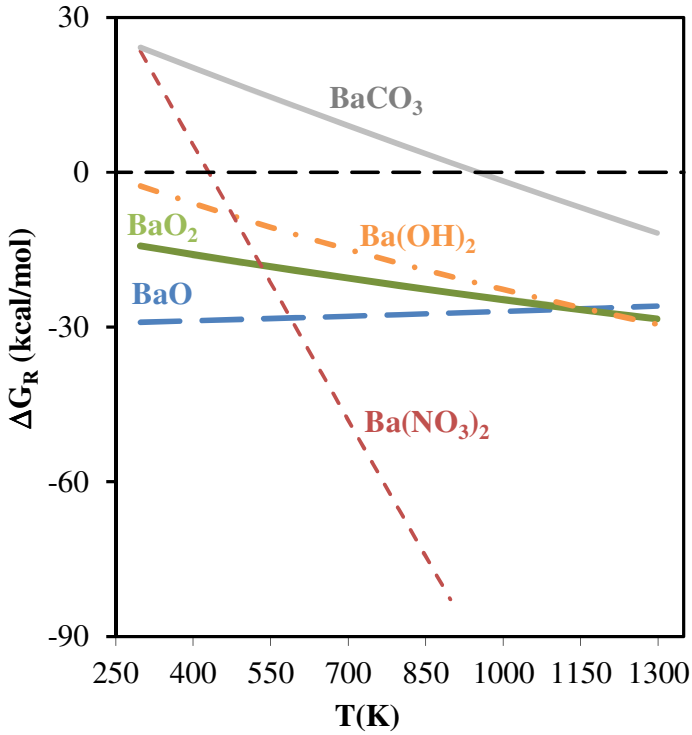

Fig. 3.1. Free energy change (ΔG_R) of formation of barium zirconate starting from zirconium oxide and different barium precursors.

According to thermodynamic data, the formation of $BaZrO_3$ from $BaCO_3$ is thermodynamically unfavorable over a wide temperature range, indicating that mechanosynthesis from this precursor is highly unfeasible. A similar limitation is predicted on using $Ba(NO_3)_2$, except possibly for conditions when high energy milling may cause heating to about 500 K.

Reactions starting from $Ba(OH)_2$, BaO_2 and BaO are thermodynamically favourable even at room temperature. Although the use of BaO as precursor reactant is thermodynamically the most favourable, this oxide reacts readily with atmospheric gases causing the onset of barium carbonate and barium hydroxide, with expected, subsequent, negative impact on mechanosynthesis [154]. The formation of $BaZrO_3$ from BaO_2 and ZrO_2 appears to be the most appropriate choice of thermodynamically favourable precursors at room temperature, as barium peroxide retains reasonable chemical inertness towards atmospheric CO_2, and

reactivity with ZrO_2, while being thermodynamically more favourable than $Ba(OH)_2$. Indeed, previous studies have reported the direct room temperature mechanosynthesis of a comparable material, $BaTiO_3$, for cases when the alkali-earth precursor was barium peroxide [155].

3.2. PHASE FORMATION

The evolution of formation of the perovskite phase of compositions $BaZr_{1-y}Y_yO_{3-\delta}$, y = 0, 0.06 and 0.15, formed by high energy milling of stoichiometric quantities of BaO_2 with zirconia precursors m-ZrO_2, $(ZrO_2)_{0.97}(Y_2O_3)_{0.03}$ and $(ZrO_2)_{0.92}(Y_2O_3)_{0.08}$, respectively, is shown in Fig. 3.2.

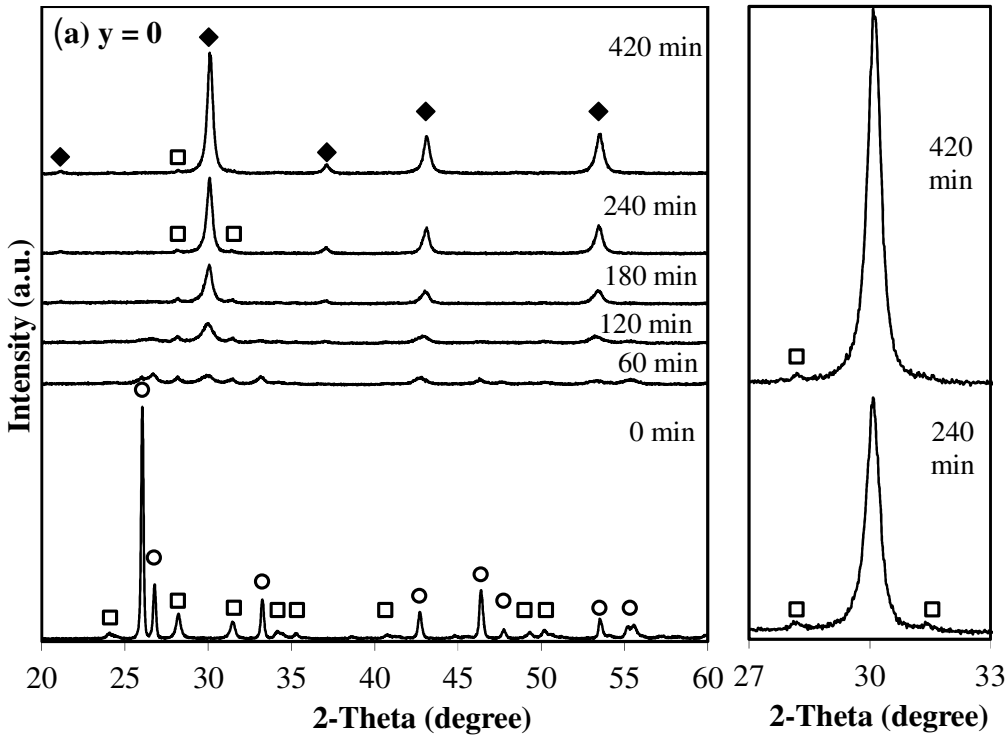

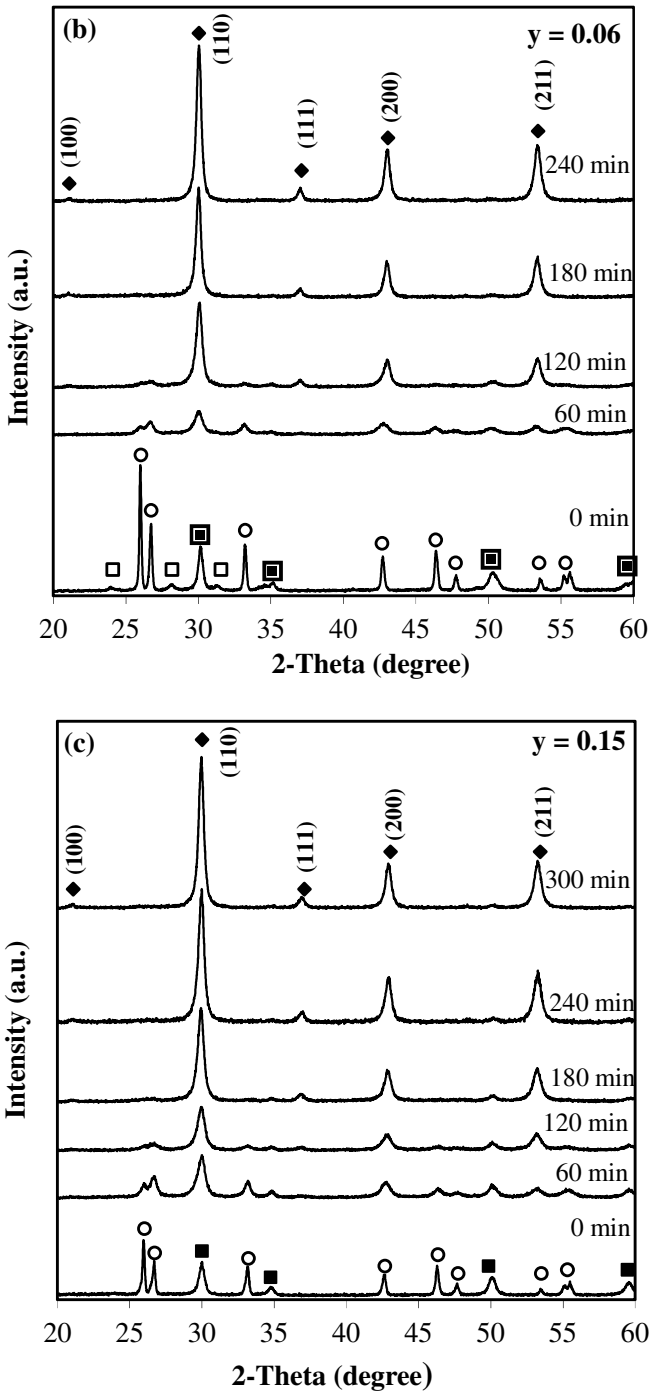

Fig. 3.2. Evolution of powder X-ray diffraction patterns with milling time for $BaZr_{1-y}Y_yO_{3-\delta}$ compositions **(a)** $y = 0$, **(b)** $y = 0.06$, **(c)** $y = 0.15$ for $BaO_2 + ZrO_2$, $(ZrO_2)_{0.97}(Y_2O_3)_{0.03}$ or $(ZrO_2)_{0.92}(Y_2O_3)_{0.08}$ precursors, respectively. The markers identify (○) barium peroxide; (▣, ■) yttria doped zirconia (3 and 8 mol%, respectively; (□) monoclinic zirconia; and (◆) perovskite phase. Partial X-ray patterns of $BaZr_{1-y}Y_yO_{3-\delta}$, $y = 0$, in (a) highlights the presence of *m*-ZrO_2 impurity.

For each composition, the onset of perovskite phase formation can be observed after 60 minutes. Further milling leads to substantial increase in intensity of the perovskite reflections indicating that mechanochemical reaction takes place at room temperature. Reaction appears to occur more rapidly in the case of $y = 0.06$ with the single perovskite phase attained after approximately 240 minutes, Fig. 3.2 (b). In contrast, phase purity in composition $y = 0.15$ requires the longest milling time of 420 minutes, Fig. 3.2 (c), while composition $y = 0$ exhibits small traces of monoclinic zirconia as an impurity phase in the XRD patterns throughout all milling times investigated, Fig. 3.2 (a). In respect to the persistent presence of zirconia in composition $y = 0$, this can be attributed to incomplete reaction with the Ba-precursor. Confirmation of this hypothesis is made by annealing the mechanosynthesised powder of $BaZrO_3$, at 1250 ºC for 5 hours. The XRD pattern (Fig. 3.3) shows a clean pattern of $BaZrO_3$ with no impurity phases and symmetrical peaks suggesting homogeneity.

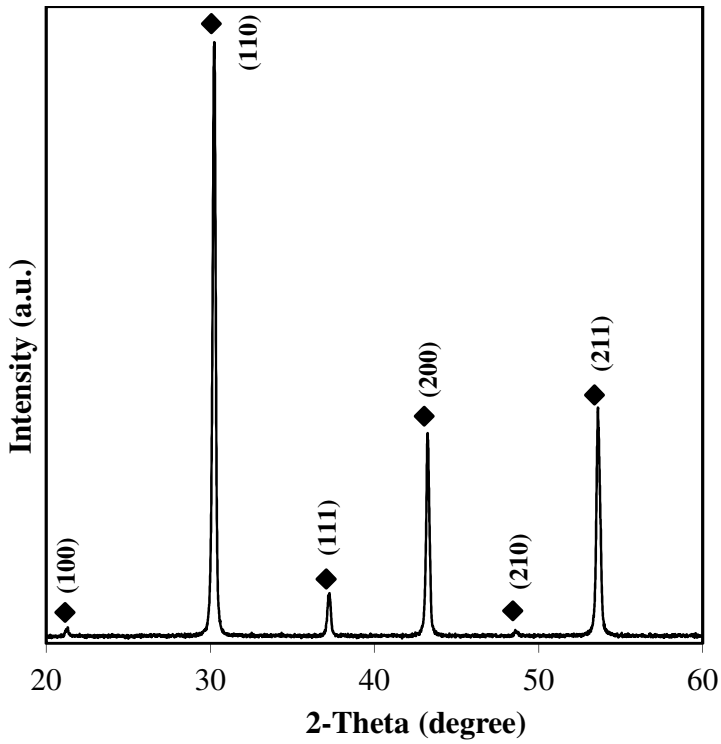

Fig. 3.3. X-ray diffraction pattern after calcination at 1250 ºC of the mechanosynthesised powder of composition $BaZr_{1-y}Y_yO_{3-\delta}$, $y = 0$. The marker (◆) identifies the perovskite phase.

It should be noted that $BaCO_3$ is present as a trace impurity phase in the commercial barium peroxide precursor, and that in accordance with thermodynamic predictions presented in the previous section, the reaction between ZrO_2 and $BaCO_3$ would be unfavourable at temperatures lower than 1000 K, at 1 atm (Fig. 3.1).

Indeed, the mechanochemical reaction of $BaCO_3$ and ZrO_2 does not occur, using the same milling conditions (Fig. 3.4). The starting materials monoclinic zirconia and $BaCO_3$ are retained even for milling times in excess of 690 minutes, with no appearance of the perovskite phase Fig. 3.4.

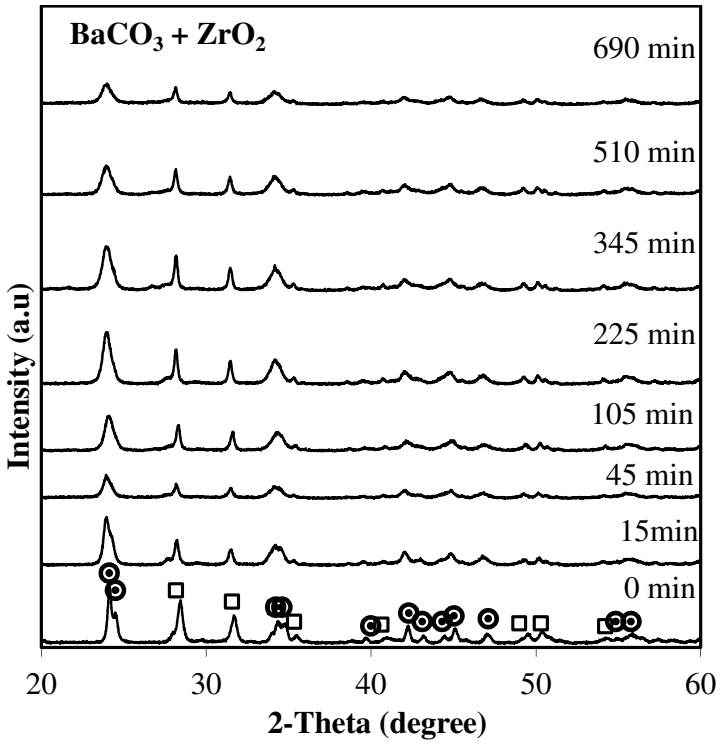

Fig. 3.4. Evolution of powder X-ray diffraction patterns with milling time for $BaZr_{1-y}Y_yO_{3-\delta}$ composition $y = 0$ for $BaCO_3 + ZrO_2$ precursors. The markers identify: (◉) barium carbonate and (□) monoclinic zirconia.

Furthermore, undoped $BaZrO_3$ has shown to have low tolerance to A-site deficiency in contrast to the aliovalent doped compositions [102]. Hence, minor deviations from stoichiometry due to the trace presence of unreacted Ba-precursor would be likely to cause the appearance of zirconia as an impurity phase in the composition $y = 0$, while a comparable compositional variation may be masked in the aliovalent doped compositions due to higher tolerances of Ba-deficiency.

ICP-AES studies have been performed to confirm nominal stoichiometry (Table 3.1). No trend can be observed that relates Zr-content to milling time and the materials studied are shown to have compositions equal to their nominal stoichiometry within the detection limit of the ICP-AES technique. Zirconia milling contaminations, if present, are, therefore, less than 1 mol%, which is in agreement with a maximum of 0.5 wt.% Zr contamination found in powders of $Ca(Ti,Mn)O_{3-\delta}$ mechanosynthesized in similar conditions [118].

Table 3.1. Summary of chemical analysis by ICP-AES of $BaZr_{1-y}Y_yO_{3-\delta}$ powders prepared by mechanosynthesis, including analysis of the initial mixture of precursors respecting to the composition $BaZr_{0.85}Y_{0.15}O_{3-\delta}$ precursor for comparative purposes.

Y- content (y)	Milling Time (minutes)	Ba mol/f.u.	Y mol/f.u.	Zr mol/f.u.
0	420	0.99	-	1.00
0.06	300	0.99	0.06	0.94
0.15	0	1.00	0.15	0.85
	420	0.99	0.15	0.85

Note: Data normalised and reported as moles of cation per formula unit (f.u.).

3.3. EFFECT OF MILLING CONDITIONS

The milling energy needs to be high for the mechanochemical reaction to progress. The use of nylon vials rather than zirconia vials was revealed to be unsuccessful for mechanosynthesis, with no perovskite phase formation for milling times in excess of 420 minutes for even the most reactive starting materials, probably due to absorption of milling energy by vial deformation.

Another interesting factor is the influence of the formed oxygen on the mechanochemical reaction. The progression of the reaction between BaO_2 and ZrO_2 yields oxygen as described in equation (3.7):

$$BaO_2 + ZrO_2 \rightleftharpoons BaZrO_3 + \frac{1}{2} O_2 \qquad (3.7)$$

Previously, the zirconia vial was opened after each 60 minutes of milling to obtain the results shown in Fig. 3.2. This repeated opening of the vial releases the oxygen produced by equation (3.7) allowing the reaction to progress to the right. In contrast, when the formed O_2 is prevented from escaping (by keeping the vial sealed) the mechanochemical reaction is shown to be seriously retarded, Fig. 3.5.

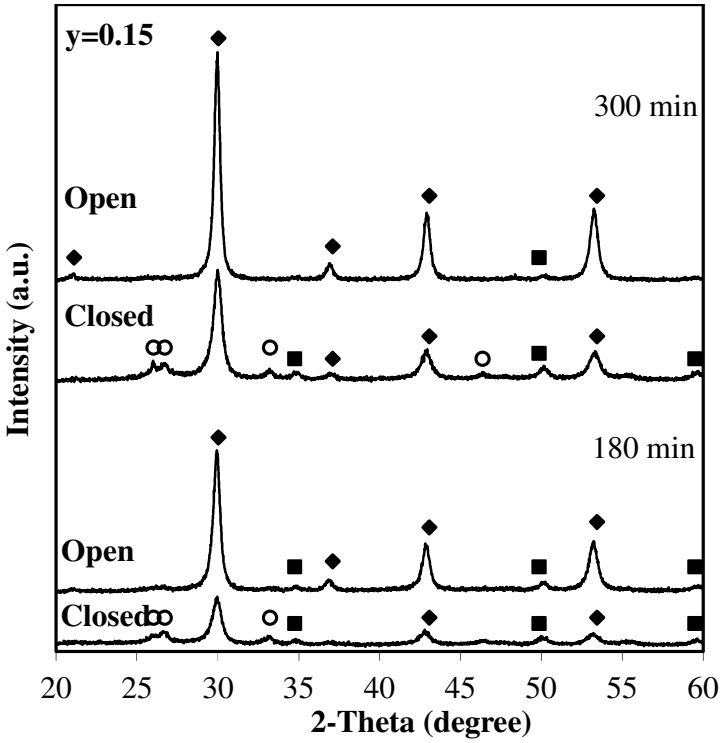

Fig. 3.5. X-ray diffraction patterns highlighting the impaired rate of perovskite phase formation when the formed oxygen is prevented from being released by keeping the vial closed. Composition $BaZr_{1-y}Y_yO_{3-\delta}$, $y = 0.15$. The markers identify: (○) barium peroxide; (■) yttria doped zirconia (8 mol%) and (◆) perovskite phase.

3.4. MICROSTRUCTURE

All XRD patterns exhibit peak broadening which may arise due to the combined effect of a crystallite size in the nanometric range and lattice strain, both typical consequences of high energy milling. The lattice strain induced by milling was assessed by adoption of an integral breadth method, as described in section 2.2.1.1. Therefore, the crystallite size and the mean value of the strain were estimated from the fitted linear data of the graphic representation of equation (2.3) based on the slope and *y*-intercept values, respectively. Size-strain plots of $BaZr_{1-y}Y_yO_{3-\delta}$ for the three compositions, $y = 0$, 0.06 and 0.15, after high energy milling, and the evolution of crystallite size during milling are presented in Fig. 3.6 (a) and (b) respectively.

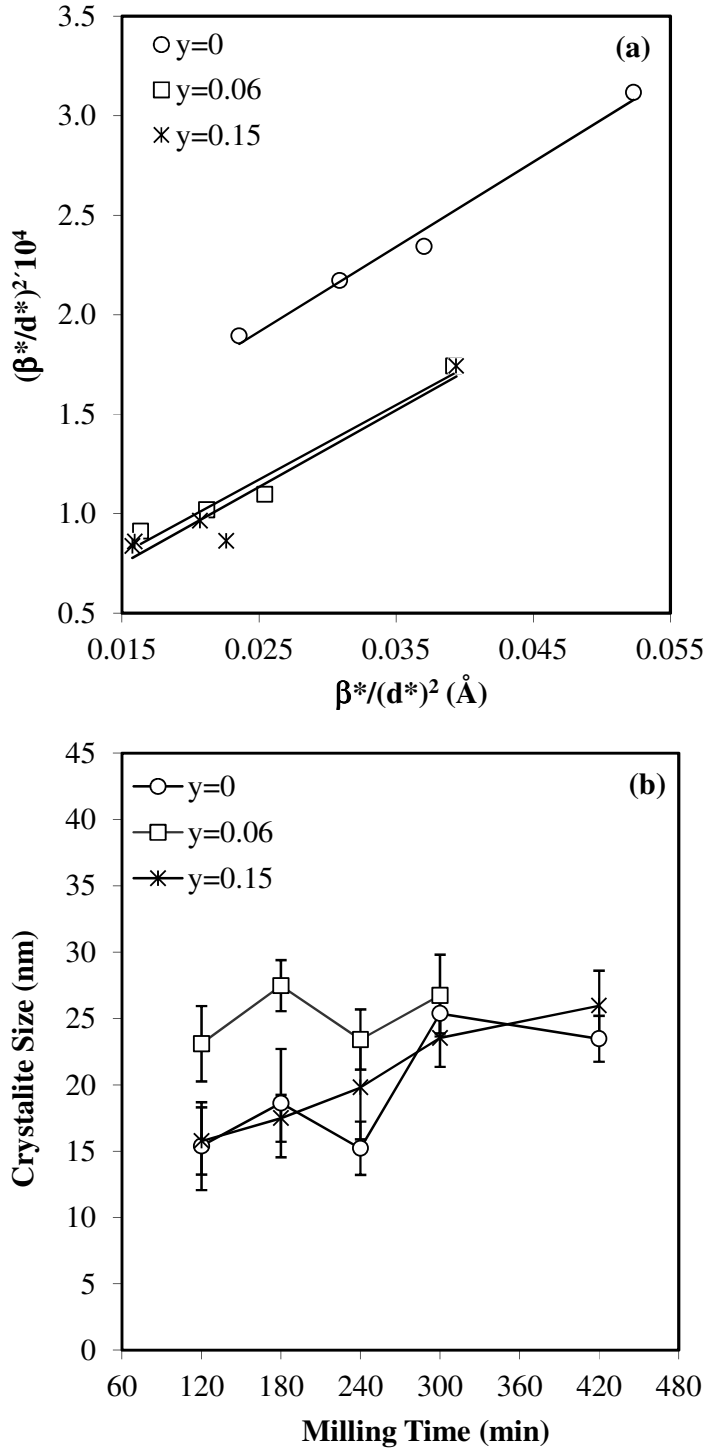

Fig. 3.6. (a) Size-strain plots shown for compositions, y = 0, 0.06 and 0.15 with 420, 300 and 420 minutes of milling time, respectively. **(b)** Crystallite size determined from XRD plotted as a function of milling time.

The crystallite size shows a slight increase with increasing milling time. The crystallite size of all materials is in the order of 15 - 35 nm. These values agree well with particle size determined from TEM images, Table 3.2.

Table 3.2. Crystallite size and root-mean-square strain calculated from size-strain plot for $y = 0$, $y = 0.06$ and $y = 0.15$ compositions, with 420, 300 and 420 minutes of milling time respectively, and comparison with particle size observed by TEM. Table also includes lattice parameters of compositions sintered at 1250 ºC for 5 hours.

y	Crystallite size (W-H), ε (nm)	Crystallite Size (TEM) (nm)	e_{rms} ($\times 10^{-4}$)	Lattice parameter(Å) ± 0.001
0	24 ± 2	14 ± 4	4.6 ± 0 .3	4.187
0.06	27 ± 3	22 ± 5	2.4 ± 0.7	4.201
0.15	26 ± 4	18 ± 2	2.1 ± 1.1	4.220

Some examples of bright field TEM images are shown in Fig. 3.7 These images also demonstrate that the crystallites are essentially spherical in shape, a geometry that has previously been suggested to favour ceramic processing [100]. Mean apparent strain values, expressed as a root-mean-square-strain, $e_{rms} \approx \eta/5$ [138], are about one order of magnitude lower than those reported for lanthanum oxyapatites [156] or manganese-substituted calcium titanate [118], both compounds with structures of lower symmetry. This observation suggests that the strains induced by milling are more easily relaxed in the cubic barium zirconate structure. It is also interesting to note that strain decreases with increasing Y doping.

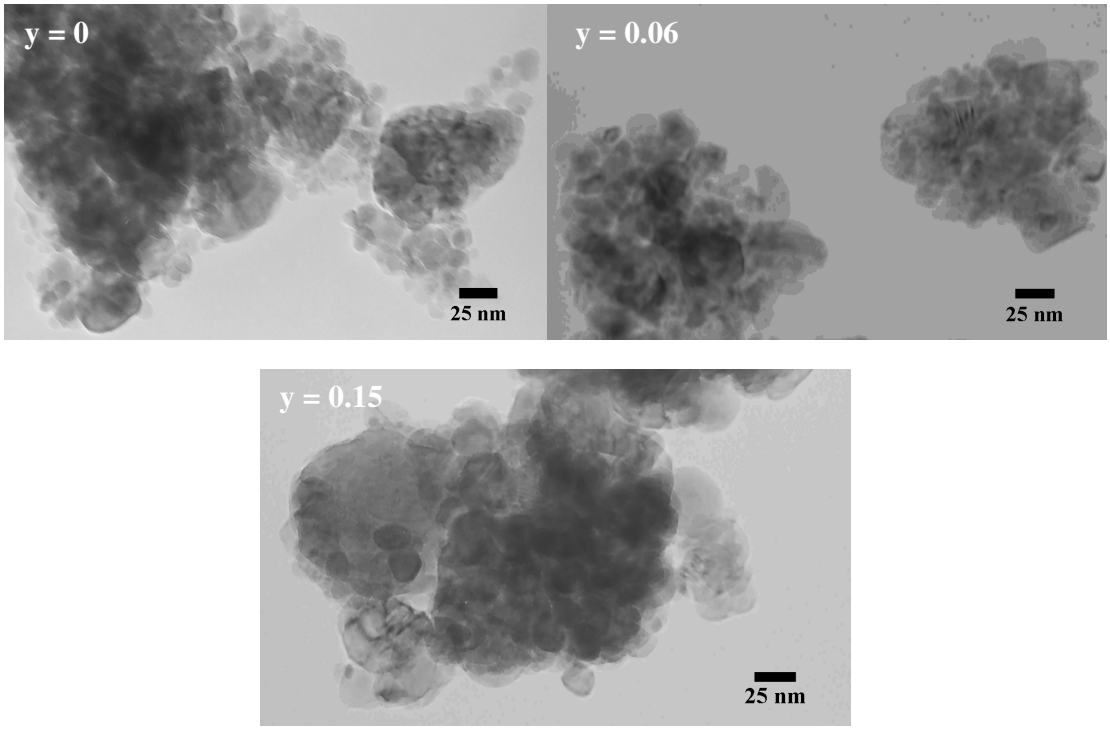

Fig. 3.7. TEM image collected for samples $y = 0$, $y = 0.06$ and $y = 0.15$, milled for 420, 300 and 420 minutes, respectively.

3.5. CARBONATE FORMATION

As already noted, the formation of $BaCO_3$ as an impurity phase on decomposition of organics is a common drawback of soft chemical synthesis routes. The formed $BaCO_3$ requires additional calcinations steps to remove and may add to compositional inhomogeneity. Moreover, the requirement of a separate calcination step may also lead to powder coarsening, defeating the primary purpose of the soft chemical synthesis route. Fig. 3.1 has shown that the mechanosynthesised powders do not exhibit $BaCO_3$ under the limit of resolution of XRD. The FT-IR technique, in contrast, offers much higher sensitivity to detect $BaCO_3$ in these materials and is used to reinforce that mechanosynthesis offers a method of producing $BaZrO_3$-related materials with very low contaminations of $BaCO_3$, as well as to assess the stabilities of the produced nanocrystallite powders upon prolonged exposure to air (Fig.3.8).

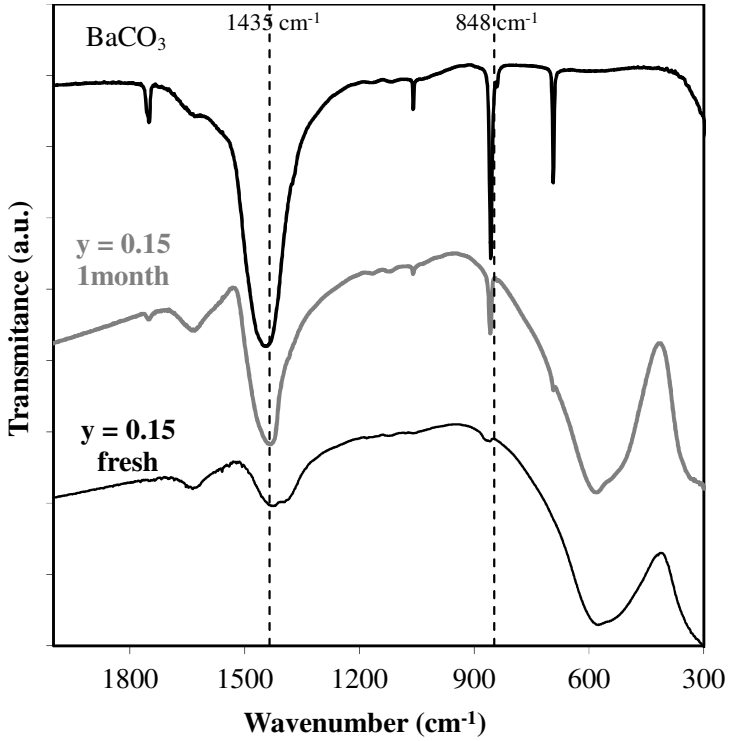

Fig. 3.8. Comparison between infrared transmission spectra of undried $BaCO_3$ commercial powder with mechanosynthesised $BaZr_{0.85}Y_{0.15}O_{3-\delta}$ powder after exposure to atmospheric conditions for 1 month, and fresh mechanosynthesised $BaZr_{0.85}Y_{0.15}O_{3-\delta}$ powder.

Typical absorption bands attributed to the vibrations in the CO_3^{2-} anion are located within the 1800 – 400 cm^{-1} region. These bands are shown in Fig. 3.8 for an undried commercial $BaCO_3$ powder for comparative purposes. The strong broad absorption centred at about 1435 cm^{-1} can be connected with the asymmetric stretching vibrations, while sharp absorption bands at approximately 848 cm^{-1} and 688 cm^{-1} can be assigned to out of plane bending vibrations and in plane vibrations respectively [157]. A weak absorption band at 1072 cm^{-1} can also be observed due to symmetric stretching vibrations, while a broad absorption band at 1460 cm^{-1} has been assigned to water uptake and OH bending [158]. Comparison of the FT-IR spectrum of $BaCO_3$ with the spectrum of the freshly made composition $BaZr_{0.85}Y_{0.15}O_{3-\delta}$ shows only very small traces of $BaCO_3$ in the mechanosynthesised powder (bands at 848 cm^{-1} and 1435 cm^{-1}), which may be a remnant from the commercial barium peroxide precursor used in

this study. Fig. 3.8 additionally shows the absorption spectrum of a mechanosynthesised $BaZr_{0.85}Y_{0.15}O_{3-\delta}$ powder after exposure to atmospheric conditions for 1 month. Clearly, the quantity of $BaCO_3$ impurity has increased substantially, with characteristic absorption bands of CO_3^{2-} now observable at 697, 859 and 1076 cm^{-1}. The broad absorption peak at around 1460 cm^{-1} also exhibits increased intensity which can be associated with either increase in $BaCO_3$ formation or water uptake due to overlap of CO_3^{2-} asymmetric stretching vibrations and OH bending at this wavelength [157,158]. It is interesting to question whether carbonation is a generic problem related to nanoscale $BaZrO_3$ powders due to their high surface energies, especially as studies of the longevity of such nanopowders against carbonation are scarce.

3.6. DENSIFICATION

Previously, authors have shown that density in $BaZrO_3$ is inversely related to particle size [100]. The current mechanosynthesis results show the formation of spherical crystallites with sizes in the region of 15 - 35 nm; properties that should, thus, favour densification in the current materials. Fig. 3.9, therefore, explores densification and grain growth for compositions $y = 0$, $y = 0.06$ and $y = 0.15$ as a function of sintering temperature.

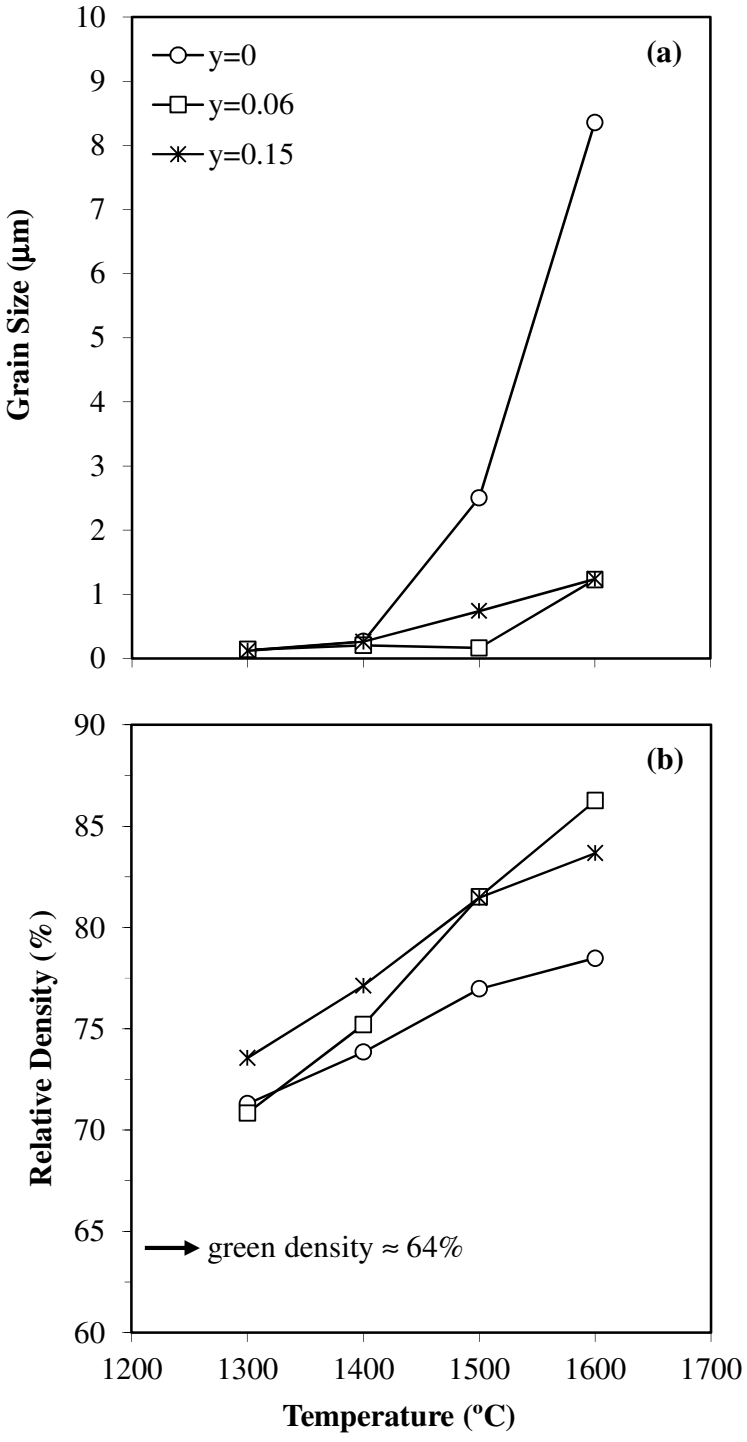

Fig. 3.9. Grain size **(a)** and relative density **(b)** for $BaZr_{1-y}Y_yO_{3-\delta}$ ceramics as a function of sintering temperature. Dwell time at each temperature is 5 hours

An increase in grain size can be observed for sintering temperatures in excess of 1500 ºC for all compositions, Fig. 3.9 (a). Grain growth, however, is much greater in the case of $BaZrO_3$, $y = 0$ (~9 μm at 1600 °C), than for the aliovalent doped compositions, $y = 0.06$ and $y = 0.15$ (~1 μm). This phenomenon demonstrates that the formation of oxygen vacancies does not enhance grain growth in these materials. A similar phenomenon has been noted by Chen et al. [159] for doped cerias where the formation of oxygen vacancies by aliovalent doping also does not enhance grain growth. Chen et al. suggested that the negative impact of solute drag was the cause of this effect. As comparable aliovalent dopant enrichment of crystallite interfaces has also been observed for nanoscale powders in the current materials [160], a similar phenomenon may be acting in the present system.

It also should be noted that a high grain growth in composition $y = 0$, does not relate to a higher density, i.e. grain growth occurs without shrinkage. In fact, data for yttrium–substituted materials indicate much higher densification rates, Fig. 3.9 (b).

Table 3.3 summarizes literature values of the percentage of the theoretical density (%ThD) obtained for aliovalent doped $BaZrO_3$ prepared by a wide range of synthesis techniques for samples sintered under comparable conditions. The densification of the current mechanosynthesised powders betters many previous works documented in the literature and competes well with peak densities reported for materials formed by state of the art soft chemical routes, such as sol-gel or spray pyrolysis, which offer densities lying in the range 90 – 95 % of the theoretical, under similar sintering conditions.

Table 3.3. Relative density (% ThD) of mechanosynthesised composition $y = 0.15$, with 420 minutes of milling time, compared with literature values for $BaZr_{1-y}Y_yO_{3-\delta}$ prepared by a wide range of synthesis routes.

y	Preparation method	% ThD	T (ºC)	Ramp rate (ºC/min)	Dwell (hour)	Particle Size (nm)	Pressing conditions (MPa)	Covered	Ref.
0.10	Sol-gel-acrylates	95	1500	1.5	15	< 20	n/a, vaccum 370	Yes	[110]
0.10	Spray pyrolysis	91	1500	n/a	1	250	Uniaxial, 170	n/a	[114]
0.10	Spray pyrolysis	68	1500	n/a	n/a	n/a	n/a, 200	n/a	[98]
0.10	Sol-gel	65	1500	n/a	n/a	n/a	n/a, 200	n/a	[98]
0.10	Solid State	64	1500	n/a	n/a	n/a	n/a, 200	n/a	[98]
0.10	Spray Dried	59	1500	n/a	n/a	n/a	n/a, 200	n/a	[98]
0.15	Mechanosyn.	90	1500	5	10	15 - 35	Isostatic, 200	Yes	This work
0.20	Sol-gel-alkoxides	99	1500	n/a	20	3 - 5	Anvil, 4000	n/a	[161]
0.20	Sol-gel polyacrymide	95	1500	n/a	10	n/a	Isostatic, n/a	Surface removed	[109]

3.7. ENHANCED $BaZrO_3$ MECHANOSYNTHESIS BY THE USE OF METASTABLE ZrO_2 PRECURSORS

In order to investigate the potential impact of crystallographic symmetry of Zr-precursor on the mechanochemical preparation of $BaZrO_3$-based materials, undoped barium zirconate was prepared from BaO_2 and different zirconia polymorphs: monoclinic (*m*-ZrO_2), and tetragonal (*t*-ZrO_2).

3.7.1. SYNTHESIS OF ZIRCONIA POLYMORPHOUS

Zirconia is susceptible to polymorphic transformation, adopting a monoclinic crystal structure at room temperature and transforming to tetragonal and cubic symmetries at respectively higher temperatures (Fig. 3.10) ([162–167].

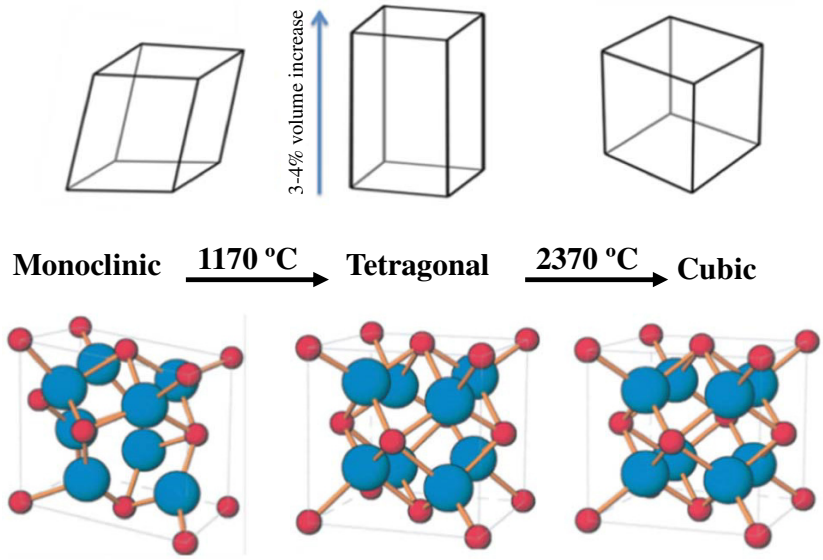

Fig. 3.10. Polymorphic transformation of ZrO_2: changes in lattice and crystal system view (adapted from [168]).

As the tetragonal polymorph of zirconia is thermodynamically stable at temperatures higher than 1170 °C and highly metastable at room temperature, stabilizing oxides are usually added to retain the tetragonal phase to low temperatures [169,170]. Nonetheless, several preparation routes have been documented that can produce the metastable tetragonal phase of pure,

undoped ZrO_2 at room temperature. These processes typically consist of precipitation of hydrous zirconia with ammonia or triethanolamine from a zirconium salt solution, leading to amorphous zirconia that is crystallized by subsequent thermal treatment of the hydrous zirconia precipitate. By changing the concentration of zirconium salt solution, adding H_2O_2 to the solution and sulphation of precipitated zirconia before heat treatment, it is possible to form metastable tetragonal zirconia at room temperature without adding stabilizing dopants [135-137].

Thus, in this study samples of *m*-ZrO_2 and *t*-ZrO_2 were prepared by slow alkaline precipitation, following the procedure described in the experimental section 2.1.1. The chemical preparation of *m*-ZrO_2 was also performed by the slow alkaline precipitation route to guarantee comparable particle size between the both precursors.

Fig. 3.11 shows the XRD patterns of synthesized tetragonal and monoclinic zirconia powders. It can be seen that the formation of pure *m*-ZrO_2 and *t*-ZrO_2 phases are achieved at room temperature.

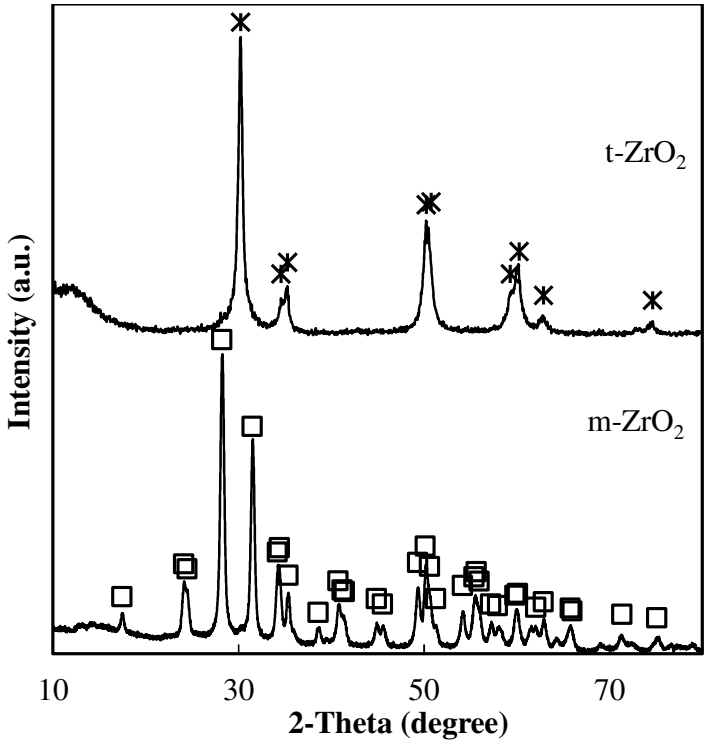

Fig. 3.11. X-ray diffraction patterns of the synthesized zirconia powders. The markers identify: (△) *m*-ZrO_2 and (○) *t*-ZrO_2.

SEM images of the ZrO_2 polymorphs powders show spherical agglomerates, consisting of particles with sizes in the nanometric range, as depicted in Fig. 3.12. The particle sizes determined by specific Brunauer-Emmett-Teller (BET) surface-area measurements were approximately 15 nm for *t*-ZrO_2 and 27 nm for *m*-ZrO_2. The close match in the particle size for each ZrO_2 precursor powder facilitates the subsequent comparison of these materials during mechanical milling.

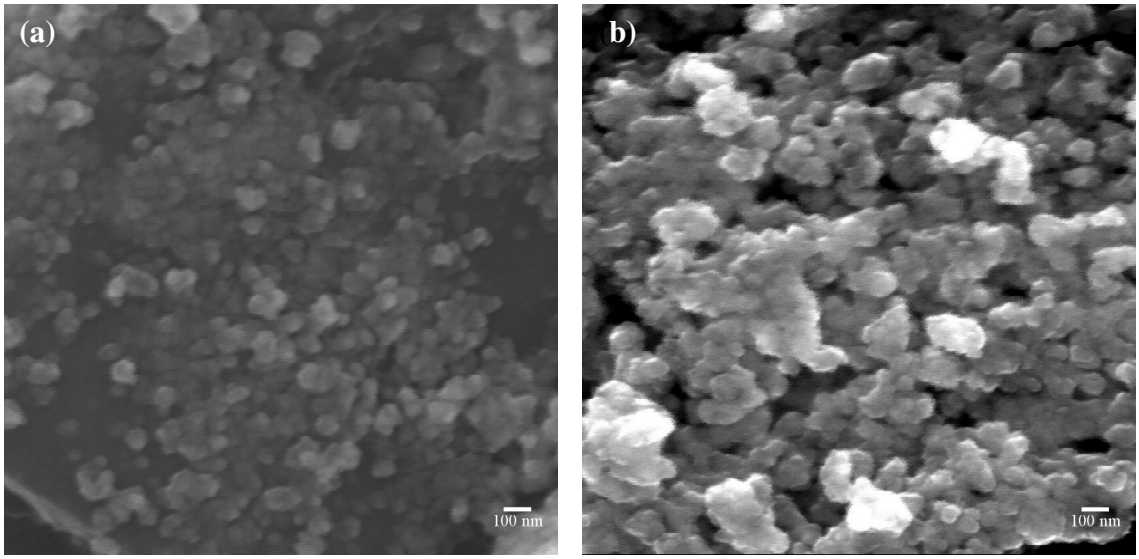

Fig. 3.12. SEM images of **(a)** monoclinic zirconia and **(b)** tetragonal zirconia powders mounted on carbon tapes.

3.7.2. TRANSFORMATION OF ZIRCONIA POLYMORPHS UNDER HIGH ENERGY MILLING

Fig. 3.13 illustrates the XRD patterns of *t*-ZrO_2 and *m*-ZrO_2 after different milling times. Starting from *t*-zirconia, one observes the partial conversion to *m*-zirconia, with appearance of *m*-ZrO_2 after 60 minutes of milling and a considerable lowering of *t*-ZrO_2 peaks, Fig. 3.13 (a). In contrast, XRD patterns of monoclinic zirconia precursor show the slow appearance of the tetragonal phase. While the *t*-ZrO_2 precursor is shown to rapidly decrease in quantity, converting partially to *m*-ZrO_2 on milling, the *m*-ZrO2 precursor demonstrates the inverse behaviour, partially converting to the higher symmetry tetragonal phase on mechanical milling.

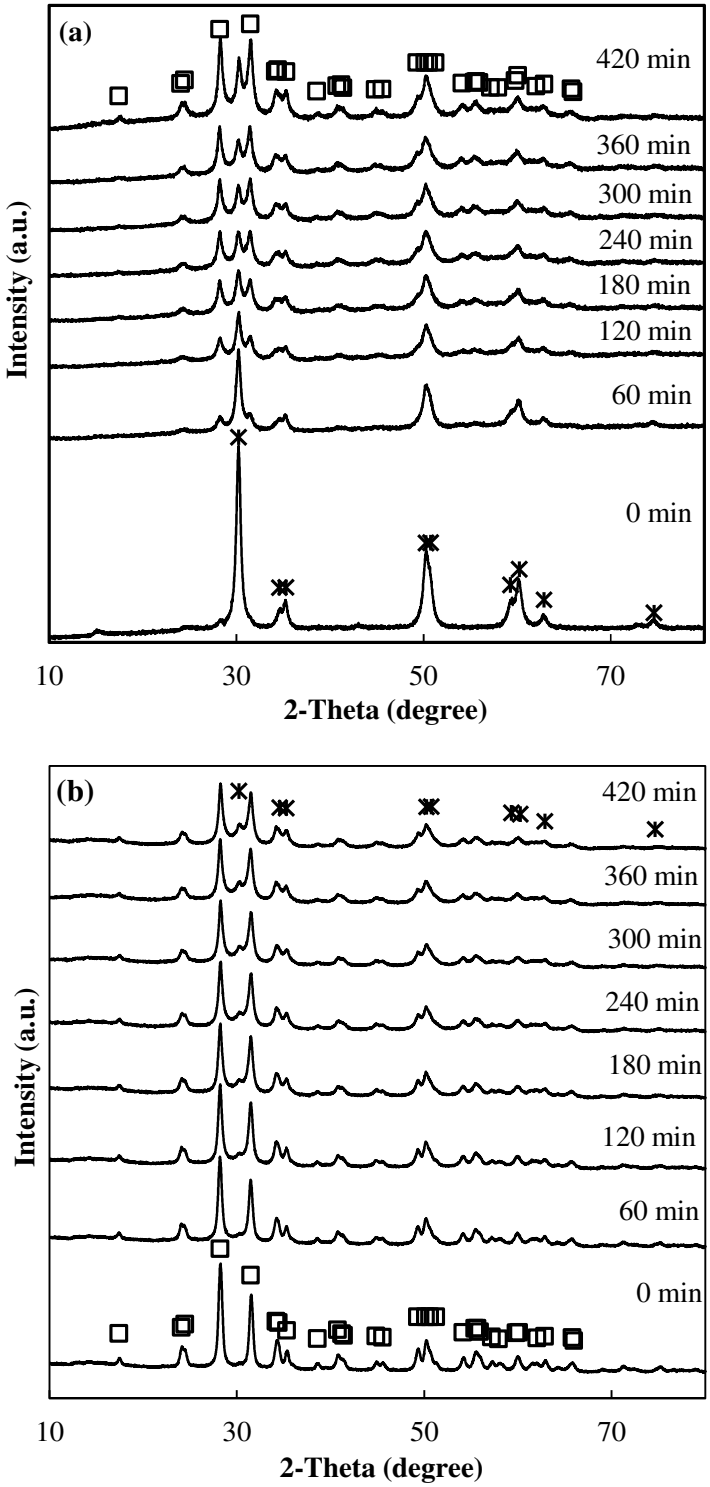

Fig. 3.13. X-ray diffraction patterns of **(a)** *t*-ZrO_2, and **(b)** *m*-ZrO_2 powders after different milling times. The markers identify: (□) *m*-ZrO_2; (∗) *t*-ZrO_2.

Weight fractions of *t*-ZrO_2 after different milling times, starting from monoclinic and tetragonal precursors (Fig. 3.14), were determined from Rietveld quantitative phase analysis. It can be seen that transformation is fast during the initial hours of milling and conversion of *t*-ZrO_2 to *m*-ZrO_2 reaches almost 50 % (w/w) after 120 minutes. For longer milling times, the rate of transformation decreases and the fraction of residual tetragonal phase tend to a plateau. Contrarily, the polymorphic modification of the monoclinic zirconia precursor upon high energy milling is shown to be slower than that of the inverse transformation of the tetragonal precursor. The rate of transformation of *m*-ZrO_2 to *t*-ZrO_2 is almost constant after 120 minutes up to the longest milling time (420 minutes). Moreover, the conversion of *m*-ZrO_2 to *t*-ZrO_2 only reaches about 20 % (w/w) after 420 minutes milling time in comparison to the modification of greater than 60 % (w/w) of *t*-ZrO_2 to *m*-ZrO_2 in the case of the tetragonal precursor in the same time period. Determination of the amount of amorphous phase in the cases of the monoclinic and tetragonal precursors indicates that the amount of amorphous phase after a milling time of 420 minutes was effectively negligible.

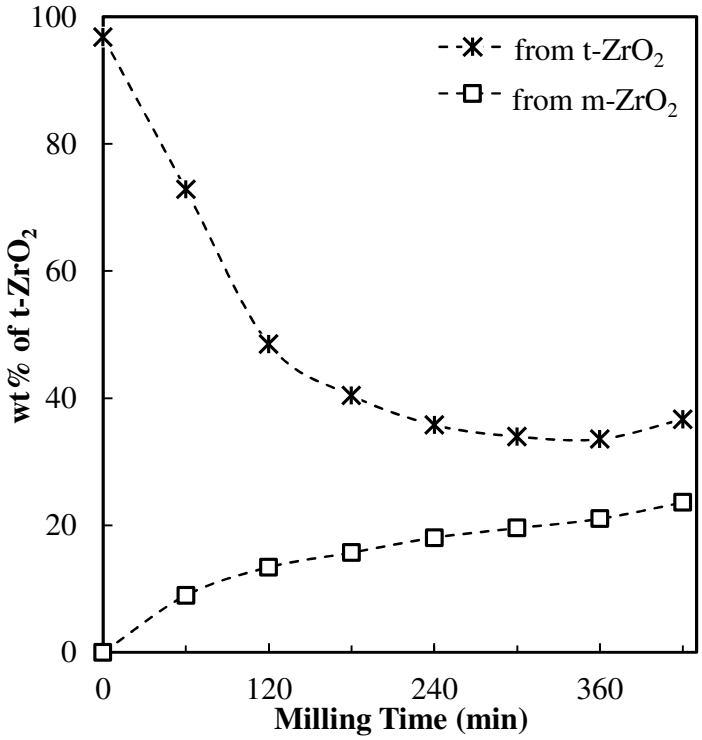

Fig. 3.14. Weight fractions of *t*-ZrO2 as a function of milling time starting from: (□) *m*-ZrO_2, and (∗) *t*-ZrO_2.

The XRD patterns after different milling times also reveal additional changes associated to peak broadening, possibly caused by changes of crystallite size in the nanometric range, lattice strain, and significant residual microstrain.

The assessment of the contributions of these effects to the integral-breadth was evaluated by the adoption of and integral-method, similarly to that described on the section 2.2.1.1. Size-strain plots of monoclinic and tetragonal zirconia before and during milling are presented in Fig. 3.15. Results for 300 minutes and 420 minutes of milling are not shown as the fitted data give excessively high errors for long milling times (above 40 % for e_{rms}). Similar difficulties have also been reported by other authors and are suggested to be due to very low particle sizes and amorphization [156,171]. In the current case, difficulties also arise as the deconvolution of XRD peaks is affected by the close proximity of coexisting tetragonal and monoclinic polymorph reflections after extended milling. In this respect, the size-strain plots of *t*-ZrO_2 proved to be particularly complex to analyse due to the rapid conversion of *t*-ZrO_2 to the monoclinic polymorph. Note that after 60 minutes and 120 minutes of milling the *t*-ZrO_2 precursor, the samples contain about 27 % and 51 % of *m*-ZrO_2 (Fig. 3.14). Thus, only the main reflections of the tetragonal phase are considered in order to minimize the risks of overlapping of XRD reflections of both *m*-ZrO_2 and *t*-ZrO_2.

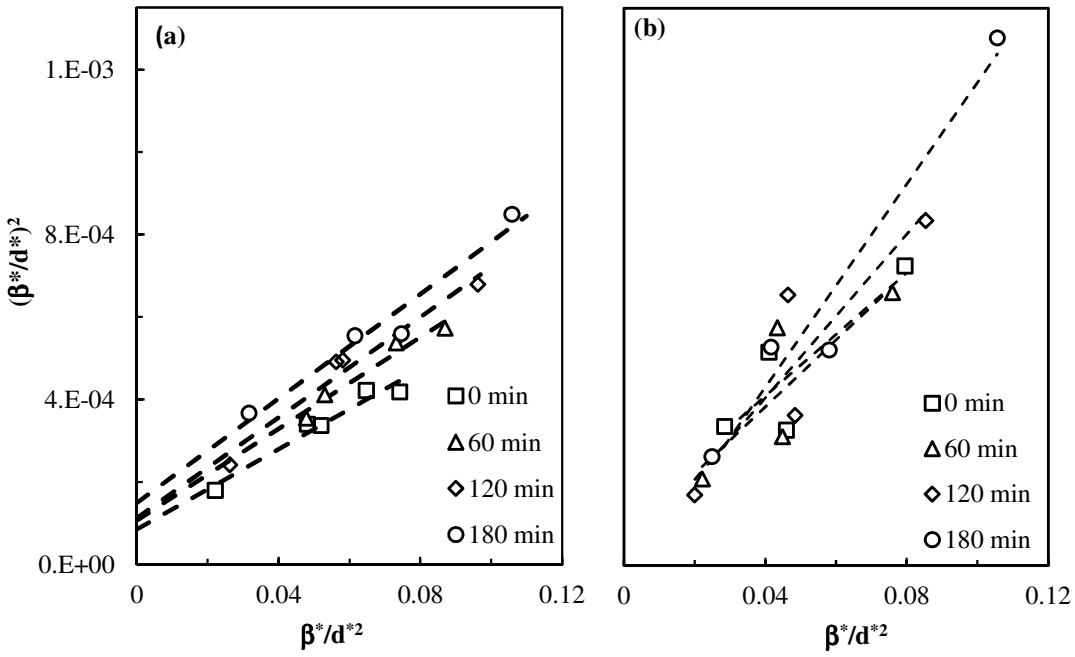

Fig. 3.15. Size-strain plots of **(a)** *m*-ZrO_2 and **(b)** *t*-ZrO_2 before milling and after 60, 120 and 180 min of high energy milling.

The results of average crystallite size and root-mean-square strain, e_{rms}, for *m*-ZrO_2 and *t*-ZrO_2, estimated from the fitted linear data of the graphic representation of equation (2.3) and considering the relation (2.4), are shown in Fig. 3.16. One notes a close correlation between the calculated crystallite sizes and those recorded by the BET technique and the decreasing of average crystallite size with milling time for both zirconia precursors.

The percentage of error associated with the determination of average crystallite size for *m*-ZrO_2 at different milling times is in the range of 11 – 23 %. The corresponding values of strain exhibit notable increases with milling time, a trend that is typical of mechanical activation [172,173], Fig. 3.16 (a).

Although major errors are associated with the estimates of average crystallite size of *t*-ZrO_2 upon milling, Fig. 3.16 (b), it may be assumed that effects of high energy milling of *t*-ZrO_2 powders include a prevailing contribution to partial transformation to *m*-ZrO_2 combined with decreases in crystallite size and strain. Contrary to what is noted in the case of *m*-ZrO_2, one

observes a clear decrease in strain with milling time in the *t*-ZrO_2 precursor. This can be ascribed to the polymorphic transformation of *t*-ZrO_2 to *m*-ZrO_2 through high energy milling, that may dissipate the increase in specific surface and elastic-strain energies induced by mechanical activation [172,173].

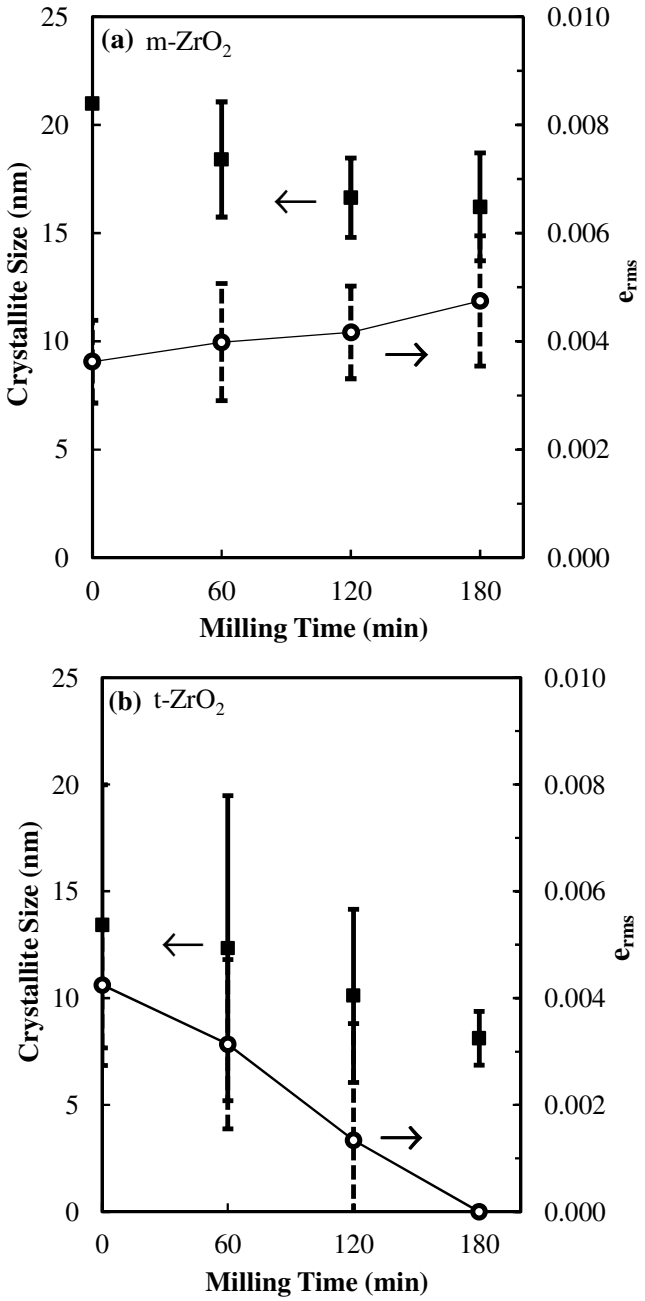

Fig. 3.16. Average crystallite size (■) and root mean square strain, e_{rms}, (○) determined from the size-strain plot as a function of milling time for: **(a)** *m*-ZrO_2, and **(b)** *t*-ZrO_2.

3.7.3. MECHANOSYNTHESIS OF $BaZrO_3$

The XRD patterns in Fig. 3.17 show the evolution of formation of barium zirconate as a function of milling time from BaO_2 and *t*-ZrO_2. It can be seen that the formation of $BaZrO_3$ using *t*-ZrO_2 is very fast and traces of precursor reactants cannot be seen in the X-ray diffractograms after only 120 minutes. This can be ascribed to the high reactivity of metastable *t*-ZrO_2 powders on high energy milling, as shown above. One should also note that no *m*-ZrO_2 can be observed during milling, suggesting that mechanical activation in the current case leads directly to chemical synthesis rather than phase modification. The presence of minor quantities of $BaCO_3$ observable after 60 minutes milling time, most likely results from the high reactivity of BaO_2 and exposure of powder to atmospheric CO_2 either during milling or before XRD can be performed.

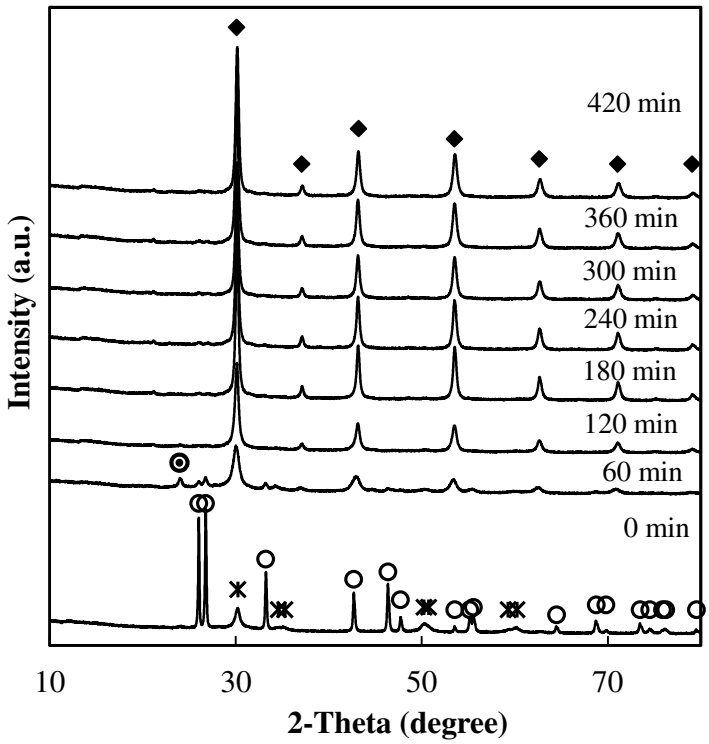

Fig. 3.17. X-ray diffraction patterns of $BaZrO_3$ after different milling time using BaO_2 and *t*-ZrO_2 as precursors. The markers identify: (○) BaO_2, (∗) *t*-ZrO_2, and (◉) $BaCO_3$ and (◆) perovskite phase.

The evolution of mechanosynthesis of $BaZrO_3$ from BaO_2 and *m*-ZrO_2 is presented in Fig. 3.18 as a function of milling time. By using *m*-ZrO_2 as precursor, the rate of $BaZrO_3$ formation is distinctly slower than that observed when using *t*-ZrO_2 as starting material, and traces of the main reflection of *m*-ZrO_2 are observed after the longest milling time. One also observes the appearance of small peaks of barium carbonate, in the XRD patterns after 360 and 420 minutes of milling, that can be ascribed to the reaction of BaO_2 with atmospheric CO_2, indicating that total conversion of BaO_2 is also incomplete even after the longest milling time when using the *m*-ZrO_2 precursor. Note that these results are in line with those reported previously, in section 3.2, for the mechanochemical reaction of $BaZrO_3$ from BaO_2 and commercial *m*-ZrO_2, under similar milling conditions: the observation of incomplete reaction by high energy milling, with consequent persistence of *m*-ZrO_2 in final mechanosynthesised powders.

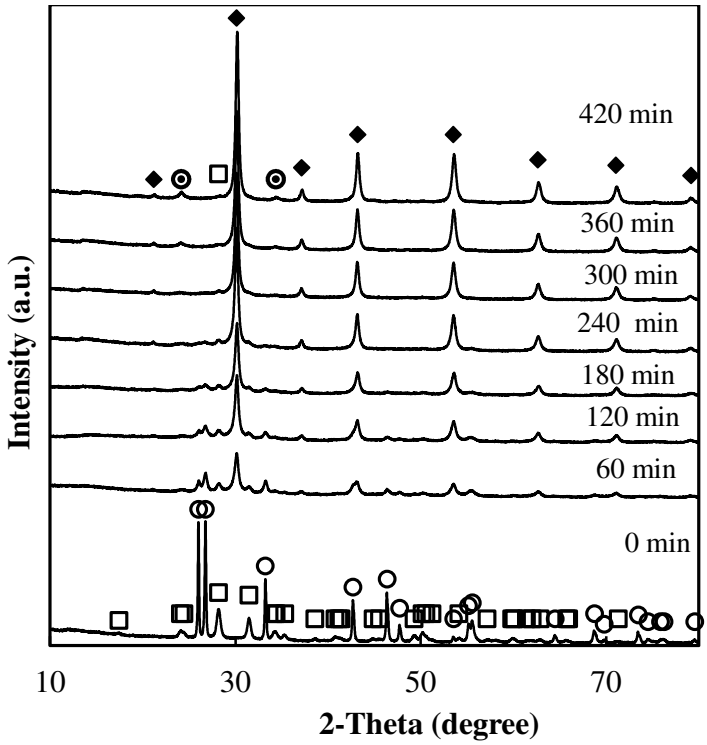

Fig. 3.18. X-ray diffraction patterns of $BaZrO_3$ after different milling time using BaO_2 and *m*-ZrO_2 as precursors. The markers identify: (○) BaO_2, (□) *m*-ZrO_2, (◉) $BaCO_3$ and (◆) perovskite phase.

The fraction of formed $BaZrO_3$, evaluated by quantitative Rietveld analysis of XRD data, summarized in Fig. 3.19, highlights the faster conversion to $BaZrO_3$ by mechanosynthesis from *t*-ZrO_2 compared to the mechanosynthesis from *m*-ZrO_2, which can be ascribed to the high reactivity of metastable *t*-ZrO_2 powders on high energy milling.

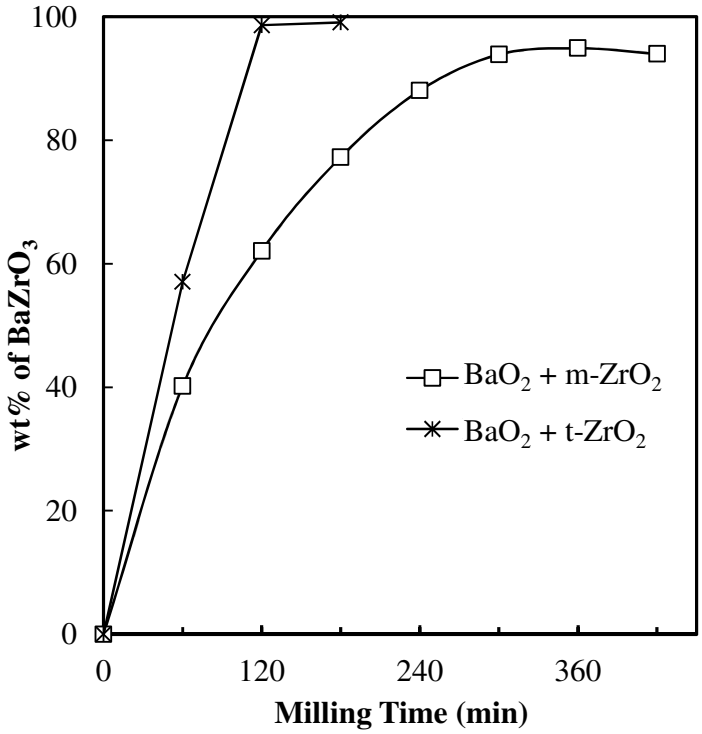

Fig. 3.19. Weight fraction of $BaZrO_3$ as a function of milling time for mixtures of barium peroxide with different zirconia precursor polymorphs.

In order to assess the yield obtainable by room-temperature mechanosynthesis under these conditions, the amount of amorphous phase was determined by Rietveld refinement of the XRD patterns after 420 minutes of milling for each set of precursors, Table 3.4. It can be seen that yields of $BaZrO_3$ of approximately 82 % and 78 % can be obtained from the precursors, *t*-ZrO_2 – BaO_2 and *m*-ZrO_2–BaO_2, respectively, under these milling conditions.

Table 3.4. Weight percentages of $BaZrO_3$, $BaCO_3$ and amorphous phase after room temperature mechanosynthesis for each set of precursors.

	t-ZrO_2 - BaO_2 (%w/w)	*m*-ZrO_2 - BaO_2 (%w/w)
$BaZrO_3$	81.5	77.7
$BaCO_3$	-	8.3
Amorphous	18.5	14

Further assessment of yield was performed by thermogravimetry (Fig. 3.20). The initial stage of weight loss starts at room temperature, reaches a maximum rate at temperatures below 100 °C and lows down to a minimum rate at $T \approx 315$ °C for *t*-ZrO_2–BaO_2/$BaZrO_3$ mixtures and at $T \approx 375$°C for *m*-ZrO_2–BaO_2/$BaZrO_3$. This stage may be ascribed to losses of adsorbed humidity. A second stage shows increasing rate of weight losses until a maximum at about $T \approx 630$ °C for *t*-ZrO_2–BaO_2/$BaZrO_3$ and $T \approx 660$ °C for *m*-ZrO_2–BaO_2/ $BaZrO_3$; most likely related to decomposition of residual barium peroxide, which is expected to occur in this temperature range [174].

One may even assume further formation of barium zirconate during the heating schedule of thermogravimetry, mainly because the fraction of weight uptake on subsequent cooling is much smaller than on heating. This suggests that the fraction of unreacted precursors nearly vanishes after the peak temperature. Note that this feature is in line with the previous observation of complete reaction by calcination of mechanosynthesised powders.

The measured weight losses of the second stage were, therefore, used to estimate the fraction of residual (amorphous) barium peroxide after mechanosynthesis of barium zirconate. It was thus concluded that the yield of barium zirconate was about 86 % for the *t*-ZrO_2-BaO_2/$BaZrO_3$, and slightly lower, 80 %, for m-ZrO_2–BaO_2/$BaZrO_3$. The incomplete conversion of the precursors to the final $BaZrO_3$ product explains the observation of traces of barium carbonate even after long milling times (Fig. 3.18). In addition, the slower formation of the $BaZrO_3$ phase in the *m*-ZrO_2–BaO_2 case may increase the time available for carbonate formation, a factor that possibly contributes to the differences in final yield, due to the aforementioned, thermodynamic, unsuitability of $BaCO_3$ for $BaZrO_3$ mechanosynthesis.

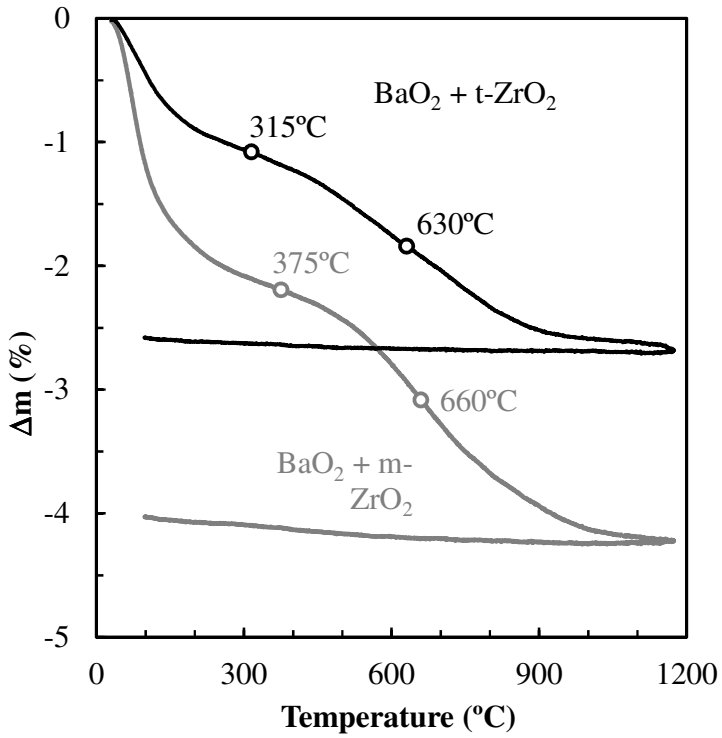

Fig. 3.20. TGA plot of $BaZrO_3$ powders obtained from *t*-ZrO_2-BaO_2 and *m*-ZrO_2-BaO_2 powder mixtures, heated and cooled under dry Ar atmosphere, at a rate of 5 ºC·min^{-1}.

3.8. CONCLUDING REMARKS

High energy milling of barium peroxide with high purity ZrO_2, $(ZrO_2)_{0.97}(Y_2O_3)_{0.03}$ or $(ZrO_2)_{0.92}(Y_2O_3)_{0.08}$ precursors at 650 rpm in zirconia vials, leads to mechanochemical reaction and the formation of perovskite $Ba(Zr_{1-y}Y_y)O_{3-\delta}$ powders at room temperature for the compositions $y = 0$, 0.06 and 0.15, respectively. High energy milling using $BaCO_3$ as a starting reagent does not allow the formation of the perovskite phase for any composition. Also, the use of nylon vials rather than hard zirconia vials do not allow the production of the perovskite phase for even the most reactive reagents. Prevention of release of formed oxygen is shown to impede the mechanochemical reaction.

The formed perovskite crystallites are spherical in shape with an average size determined from XRD of ca. 30 nm in agreement with transmission electron microscopy observations. A spherical crystallite shape at the nanoscale allows highly competitive densification levels when compared to $BaZrO_3$-based materials formed by alternative synthesis techniques in the

literature under similar sintering conditions. FT-IR spectra demonstrate that contamination levels of $BaCO_3$ in the mechanosynthesized powders are very low offering an important advantage over many common alternative low temperature synthesis routes. These advantages together with the use of cheap precursors, fast preparation times, and the absence of pollutant gases demonstrate mechanosynthesis to be a highly attractive method for the formation of $BaZrO_3$-related nanopowders.

The use of metastable tetragonal zirconia as precursor in the mechanosynthesis of $BaZrO_3$ yields faster conversion to barium zirconate by mechanochemical reaction with barium peroxide, as compared to monoclinic zirconia precursor.

Also, tetragonal and monoclinic polymorphs of zirconia show different behaviour upon high energy milling activation. Faster transformation of the metastable tetragonal zirconia is observed, yielding substantial quantities of the monoclinic zirconia after short milling times. In contrast, mechanical activation of the *m*-ZrO_2 precursor shows a slow transformation to small quantities of the tetragonal polymorph, even after relatively long milling times. The integral-breadth method applied to the XRD patterns, after different milling times, suggests a slight decrease in crystallite size for both *t*-ZrO_2 and *m*-ZrO_2 precursors upon milling. In the case of *m*-ZrO_2, milling also leads to increases in strain. In contrast, the rapid polymorphic change to lower symmetry on milling the *t*-ZrO_2 precursor appears to liberate the strain associated with mechanical activation.

4. PHASE PURITY, MICROSTRUCTURE AND ELECTRICAL PROPERTIES OF $BaZr_{1-y}Y_yO_{3-\delta}$ ($y = 0.15, 0.20$) PREPARED BY MECHANOCHEMICAL PROCESSING

As reported in Chapter 3, mechanosynthesis is shown to be an efficient preparation method for $Ba(Zr,Y)O_{3-\delta}$ materials, producing pure powders, containing nanometric crystallites, that offer good densification. The present chapter aims to investigate the phase formation, microstructure and electrical properties of promising $BaZr_{1-y}Y_yO_{3-\delta}$ compositions with yttrium contents of $y = 0.15$ (BZY15) and $y = 0.20$ (BZY20) formed upon sintering of mechanosynthesised nanopowders, in comparison to literature data of similar compositions formed by other preparation routes, with the goal to establish relations between processing, purity, composition, structure and electrical properties.

Modelling of electrical conductivity based on defect structure equilibria was also performed in order to separate the partial conductivities of protons, oxygen vacancies and electron holes.

4.1. PHASE FORMATION AND COMPOSITIONAL ANALYSIS

The segregation of $Ba(Zr,Y)O_{3-\delta}$ materials into two separate perovskites of differing Y-contents is a frequently reported phenomenon that remains extremely controversial. It has been suggested by several authors to occur upon high temperature sintering [98,175], while this has been negated by others [102]. Additional authors have advocated that phase segregation occurs only after subsequent lower temperature calcination [176]. Typically, authors that have experienced this phenomenon have used standard solid state routes for materials preparation with multiple firing and regrinding cycles, a route that, potentially, may not provide good homogeneity.

The X-ray diffraction patterns of $BaZr_{0.85}Y_{0.15}O_{3-\delta}$ (BZY15) and $BaZr_{0.80}Y_{0.20}O_{3-\delta}$ (BZY20) materials prepared by one-step sintering of nanopowders prepared by mechanosynthesis are presented in Fig. 4.1 after heat treatment at 1250 ºC and 1600 ºC, for 1 and 5 hours, respectively.

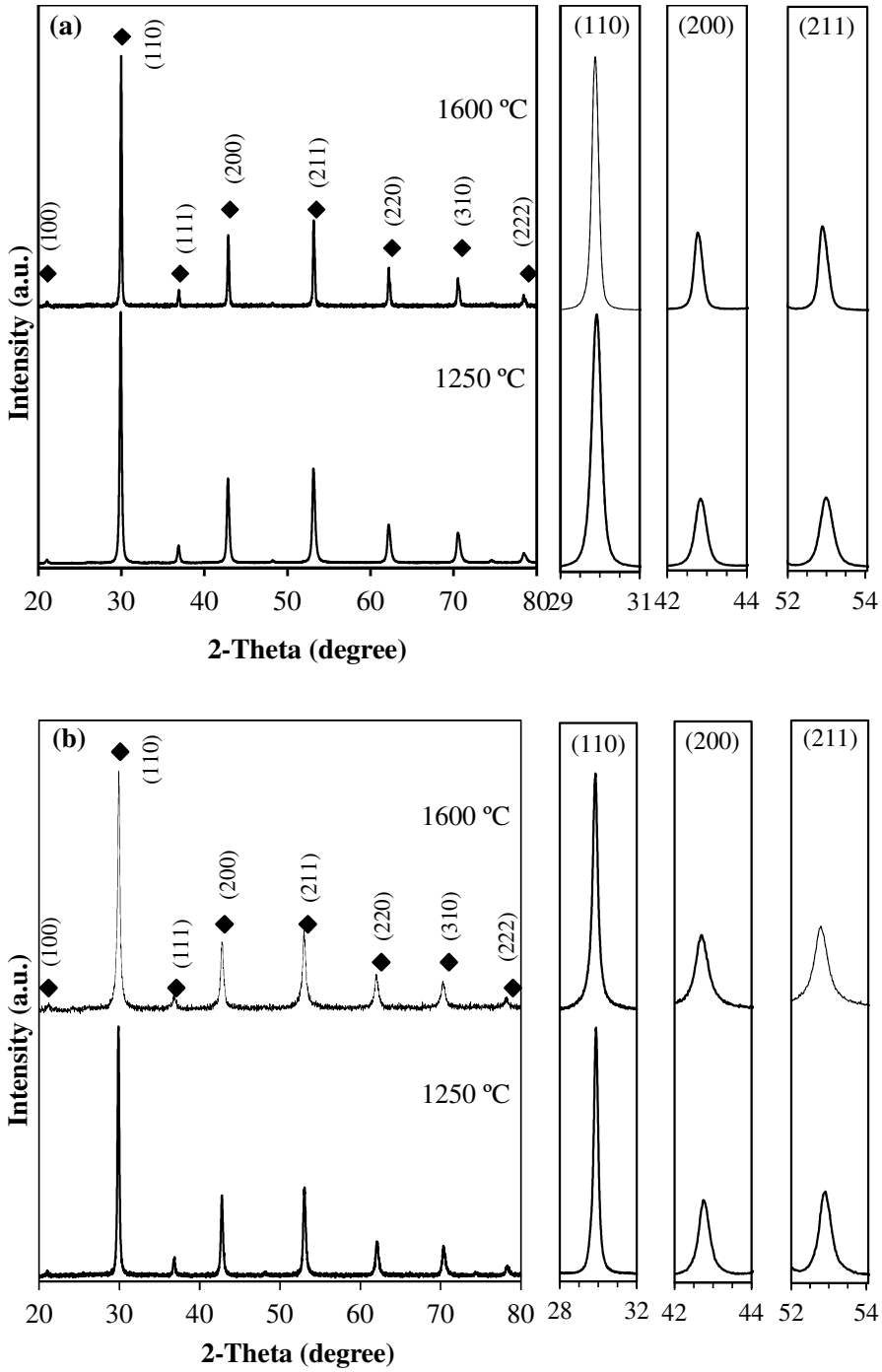

Fig. 4.1. X-ray diffraction patterns of: **(a)** $BaZr_{0.85}Y_{0.15}O_{3-\delta}$ (BZY15) and **(b)** $BaZr_{0.80}Y_{0.20}O_{3-\delta}$ (BZY20) prepared by sintering of nanopowders formed by mechanosynthesis, at 1250 ºC and 1600 ºC, for 1 and 5 hours, respectively; and the correspondent partial X-ray diffraction patterns in the vicinity of major $BaZrO_3$ (110), (200) and (211) peaks.

The X-ray diffraction patterns of $BaZr_{1-y}Y_yO_{3-\delta}$ compositions ($y = 0.15$ and $y = 0.20$) formed by mechanosynthesis show the formation of pure perovskite phases, with no secondary or separate $BaZrO_3$ phases formation, for either temperature.

For these compositions, under similar heat treatment temperatures, different results have been reported for different powder preparation routes. For instance, a recent work of Park et al. [177] similarly reported the formation of single perovskite phases of $BaZr_{0.85}Y_{0.15}O_{3-\delta}$ prepared by different methods such as, combustion synthesis, polymer gelation and hydrothermal method after sintering at 1670 ºC for 24 hours. Yamazaki et al. [145] also reported the formation of the single perovskite phase of $BaZr_{0.80}Y_{0.20}O_{3-\delta}$ sintered at 1600 ºC, with no evidence of phase separation. In contrast, other works have reported the existence of segregated perovskite phases under similar conditions [175,178]. For example, Oyama et al. [175] studied phase formation in the Y-doped $BaZrO_3$ system using solid-state reaction and a processing temperature of 1600 ºC. These authors observed the stable co-existence of two cubic phases of $BaZrO_3$, with different yttrium concentrations. In contrast to these authors, Imashuku et al. [178] showed the occurrence of phase separation into two perovskites structures at a heat treatment temperature of 1300 ºC. However at 1600 ºC no phase separation was observed. The authors, therefore, attributed the phase separation to a contracting phase field for the pure perovskite phase at the lower temperature [176].

It is worth noting that the variety of results in the literature may derive from the various synthesis methods and sintering profiles used. Thus, in order to separate the influence of powder preparation route and thermal history on phase purity, $BaZr_{0.85}Y_{0.15}O_{3-\delta}$ and $BaZr_{0.80}Y_{0.20}O_{3-\delta}$ were processed from mechanosynthesised nanopowders, while reproducing the temperature profile and experimental conditions employed by Oyama et al. [175], which comprised of two thermal steps, 1350 ºC for 10 hours and 1600 ºC, for 10 hours, and the use of sacrificial powder of the same composition to control Ba-loss by evaporation.

The resultant X-ray diffraction patterns, Fig. 4.2, confirm the presence of a single perovskite phase after sintering mechanosynthesised powders under these conditions. This result suggests

that it is very likely that the phase separation reported in the literature comes from inhomogeneities present due to the processing route, rather than being an intrinsic materials property. As such, the segregation of the phase into two separate perovskites can be avoided by the use of methods of synthesis that produce powders with high levels of homogeneity. In this context, mechanochemical processing is shown to be a highly attractive method for the preparation of pure $BaZr_{1-y}Y_yO_{3-\delta}$ materials.

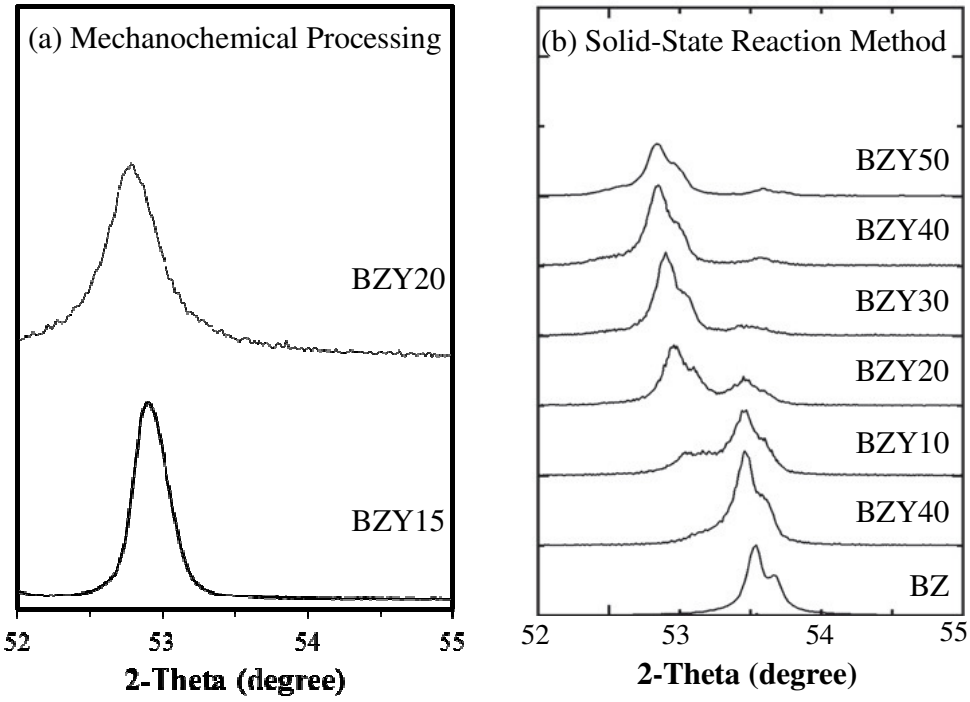

Fig. 4.2. Partial powders X-ray diffraction patterns in the vicinity of major $BaZrO_3$ (211) peak of: **(a)** $BaZr_{0.85}Y_{0.15}O_{3-\delta}$ (BZY15) and $BaZr_{0.80}Y_{0.20}O_{3-\delta}$ (BZY20) compositions prepared by mechanochemical processing using the sintering conditions adopted by Oyama et al. [175]; **(b)** obtained by Oyama et al. [175] for $BaZr_{1-y}Y_yO_{3-\delta}$, with $0 \leq y \leq 0.50$, prepared by solid-state reaction.

4.2. MICROSTRUCTURE

Ceramic samples of $BaZr_{0.85}Y_{0.15}O_{3-\delta}$ (BZY15) and $BaZr_{0.80}Y_{0.20}O_{3-\delta}$ (BZY20) with density of approaching 90 % with respect to the theoretical density were obtained by sintering at 1600 ºC, for 5 hours. SEM images reveal the formation of polyhedral grains, with a calculated average grain size of 0.9 ± 0.1 μm and 1.5 ± 0.2 μm (Fig. 4.3) for BZY15 and BZY20 compositions, respectively. The increase of grain size with the increase of Y-content has been noted in other works [179,180].

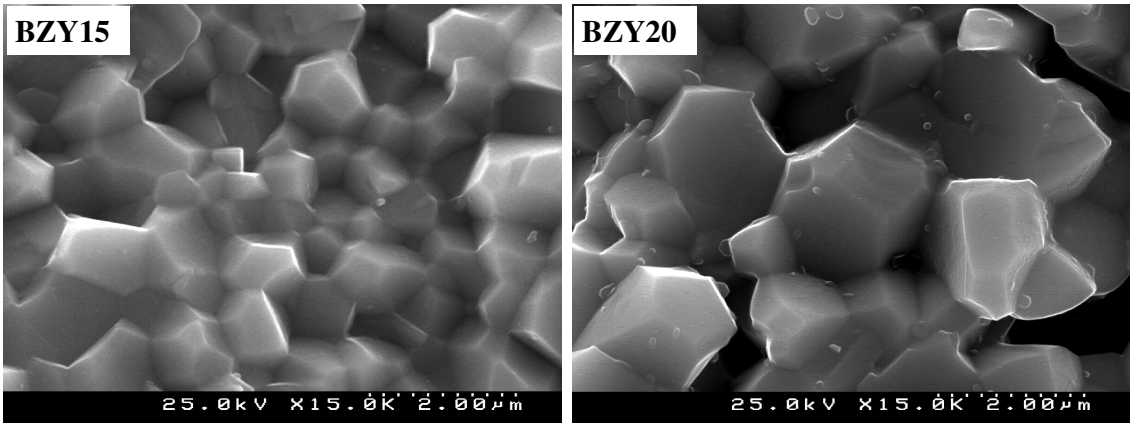

Fig. 4.3. SEM micrographs of fractured $BaZr_{0.85}Y_{0.15}O_{3-\delta}$ (BZY15) and $BaZr_{0.80}Y_{0.20}O_{3-\delta}$ (BZY20) pellets after sintering in air at 1600 ºC, for 5 hours.

By comparison with literature results of other powder processing routes, for the same compositions and at similar sintering temperatures (Table 4.1) the grain sizes obtained from mechanochemical processing are noted to be higher, despite the significantly lower sintering times used in the current work (5 hours in this work against 8 - 24 hours in other studies). Thus, mechanochemical processing is again proven to be a highly attractive route for the preparation of active powders to produce larger grain sizes under shorter sintering conditions with respect to standard solid-state reaction or typical soft chemistry techniques.

Table 4.1. Processing methods, sintering profile and characteristics of compositions of $BaZr_{0.85}Y_{0.15}O_{3-\delta}$ (BZY15) and $BaZr_{0.80}Y_{0.20}O_{3-\delta}$ (BZY20) obtained in this study, and reported in the literature.

No.	Y content (mol %)	Synthesis Method	Sintering		Pressure (MPa)	Average Grain Size (μm)	Relative Density (%)	Conductivity Measurements in wet atmosphere	Authors [Ref]
			T (ºC)	Time (hour)					
1	15	mechanosynthesis	1600	5	300	0.90	87.2	10 % H_2/N_2	current work
2	15	polymer gelation	1670	24	200	0.41	95.3	5 % H_2/N_2	Park et al. [177]
3	15	solid state reaction	1800	20	220	2.70	> 95	air	Iguchi et al. [180]
4	15	nitrate freeze-drying	1600	24	392	-	97.8	Ar	Imashuku et al. [181]
5	15	solid state reaction	1670	24	200	0.17	94.0	5 % H_2/N_2	Park et al. [177]
6	15	solid state reaction	1700	20	-	-	-	N_2	Kreuer [47]
7	15	combustion	1670	24	200	0.22	80.1	5 % H_2/N_2	Park et al. [177]
8	15	hydrothermal	1670	24	200	0.28	86.5	5 % H_2/N_2	Park et al. [177]
9	20	mechanosynthesis	1600	5	300	1.50	87.5	10 % H_2/N_2	current work
10	20	sol-gel / reactive sintering	1600	24	300-379	0.44	90	N_2 or Ar	Yamazaki et al. [48]
11	20	glycine-nitrate combustion	1600	24	400	0.46	99.2	N_2	Babilo et al. [101]
12	20	modified Pechini	1600	12	450	0.5	90	10 % H_2/Ar	Fabbri et al. [179]
13	20	sol-gel	1600	8	250	0.10 - 0.30	80	H_2	Fabbri et al. [182]
14	20	sol-gel	1500	20	4000	0.20	99.4	Ar	Cervera et al. [161]
15	20	solid state reaction	1675	10	200	-	96	40 % H_2/Ar	Nomura et al. [183]
16	20	sol-gel	1600	10	50	0.25 - 0.60	92.1	10 % H_2/Ar	Liu et al. [184]
17	20	solid state reaction	1600	24	392	-	-	H_2	Han et al. [185]
18	20	solid state reaction	1700	20	-	-	-	-	Kreuer [47]

4.3. ELECTRICAL CONDUCTIVITY

4.3.1. COMPARISON OF TOTAL ELECTRICAL CONDUCTIVITY WITH LITERATURE DATA

The total conductivities measured in wet atmospheres of $BaZr_{0.85}Y_{0.15}O_{3-\delta}$ (BZY15) and $BaZr_{0.80}Y_{0.20}O_{3-\delta}$ (BZY20) samples prepared from mechanosynthesised powders are compared in Fig. 3.4. to literature values of similar materials prepared from alterative preparation routes, Table 4.1.

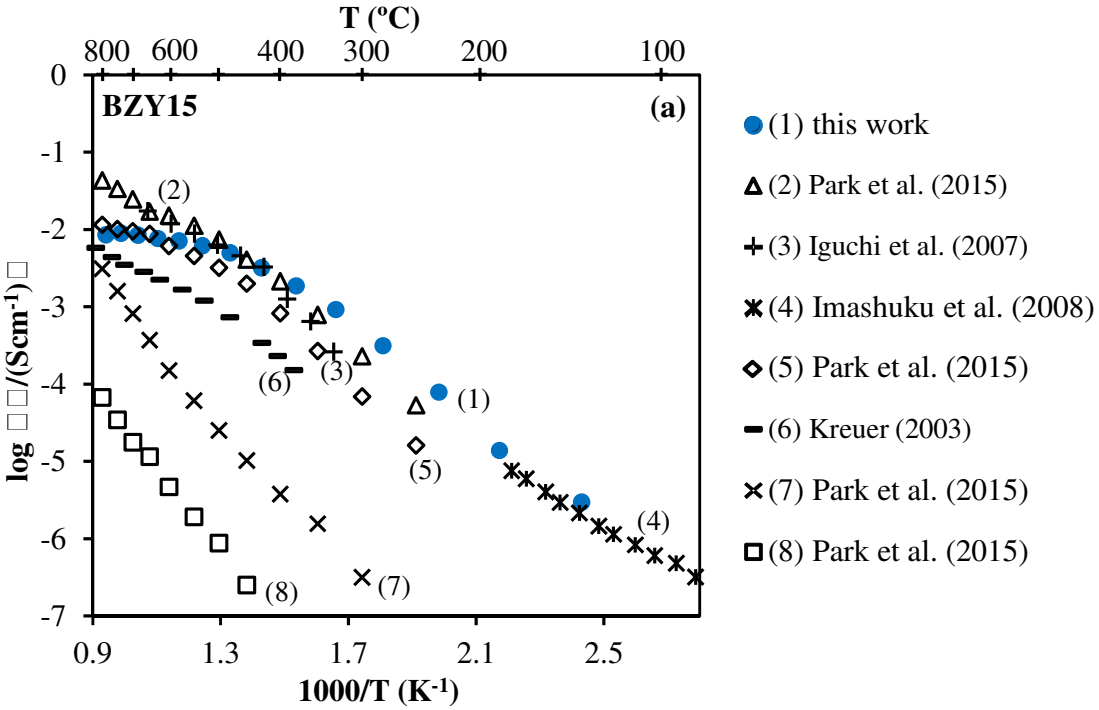

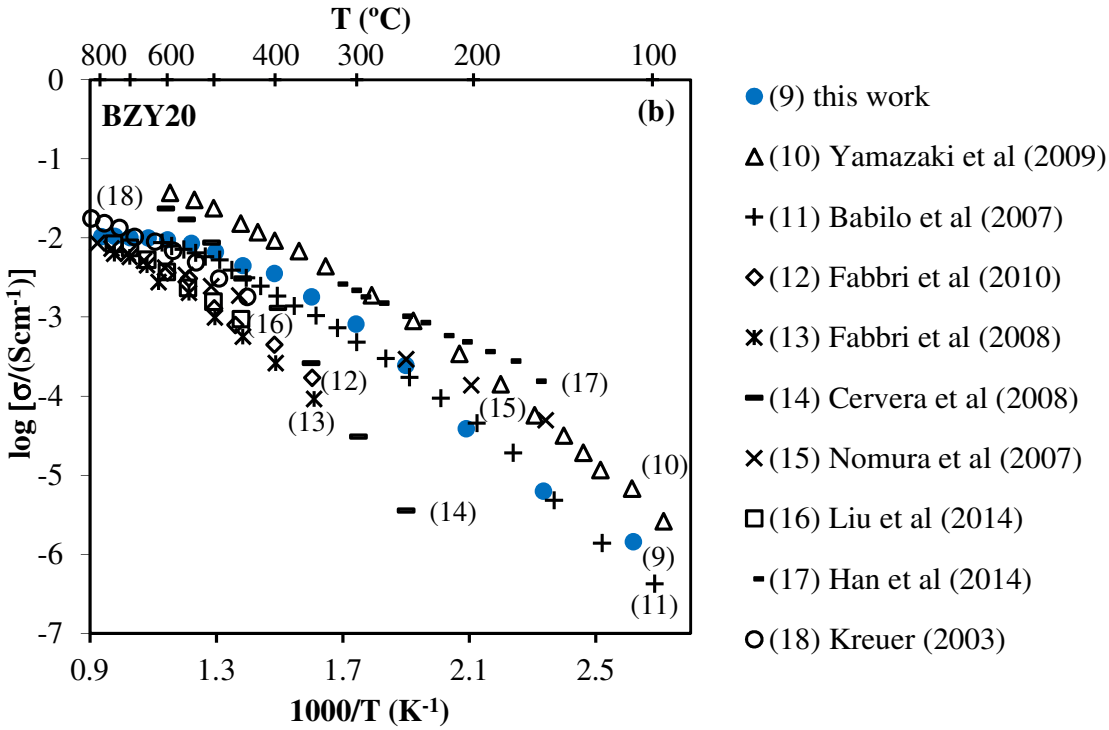

Fig. 4.4. Total electrical conductivity of **(a)** $BaZr_{0.85}Y_{0.15}O_{3-\delta}$ (BZY15) and **(b)** $BaZr_{0.80}Y_{0.20}O_{3-\delta}$ (BZY20) obtained in this work and reported in the literature, in wet atmospheres (H_2, N_2, Ar or air). The number of each curve corresponds to the samples and testing conditions described in Table 4.1.

According to the data, the preparation by mechanochemical processing shows values of total electrical conductivity similar to the highest values reported in literature, thus, being clearly competitive with both the conventional solid state and state of the art wet soft chemical techniques for phase preparation. The performance of the current samples prepared by the mechanosynthesised route is only beaten by the values at similar testing conditions recorded by Park et al. [177] for $BaZr_{0.85}Y_{0.15}O_{3-\delta}$, and by Han et al. [185] for $BaZr_{0.80}Y_{0.20}O_{3-\delta}$ composition.

4.3.2. ELECTROCHEMICAL CHARACTERIZATION

The bulk and grain boundary conductivities in wet 10 % H_2/N_2, of the selected compositions formed by mechanosynthesis, were separated by impedance spectroscopy measurements. Typical impedance spectra and the corresponding equivalent circuits are shown in Fig. 4.5.

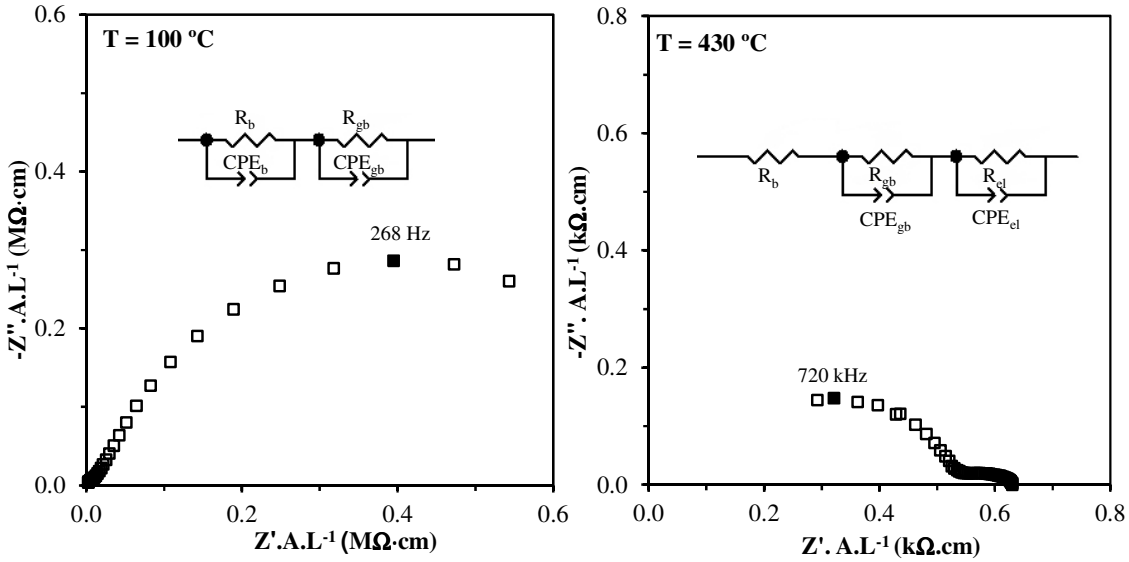

Fig. 4.5. Typical electrochemical impedance spectroscopy spectra measured in composition $BaZr_{0.85}Y_{0.15}O_{3-\delta}$, at 100 ºC and 430 ºC, in wet 10 % H_2/N_2 atmosphere, and correspondent equivalent circuits.

Fig. 4.6 shows the Arrhenius plots of total, bulk and grain boundary conductivity and the area specific grain boundary condutance, determined according to equations 2.13, 2.16, 2.20 and 2.21 respectively, for BZY15 and BZY20 compositions in wet 10 % H_2/N_2. Table 4.2 summarizes the respective activation energies (E_a).

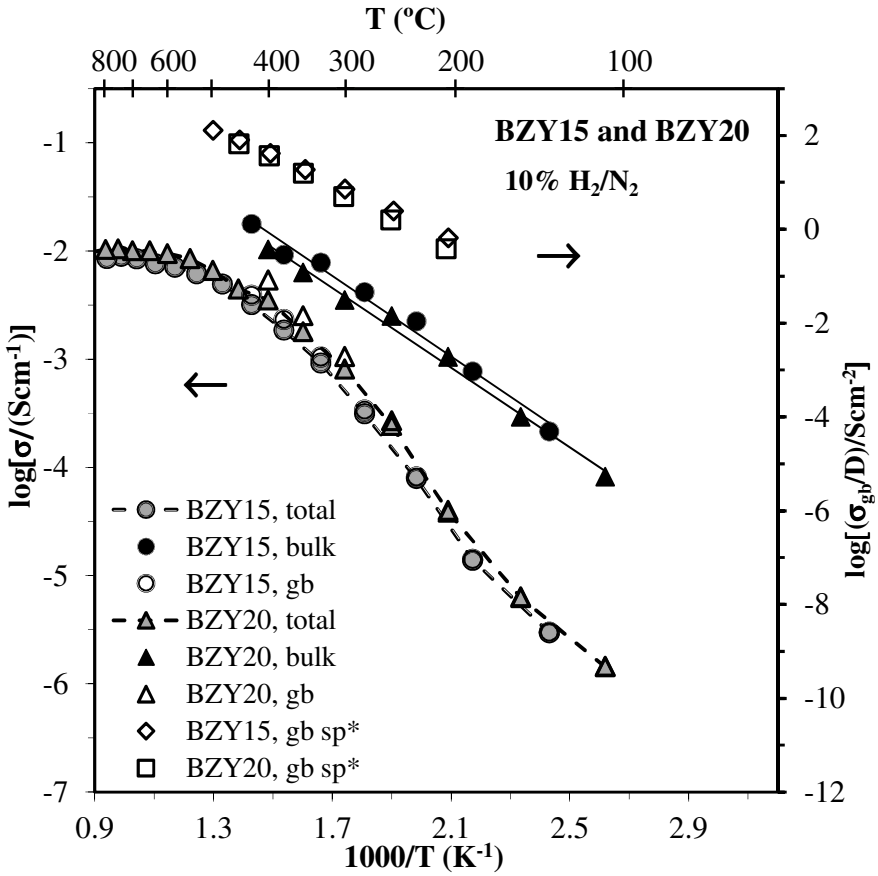

Fig. 4.6. The temperature dependence of total, bulk, grain boundary conductivities (primary axis), and area specific grain boundary condutance (secondary axis), in wet 10 % H_2/N_2 atmosphere of compositions $BaZr_{0.85}Y_{0.15}O_{3-\delta}$ (BZY15) and $BaZr_{0.80}Y_{0.20}O_{3-\delta}$ (BZY20).

Table 4.2. Comparison of the activation energy (E_a) of bulk, grain boundary, and total conductivity of $BaZr_{0.85}Y_{0.15}O_{3-\delta}$ (BZY15) and $BaZr_{0.80}Y_{0.20}O_{3-\delta}$ (BZY20), in wet 10 % H_2/N_2.

	BZY15	BZY20
	E_a (eV) (140 – 480 ºC)	E_a (eV) (100 – 400 ºC)
bulk	0.31	0.40
grain boundary	0.63	0.70
total	0.57	0.66

In both compositions the bulk conductivity is observed to be much larger than the grain boundary conductivity, in accordance with previous literature results obtained for Y-doped barium zirconate oxides of similar Y-content [47,48,179,186]. The total conductivity values of BZY15 and BZY20 are noted to be very close, with only slighly higher total conductivities in the case of BZY20.

Despite the similarity in values of total conductivity for both compositions, higher values of bulk conductivity are recorded for the BZY15 composition than the BZY20 composition. In contrast, the grain boundary conductivity is recorded to be slighty higher in the case of BZY20. From the effectively equal values of area specific grain boundary conductance, this higher noted grain boundary conductivity for BZY20 should be attributed to microstructural effects, related to its larger grain size, documented in Table 4.1, corresponding to a lower grain boundary area. Concerning the total condutivity, the obtained results are in line with those of the literature, which reported minor increases in total conductivity with increasing Y-content up to $y = 0.20$. Interestingly, in the literature, such an increase is followed by a decrease in total conductivity with Y-content for compositions of $y > 0.20$, commonly attributed to larger local distortions, proton-dopant association trapping the dopant sites and/or stoichiometry changes upon environment exposure [187,188], which dominate a monotonous increase in proton uptake with the increase of Y-content [90,179].

The activation energies (E_a) for proton transport across the bulk and the grain-boundary are effectively composition independent, while being higher in magnitude for the grain boundary contribution.

4.3.3. MODELLING OF ELECTRICAL CONDUCTIVITY

4.3.3.1. METHODOLOGY

The contributions of ionic and electronic conductivity as well as the ionic conduction domain were assessed using a methodology for electrical conductivity modelling outlined by Lim et al. [189] and Baek [190] that describe the defect structure of high-temperature proton-conducting oxides with an acceptor dopant of single negative effective charge, in the current case Y'_{Zr}, by the following formulas:

$$\frac{\sigma_{OH_o^\bullet}}{\sigma^*_{OH_o^\bullet}} = \left[\left(1+\frac{\alpha}{P_{H_2O}}\right)^{1/2} - 1\right]\left(\frac{P_{H_2O}}{(1+\alpha)^{1/2}-1}\right) \tag{4.1}$$

$$\frac{\sigma_{V_O^{\bullet\bullet}}}{\sigma^*_{V_O^{\bullet\bullet}}} = \left[\left(1+\frac{\alpha}{P_{H_2O}}\right)^{1/2} - 1\right]^2\left(\frac{P_{H_2O}}{\alpha}\right) \tag{4.2}$$

$$\frac{\sigma_p}{\sigma^*_p} = \left[\left(1+\frac{\alpha}{P_{H_2O}}\right)^{1/2} - 1\right]\left(\frac{P_{H_2O}}{\alpha}\right)^{1/2} P_{O_2}{}^{1/4} \tag{4.3}$$

where $\sigma_{OH_o^\bullet}$ is the proton conductivity, $\sigma_{V_O^{\bullet\bullet}}$ is the oxide-ion conductivity, σ_p is the hole conductivity, $\sigma^*_{OH_o^\bullet}$ is the proton conductivity at $P_{H_2O} = 1$ atm, σ^*_p is the hole conductivity at $P_{O_2} = 1$ atm and $P_{H_2O} = 0$ atm, $\sigma^*_{V_O^{\bullet\bullet}}$ is the oxide-ion conductivity when $P_{H_2O} = 0$ atm and α is a constant determined by:

$$\alpha = \frac{8[Y'_{Zr}]}{K_W} \tag{4.4}$$

$\left[\mathrm{Y}'_{\mathrm{Zr}}\right]$ is the acceptor dopant concentration, and K_{W} is the equilibrium constant of the hydration.

$\left[\mathrm{Y}'_{\mathrm{Zr}}\right]$ is given by:

$$[\mathrm{Y}'_{\mathrm{Zr}}] = \frac{Z \cdot x}{a^3} \tag{4.5}$$

with Z the number of formula units per unit cell, x is the fraction of acceptor dopant atoms in a unit cell, and a is the unit cell lattice parameter.

According to the above equations (4.1), (4.2) and (4.3) only σ_{p} shows a direct dependency on P_{O_2}, and, thus, total conductivity can be determined by:

$$\sigma_{\mathrm{tot}} = \sigma_{\mathrm{OH}_{\mathrm{o}}^{\bullet}} + \sigma_{\mathrm{V}_{\mathrm{O}}^{\bullet\bullet}} + \sigma_{\mathrm{p}} \tag{4.6}$$

can be represented as:

$$\sigma_{\mathrm{tot}} = a + b \cdot P_{\mathrm{O}_2}^{1/4} \tag{4.7}$$

where, in combination with the equations (4.1), (4.2) and (4.6):

$$a = \sigma_{\mathrm{OH}_{\mathrm{o}}^{\bullet}} + \sigma_{\mathrm{V}_{\mathrm{O}}^{\bullet\bullet}} = \sigma^{*}_{\mathrm{OH}_{\mathrm{o}}^{\bullet}} \left[\left(1+\frac{\alpha}{P_{\mathrm{H_2O}}}\right)^{1/2} - 1\right]\left(\frac{P_{\mathrm{H_2O}}}{(1+\alpha)^{1/2}-1}\right) + \tag{4.8}$$

$$\sigma^{*}_{\mathrm{V}_{\mathrm{O}}^{\bullet\bullet}} \left[\left(1+\frac{\alpha}{P_{\mathrm{H_2O}}}\right)^{1/2} - 1\right]^2 \left(\frac{P_{\mathrm{H_2O}}}{\alpha}\right)$$

and,

$$b = \sigma_p^* \left[\left(1 + \frac{P_{H_2O}}{\alpha} \right)^{1/2} - \left(\frac{P_{H_2O}}{\alpha} \right)^{1/2} \right] \quad (4.9)$$

From the slope of plots of σ_{tot} vs $P_{O_2}^{1/4}$ measured for two different water vapour pressures ($P_{H_2O,1}$ and $P_{H_2O,2}$), α can be determined from the ratio of the two slopes, as:

$$\frac{b_1}{b_2} = \frac{\left[\left(1 + \frac{P_{H_2O,1}}{\alpha} \right)^{1/2} - \left(\frac{P_{H_2O,1}}{\alpha} \right)^{1/2} \right]}{\left[\left(1 + \frac{P_{H_2O,2}}{\alpha} \right)^{1/2} - \left(\frac{P_{H_2O,2}}{\alpha} \right)^{1/2} \right]} \quad (4.10)$$

After determination of α, the constants σ_p^* and K_w can be calculated from the equations (4.4) and (4.9), respectively.

In addition, by measuring the intercepts of plots of σ_{tot} vs $P_{O_2}^{1/4}$ at two different water partial pressures the constants, $\sigma_{OH_O^\bullet}^*$ and $\sigma_{V_O^{\bullet\bullet}}^*$ can be determined from equation (4.8).

Subsequently, if the constants $\sigma_{OH_O^\bullet}^*$, $\sigma_{V_O^{\bullet\bullet}}^*$ and σ_p^* are known the partial and total conductivities can be calculated.

4.3.3.2. RESULTS OF MODELLING

Pursuing this modelling strategy, plots of total conductivity vs $P_{O_2}^{1/4}$ at different water partial pressures were constructed for $BaZr_{0.85}Y_{0.15}O_{3-\delta}$ and $BaZr_{0.80}Y_{0.20}O_{3-\delta}$ compositions. Linear plots exhibiting the σ_{tot} vs $P_{O_2}^{1/4}$ dependency are illustrated in Fig. 4.7 for the composition $BaZr_{0.85}Y_{0.15}O_{3-\delta}$, as an example; the behaviour of the $BaZr_{0.80}Y_{0.20}O_{3-\delta}$composition is similar.

The corresponding slopes, intercepts and linear correlation coefficients obtained by linear regression of the σ_{tot} vs $P_{O_2}^{1/4}$ plots are summarized in Table 4.3 for both compositions.

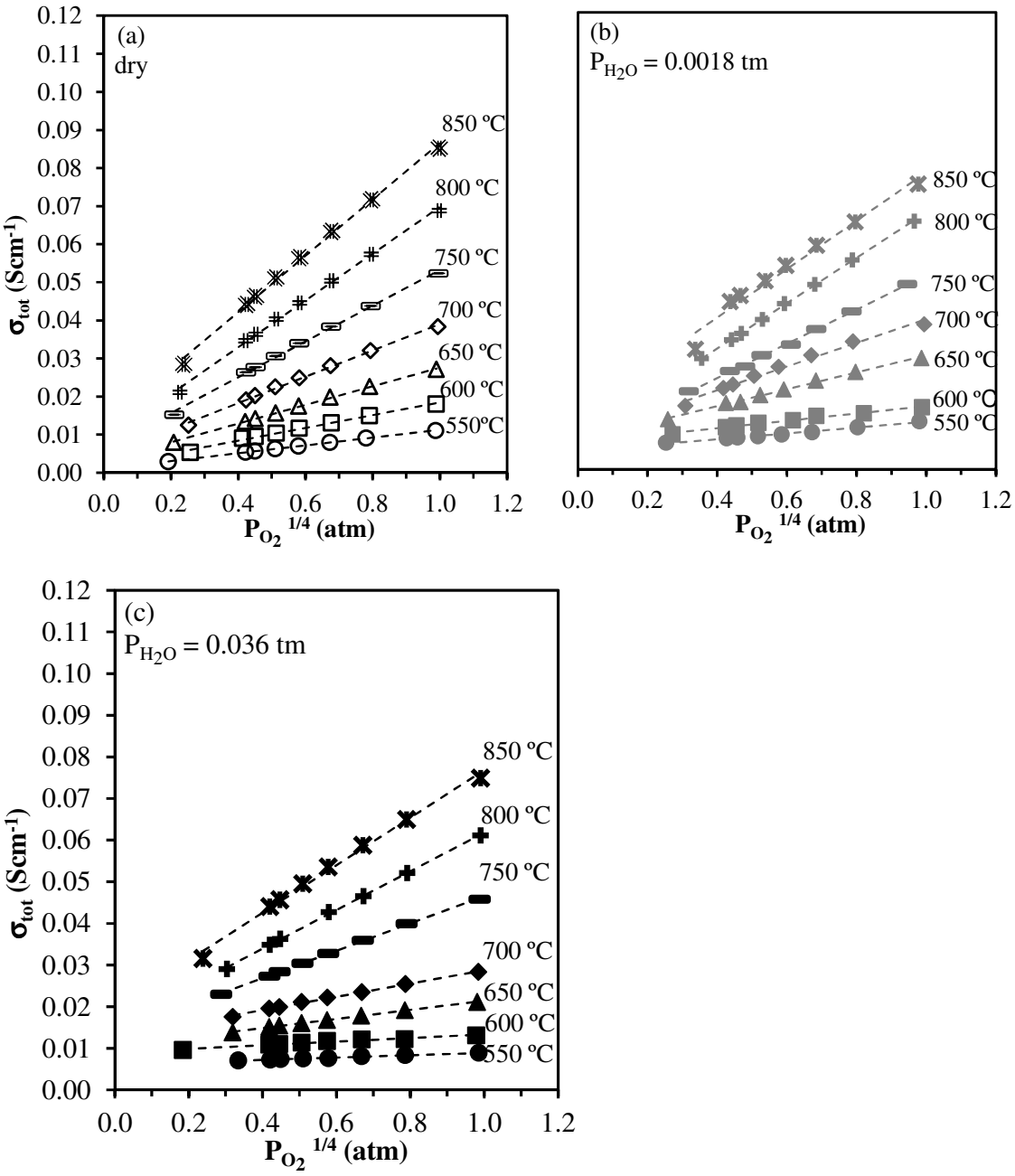

Fig. 4.7. Total conductivity of $BaZr_{0.85}Y_{0.15}O_{3-\delta}$ vs $P_{O_2}^{1/4}$, under constant P_{H_2O} at various temperatures **(a)** dry, **(b)** P_{H_2O} = 0.0018 atm, and **(c)** P_{H_2O} = 0.036 atm.

Table 4.3. The slopes, intercepts and linear correlation coefficients, *r*, obtained by linear fitting of σ_{tot} vs $P_{O_2}^{1/4}$ plots for the compositions $BaZr_{0.85}Y_{0.15}O_{3-\delta}$ and $BaZr_{0.80}Y_{0.20}O_{3-\delta}$.

P_{H_2O} (atm)	Temperature (ºC)	$BaZr_{0.85}Y_{0.15}O_{3-\delta}$			$BaZr_{0.80}Y_{0.20}O_{3-\delta}$		
		slope (*b*) ($S\cdot cm^{-1}\cdot atm^{-1/4}$)	intercept (*a*) ($S\cdot cm^{-1}$)	*r*	slope (*b*) ($S\cdot cm^{-1}\cdot atm^{-1/4}$)	intercept (*a*) ($S\cdot cm^{-1}$)	*r*
≈ 0	550	1.03E-02	1.01E-03	1.000	1.11E-02	< 1.0E-04	1.000
	600	1.68E-02	1.70E-03	0.992	1.79E-02	3.53E-05	1.000
	650	2.45E-02	3.08E-03	0.999	2.83E-02	< 1.0E-04	1.000
	700	3.46E-02	4.46E-03	0.998	4.19E-02	<1.0E-04	1.000
	750	4.70E-02	6.27E-03	0.998	5.86E-02	3.88E-04	1.000
	800	6.14E-02	8.37E-03	0.998	8.03E-02	5.23E-04	1.000
	850	7.41E-02	1.25E-02	0.997	1.04E-01	1.93E-03	1.000
0.0018	550	7.68E-03	4.81E-03	0.991	7.68E-03	4.81E-03	0.991
	600	9.68E-03	6.91E-03	0.987	9.68E-03	6.91E-03	0.987
	650	2.22E-02	7.65E-03	0.996	2.22E-02	7.65E-03	0.996
	700	3.11E-02	8.29E-03	0.986	3.11E-02	8.29E-03	0.986
	750	4.51E-02	5.86E-03	0.998	4.51E-02	5.86E-03	0.998
	800	5.95E-02	7.89E-03	1.000	5.95E-02	7.89E-03	1.000
	850	7.24E-02	1.21E-02	0.998	7.24E-02	1.21E-02	0.998
0.036	550	2.78E-03	6.14E-03	0.989	3.67E-03	6.21E-03	0.995
	600	4.32E-03	9.03E-03	0.972	7.92E-03	7.52E-03	0.957
	650	1.09E-02	1.05E-02	0.999	1.47E-02	9.79E-03	0.999
	700	1.59E-02	1.28E-02	0.997	2.52E-02	9.86E-03	1.000
	750	3.29E-02	1.37E-02	0.999	4.05E-02	9.92E-03	0.997
	800	4.64E-02	1.54E-02	0.999	6.03E-02	1.02E-02	0.984
	850	5.70E-02	1.98E-02	0.994	7.79E-02	1.25E-02	1.000

The excellent linear correlation obtained for both compositions indicates that the proposed defect model can be applied to the current materials. Higher gradients and a lower intercepts are observed with decreasing water vapour partial pressure, suggesting, from equations (4.8) and (4.9), that the hole contribution for the total conductivity increases, while the ionic contribution decreases with decreasing P_{H_2O}.

The corresponding parameters α, K_w, $\sigma^*_{OH^{\bullet}_o}$, $\sigma^*_{V^{\bullet\bullet}_O}$ and σ^*_p estimated according to the methodology outlined above are reported in Table 4.4.

Table 4.4. Calculated parameters α, K_w, $\sigma^*_{OH^{\bullet}_o}$, $\sigma^*_{V^{\bullet\bullet}_O}$ and σ^*_p at different temperatures for the compositions $BaZr_{0.85}Y_{0.15}O_{3-\delta}$ and $BaZr_{0.80}Y_{0.20}O_{3-\delta}$.

Composition	Temperature (ºC)	α	K_w ($atm^{-1}\cdot cm^{-3}$)	σ^*_p ($S\cdot cm^{-1}$)	$\sigma^*_{OH^{\bullet}_o}$ ($S\cdot cm^{-1}$)	$\sigma^*_{V^{\bullet\bullet}_O}$ ($S\cdot cm^{-1}$)
$BaZr_{0.85}Y_{0.15}O_{3-\delta}$	550	0.011	6.01E+24	0.011	6.322E-03	(3.278E-03)
	600	0.020	3.17E+24	0.013	9.507E-03	(4.778E-03)
	650	0.029	2.17E+24	0.028	1.132E-02	(5.263E-03)
	700	0.035	1.82E+24	0.039	1.431E-02	(4.780E-03)
	750	0.204	3.12E+23	0.050	2.154E-02	(2.397E-03)
	800	0.334	1.90E+23	0.064	2.517E-02	(4.846E-03)
	850	0.369	1.72E+23	0.078	2.981E-02	(9.040E-03)
$BaZr_{0.80}Y_{0.20}O_{3-\delta}$	550	0.038	2.21E+24	0.009	7.395E-03	(4.190E-04)
	600	0.116	7.23E+23	0.013	1.029E-02	(1.714E-03)
	650	0.135	6.24E+23	0.024	1.488E-02	(3.030E-04)
	700	0.286	2.93E+23	0.036	1.738E-02	(1.133E-03)
	750	0.401	2.09E+23	0.054	1.968E-02	(6.045E-04)
	800	0.706	1.29E+23	0.075	2.380E-02	(4.848E-04)
	850	0.564	1.49E+23	0.100	2.643E-02	(1.369E-03)

From the values of the equilibrium constant of hydration for different temperatures, the standard solution enthalpies for water uptake were determined according to the relation (1.11):

$$\ln(K_W) = \frac{\Delta H_W}{RT} - \frac{\Delta S_W}{R}$$

from the slope of $\ln(K_W)$ vs inverse temperature, Fig. 4.8.

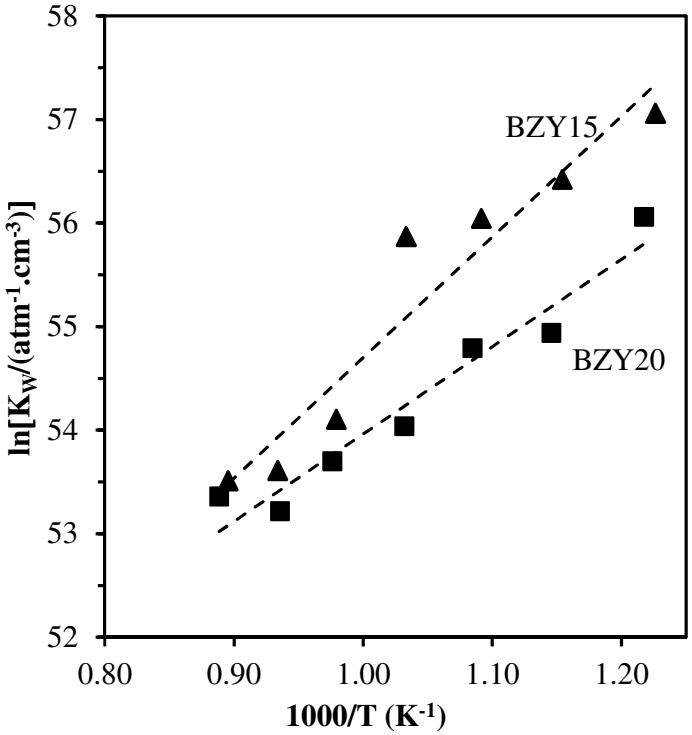

Fig. 4.8. The equilibrium constant of hydration as a function of inverse temperature for the compositions $BaZr_{0.85}Y_{0.15}O_{3-\delta}$ (BZY15) and $BaZr_{0.80}Y_{0.20}O_{3-\delta}$ (BZY20).

The standard solution enthalpies of hydration determined for $BaZr_{0.85}Y_{0.15}O_{3-\delta}$ (BZY15) and $BaZr_{0.80}Y_{0.20}O_{3-\delta}$ (BZY20) are, respectively, -96.8 kJ·mol^{-1} and -70.1 kJ·mol^{-1}. The trend of a less negative hydration enthalpy with increasing Y-content conflicts with that previously reported by Kreuer [47], who calculated the value of -83.4 kJ·mol^{-1} for $BaZr_{0.85}Y_{0.15}O_{3-\delta}$, and -93.3 kJ·mol^{-1} for $BaZr_{0.80}Y_{0.20}O_{3-\delta}$ measured by the thermogravimetric technique in the high temperature range ~500 – 900 ºC [191]. The more negative value of the enthalpy of hydration obtained for the composition BZY20 in the work of Kreuer et al. [191] in comparison with the current results may derive from the assumption of negligible hole concentration inherent to the use of this relation in thermogravimetrically obtained results, which has not been verified for high temperatures [90]. In this respect, the following work will demonstrate that the p-type electronic contribution increases with increasing acceptor dopant concentration. This result, thus, predicts greater deviations from Arrhenius behaviour with increasing temperature for the

BZY20 composition, potentially increasing error in thermogravimetrically derived results of hydration equilibrium constants obtained under these conditions [191]. Fig. 4.9 shows calculated partial and total conductivities plotted as a function of water vapour partial pressure in P_{O_2} = 0.01 atm at 600 ºC for compositions BZY15 and BZY20.

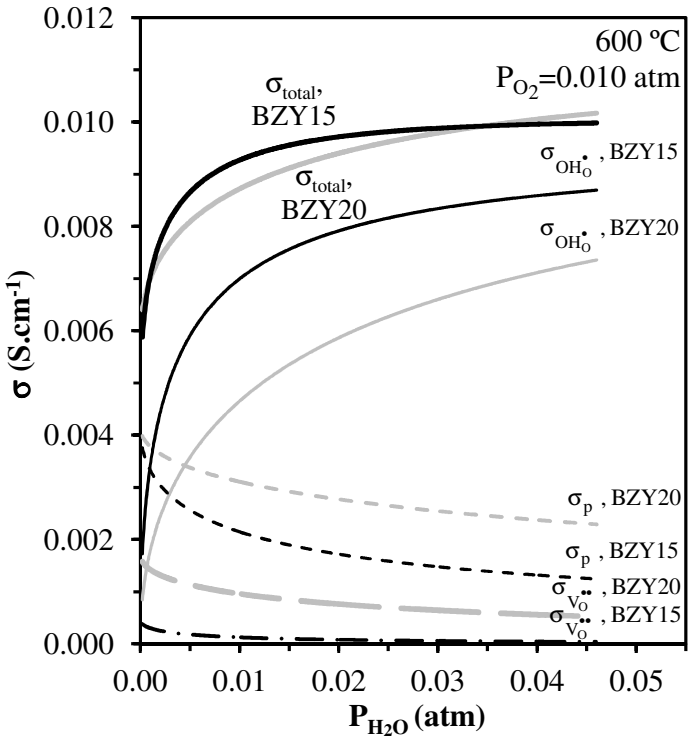

Fig. 4.9. Calculated total and partial conductivities in P_{O_2} = 0.01 atm at 600 ºC, as a function of water vapour partial pressure.

The analysis of resultant graph reveals that, for the conditions analysed, the proton conductivity is the dominant conduction mechanism for both compositions, increasing with increasing P_{H_2O} and significantly higher in magnitude for the BZY15 composition. Conversely, the minority oxide-ion conductivity and hole conductivities can be noted to be higher in the BZY20 composition than the BZY15 composition over the complete water vapour partial pressure range.

The temperature dependencies of the partial conductivities calculated for $P_{O_2} = 1$ atm and $P_{O_2} = 0.01$ atm at the water vapour partial pressure of 0.036 atm for both compositions are shown in Fig. 4.10. At the highest temperatures for both compositions, the p-type conductivity can be observed to take over the role of dominant charge carrier, exceeding the protonic contribution. This change over from protonic to p-type conductivity is noted to occur at lower temperatures under more oxidising conditions.

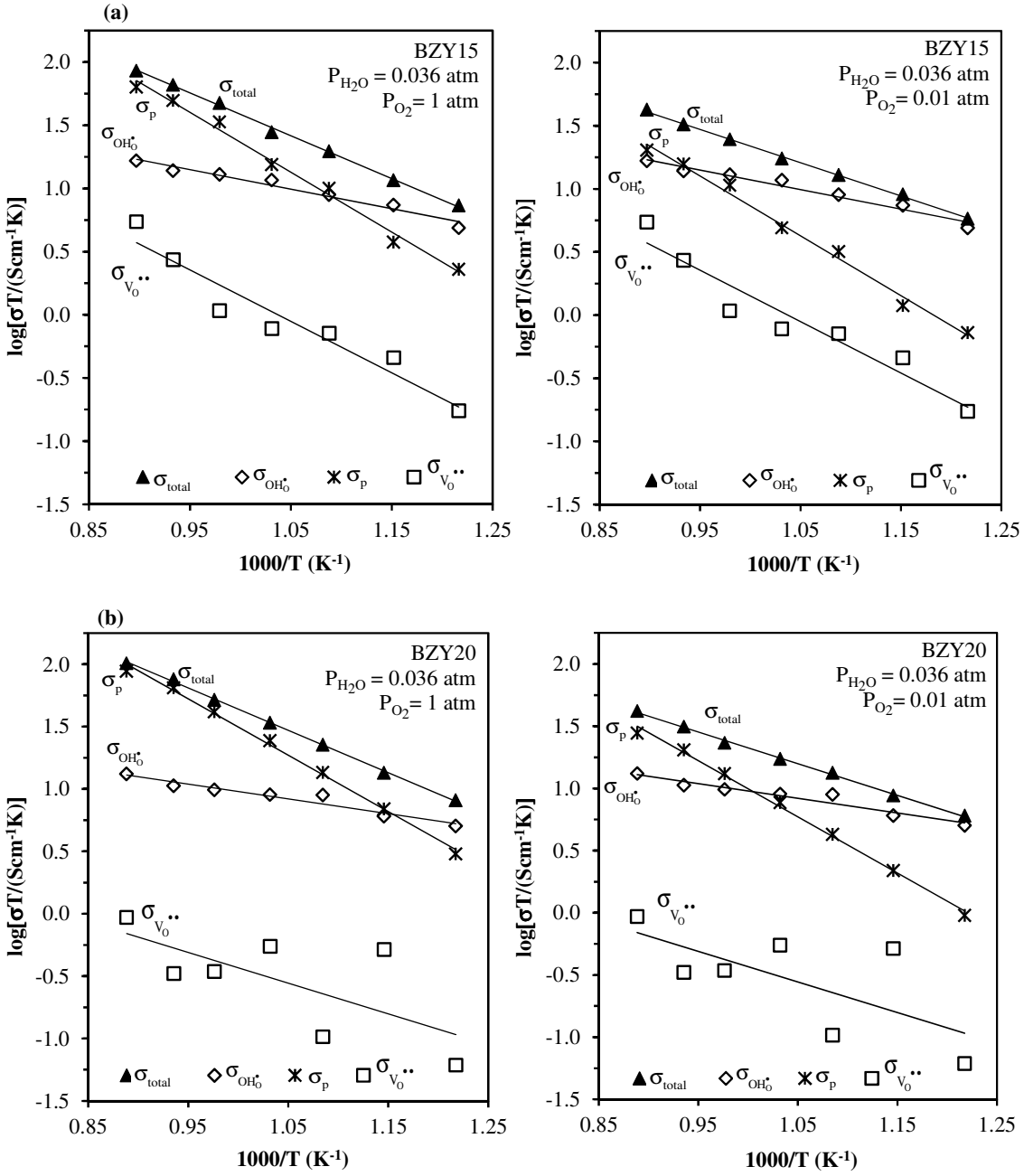

Fig. 4.10. Total and partial conductivities at P_{O_2} = 1atm and P_{O_2} = 0.01 atm, with P_{H_2O} = 0.036 atm, for: **(a)** BZY15 and **(b)** BZY20.

The activation energy respecting to ionic, oxide-ion and proton, as well as the electronic p-type conductivities are presented in Table 4.5.

Table 4.5. Activation energy (E_a) of proton, oxide-ion and p-type conductivity for compositions BZY15 and BZY20.

E_a (eV)	BZY15	BZY20
$\sigma_{OH_O^{\bullet}}$	0.31 ± 0.03	0.24 ± 0.03
$\sigma_{V_O^{\bullet\bullet}}$	0.81 ± 0.10	(0.49 ± 0.23)
σ_p	0.94 ± 0.04	0.90 ± 0.02

The corresponding temperature dependences of the transference numbers for proton, oxide-ion and p-type conduction are shown in Fig. 4.11 and reiterate the previous discussion. In more oxidising conditions there is a transition of dominant transport from hole to proton and oxide-ion, with decreasing temperature for both compositions, Fig. 4.11 (a). In contrast, in more reducing atmospheres, the ionic conductivity (proton and oxide-ion) is dominant over all the temperature range in BZY15, while transition of hole to ionic conductivity occurs in BZY20, Fig. 4.11 (b).

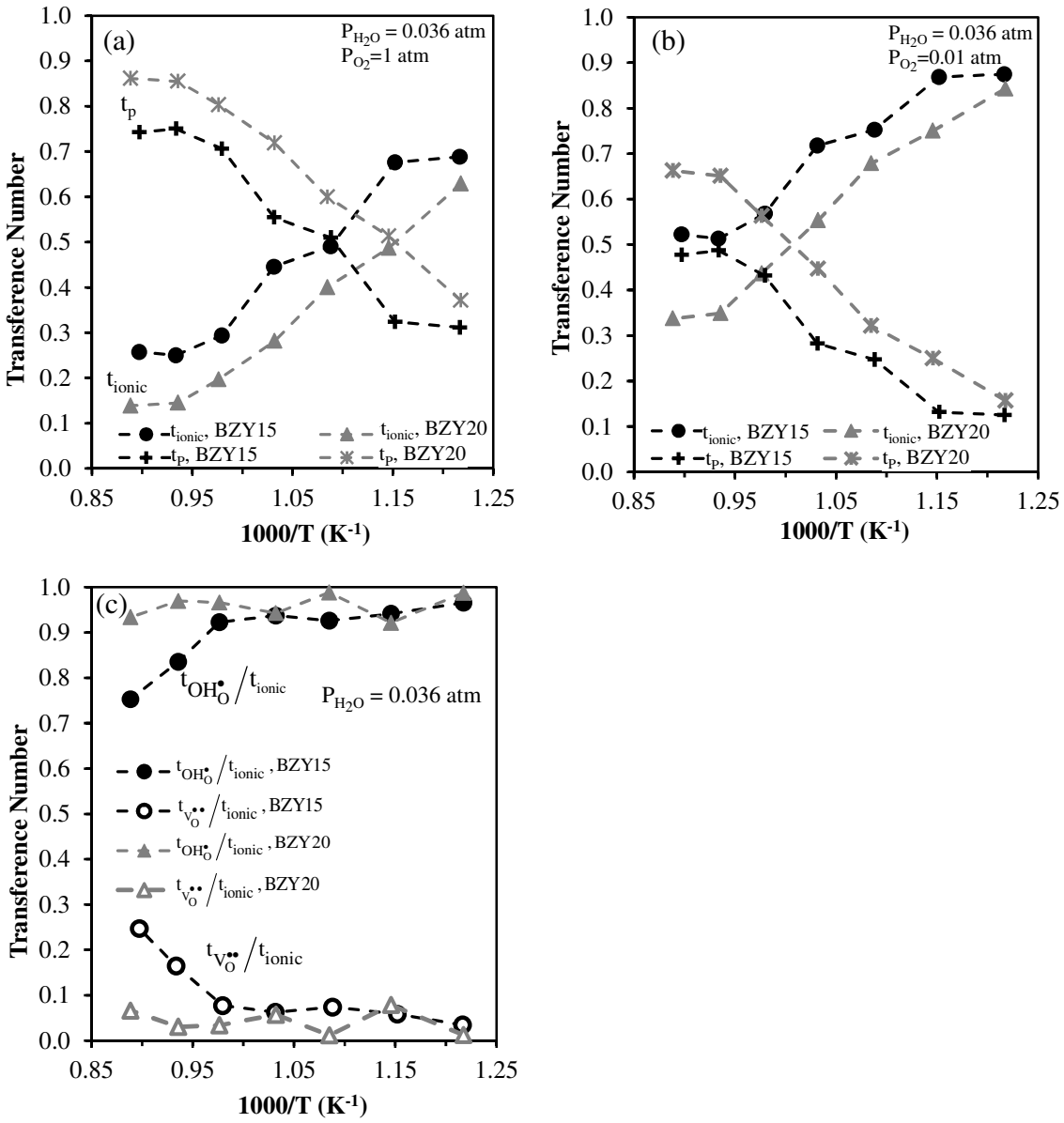

Fig. 4.11. Transference number vs 1000/T at P_{H_2O} = 0.036 atm for BZY15 and BZY20 **(a)** t_{ionic} and t_p at P_{O_2} = 1 atm, **(b)** t_{ionic} and t_p at P_{O_2} = 0.01 atm, and **(c)** $t_{V_O^{\bullet\bullet}}/t_{ionic}$ and $t_{OH_O^\bullet}/t_{ionic}$,where $t_{ionic} = t_{V_O^{\bullet\bullet}} + t_{OH_O^\bullet}$.

4.4. CONCLUDING REMARKS

Mechanochemical processing is shown to be a highly attractive method for the preparation of pure $BaZr_{1-y}Y_yO_{3-\delta}$ materials. The total electrical conductivity data of compositions prepared by this method show values of total electrical conductivity similar to the highest values reported in literature, being clearly competitive with both the conventional solid state and state of the art wet soft chemical techniques for phase preparation of these materials.

The use of modelling, based on a typical defect model derived for protonic ceramic materials with an acceptor dopant of single effective negative charge, allowed the calculation of partial conductivities of protons, oxide-ions, and electron holes. At the highest temperatures for both compositions, the p-type conductivity can be observed to take over the role of dominant charge carrier, exceeding the protonic contribution. This change over from protonic to p-type electronic conductivity is noted to occur at lower temperatures under more oxidising conditions. The standard solution enthalpies of hydration determined for $BaZr_{0.85}Y_{0.15}O_{3-\delta}$ (BZY15) and $BaZr_{0.80}Y_{0.20}O_{3-\delta}$ (BZYO) are -96.8 $kJ \cdot mol^{-1}$ and -70.1 $kJ \cdot mol^{-1}$, respectively.

5. EFFECT OF Ba-DEFICIENCY ON $Ba(Zr,Y)O_{3-\delta}$ PROPERTIES

5.1. INTRODUCTION

The high scatter in reported conductivity values for Y-doped $BaZrO_3$ materials has been associated to their processing difficulties, in which extreme sintering temperatures as high as 1700-1800 ºC are commonly required to achieve full densities. Exposure to such elevated temperatures for prolonged periods of time was found to induce BaO vaporization from alkaline earth cerates and zirconates, with consequent formation of Ba-deficient compositions [102], coupled with the coexistence of separate perovskite phases [175,192–194], and/or the formation of segregated phases of the acceptor dopant [145,195,196]. Such effects have been found to have a potentially detrimental effect on both grain interior (bulk) and grain boundary conductivities [47,145,192,195–197]. In the work carried out by Yamazaki et al. [145], a pseudo-ternary diagram of $BaO\text{-}ZrO_2\text{-}YO_{1.5}$, at 1600 ºC, was estimated, based on the compositional and structural characterization of the perovskite series $Ba_{1-x}Zr_{0.80}Y_{0.20}O_{3-\delta}$, considering the well documented phase equilibria in the $ZrO_2\text{-}Y_2O_3$ system and negligible solubility of barium in yttria and zirconia phases (Fig. 5.1).

According to this phase diagram, $Ba_{1-x}Zr_{1-y}Y_yO_{3-\delta}$ structures are suggested to accommodate a limited Ba-deficiency in the single phase perovskite region. Such tolerance to Ba-deficiency is predicted to decrease with decreasing Y-content, with the undoped $BaZrO_3$ composition offering negligible Ba-deficiency. When Ba-deficiency is extended beyond the content tolerated by the perovskite structure, the system is predicted to enter into multi-phase regions, consisting of the perovskite based phase with the exsolution of yttria and/or zirconia phases.

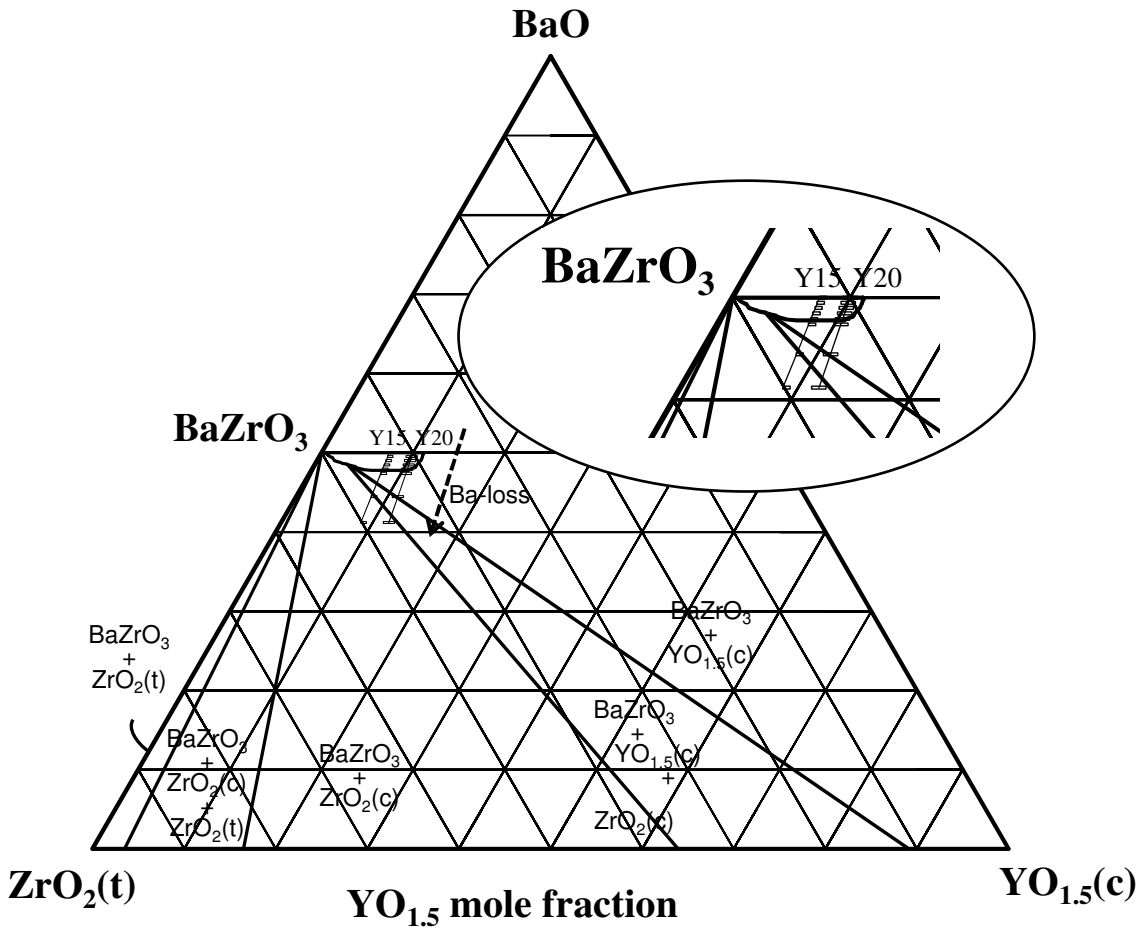

Fig. 5.1. Phase diagram of BaO–$YO_{1.5}$–ZrO_2 adapted from ref. [145] showing the location of non-stoichiometric compositions of $Ba_{1-x}Zr_{1-y}Y_yO_{3-\delta}$, with $y = 0.20$ (Y20) and $y = 0.15$ (Y15), and x=0, 0.02, 0.04, 0.06, 0.08, 0.10, 0.20 and 0.30. Area around $BaZrO_3$ expanded in inset.

The simple approximation of the BaO-ZrO_2-$YO_{1.5}$ phase diagram offered by Yamazaki et al. agrees well with an experimentally derived, more complete, phase diagram offered by Imashuku et al. [176]. Nonetheless, an alternative phase diagram at the same temperature proposed by Oyama et al. [175], predicts the coexistence of two stables perovskites, with different dopant concentrations for Ba-deficient compositions. Although separation of the perovskite phase field has also been supported by Azad et al. [192], Chapter 4 clearly

highlighted that such splitting of the perovskite phase is related to powder processing routes and can be avoided by the use of homogenous preparation methods such as mechanosynthesis.

Irrespective of such literature discrepancies in phase formation reported for Ba-deficient Y-doped $BaZrO_3$ compositions, several research works have suggested potential charge-compensation mechanisms to accommodate A-site-cation deficiency in zirconates and cerates to discuss their possible effect on the structure, microstructure, densification and grain interior (bulk) proton conductivity.

The mechanisms suggested have comprised of [47,102,192,195–198]:

a) the formation of A-site cation and oxygen vacancies (A-site-cation vacancy mechanism):

$$Ba_{Ba}^{\times} + O_{O}^{\times} \longrightarrow V_{Ba}^{//} + V_{O}^{\bullet\bullet} + BaO \qquad (5.1)$$

b) the partitioning of the dopant cation on A and B-sites of the perovskite and consumption of oxygen vacancies (dopant-partitioning mechanism):

$$2Ba_{Ba}^{\times} + 2O_{O}^{\times} + Y_{Zr}^{/} + V_{O}^{\bullet\bullet} \longrightarrow Y_{Ba}^{\bullet} + 2BaO \qquad (5.2)$$

c) occupation of the A-site by the dopant cation (or another B-site cation) with formation of B-site cation vacancies (B-site-vacancy mechanism):

$$Ba_{Ba}^{\times} + O_{O}^{\times} + Y_{Zr}^{/} \longrightarrow Y_{Ba}^{\bullet} + V_{Zr}^{////} + V_{O}^{\bullet\bullet} + BaO \qquad (5.3)$$

d) occupation of the A site by the dopant cation with the formation of oxygen interstitials (interstitial mechanism):

$$Ba_{Ba}^{\times} + 2O_{O}^{\times} + Y_{Zr}^{/} \longrightarrow Y_{Ba}^{\bullet} + O_{i}^{//} + V_{Zr}^{////} + 2V_{O}^{\bullet\bullet} + BaO \qquad (5.4)$$

Of these potential mechanisms, the occurrence of c) and d) have been stated to be unlikely as the formation of vacancies in low-coordination sites at expense of vacancies in high-coordination sites (predicted in B-site-vacancy mechanism) are shown to be energetically unfavourable [199,200], while the formation of oxygen interstitials in perovskites oxides is uncommon.

The reported lower likelihood for barium-deficiency in undoped zirconates and cerates perovskites [102,145,195], may suggest that the formation of Ba- and oxygen vacancies via the A-site-cation vacancy mechanism (equation (5.1)) is structurally unfavourable.

In contrast, alkaline-earth-doped zirconates and cerates have shown higher facility to accommodate significant A-site deficiency, possibly due to their ability to refine associated steric strain by the existence of the dopant-partitioning mechanism [47,102,145], equation (5.2). Such occupation of the dopants cation in both A- and B-sites has been supported by atomistic studies, for example by Davies et al. [201], that estimated and compared energies of dissolution of different trivalent dopants (Sc^{3+}, Lu^{3+}, Yb^{3+}, Y^{3+}, Ho^{3+}, Gd^{3+}, Eu^{3+}, Nd^{3+}, Ce^{3+}, La^{3+}) in A-and B-site of $CaZrO_3$ and $SrZrO_3$ perovskites. The results showed that, for the same base composition and dopant charge, lower energies for dissolution correspond to the compositions with lower size mismatch between the dopant species and the cation, in the same lattice site. For such a scenario, dopant site selectivity would be dominated by ion size effects, with the smaller dopants ions preferentially incorporated in the B-site, the large dopants in the A-site, and the intermediate size dopants, potentially, in both A- and B-sites.

In the case of Y-doped $BaZrO_3$ materials the incorporation in both A- and B-site is plausible as the size mismatch of yttrium in both sites is similar: Y^{3+} in six-fold coordination has a ionic radius of 0.9 Å [97], 25 % higher than $_{VI}Zr^{4+}$ (0.72 Å [97]), and Y^{3+} in twelve-fold coordination has a ionic radius of 1.251 Å [202], 22 % smaller than $_{XII}Ba^{2+}$ (1.61 Å [97]).

From this brief introduction it can be realised that the likelihood for barium losses during densification of barium zirconate materials is high, while the mechanism for its accommodation may impact, not only on the bulk composition, but also on phase purity. Moreover, the exact nature of these effects is likely to depend on both the concentration and

nature of the acceptor dopant and the extent of Ba-loss. In the previous chapter, mechanosynthesis was shown to be an efficient method of preparation on $Ba(Zr,Y)O_{3-\delta}$ nanopowders, at room temperature, offering high levels of homogeneity. In this context, mechanosynthesised powders can be used to form homogenous base materials from which links between Ba-loss, densification, grain growth and conductivity for Y-doped $BaZrO_3$ materials can be studied. In the current chapter, the $Ba_{1-x}Zr_{0.85}Y_{0.15}O_{3-\delta}$ series, $0 \leq x \leq 0.1$ will, thus, be analysed to clarify the effect of Ba-loss on the phase purity, microstructure, and physical and electrical properties of a model system.

5.2. PHASE FORMATION AND COMPOSITIONAL ANALYSIS

The X-ray powder diffraction patterns of $Ba_{1-x}Zr_{0.85}Y_{0.15}O_{3-\delta}$ compositions (x = 0, 0.02, 0.04, 0.06, 0.08 and 0.10) after 420 minutes of high energy milling of precursors oxides, according to the standard high energy milling procedure adopted in this work (Chapter 2, Section 2.1) ,Fig. 5.2, show the formation of crystalline perovskite phase for all the compositions. Traces of yttrium-doped zirconia are also detectable, and correspond to vestiges of unreacted precursor.

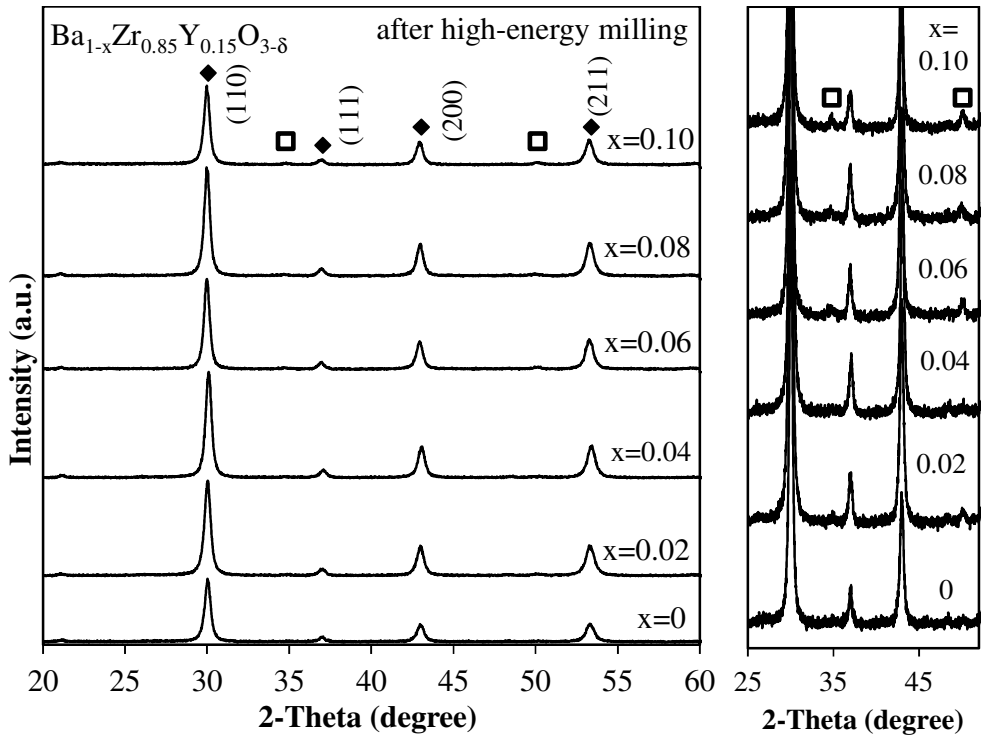

Fig. 5.2. X-ray diffraction patterns of $Ba_{1-x}Zr_{0.85}Y_{0.15}O_{3-\delta}$ compositions, $0 \leq x \leq 0.10$, 420 minutes after high energy milling, and the corresponding expanded profile for 2-theta range 25º - 50º . (♦) identifies perovskite phase, and (□) identifies yttrium-doped zirconia.

X-ray diffraction pattern profiles after sintering isostatically pressed pellets, 200 MPa, of the mechanosynthesised powders at 1250 ºC, using sacrificial powders of the same compositions to avoid additional Ba losses, Fig. 5.3, present a single perovskite phase for compositions with Ba-deficiency (x) lower than 0.08. For compositions with higher Ba-deficiency, of 0.08 and 0.10, a secondary phase of Y_2O_3 is observable besides the primary perovskite phase (Fig. 5.3). In all compositions the primary phase is noted to be that of cubic perovskite, with no evidence of tetragonal perovskite structures [191] or perovskite phase separation [193,203].

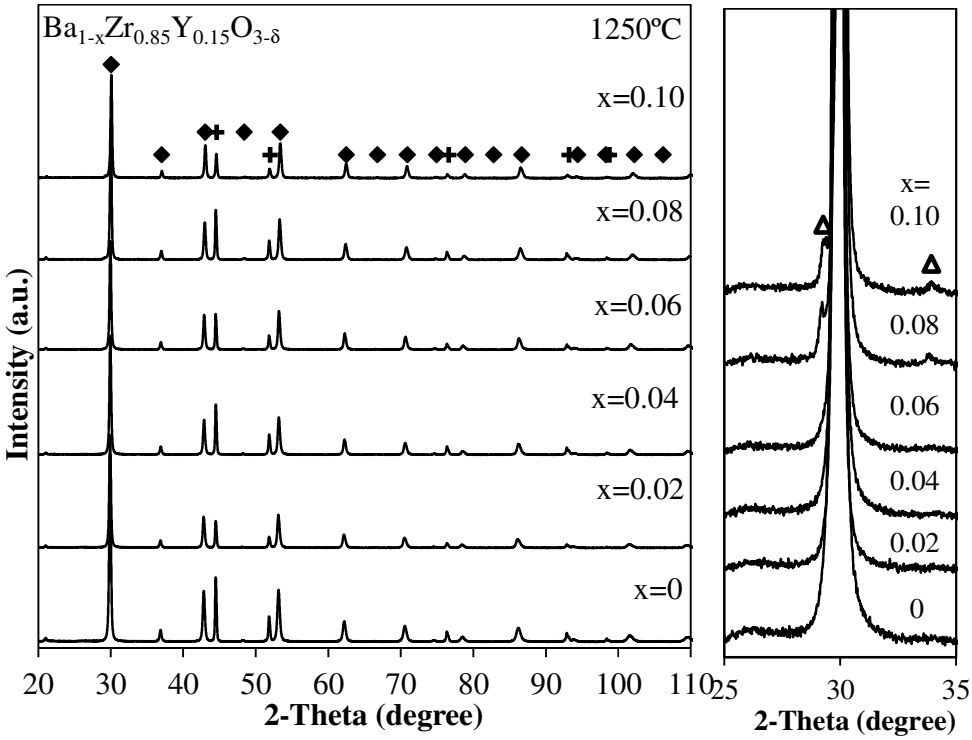

Fig. 5.3. X-ray diffraction patterns of $Ba_{1-x}Zr_{0.85}Y_{0.15}O_{3-\delta}$ compositions, $0 \leq x \leq 0.1$, after annealing the mechanosynthesized powders, at 1250 ºC, for 5 hours, and the corresponding expanded profile for 2-theta range of 25º - 35º. (♦) identifies perovskite phase, (△) identifies Y_2O_3, and (+) identifies Ni used as internal standard.

Similar X-ray diffraction patterns of increased crystallinity were exhibited by fully densified samples after sintering at higher temperature, 1600 ºC, for 5 hours, again using sacrificial powders (Fig. 5.4). The obtained results are in accordance to the ternary $BaO–YO_{1.5}–ZrO_2$ phase diagram, at 1600 ºC, proposed by Yamazaki [145], that predicts formation of yttria with the increase of the Ba-deficiency beyond the single perovskite phase region (Fig. 5.1).

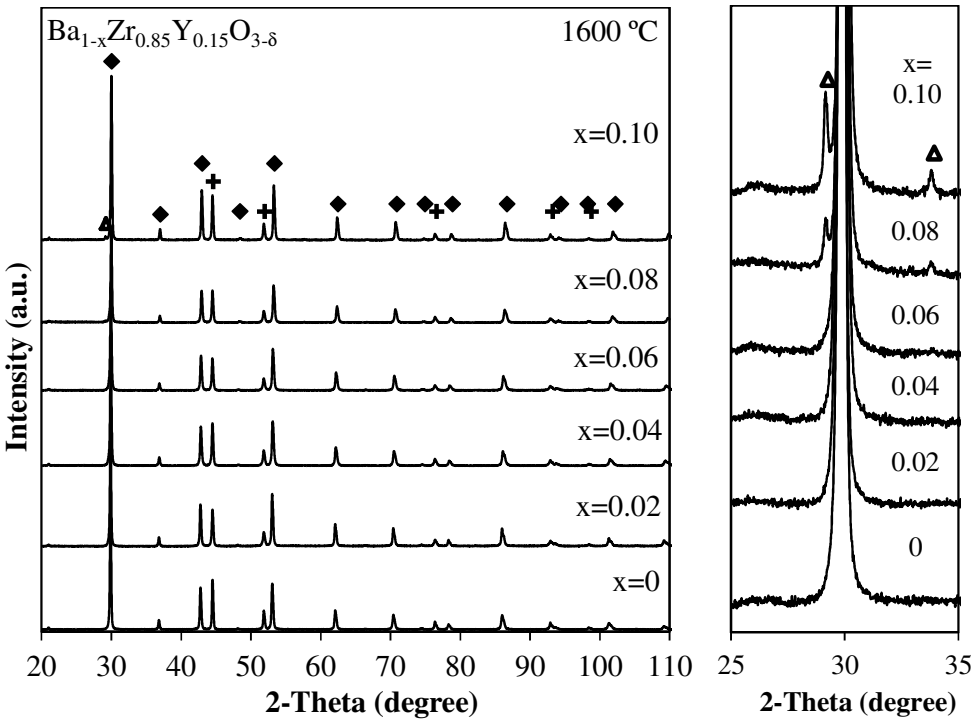

Fig. 5.4. X-ray diffraction patterns of $Ba_{1-x}Zr_{0.85}Y_{0.15}O_{3-\delta}$ compositions, $0 \leq x \leq 0.1$, after annealing the mechanosynthesized powders, at 1600 ºC, for 5 hours and the corresponding extended profile for 2-theta range of 25º - 35º. (♦) identifies perovskite phase, (△) identifies Y_2O_3, and (+) identifies Ni used as internal standard.

To assess actual stoichiometry after heat treatments, compositional analysis was performed by Electron-Probe Micro-Analysis (EPMA) for samples sintered at different temperatures (1250 ºC, 1500 ºC and 1600 ºC). The results shown in Fig. 5.5, confirm compositional accuracy. The procedure adopted, namely the use of mechanochemical processing, and the coverage of pellets with sacrificial powder on sintering at the different temperatures, is, thus, proven to be effective for the control of Ba-volatilisation, resulting in minimal compositional drift.

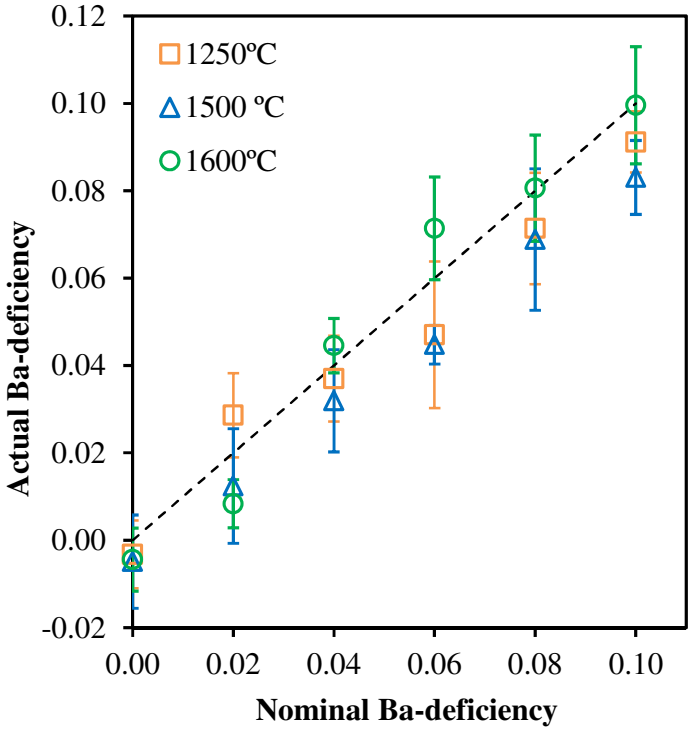

Fig. 5.5. Nominal and actual Ba-deficiency of $Ba_{1-x}Zr_{0.85}Y_{0.15}O_{3-\delta}$ pellets sintered at 1250, 1500 and 1600 ºC, assessed by EPMA, $0 \leq x \leq 0.1$.

5.3. STRUCTURAL CHARACTERISATION

Structural characterization was performed by Rietveld refinement of powder X-ray diffraction data, using Ni powder as an internal standard. The $Ba_{1-x}Zr_{0.85}Y_{0.15}O_{3-\delta}$ ($0 \leq x \leq 0.10$) series were indexed to a cubic unit cell in space group $Pm\bar{3}m$. The determined lattice parameters of $Ba_{1-x}Zr_{0.85}Y_{0.15}O_{3-\delta}$ compositions sintered at different temperatures are observed to pass through a maximum at $x = 0.02$, and to decrease with further increases of x, Fig. 5.6.

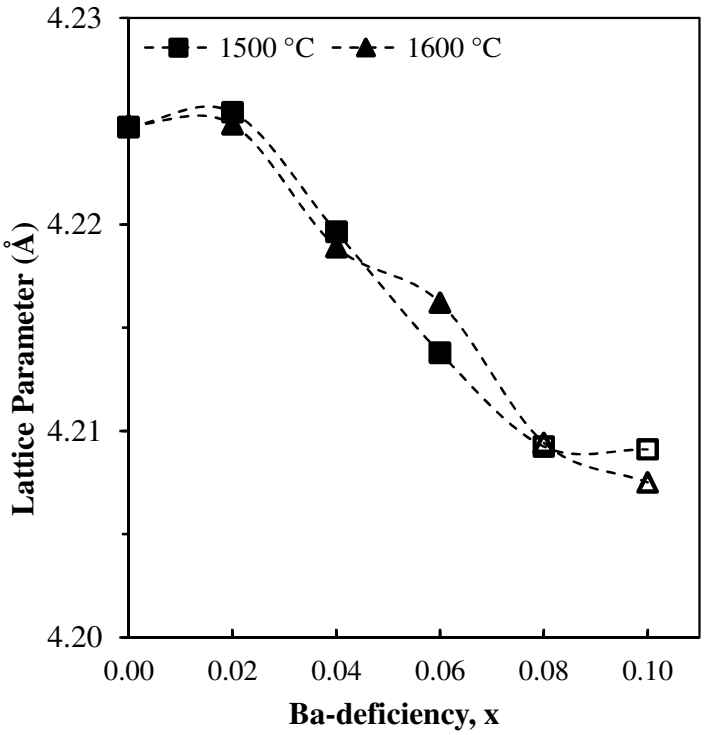

Fig. 5.6. Lattice parameter of $Ba_{1-x}Zr_{0.85}Y_{0.15}O_{3-\delta}$ compositions ($0 \leq x \leq 0.10$) sintered at 1500 and 1600 ºC. Open symbols correspond to multiphase-samples.

Similar anomalous variations of lattice parameters have been reported for related systems $A_{1-x}Ce_{0.9}M_{0.1}O_{3-\delta}$ (A = Ba, Sr; B = Y, Gd, Yb) [197,204]; with a detailed structural analysis of $Sr_{1-x}Ce_{0.9}Yb_{0.1}O_{3-\delta}$ series compositions being presented by Rietveld refinement of X-ray and neutron diffraction data by Mather et al. [197]. Considering the prevalence of cation size effects on the lattice volume, in comparison to the impact of potential defect clustering, Mather et al. suggested that the irregular variation of lattice parameter with Ba-deficiency may likely be interpreted as a consequence of the potential for two different charge compensations mechanisms: A-site-cation vacancy mechanism (equation (5.1)), and dopant-partitioning mechanism (equation (5.2)) [197].

Following a similar analogy, the increase of lattice parameter observed in composition with $x = 0.02$ in comparison with stoichiometric composition, may, therefore, be related to the

initial prevalence of A-site-cation vacancy mechanism, equation (5.1), where the structural expansion can be attributed to the introduction of vacancies and subsequent lattice relaxation [197].

In contrast, the decrease of lattice parameter with Ba-deficiency observed for compositions with $x > 0.02$ would be consistent with the prevalence of the dopant partitioning mechanism (equation (5.2)) that would result in the replacement of larger barium cations ($_{XII}Ba^{2+}$ = 1.61 Å [97]) by smaller yttrium cations ($_{XII}Y^{3+}$ = 1.251 Å [202], while simultaneously increasing the relative concentration of smaller zirconium cations on the B-site ($_{VI}Zr^{4+}$ = 0.72 Å [97] with respect to the yttrium cations ($_{VI}Y^{3+}$ = 0.9 Å [97]).

5.4. Grain Growth and Densification

Example SEM pictures of $Ba_{1-x}Zr_{0.85}Y_{0.15}O_{3-\delta}$, $x = 0.02$ and $x = 0.08$, sintered at 1600 ºC, are shown in (Fig. 5.7) and exhibit significant microstructural changes with barium deficiency.

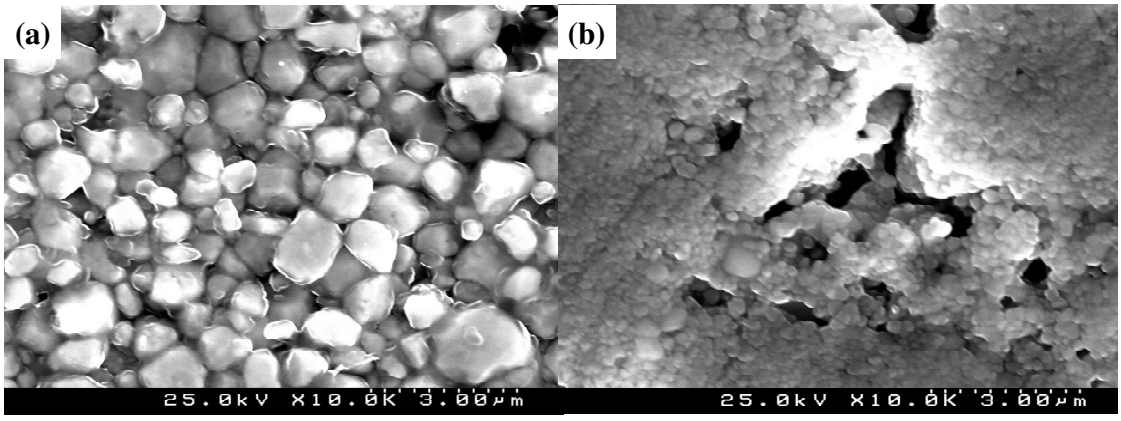

Fig. 5.7. SEM images of $Ba_{1-x}Zr_{0.85}Y_{0.15}O_{3-\delta}$, sintered at 1600 ºC: **(a)** x= 0.02 and **(b)** x = 0.08.

To clarify the impact of Ba-deficiency on the average grain size, estimation of average grain sizes was performed from SEM pictures of $Ba_{1-x}Zr_{0.85}Y_{0.15}O_{3-\delta}$, $0 \le x \le 0.10$, sintered at 1300, 1400, 1500 and 1600 ºC. The results (Fig. 5.8) reveal that even minor Ba-deficiency in the single perovskite region leads to a significant decrease in grain size. Furthermore, the negative

impact of Ba-deficiency on grain growth is observed to become more pronounced with increasing temperature, as predicted by its thermally activated nature [205].

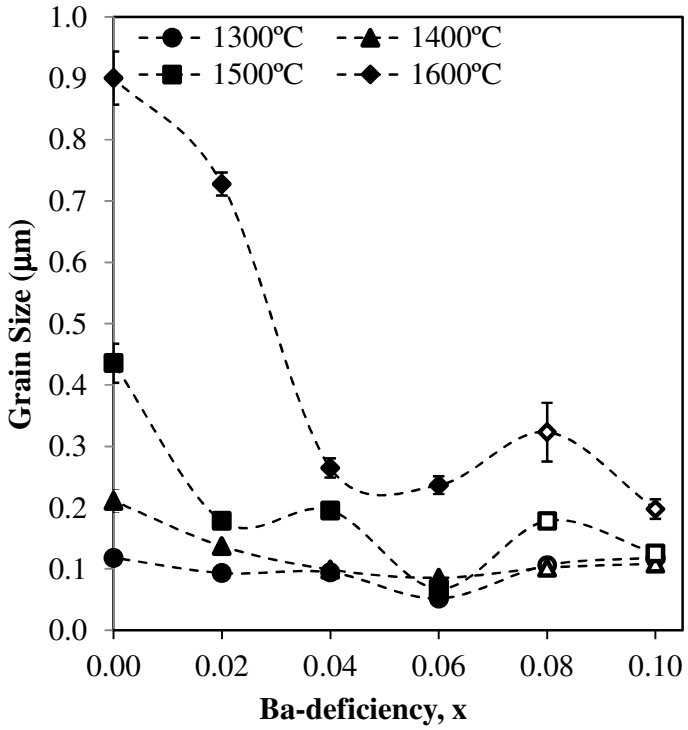

Fig. 5.8. Grain size of $Ba_{1-x}Zr_{0.85}Y_{0.15}O_{3-\delta}$, after sintering at 1300, 1400, 1500 and 1600 ºC, as a function of Ba-deficiency, x. Open symbols correspond to multiphase-samples.

The obtained results are in accordance with the poor grain growth reported for alkaline earth cerates and zirconate exposed to elevated temperatures for prolonged periods of time [101,102] where significant BaO vaporization would be expected.

Referring back to the results of phase formation and lattice behaviour described in the previous sections, the general decrease in grain size with Ba-deficiency within the single perovskite phase region, $0 \leq x \leq 0.06$, is contrary to that expected from the formation of point defects, such as oxygen and cation vacancies via equation (5.1), where an associated increase in diffusion coefficients, would predict an increase in grain growth with increasing Ba-deficiency. In this respect, note that a decrease in grain growth even is observed for composition $x = 0.02$ that showed an increase in lattice parameter over that of the

stoichiometric composition; a feature that was explained in Section 5.3 to potentially be due to the combined formation of barium and oxygen vacancies, equation (5.1).

Conversely, the alternative concept of dopant-partitioning, equation (5.2), would predict the elimination of point defects and an associated decrease in the expected diffusion coefficients for grain growth. Thus, this mechanism could potentially explain the observed impaired grain growth for Ba-deficient materials with values of $x > 0.02$. Nonetheless, previous literature has also suggested that poor grain growth in doped $BaZr_{0.85}M_{0.15}O_{3-\delta}$ materials (M = Y, In; Ga) to be associated with aliovalent dopant enrichment in grain boundaries[160]; an analogous argument to that proposed for similar behaviour in doped cerias [159]. This phenomenon would agree with the study of grain growth in $BaZr_{1-y}Y_yO_{3-\delta}$ materials (y = 0, 0.06 and 0.15), presented in Figure 3.9 of Chapter 3, where greater grain growth was noted for the undoped compositions than for acceptor doped materials.

To try to separate these two potential effects, preliminary EDS-TEM analysis of grain interior and triple points were performed for compositions with x = 0, 0.02, 0.04 and 0.06 to assess the presence of yttrium enrichment in grain boundaries (Fig. 5.9).

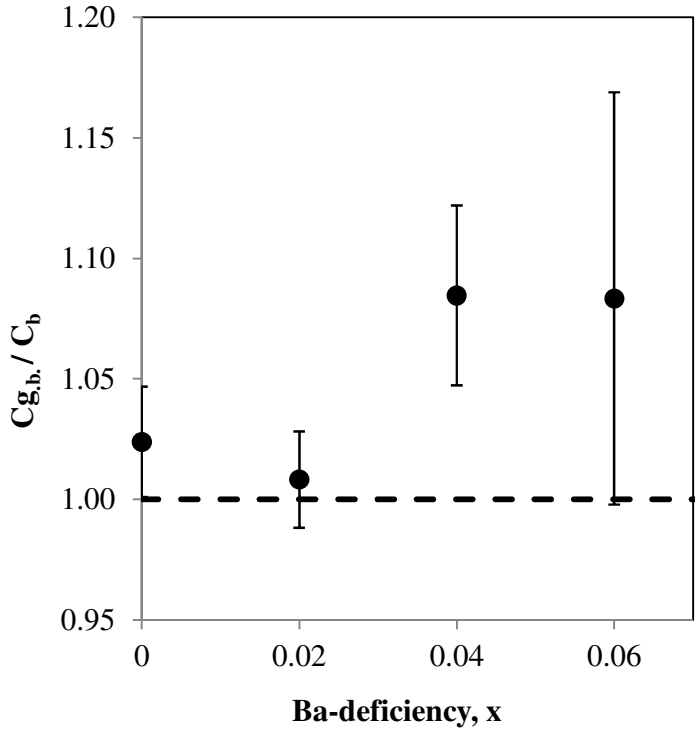

Fig. 5.9. Ratio between yttrium concentration in grain boundary (C_{gb}) and yttrium concentration in grain interior (C_b) in $Ba_{1-x}Zr_{0.85}Y_{0.15}O_{3-\delta}$ (x = 0, 0.02, 0.04 and 0.06), measure by EDS-TEM analysis, and corresponding error bars.

The data obtained suggest higher average concentration of yttrium in grain boundary triple points than grain interior, for the composition with $x = 0.04$, while for compositions with $x = 0$ and $x = 0.02$ less pronounced compositional changes are revealed. Unfortunately, the magnitude of the error bars for the composition $x = 0.06$ prevent conclusion for this composition for the current data set. This is related to the increased complication of this measurement upon decreasing grain size, which demands a more extensive sample pool to be analysed. Further experiments are currently underway to finalise the result for this composition. Nonetheless, potential Y-enrichment at grain boundaries in intermediate compositions, $x = 0.04$ and $x = 0.06$, could explain the steeper decrease in the grain size observed, respecting to the other single perovskite phase compositions (x = 0 and x = 0.02).

With respect to compositions with clear secondary phases of the acceptor dopant, $x = 0.08$ and $x = 0.10$, these samples present similar average grain sizes to that of neighbouring less Ba-deficiency compositions, inferring that similar restrictions to grain growth may occur. In this respect, limitation of grain growth by partial segregation of the acceptor dopant is in accordance with research studies on Ba-deficient perovskites [102] that also attributed this effect to the formation of precipitates in intergranular regions that pin grain boundaries, preventing pore break away.

The densification of Ba-deficient compositions as a function of temperature, obtained by geometric measurement of sintered samples, shows that there is no significant relation between densification levels and Ba-deficiency, or indeed the segregated presence of secondary phases of the acceptor dopant (Fig. 5.10).

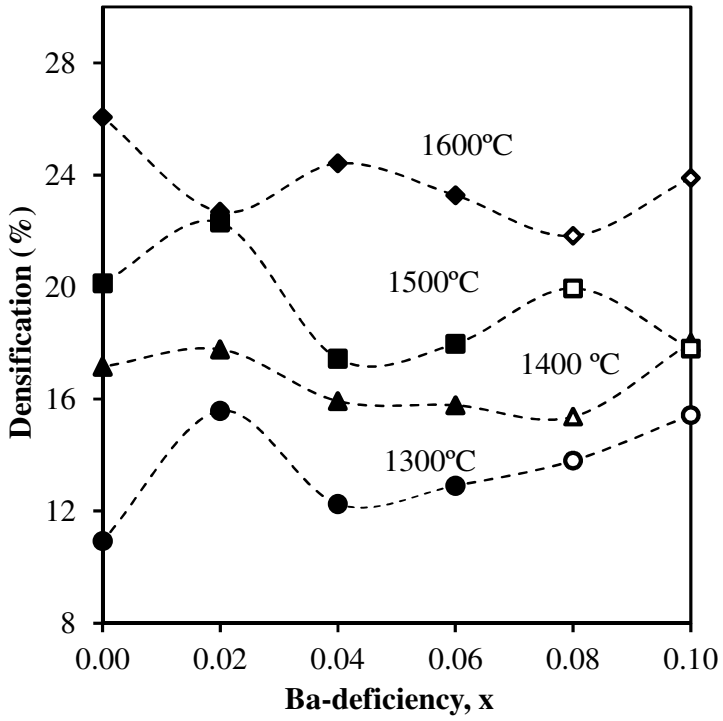

Fig. 5.10. Densification (%) in function of Ba-deficiency, x, for $Ba_{1-x}Zr_{0.85}Y_{0.15}O_{3-\delta}$, sintered at 1300, 1400, 1500 and 1600 ºC, for 5 hours. Open symbols correspond to multiphase-samples.

Moreover, the levels of densification (Fig. 5.10) appear to be independent of grain growth (Fig. 5.8), indicating that the relative densification rate exceeds that of the relative grain growth rate [205]. Note that shrinkage without significant grain growth was reported, for acceptor doped $BaZr_{1-y}Y_yO_{3-\delta}$ materials in Chapter 3, Figure 3.9.

On the contrary, final density in these materials is shown to be dependent only on sintering temperature and green density (Fig. 5.11).

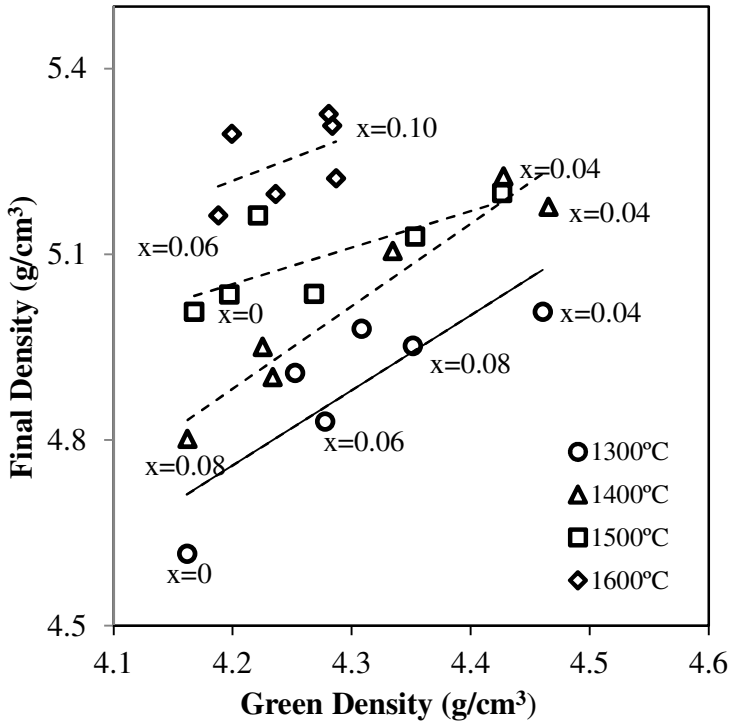

Fig. 5.11. Final density in function of green density of compositions for $Ba_{1-x}Zr_{0.85}Y_{0.15}O_{3-\delta}$, $0 \leq x \leq 0.10$, sintered at 1300, 1400, 1500 and 1600 ºC, for 5 hours.

5.5. ELECTRICAL CHARACTERISATION

The impedance spectra, obtained from *AC* impedance spectroscopy measurements under 10 % H_2/N_2 atmospheres, for selected compositions with $x = 0.02$ and $x = 0.10$ are presented in Fig. 5.12 in Nyquist form. The spectra obtained are typical of this class of protonic conductors, with distinct arcs, corresponding to bulk (grain interior), grain boundary and electrochemical interface transport; and are analysed in terms of an equivalent circuit model formed by series combination of RQ sub-circuits corresponding to distinct phenomenon.

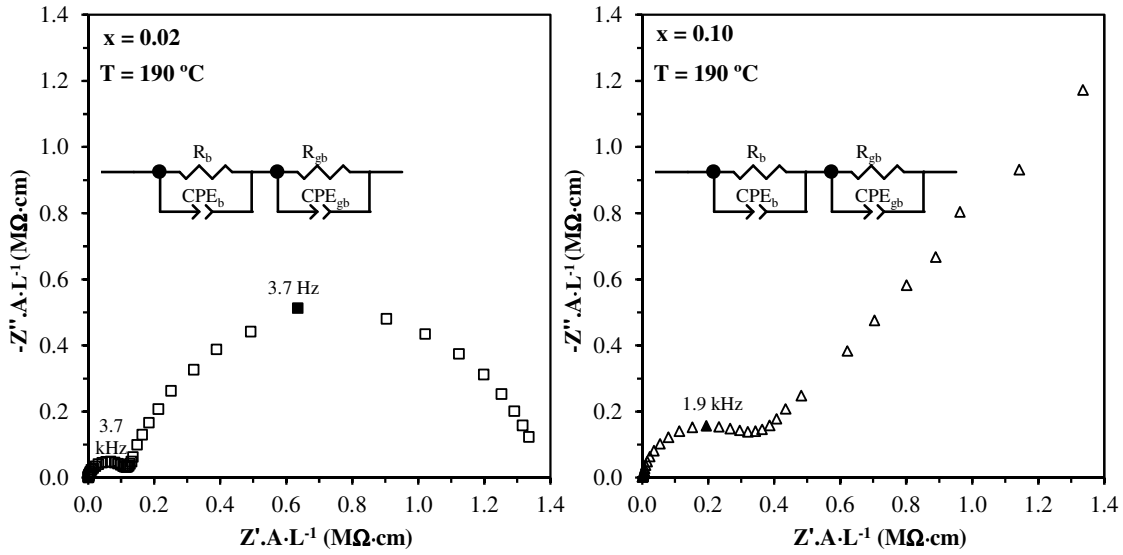

Fig. 5.12. Nyquist plots collected at 190 ºC for Ba-deficient samples of $x = 0.02$ and $x = 0.10$, under wet 10 % H_2/N_2 atmosphere, and respective equivalent circuits models.

Arrhenius plots of total and bulk conductivity, as a function of Ba-deficiency (Fig. 5.13) reveals the detrimental effect of Ba-deficiency on the total conductivity of Y-doped $BaZrO_3$.

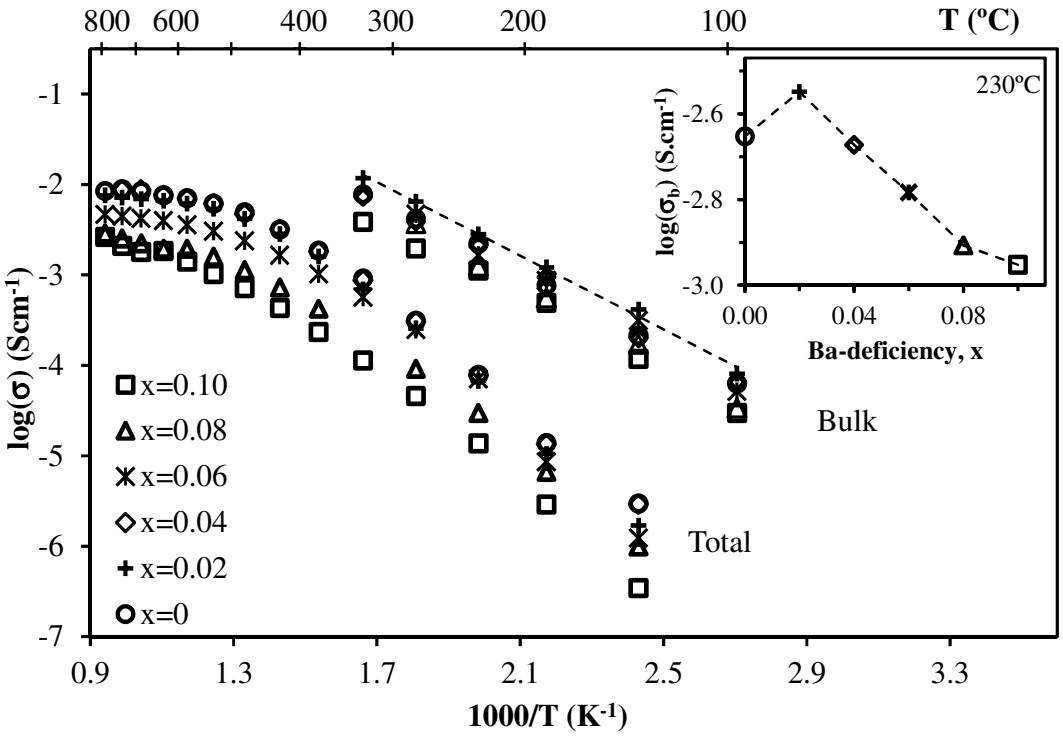

Fig. 5.13. Arrhenius plot of total and bulk electrical conductivity, under wet 10 % H_2/N2, of $Ba_{1-x}Zr_{0.85}Y_{0.15}O_{3-\delta}$ samples, $0 \leq x \leq 0.10$, sintered at 1600 ºC. The inset shows a comparison of the bulk conductivity of the series at 230 ºC as a function of Ba-deficiency.

A decrease in total conductivity can be observed in Ba-deficient compositions, as compared to the stoichiometric composition. In contrast, bulk conductivity data follow the shape of the measured lattice parameter trend observed in Fig. 5.6: an increase in bulk conductivity until $x = 0.02$, then a drop as $x > 0.02$. The conductivity behaviour, therefore, appears to reinforces the assumption of presence of different charge compensation mechanisms in $Ba_{1-x}Zr_{0.85}Y_{0.15}O_{3-\delta}$ series compositions with increasing Ba-deficiency: an increase of oxygen and A-site vacancies caused by A-site-cation vacancy mechanism, equation (5.1), that can be hydrated with consequent increase of bulk conductivity at $x \leq 0.02$, followed by an increasing consumption of oxygen vacancies via the dopant-partitioning mechanism (equation (5.2)), in compositions with $x > 0.02$, associated with decreased proton concentration.

Such correspondence between the shape of the non-linear lattice parameter within the pure perovskite phase, observed in Fig. 5.6, and the bulk conductivity behaviour, thus suggest the presence of a real phenomenon, rather than an experimental artefact. In this respect, note that links between anomalous variations in lattice parameter and bulk conductivity trends have also been reported in other A-site deficient perovskite systems [197].

Grain size and activation energy values of bulk and grain boundary conductivities in the temperature range 140 – 280 ºC are presented in Table 5.1. Bulk activation energies correspond well with those for proton conduction reported for similar materials in the literature [145].

Table 5.1. Average grain size and activation energy values of bulk and grain boundary conductivities of $Ba_{1-x}Zr_{0.85}Y_{0.15}O_{3-\delta}$, $0 \leq x \leq 0.10$, in the temperature range of 140 – 280 ºC.

Ba-deficiency x	Average Grain Size (μm)	E_a (bulk) (eV)	E_a (grain boundary) (eV)
0	0.90 ± 0.04	0.46 ± 0.02	0.70 ± 0.04
0.02	0.73 ± 0.02	0.42 ± 0.05	0.75 ± 0.03
0.04	0.26 ± 0.02	0.45 ± 0.03	0.70 ± 0.05
0.06	0.26 ± 0.02	0.41 ± 0.03	0.80 ± 0.05
0.08	0.32 ± 0.02	0.46 ± 0.02	0.68 ± 0.01
0.10	0.20 ± 0.02	0.43 ± 0.03	0.73 ± 0.01

With respect to the impact of Ba-deficiency on grain boundary conductivity, one should first take into account microstructural effects. Poor grain growth will result in an increased grain boundary density and, hence higher grain boundary resistivity. Thus, determination of area specific grain boundary conductance (2.20), needs to be performed to allow comparison of grain-boundary resistances of samples with differing microstructure (Fig. 5.14).

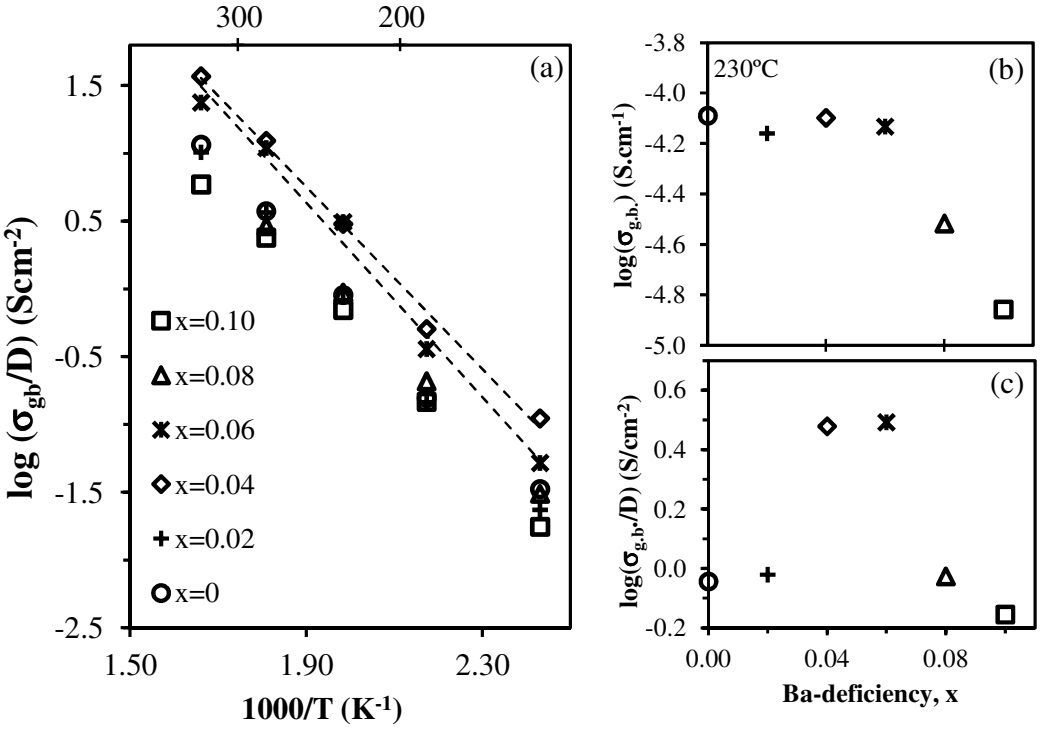

Fig. 5.14. Impact of Ba-deficiency on grain boundary conductivity, under wet 10 % H_2/N2, in $Ba_{1-x}Zr_{0.85}Y_{0.15}O_{3-\delta}$ samples, $0 \leq x \leq 0.10$, sintered at 1600 ºC. **(a)** Arrhenius plot of area specific grain boundary conductance; **(b)** grain boundary conductivity and **(c)** area specific grain boundary conductance, determined at 230 ºC, as a function of *x*.

The area specific grain boundary conductance is observed to be higher for the intermediate Ba-deficient compositions $x = 0.04$ and $x = 0.06$ than the other compositions studied. Such an increase serves to mask the expected negative effect of poor grain growth on the overall grain boundary conductivity in these compositions. Indeed, the total grain boundary conductivity of these compositions is similar to those shown by the stoichiometric ($x = 0$) and slight Ba-deficient ($x = 0.02$) compositions (Fig. 5.14 (b)), whereas, significantly lower grain boundary conductivities are observed in compositions $x = 0.08$ and $x = 0.10$ that show not only a small grain size but also the presence of yttria as a secondary phase, Fig.5.7 and Fig. 5.4.

The higher specific grain boundary conductivity suggested for compositions $x = 0.04$ and $x = 0.06$ may arise from yttrium enrichment of grain boundaries observed for these compositions in Fig. 5.9. Indeed a favourable effect of yttrium enrichment on grain boundary

conductivity has been previously reported [206] and attributed to decreasing of the apparent barrier height caused by the space charge effect, with consequent improvement of proton transport across grain-boundaries.

5.6. CONCLUDING REMARKS

Ba-loss is a common problem when one tries to densify barium zirconate based materials due to the requirement of very high sintering temperatures. Many authors have attempted to link Ba-loss with poor total conductivity values and the large scatter in reported data. In this context, the present work aimed to established links between Ba-loss, densification, grain growth and conductivity for Y-doped $BaZrO_3$ materials.

XRD analysis revealed the formation of a single perovskite phase for compositions with Ba-deficiency (x) lower than 0.08, while compositions with higher Ba-deficiency a secondary phase of Y_2O_3 is observable besides the primary perovskite phase. The obtained results are in accordance to the ternary $BaO–YO_{1.5}–ZrO_2$ phase diagram proposed in the literature. Structural characterization revealed a non-linear trend in lattice parameter, with the lattice parameter passing through a maximum within the pure perovskite phase region, then decreasing with increasing Ba-deficiency. The bulk conductivity data follow the measured parameter trend, suggesting the occurrence of different charge compensation mechanisms in Ba-deficient compositions.

Microstructural analysis revealed the detrimental effect of Ba-deficiency on grain growth. One observes that even minor Ba-deficiency in the single perovskite region, leads to significant decrease in grain size.

Compositional analysis in grain interior and grain boundary triple point suggests yttrium-enrichment in grain boundaries for intermediate Ba-deficiency compositions, $x = 0.04$ and $x = 0.06$, which can be associated to the higher specific grain boundary conductivity observed for these compositions.

6. MECHANOCHEMICAL PREPARATION AND STABILITY STUDIES OF $Ba(Pr,Zr,Y)O_{3-\delta}$ MATERIALS AS POTENTIAL ELECTRODES FOR PROTONIC SOFC

The study of homogeneous mixed proton and electron conductors, where mixed conductivity is introduced in a single phase is still in its infancy. Such materials would find application as electrodes in solid oxide fuel cells or as separation membranes. Alkaline earth perovskite materials, such as $Ba(Pr,R)O_{3-\delta}$, R = Rare Earth, would be possible candidates, once it is expected that the presence of mixed valence Pr introduces electronic conductivity [85,207]. However, several studies have shown that $Ba(Pr,R)O_{3-\delta}$ materials are predominantly electronic conductors, offering only minimal proton conductivity and are susceptible to decomposition in both wet and dry reducing conditions, moist oxidising conditions, CO_2-containing atmospheres and also upon high temperature processing [208–210]. This high level of instability has led several authors to render these materials as "not useful" for SOFC purposes [209,210].

It is widely documented that the stability of the perovskite phase is related to the tolerance factor, equation 1.7, with compositions that are closer to the ideal cubic form ($t = 1$) presenting the higher stabilities [211]. A work of Magrasó et al. [212], on the related compositions $BaPr_{0.7-x}Zr_xGd_{0.3}O_{3-\delta}$, followed this guideline and showed the perovskite phase to offer improved stability when progressing from orthorhombically distorted to cubic symmetry with increasing Zr content. However, these materials also revealed gadolinium segregation at high sintering temperature. The documented orthorhombic lattice distortion arises because the average B-site ionic radius becomes too large for the ideal $Pm\bar{3}m$ aristotype with increasing Pr concentration. This factor is also aggravated by the presence of a high concentration of large gadolinium dopant ions.

In this context, it was intended to investigate related materials with improved stability, by reducing the acceptor dopant concentration and by selection of a smaller dopant (yttrium). The compositions studied are, thus, $Ba(Pr_{1-x}Zr_x)_{1-y}Y_yO_{3-\delta}$, with $y = 0.1$ and $y = 0.2$, for $0 \leq x \leq 1$.

6.1. PHASE FORMATION

Despite repeated cycles of high-temperature firing (1500 ºC, 5 hours) and regrinding, phase purity was not obtained for the compositions $Ba(Pr,Zr,Y)O_{3-\delta}$, by conventional solid-state preparation from stoichiometric mixtures of $BaCO_3$, ZrO_2, Y_2O_3 and Pr_6O_{11}. On the contrary, the X-ray powder diffraction patterns of the system $Ba(Pr_{1-x}Zr_x)_{0.8}Y_{0.2}O_{3-\delta}$ exhibit broad asymmetric peak shapes, suggesting the presence of inhomogenities and distinct secondary phases at high Zr-contents corresponding to a secondary perovskite phase of smaller lattice parameter (Fig. 6.1).

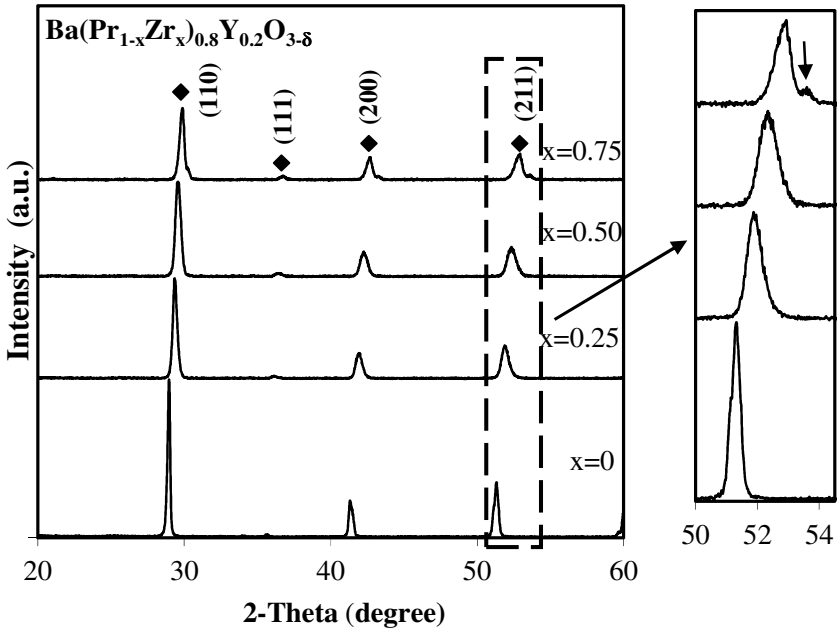

Fig. 6.1. X-ray diffraction pattern of the $Ba(Pr_{1-x}Zr_x)_{0.8}Y_{0.2}O_{3-\delta}$ system prepared by solid-state synthesis, after a second sintering at 1500 ºC, highlighting broad asymmetric peak shapes suggesting the presence of inhomogenities. Arrow indicates secondary phase in composition $x = 0.75$. The marker (◆) identifies the perovskite phase.

When using the standard high energy milling procedure as performed for $Ba(Zr,Y)O_{3-\delta}$ materials (section 2.1.1), one observed that it is insufficient to synthesise a single-phase perovskite, forming instead a mixture of the perovskite phase and PrO_2. In contrast, samples mechanically activated for 300 minutes and annealed at 1250 ºC for 5 hours show pure phases with well-defined peak shapes suggesting good homogeneity, Fig. 6.2 (a). Single-phase perovskite materials were obtained for all values of x in the two studied systems, $Ba(Pr_{1-x}Zr_x)_{0.9}Y_{0.1}O_{3-\delta}$ and $Ba(Pr_{1-x}Zr_x)_{0.8}Y_{0.2}O_{3-\delta}$ XRD powder patterns are shown in Fig. 6.2 (b) for the latter system.

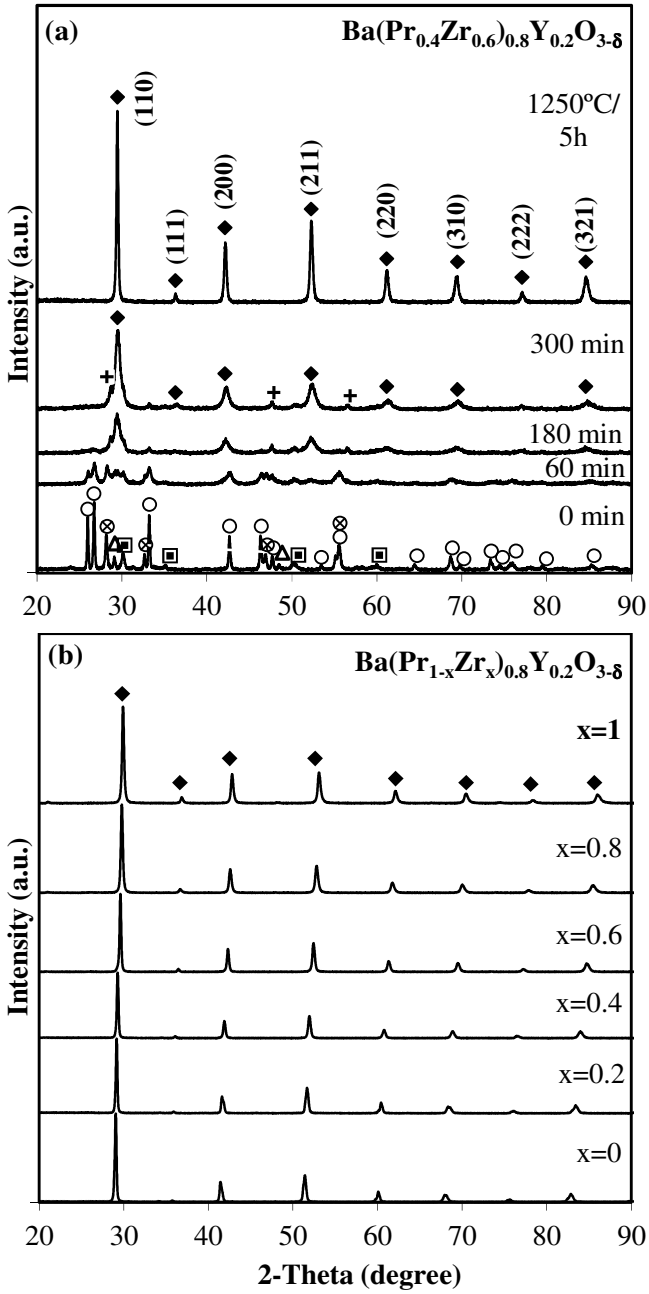

Fig. 6.2.(a) X-ray diffraction patterns demonstrating the evolution of mechanical activation with milling time and formation of single-phase $Ba(Pr_{0.4}Zr_{0.6})_{0.8}Y_{0.2}O_{3-\delta}$ perovskite after annealing at 1250 ºC for 5 hours; **(b)** X-ray diffraction patterns of the $Ba(Pr_{1-x}Zr_x)_{0.8}Y_{0.2}O_{3-\delta}$ system prepared by a combination of high energy milling and annealing at 1250 ºC for 5 hours. Phase purity is obtained for all values of *x*. The markers identify (○) barium peroxide; (▣) yttria doped zirconia (3 mol %); (△) yttria oxide; (⊗) Pr_6O_{11}; (+) PrO_2; and (◆) perovskite phase.

6.2. STRUCTURAL CHARACTERIZATION

Detailed structural characterization by Rietveld refinement, Fig. 6.3 (a) and Fig. 6.3 (b), show the reduced cell (pseudo-cubic) lattice parameters of the two systems as a function of composition, superimposed by: i) delimitation of the regions where a certain type of tilting regime may be expected; ii) variations in the tolerance factor [87,88]; and iii) by stability information at different atmospheres, a factor that will be discussed in the later text.

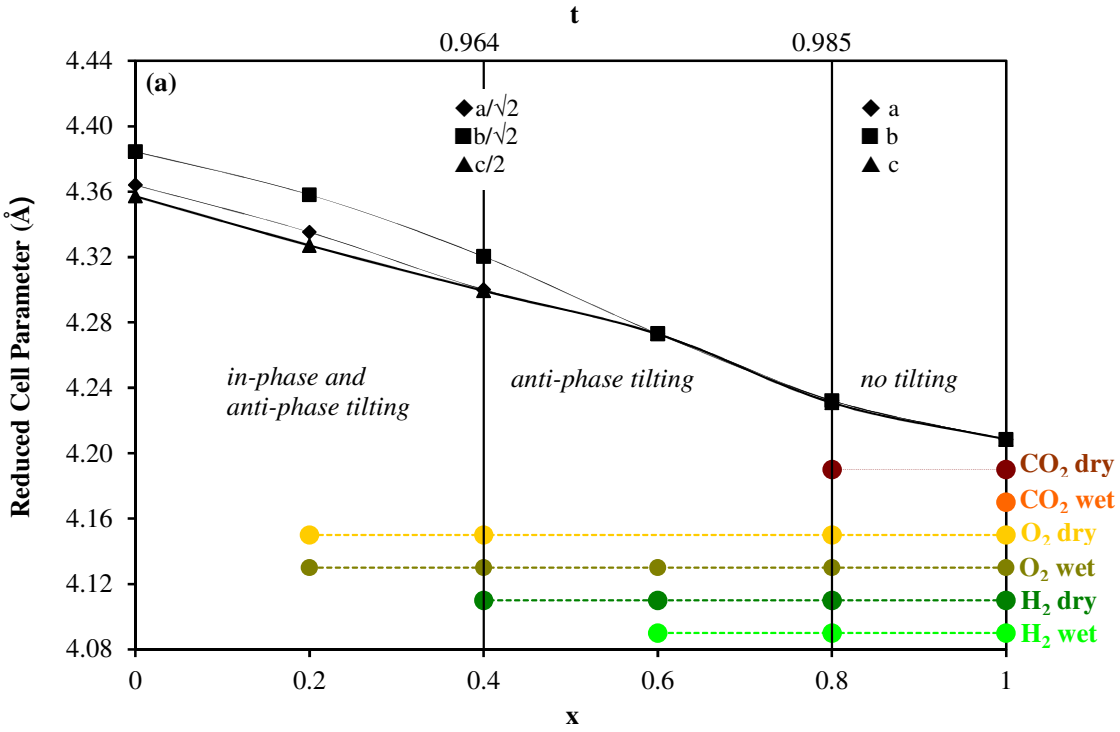

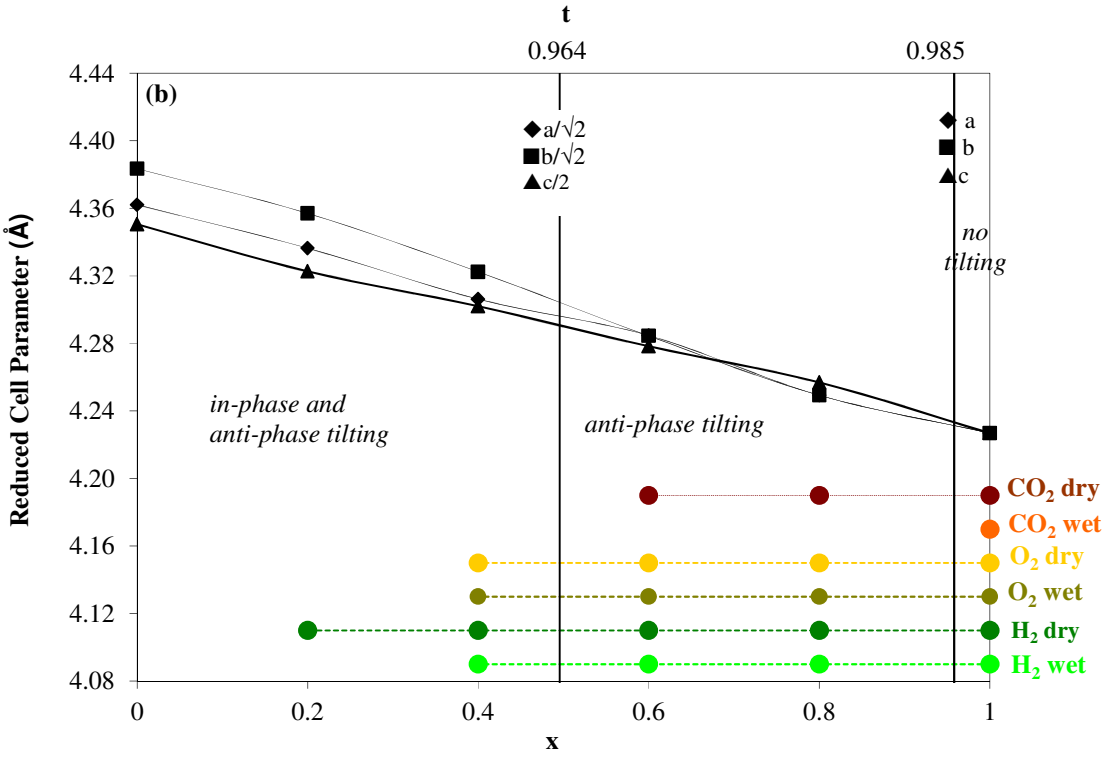

Fig. 6.3. Reduced unit-cell parameter as a function of composition, superimposed with stability information under different atmospheres for: **(a)** $Ba(Pr_{1-x}Zr_x)_{0.9}Y_{0.1}O_{3-\delta}$ and **(b)** $Ba(Pr_{1-x}Zr_x)_{0.8}Y_{0.2}O_{3-\delta}$. Stability was analysed by X-ray diffraction analysis after heat treatment at 600 ºC. Bullet points signify stable compositions for each atmosphere.

In both systems there is a decrease in unit-cell parameter with increase in the Zr content, which is consistent with the substitution of Pr^{4+}_{VI} (0.85 Å) with the smaller Zr^{4+}_{VI} (0.72 Å) cation [97].

In the $Ba(Pr_{1-x}Zr_x)_{0.9}Y_{0.1}O_{3-\delta}$ family (Fig. 6.3 (a)), indexing and subsequent Rietveld analysis indicates that the symmetry changes from orthorhombic (*Pbnm*) for $x = 0$ [86] and $x = 0.2$ through tetragonal (*I4/mcm*) or rhombohedral ($R\bar{3}c$) for $x = 0.4$ and $x = 0.6$ to cubic ($x = 0.8$ and $x = 1.0$). It is noteworthy that composition $x = 0.4$ with tolerance factor 0.964 lies on the transition between regions of in-phase and anti-phase tilting and anti-phase tilting only, whereas composition $x = 0.8$ has a tolerance factor of 0.985, which forms the boundary between zones of anti-phase tilted and untilted structures.

The $Ba(Pr_{1-x}Zr_x)_{0.8}Y_{0.2}O_{3-\delta}$ system displays a similar increase in symmetry and lowering of reduced unit-cell parameter with increase in the Zr content, Fig. 6.3 (b). Again, the indexation and Rietveld analysis are consistent with orthorhombic and cubic symmetries for the end-member phases, which are also the symmetries predicted on the basis of tolerance factor. Orthorhombic symmetry associated with in-phase and anti-phase tilting is also expected for compositions $x = 0.2$ and $x = 0.4$ on considering their respective tolerance factors; the lattice parameters for these compositions and the end-member phase ($x = 0$) were thus obtained on refining in the *Pbnm* space group. With further increase in the Zr content, the observed symmetry changes to tetragonal (or pseudo-tetragonal); accordingly the lattice parameters for compositions $x = 0.6$ and $x = 0.8$ were determined on refinement in *I4/mcm*. This space group is associated with anti-phase tilting only, which is to be expected from the corresponding tolerance factors. In comparison to the $Ba(Pr_{1-x}Zr_x)_{0.9}Y_{0.1}O_{3-\delta}$ system, the higher Y^{3+} content lowers the tolerance factor with the effect that the orthorhombic crystal system is observed up to a higher Zr content.

6.3. STABILITY STUDIES

The stability of the perovskite phase is commonly related to the tolerance factor [211]; hence, the stability information of the title materials on annealing in various gas atmospheres at 600 ºC for 12 hours is displayed collectively with the structural information present in the previous figure (Fig. 6.3). Stability, for the current purposes, is defined to be the absence of secondary phases on post-operative examination at the resolution of X-ray diffraction. Samples that meet this criterion are represented by bullet points in Fig. 6.3 (a) and (b), for each gas environment.

6.3.1. DRY AND WET O_2

In both dry and wet oxygen atmospheres, it has been shown the improvement in stability with the increase in the Zr content. In general, these results concur with the increase in the tolerance factor, and associated increase in symmetry with increase in Zr content (Fig. 6.3).

The instability of $BaPr_{1-x}Y_xO_{3-\delta}$ compositions in wet and dry oxygen environments, $BaPr_{1-x}Y_xO_{3-\delta}$ is revealed by the decomposition of the perovskite phase to form praseodymium oxide and barium carbonate; the later probably formed by rapid reaction between BaO and CO_2 after annealing. Signs of hydroxide formation, as documented for $BaPr_{0.7}Gd_{0.3}O_{3-\delta}$ in wet oxygen [209], could not be observed for the current Y-containing systems.

Interestingly, the intermediate composition $Ba(Pr_{0.4}Zr_{0.6})_{0.9}Y_{0.1}O_{3-\delta}$ decomposes into two perovskite phases of differing lattice parameters on annealing in dry oxygen (Fig. 6.4). Note that a $BaZrO_3$-based perovskite is probably the minority phase, while the positions of the reflections of the main phase are still relatively close to corresponding reflections of the single-phase composition retained in wet O_2. This suggests that the prevailing phase might still be a mixed $Ba(Pr_{1-x}Zr_x)_{1-y}Y_yO_{3-\delta}$ composition.

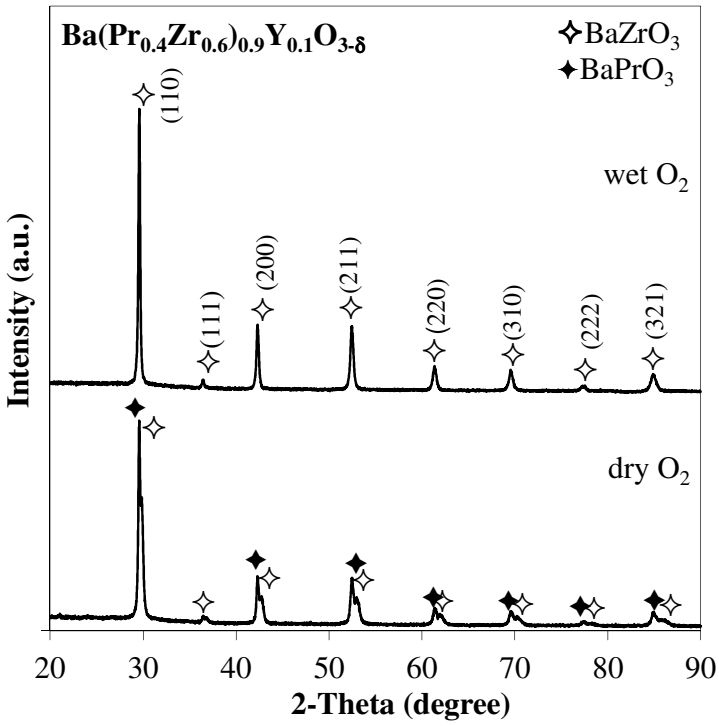

Fig. 6.4. X-ray diffraction patterns of $Ba(Pr_{0.4}Zr_{0.6})_{0.9}Y_{0.1}O_{3-\delta}$, after annealing at 600 ºC in dry and wet O_2 atmospheres, highlighting instability in dry O_2. Filled and open stars indicate perovskite phases of differing lattice parameter.

6.3.2. 10% H_2/N_2

In H_2 environments, chemical instability is observed for the both compositions of $BaPr_{1-x}Y_yO_{3-\delta}$ (y = 0.1 and y = 0.2), Fig. 6.3, leading to the formation of $BaPr_2O_4$-based phase under dry conditions or, $Pr(OH)_3$ under wet conditions and some $BaCO_3$ resulting from the ready reaction between $Ba(OH)_2$ and CO_2. These observations are consistent with the work carried out by Magrasó et al. [212], for the related materials $BaPr_{0.7-x}Zr_xGd_{0.3}O_{3-\delta}$. One may describe the formation of secondary phases as follows:

$$Ba(Pr,Y)O_{3-\delta} + x\ H_2 \rightarrow x\ Ba(Pr,Y)_2O_4 + x\ Ba(OH)_2 + (1-2x)\ Ba(Pr,Y)O_{3-\delta} \qquad (6.1)$$

for dry conditions, or:

$$Ba(Pr,Y)O_{3-\delta} + 0.5x\ H_2 + 2x\ H_2O \rightarrow x\ Pr(OH)_3 + x\ Ba(OH)_2 + (1-x)\ Ba(Pr,Y)O_{3-\delta} \quad (6.2)$$

for wet conditions, followed by ready conversion of barium hydroxide in the presence of atmospheric CO_2:

$$x\ Ba(OH)_2 + x\ CO_2 \rightarrow x\ BaCO_3 + x\ H_2O \quad (6.3)$$

For low Zr-content, decomposition under H_2 atmosphere is generally manifested showing the presence of $BaCO_3$ and splitting in the perovskite phases (Fig. 6.5). Nevertheless, the composition, $Ba(Pr_{0.8}Zr_{0.2})_{0.8}Y_{0.2}O_{3-\delta}$, containing large quantities of Pr, is stable under dry hydrogen Fig. 6.5.

Hence, in comparison with the $BaPr_{0.7-x}Zr_xGd_{0.3}O_{3-\delta}$ system, which shows substantial instability under reducing and water conditions, for values of $x < 0.5$, [212], the current materials present an extension of stability under reducing atmospheres to samples of higher Pr-content.

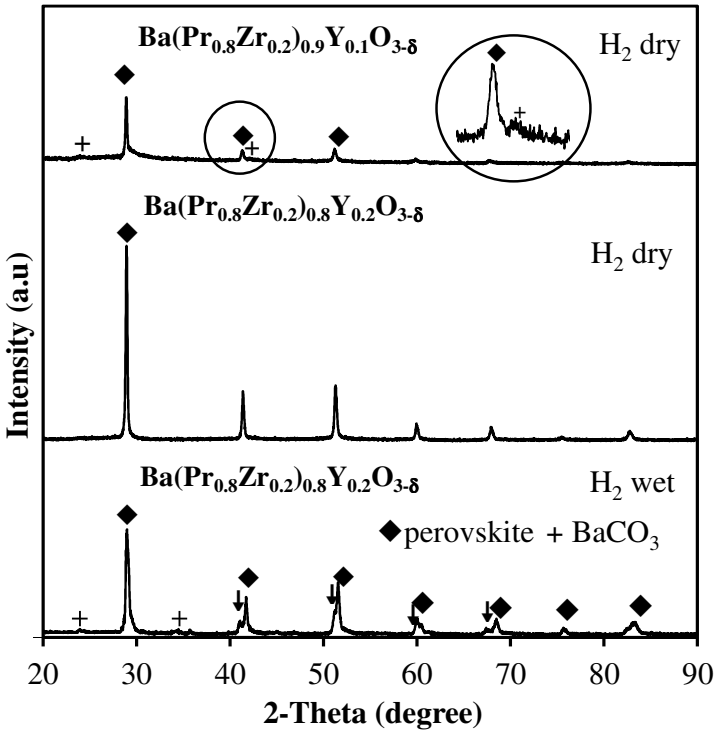

Fig. 6.5. X-ray diffraction patterns of compositions from the systems $Ba(Pr_{1-x}Zr_x)_{0.9}Y_{0.1}O_{3-\delta}$ and $Ba(Pr_{1-x}Zr_x)_{0.8}Y_{0.2}O_{3-\delta}$ with $x = 0.2$, after annealing at 600 ºC in wet and dry H_2 atmospheres, highlighting greater stability in the system with higher Y-content and greater stabilities on dry atmospheres.

Furthermore, the current work provides the additional information that stability is greater in dry reducing conditions and is retained to a higher Pr content (lower x) in the system with the greatest Y-content, $Ba(Pr_{1-x}Zr_x)_{0.8}Y_{0.2}O_{3-\delta}$ (Fig. 6.3 and Fig. 6.5). The latter phenomenon can possibly be explained with reference to Fig. 6.6. , which plots the expected tolerance factor with respect to the ionic size of praseodymium in different oxidation states. The formation of the decomposition product $BaPr_2O_4$ in dry 10 % H_2/N_2 clearly indicates reduction of Pr^{4+}-Pr^{3+} in this atmosphere. When Pr is in the 3+ oxidation state, the expected trends in tolerance factor of the two systems cross at approximately $x = 0.4$ (Fig. 6.6.). Hence, at low values of x, the compositions with highest tolerance factor will be those with the higher Y-content, i.e. $Ba(Pr_{1-x}Zr_x)_{0.8}Y_{0.2}O_{3-\delta}$. This is in agreement with the observed experimental data in Fig. 6.3 and Fig. 6.5 on annealing in 10 % H_2/N_2. Thus, it appears to be possible to predict the

observed stability even in reducing conditions from simple tolerance factor calculations on consideration of the reduction of Pr and its associated increase in ionic size.

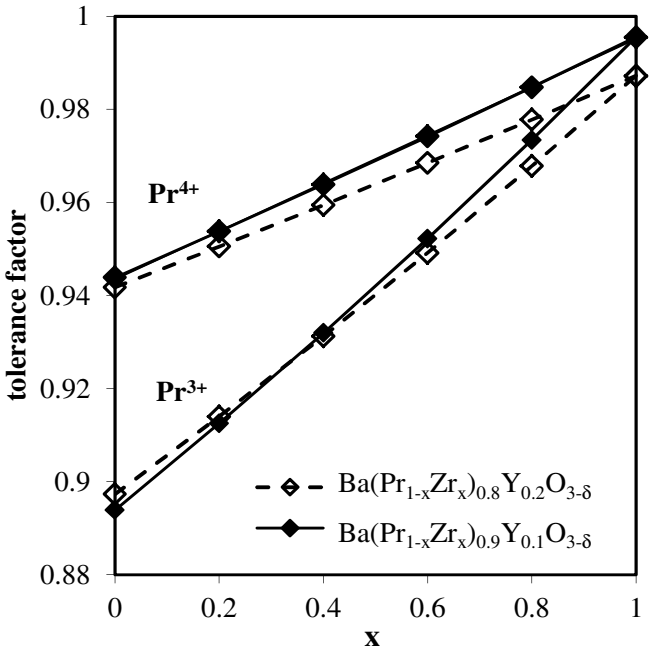

Fig. 6.6. Expected trends in tolerance factor with respect to the ionic size of praseodymium in different oxidation states for the $Ba(Pr_{1-x}Zr_x)_{0.9}Y_{0.1}O_{3-\delta}$ and $Ba(Pr_{1-x}Zr_x)_{0.8}Y_{0.2}O_{3-\delta}$ systems.

6.3.3. PURE CO_2

The stability of the systems in flowing dry CO_2 measured by TGA is shown in Fig. 6.7. Major weight gains can be observed for both systems for compositions of low Zr-content above 500 ºC and the total weight gain increases with decrease in the Zr-content. The uptake of CO_2 occurs in two stages, a low-temperature stage corresponding to minor weight gain followed by a dominant high-temperature regime in which the majority of the weight gain takes place. This behaviour resembles that reported for the $BaPr_{0.7-x}Zr_xGd_{0.3}O_{3-\delta}$ [212] and $BaCe_{1-x}R_xO_{3-\delta}$ systems [213]. In general, the onset temperature of the low- and high- temperature ranges increases with increasing Zr-content, reflecting an increased stability associated with increase in tolerance factor and symmetry, and lower basicity of the B-site cation [214], Fig. 6.3. For samples of high Pr-content, the presence of maxima in weight gain can be observed followed

by weight loss at the highest temperatures. This phenomenon is analogous to the carbonation behaviour of $BaCeO_3$ reported by Zakowsky et al. [213] who demonstrated that the formed $BaCO_3$ decomposes at high temperatures with reformation of the perovskite phase. Note that the location of these maxima shifts to higher temperatures with increase in the Zr-content, reflecting a higher stability of $BaZrO_3$ than $BaCeO_3$, in agreement with the corresponding thermodynamic predictions [215].

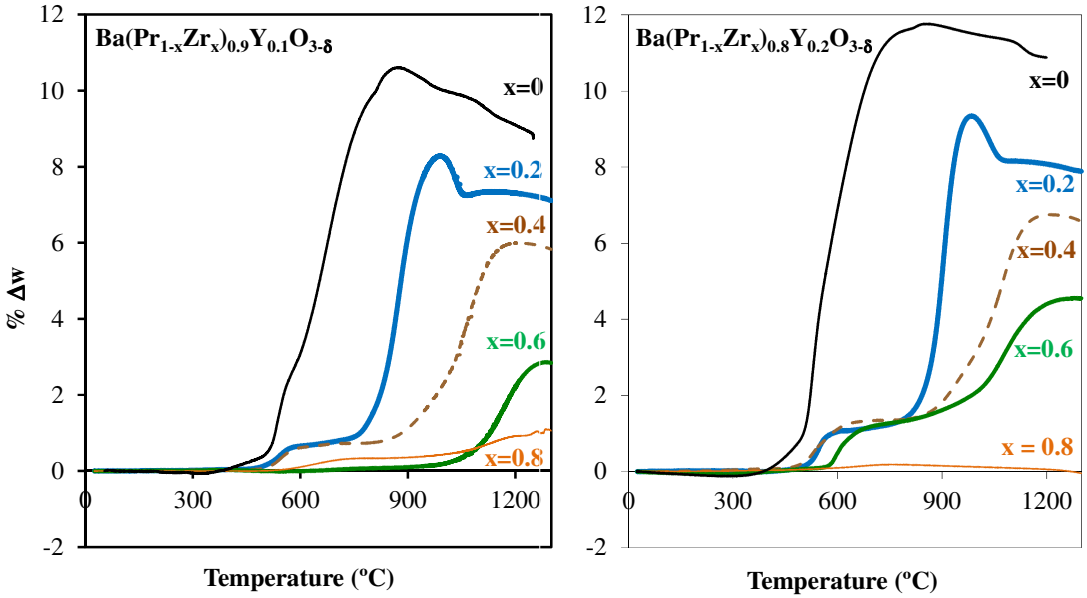

Fig. 6.7. TGA plot for the $Ba(Pr_{1-x}Zr_x)_{0.9}Y_{0.1}O_{3-\delta}$ and $Ba(Pr_{1-x}Zr_x)_{0.8}Y_{0.2}O_{3-\delta}$ systems heated under dry, flowing 100 % CO_2 at a rate of 1ºC·min^{-1}.

Post-mortem analysis of powdered samples by XRD after high temperature carbonation showed the presence of the component oxides and barium carbonate. In Fig. 6.8. the maximum CO_2 uptake on value second stage carbonation is compared with the theoretical calculated for the stoichiometric formation of $BaCO_3$. Fig. 6.8. shows an approximately linear, inverse relationship between the value of *x* and the extent of carbonation and higher carbonation in the system with the highest Y-content. Note that this is the opposite dependence to that observed in more reducing conditions, in section 6.3.2, in agreement with tolerance factor considerations outlined in Fig. 6.6. .These predictions of carbonation may even be somewhat

underestimated due to a counter effect of weight losses by gradual reduction of Pr^{4+} to Pr^{3+}. If one assumes close to 50 % conversion to Pr^{3+} one obtains up to about 93 % carbonation for $BaPr_{0.8}Y_{0.2}O_{3-\delta}$ and about 87 % for $BaPr_{0.9}Y_{0.1}O_{3-\delta}$.

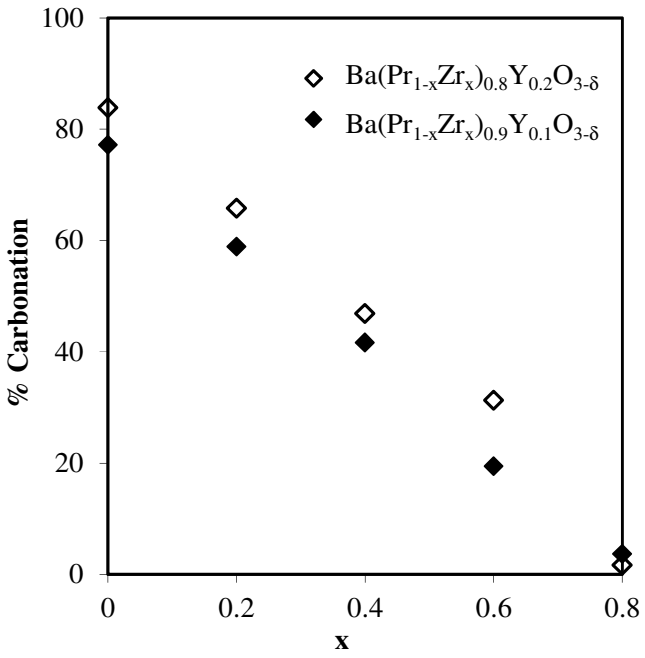

Fig. 6.8. Comparison of the maximum CO_2 uptake on second stage carbonation in dry flowing CO_2 with the theoretical value calculated for the stoichiometric formation of $BaCO_3$ for each composition for the systems $Ba(Pr_{1-x}Zr_x)_{0.9}Y_{0.1}O_{3-\delta}$ and $Ba(Pr_{1-x}Zr_x)_{0.8}Y_{0.2}O_{3-\delta}$.

Zakowsky et al. [213] suggested that the low-temperature stage could be due to carbonation of exolved BaO following formation of a Ba-deficient phase during sample preparation. Alternatively, it may be that the low-temperature regime is related to surface carbonation, while the second stage, corresponding to bulk carbonation, would be displaced to higher temperatures due to kinetic limitations. In order to assess the low-temperature stage more fully, subsequent XRD analysis was performed on samples annealed at 600 ºC for 12 hours under dry CO_2. The results, summarised in Fig. 6.3, show the stability limit at 600 ºC to be wider in $Ba(Pr_{1-x}Zr_x)_{0.9}Y_{0.1}O_{3-\delta}$ ($x \geq 0.6$) than in the system $Ba(Pr_{1-x}Zr_x)_{0.8}Y_{0.2}O_{3-\delta}$ ($x \geq 0.8$). To highlight this point, Fig. 6.9. plots the intensity ratio between the most intense (111) reflection

in the $BaCO_3$ phase and the most intense (110) reflection in the perovskite phase for samples carbonated at 600 ºC for 12 hours in wet and dry atmospheres. This intensity ratio allows an estimation of variations in the relative amounts of the perovskite and $BaCO_3$ phases with changes in composition.

Fig. 6.9. shows that the amount of first stage carbonation is greater with decrease in the Zr-content and greater in the system with the highest Y-content. Hence, the extents of both low temperature and high temperature carbonation have the same tendencies, reinforcing the relationship between stability, increased tolerance factor, crystallographic symmetry, and basicity. Another important observation is that much greater carbonation occurs in a wet rather than a dry atmosphere. The corresponding diffraction patterns for low temperature carbonation, in compositions with values of $x \geq 0.2$ up to the stability limit for each system, show predominantly the perovskite phase with the additional presence of $BaCO_3$. In contrast, significant decomposition is observed for the Zr-free samples at this temperature, with formation of the component oxides and $BaCO_3$ accompanied by substantial decrease in the relative XRD peak intensities of the perovskite phase.

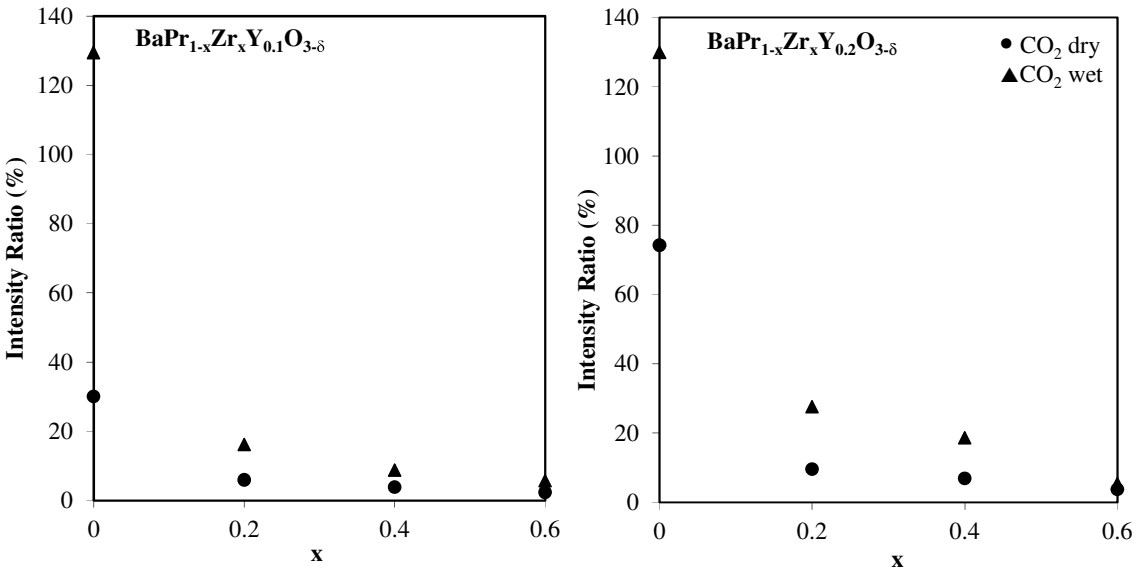

Fig. 6.9. The X-ray diffraction intensity ratio between the most intense (111) reflection of the $BaCO_3$ phase and the most intense (110) reflection in the perovskite phase for samples carbonated at 600 ºC for 12 hours in wet and dry atmospheres for the systems $Ba(Pr_{1-x}Zr_x)_{0.9}Y_{0.1}O_{3-\delta}$ and $Ba(Pr_{1-x}Zr_x)_{0.8}Y_{0.2}O_{3-\delta}$, corresponding to the first stage carbonation.

6.3.4. STABILITY IN WET COMPARED TO DRY CONDITIONS

Both systems show higher stabilities in dry than in wet conditions (Fig. 6.3, Fig. 6.4, Fig. 6.5 and Fig. 6.9.). Water has been suggested to have a reducing effect in $BaPrO_3$, and to lead to hydration of Ba^{2+} and Pr^{4+} to form $Ba(OH)_2$ and $Pr(OH)_3$ [209,212]:

$$BaPrO_3 + 2.5\ H_2O \rightarrow Pr(OH)_3 + Ba(OH)_2 + 0.5\ O_2 \qquad (6.4)$$

The reduction of Pr will lead to substantial increases in average B-site cation radius; hence, complete or partial decomposition may be considered likely to occur in wet reducing atmospheres in the studied materials.

6.4. CONCLUDING REMARKS

The mechanochemical preparation of $Ba(Pr,Zr,Y)O_{3-\delta}$ based materials proved to be efficient in preparation of novel materials, which cannot be formed by conventional solid state synthesis. Furthermore, detailed structural analysis of $Ba(Pr_{1-x}Zr_x)_{1-y}Y_yO_{3-\delta}$ materials allowed to stablish a strong dependence of unit cell volume and lattice distortion on composition in accord with variations in the tolerance factor, and their role in chemical stability. Close correlations between the stability under different atmospheres and the tolerance factor were found. Stability ranges of the perovskite phase showed to be significantly lower in wet CO_2 or wet H_2 than for the corresponding dry atmospheres.

Thus, this work has highlighted the importance of the Goldschmidt tolerance factor on the stability of perovskite materials allowing guidelines for further research for the design and characterization of novel related compositions.

7. PHASE FORMATION, STRUCTURAL AND ELECTRICAL PROPERTIES OF $BaPr_{1-x}Zr_xO_{3-\delta}$ MATERIALS

In the previous chapter, a detailed structural and chemical stability study was performed for the system $Ba(Pr,Zr,Y)O_{3-\delta}$, due to their potential applications as single phase mixed protonic and electronic conductors. More recent studies carried out by Fabbri et al. [216–218] on $BaPr_{0.8-x}Zr_xY_{0.2}O_{3-\delta}$ systems reveal that compositions with intermediate composition Pr/Zr contents exhibit reasonable levels of mixed ionic-electronic conductivity, however still too low for application as a single-phase conductor in SOFC. However, as a composite cathode with the p-type electronic conductor $La_{0.6}Sr_{0.4}Co_{0.2}Fe_{0.8}O_{3-\delta}$, the phase $BaZr_{0.5}Pr_{0.3}Y_{0.2}O_{3-\delta}$ showed good performance [217].

As potential cathode components and as mixed conductors for other high-temperature applications such as hydrogen-separation membranes, little is still known about the transport and structural properties of the Pr-doped $BaZrO_3$ system. One may expect that in the $BaPr_{1-x}Zr_xO_{3-\delta}$ system the mixed valence state of praseodymium, besides favouring the appearance of electronic conductivity, would also act as the required acceptor dopant to create oxygen vacancies needed for proton conduction. In this context, the role of Pr substitution in $BaZrO_3$ on solid-solution formation through a mechanosynthesis route was analysed from the structural characterization via Raman spectroscopy and Rietveld refinement of X-ray diffraction data, coupled with the study of defect chemistry, its relation to conductivity in oxidising conditions with a view to optimising composition for employment in composite PCFC cathodes.

7.1. PHASE FORMATION

On high energy milling of $BaZr_{1-x}Pr_xO_{3-\delta}$ compositions, a single perovskite phase is obtained for composition $x = 0.80$, whereas a mixture of the perovskite phase and praseodymium oxide is observed for the remaining compositions (Fig. 7.1).

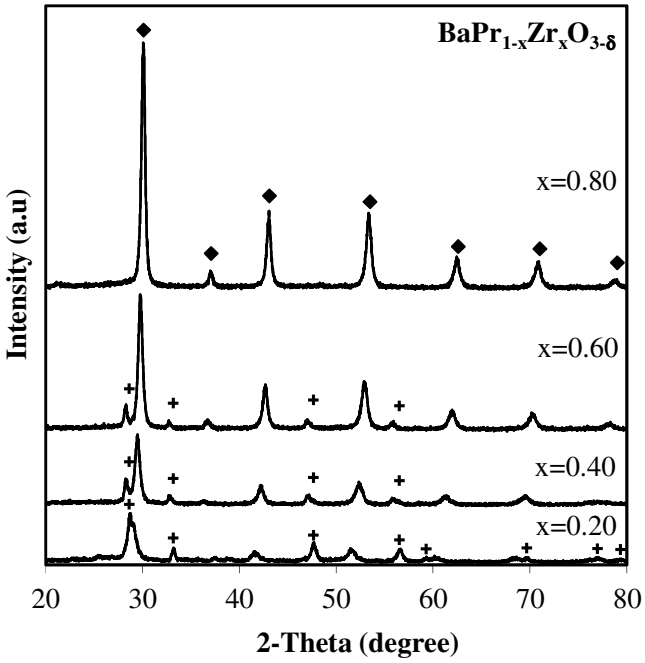

Fig. 7.1. X-ray diffraction patterns of $Ba(Pr_{1-x}Zr_x)_{0.8}Y_{0.2}O_{3-\delta}$ ($0.20 \leq x \leq 0.80$) after high energy milling. The markers identify: (+) PrO_2; and (◆) perovskite phase.

Analysis of the evolution of the mechanochemical reaction of $BaPr_{0.20}Zr_{0.80}O_{3-\delta}$ with time, Fig. 7.2, shows amorphisation of the oxide precursors and formation of perovskite phase during the initial stages of high energy milling (60 minutes). Further milling leads to a substantial increase in the perovskite reflection intensity and concomitant decrease of the praseodymium oxide reflection intensity due to the gradual incorporation of Pr in the perovskite structure. Note the retention of Pr in +4 oxidation state during high energy milling, through formation of PrO_2.

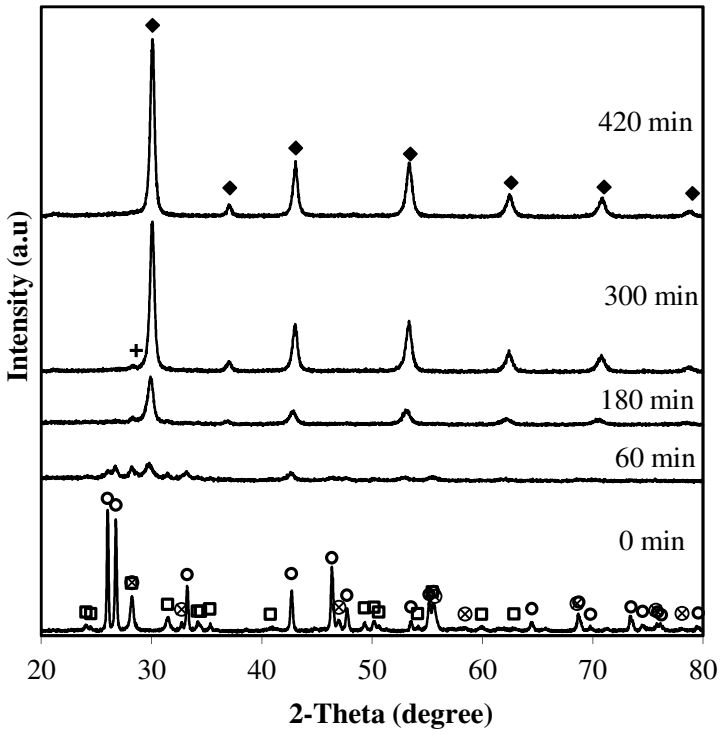

Fig. 7.2. Evolution of powder X-ray diffraction patterns with milling time for composition $BaPr_{0.20}Zr_{0.80}O_{3-\delta}$. The markers identify: (○) barium peroxide; (□) zirconia oxide; (⊗) Pr_6O_{11}; (+) PrO_2; and (◆) perovskite phase.

Although a high energy milling is insufficient to form monophasic perovskite for compositions with $x < 0.80$, single phase materials can be obtained by a two-step process of mechanical activation followed by annealing at 1250 ºC in air, Fig. 7.3.

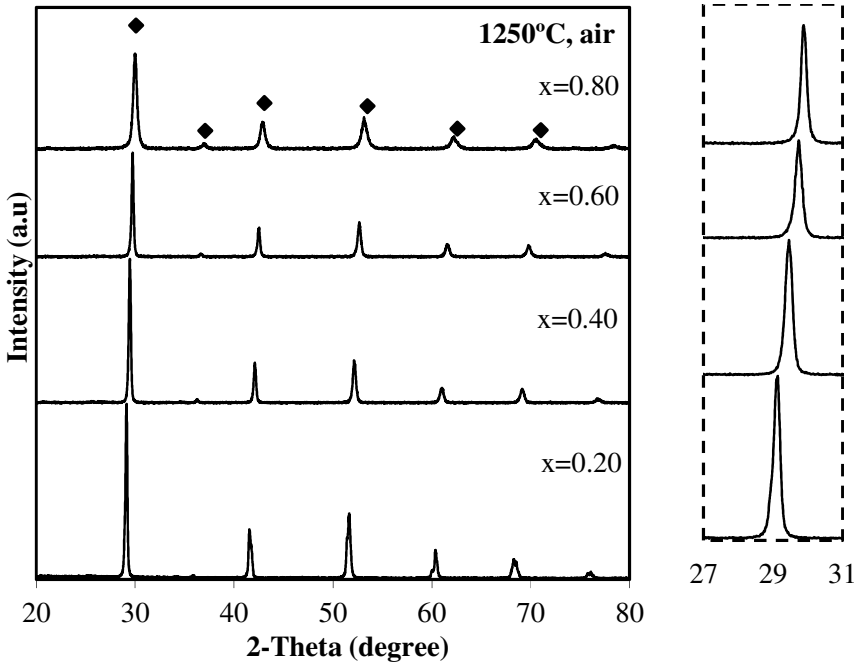

Fig. 7.3. X-ray diffraction patterns of mechanically produced powders of compositions $BaPr_{1-x}Zr_xO_{3-\delta}$ ($0.2 \leq x \leq 0.8$), after annealing 1250 ºC in air. (◆) identifies perovskite phase.

7.2. STRUCTURAL CHARACTERIZATION

The analysis of the structures in the $BaPr_{1-x}Zr_xO_{3-\delta}$ system, $0 \leq x \leq 1$, was performed by Rietveld refinement of laboratory X-ray data and Raman spectroscopy. Structural changes throughout the series would be expected, due to the differing symmetries of the end-members. Cubic $BaZrO_3$ (space group $Pm\bar{3}m$, tilt sequence $a^0a^0a^0$ in Glazer notation [77] and orthorhombic $BaPrO_3$ (*Pnma*, $a^+b^-b^-$) phases have been resolved by high-resolution X-ray [219] and neutron diffraction [86], respectively.

Raman spectroscopy was performed with the aim to obtain information of potential structural changes with composition, (e.g. changes on space group), at a higher resolution than possible by X-ray diffraction analysis. Room temperature unpolarized Raman spectra of $BaPr_{1-x}Zr_xO_{3-\delta}$ samples ($0 \leq x \leq 1$) are shown in Fig. 7.4, where the end-member phases ($BaPrO_3$ and $BaZrO_3$) correspond to materials prepared under the same conditions.

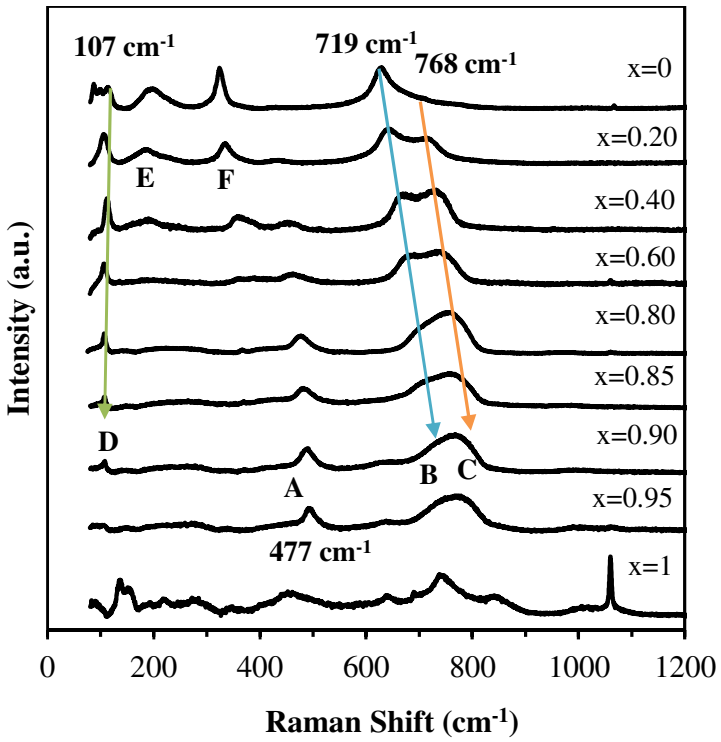

Fig. 7.4. Room temperature Raman spectra of polycrystalline $BaPr_{1-x}Zr_xO_{3-\delta}$ samples ($0 \leq x \leq 1$).

Experimental results show considerable changes in the Raman spectra by zirconium substitution. One observes the deviation of bands to higher values of Raman shift, with increasing of Zr content (bands B and C), as well as the attenuation of bands (bands E and F) and appearance of another band (band A).

The modifications occurring in the regions 400 - 500 cm^{-1} and 700 - 900 cm^{-1}, corresponding to the bands A, B and C, are associated with the vibrational modes on the B-O octahedra [220,221]. The deviation to higher wavenumber with increasing Zr content is compatible with the substitution of the Pr cation by the lighter Zr cation.

The peak position of the narrowest Raman line at 107 cm^{-1} (B) is, within experimental accuracy, independent of the Zr content, even though its relative intensity decreases significantly with Zr content; this mode is attributable to long-range interactions of the

A-cation sublattice, which indicates that the presence of Pr on the A-site should be residual [220,221].

The presence of carbonates, identified by the presence of a band over 1000 cm^{-1} [222], is evident in several spectra, resulting from reaction with CO_2 in the atmosphere. This band is most evident in the $BaZrO_3$ spectrum, due to the low relative intensity of further bands in the Raman spectra for this composition. Note the Raman spectrum of $BaZrO_3$ would not be expected to present Raman active modes as this composition is associated to a cubic symmetry. Nonethless, the existence of some distortion on octahedra ZrO_6 [223], in addition to the presence of carbonates, may explain the spectrum obtained.

The exact determination of space group from the Raman results is complicated by the presence of broad bands, which hampers the fitting of experimental data, and the secondary phase of carbonate, which affects the number of active modes observed. Despite these limitations, analysis of the Raman spectra allows the qualitative identification of structural changes across the series, allowing estimation of most probable symmetries.

The characterization of the three most intense bands in compositions with higher zirconium content (A, B and C), and their variations with composition, may assist the observation of symmetry changes. Fig. 7.5 presents Raman shift and Full Width at Half Maximum (FWHM) for these bands.

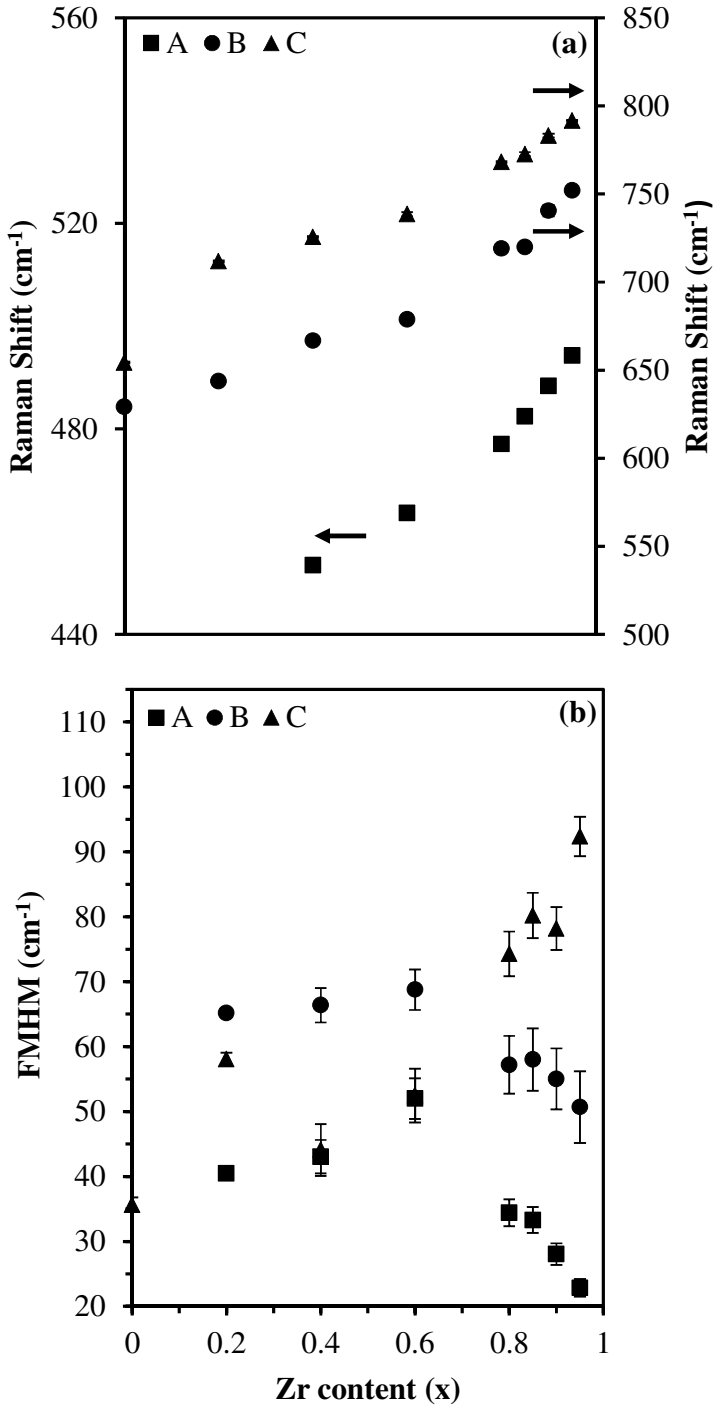

Fig. 7.5. (a) Raman shift and **(b)** FWHM of bands A, B, C, marked at Fig. 7.4, as function of Zr content for $BaPr_{1-x}Zr_xO_{3-\delta}$.

In compositions with Zr contents lower than $x = 0.80$, the Raman shift of bands A, B and C are shown to increase with increasing Zr content, as does the parameter FWHM. At the lowest Zr contents the appearance of bands (E and F) in Fig. 7.4, coincides with the absence of band A and the fusion of bands B and C, in composition $BaPrO_{3-\delta}$. Fig. 7.5. At extended Zr contents, above $x = 0.80$, a sharp increase in the linear dependence of Raman shift to higher wavenumber is observed with increasing Zr content. With respect to the parameter FWHM, one verifies a decrease for the bands A and B with increasing Zr content over the same range of compositions, while band C is observed to continue to increase monotonously. The noted decrease of FWHM in A and B bands at $x > 0.80$ is associated a sudden decrease in disorder in the structure upon Zr substitution of Pr, whereas the FWHM of band C, related to the vibration of atoms in octahedra with both Pr and Zr atoms, appears to rise continuously with Zr content [224].

These results suggest that the structure alters to adopt a different space group around composition $x = 0.80$. Nonetheless, the current results cannot provide information of the exact change of symmetry along the system.

In this context, the Rietveld refinements of the XRD data considered a provisional space group, taking into account the space groups which are known to be or are possibly adopted by the $BaPrO_3$ and $BaZrO_3$ end-member phases as a function of temperature or compositional changes, namely *Imma*, *I4/mcm*, P4/mbm and $R\bar{3}c$ [80,86,219,225].

The refinements converged successfully in $R\bar{3}c$ for all series members, while the other attempted space groups generally gave higher agreement factors, unrealistic thermal factors and/or did not converge successfully. Interestingly, however, all series members refined successfully in $Pm\bar{3}m$ with only slightly higher agreement factors than for $R\bar{3}c$ which supports the premise that the distortions from cubic symmetry are slight. Although the refinements proceeded satisfactorily in space group $R\bar{3}c$, marginally negative oxygen thermal factors were obtained for certain compositions. Such a scenario may arise as a result of some compositional or symmetrical inhomogeneities. Given that further structural detail was not accessible under the resolution of X-ray diffraction, the final structural parameters and agreement factors, given

in Table 7.1, were obtained assuming $R\bar{3}c$ as space group; additional structural information including average bond lengths and unit-cell volume are also given.

The results of Raman spectroscopy and XRD here presented, thus, suggest a likely space group change around composition $x = 0.80$ with minor distortions from cubic symmetry. Nonetheless, further work by a more sensitive technique such as neutron diffraction is necessary to conclude the exact space groups of these materials. In this respect a beamtime application has been recently submitted to the "Institut Laue-Langevin" (ILL) on this system to resolve this issue.

Table 7.1. Structural parameters, agreement factors and additional structural information for $BaPr_{1-x}Zr_xO_{3-\delta}$ obtained from Rietveld refinement of XRD data[a].

x	0.40	0.60	0.80	0.85	0.90	0.95
a /Å	6.0919(5)	6.0417(4)	5.9820(6)	5.96408(3)	5.9539(8)	5.940(1)
c /Å	14.866(3)	14.740(2)	14.630(3)	14.6098(6)	14.570(4)	14.541(5)
O x	0.557(2)	0.545(3)	0.541(2)	0.527(3)	0.538(2)	0.517(5)
R_p / %	4.46	4.41	4.21	3.80	4.10	3.68
R_{wp} / %	5.76	5.66	5.42	4.90	5.38	4.81
R_B / %	2.99	3.40	4.09	2.27	3.12	2.04
Ave. A–O /Å	3.1195	3.023(3)	2.994(2)	2.984(3)	2.980(2)	2.970(5)
Ave. B–O / Å	2.179(3)	2.150(4)	2.128(3)	2.115(4)	2.116(3)	2.102(7)
Vol. / Å^3	477.8(1)	465.95(8)	453.4(1)	450.05(2)	447.3(1)	444.3(2)

[a] Space group $R\bar{3}c$ (#167, hexagonal axes): A position 6a (0 0 ¼); B position 6b (0 0 0); O position 18e (x 0 ¼).

The reduced cell (pseudo-cubic) lattice parameters of the title system as a function of composition are shown in Fig.7.6. The monotonous Vegard's decrease in cell parameter with *x* is consistent with substitution of the larger Pr_{VI}^{4+} cation (0.85Å, [97]) by the smaller Zr_{VI}^{4+} cation (0.72 Å, [97]).

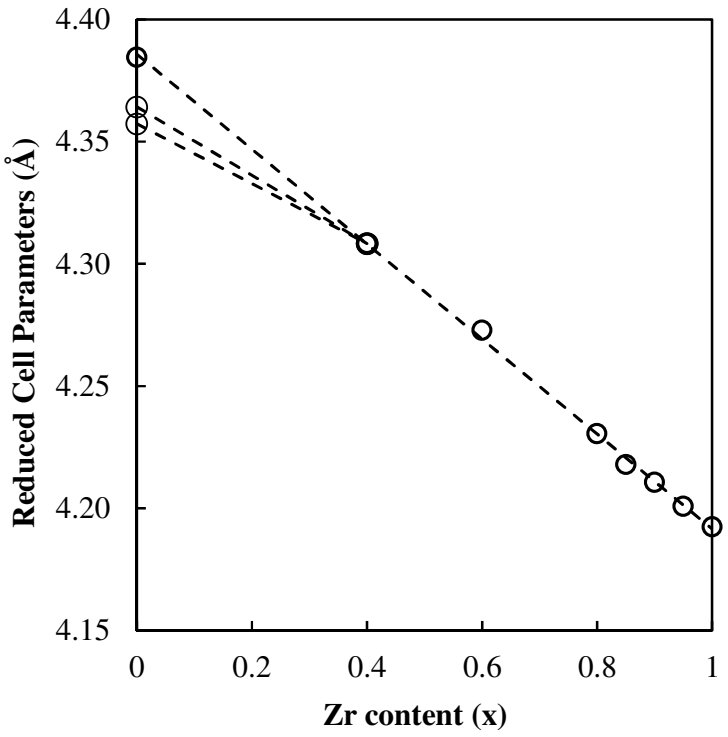

Fig.7.6. Reduced (pseudo-cubic) unit-cell parameter as a function of *x* for $BaPr_{1-x}Zr_xO_{3-\delta}$. Data for the end-member phase $BaPrO_3$ (*Pnma*) are taken from ref. [86].

7.3. ELECTRICAL PROPERTIES

For compositions $BaPr_{1-x}Zr_xO_{3-\delta}$ one expects dependence of concentrations of oxygen vacancies, protonic species or electron holes provided by redox changes of the variable valent Pr-cation (Pr^{n+} with n = 3, 4) in accordance with following competitive defect relations:

$$2\,Pr_{Pr}^{\times} + O_O^{\times} \underset{\leftarrow}{\overset{K_{red}}{\rightleftharpoons}} 2\,Pr_{Pr}^{/} + V_O^{\bullet\bullet} + \frac{1}{2}O_2\,(g) \qquad (7.1)$$

and hydration of oxygen vacancies to create protonic species:

$$H_2O\,(g) + V_O^{\bullet\bullet} + O_O^{\times} \underset{\leftarrow}{\overset{K_{hyd}}{\rightleftharpoons}} 2\,OH_O^{\bullet} \qquad (7.2)$$

The prevailing mechanism of charge compensation for trivalent Pr^{3+}, thus, depends on the combination of mass action constants of reaction (7.1) and (7.2). The temperature dependencies of the total conductivities for the $BaPr_{1-x}Zr_xO_{3-\delta}$ series in dry N_2 and O_2 are shown in Fig. 7.7.

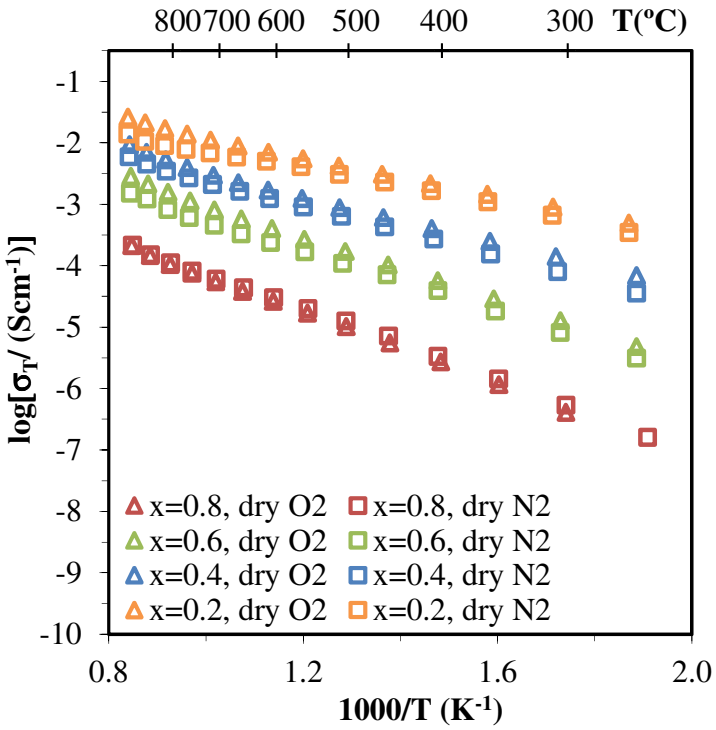

Fig. 7.7. The temperature dependence of total conductivity in dry O_2 (△) and dry N_2 (□) atmospheres of compositions $BaPr_{1-x}Zr_xO_{3-\delta}$, with x = 0.20, 0.40, 0.60 and 0.80.

In previous literature predominant-electronic conductivity has been suggested for $BaPrO_{3-\delta}$ based compositions [86], implying a low concentration of oxygen vacancies, combined with a lower mobility of oxygen vacancies in comparison to electronic carriers.

Fig. 7.7 shows that the effect of substituting Pr with Zr is to decrease the conductivity in dry conditions by over two orders of magnitude. This result can be expected, due to a lower concentration of electronic species when the multivalent Pr is partially replaced by Zr^{4+}. Samples with higher contents of Pr ($x < 0.80$) show an enhanced conductivity in dry O_2 when compared to dry N_2 in the whole range of temperature, suggesting a predominantly p-type contribution to the overall electrical transport [86,210]. A different behaviour is observed for the sample with the lower content of Pr ($x = 0.80$), which presents a very similar conductivity under dry conditions of O_2 and N_2. This may be tentatively ascribed to a high stabilization of Pr^{4+} in this composition to its small average B-site ionic radius and an electronic contribution

derived from a fixed concentration of carriers. Comparison of the total conductivity as a function of temperature at dry and wet conditions, in O_2 and N_2 atmospheres are presented in Fig. 7.8 (a) and (b), respectively.

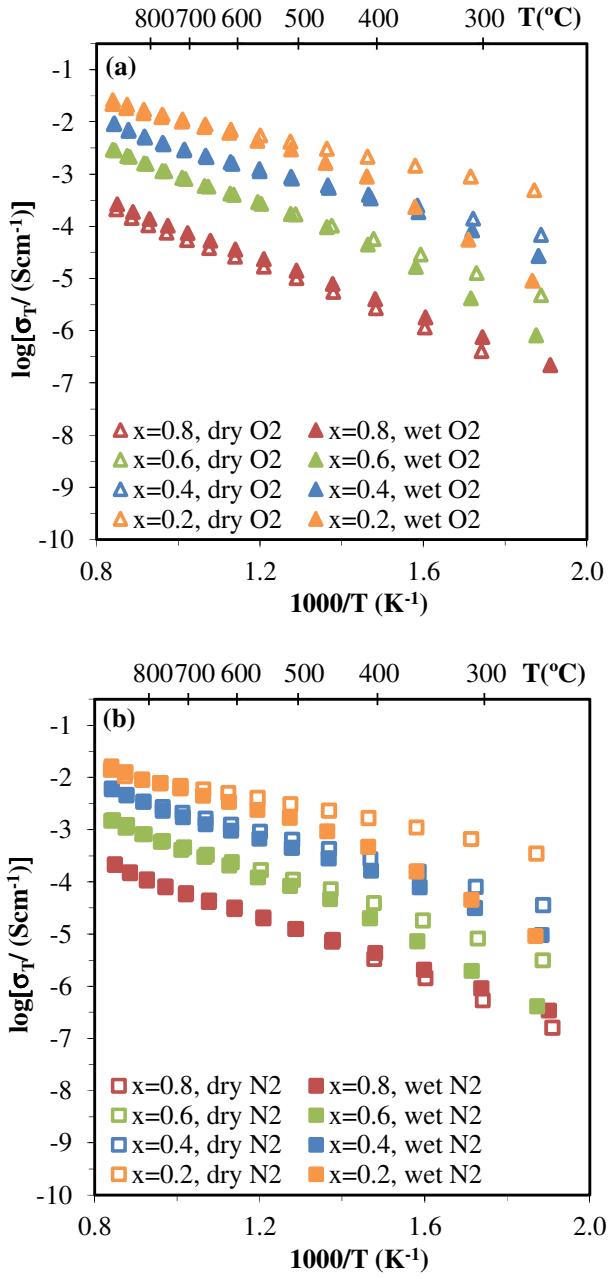

Fig. 7.8. The temperature dependence of total conductivity of compositions $BaPr_{1-x}Zr_xO_{3-\delta}$ in **(a)** dry and wet O_2 atmosphere; and **(b)** dry and wet N_2 atmosphere. Open symbols correspond to dry conditions, and filled symbol to wet conditions.

For compositions of higher Pr content ($x < 0.80$), enhanced conductivities are shown in dry conditions with respect to the moistened atmosphere, in the temperature range of ~250 - 600 ºC in both O_2 and N_2. Moreover, the greatest increase in transport between dry and wet conditions is recorded for the Pr-rich composition $x = 0.20$. This trend is likely to reflect a lowering of p-type electronic conductivity under wet conditions, as it is derived from a lower concentration of holes as the water partial pressure increases, reaction (7.3):

$$\frac{1}{2}H_2O(g) + h^{\bullet} + O_O^{\times} \rightleftharpoons OH_O^{\bullet} + \frac{1}{4}O_2(g) \qquad (7.3)$$

At higher temperature, the conductivities in wet and dry conditions of the same carrier gas converge, most probably as a result of exothermic loss of protonic species in wet conditions; hence, at high temperatures a similar contribution from p-type carriers is expected in both wet and dry atmospheres. In contrast, for the Zr-rich composition ($x = 0.80$), the conductivity is does not show such marked differences between wet and dry conditions with the conductivity being effectively similar for all conditions. This observation may again possibly reflect an increased stability of Pr^{4+} in this composition and a corresponding lack of oxygen vacancies that can be hydrated.

The activation energy, in wet and dry conditions, increases with the increase of x, Table 7.2.

Table 7.2. Activation energy of electrical conductivity in $BaPr_{1-x}Zr_xO_{3-\delta}$ as a function of Zr concentration, in O_2 and N_2 atmospheres, at 500 – 1000 ºC

E_a (eV) / x	Dry		Wet	
	O_2	N_2	O_2	N_2
0.20	0.39 ± 0.01	0.36 ± 0.02	0.47 ± 0.01	0.52 ± 0.01
0.40	0.46 ± 0.01	0.47 ± 0.01	0.50 ± 0.02	0.59 ± 0.01
0.60	0.58 ± 0.01	0.56 ± 0.01	0.63 ± 0.01	0.66 ± 0.01
0.80	0.65 ± 0.02	0.64 ± 0.01	0.78 ± 0.01	0.62 ± 0.02

This behaviour contrasts with related materials $BaPr_{1-x}Yb_xO_{3-\delta}$ [207], which reported independency between the dopant concentration and activation energy for the total conductivity, despites the increase of conductivity with the dopant concentration.

Current results of activation energy and conductivity suggest possible changes in the nature and/or the mobility of electronic species with composition, especially with respect the composition of high zirconium content $x = 0.80$. These variations may be related to the small average B-site ionic radius for this composition, which would be unfavourable for Pr^{3+} formation, and the associated structural changes at this composition highlighted by Raman Spectroscopy in Section 7.2.

7.4. CONCLUDING REMARKS

The $BaPr_{1-x}Zr_xO_{3-\delta}$ solid solution has been synthesized by mechanical activation followed by high-temperature annealing. The system crystallizes with a slightly distorted perovskite structure with no phase transformations exhibited with composition throughout the series under the resolution of XRD. On the contrary, Raman spectroscopy reveals subtle differences between the compositions with a possible structural change at the Zr rich composition $x = 0.80$, highlighting the need for further investigation by a technique offering higher resolution such as Neutron Diffraction.

The effect of substituting Zr for Pr is to substantially increase the electronic conductivity for samples with higher contents of Pr. However, the Zr-rich end member ($x = 0.80$) shows an apparent modification of the electrical behaviour, with low dependence on the oxygen partial pressure and water partial pressure. Such variation of electrical behaviour in this composition can, thus, potentially be linked with the suggestion of structural changes for this composition noted by Raman spectroscopy. Although the system presents moderate values of electronic conductivity, potentially useful properties can be maintained at intermediate temperatures, such as weak dependences of transport properties on changing from oxidizing to reducing conditions.

8. FURTHER CONSIDERATIONS

The work of this thesis highlighted that phase formation of $BaZrO_3$–based materials by mechanosynthesis was highly dependent on precursor choice. Moreover, thermodynamic considerations were shown to provide vital information for this selection. Mechanosynthesised materials were proven to offer high levels of homogeneity, exceeding that obtainable by traditional solid state routes, while compositional accuracy and phase homogeneity were also shown to be vital criteria that had strong impacts on resultant conduction behaviour.

The tailoring of the yttrium containing $Ba(Zr,Pr,Y)O_{3-\delta}$ analogues was designed taking into account the Goldschmidt's tolerance factor. Based on this research, strong dependences of unit cell volume and lattice distortion were found with variations in the tolerance factor, as well as close correlations with stability. The development of novel $Ba(Zr,Pr)O_{3-\delta}$-based materials extended relations between composition, structure and properties. Of these two Pr-containing perovskite systems, only compositions $BaZr_{1-x}Pr_x0_{3-\delta}$ with up to x=0.20 could be directly made by mechanosynthesis from BaO_2 and the relevant oxide precursors, while all compositions from the $Ba(Zr,Pr,Y)O_{3-\delta}$ and $Ba(Zr,Pr)O_{3-\delta}$ series could be formed by combination of mechanical activation and calcination. In this respect, one notes that the composition formable by mechanosynthesis, $BaZr_{0.80}Pr_{0.20}O_{3-\delta}$, possessed the highest tolerance factor of the tested Pr-containing compositions, reinforcing the importance of the perovskite tolerance factor with respect to phase formability. On the other hand, by simply following the Goldschmidt's tolerance factor guideline (*t*), greater stability was expected for the base $Ba(Zr,Pr)O_{3-\delta}$ series as they offer higher tolerance factors in oxidising and reducing conditions in comparison to the $Ba(Zr,Pr,Y)O_{3-\delta}$ system. Nonetheless, this expected stability improvement is not observed for this series in practice.

These results may, therefore, infer that the Goldschmidt's tolerance factor guideline on its own is a necessary, but insufficient condition for the design of new materials. In this context, future work can be based on the adoption of several additional guidelines to assist the refinement of compositional design.

Beyond the tolerance factor, the octahedral factor has also been referred to as a relevant criterion for assessment of the formability and stability of perovskites. The octahedral factor is defined as the ionic ratio of r_B/r_O, which r_B and r_O are the ionic radii of the B-site and the oxide-ions that form the octahedra of the perovskite structure ABO_3, respectively. In general, the octahedral factor should be vary within the limited range 0.414 - 0.732 [226] in stable perovskites.

Several works [227–230] have used both tolerance and octahedral factors to build a two-dimensional structure map to predict the formability of perovskite-oxides, based on empirical information of formability of perovskite structure provided in the literature. Besides similar strategies adopted in different literature works, slight variations in the suggested limits of the perovskite phase are noted between the different authors. Nonetheless, using the information of formability of collected data in the different works [227–230] and the tolerance and octahedral factors calculated from radii of A- and B-cation for twelve and six-coordination number, respectively, [97] the following structural map was built Fig. 8.1 to best express the limits of the perovskite phase. The criterion of perovskite formability can be expressed by the following equations:

$$t \leq 1.08 \tag{8.1}$$

$$0.286 \leq \frac{r_B}{r_O} \leq 0.680 \tag{8.2}$$

$$\frac{r_B}{r_O} = -1.556\, t + 1.920 \tag{8.3}$$

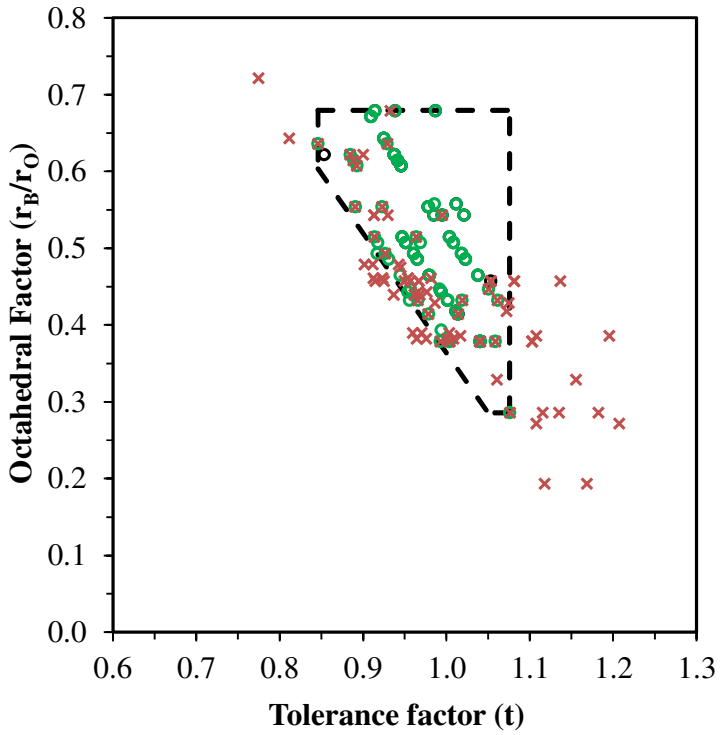

Fig. 8.1. Structure maps plotted by the tolerance and octahedral factors. Circles represent the perovskite structure and crosses the non-perovskite structure of $A^{2+}B^{4+}O_3$-type compounds, according to the collected data in the literature [227–230].

For instance, *ab initio* prediction of the formability of complex perovskites $BaPr_{1-x}M_xO_{3-\delta}$ (M = Zr, Ti, Ce), for different x values ($x = 0.20$, 0.40, 0.60 and 0.80) by plotting the correspondent tolerance and octahedral factors on the structural map (Fig. 8.2), indicates formability of perovskite for all three systems.

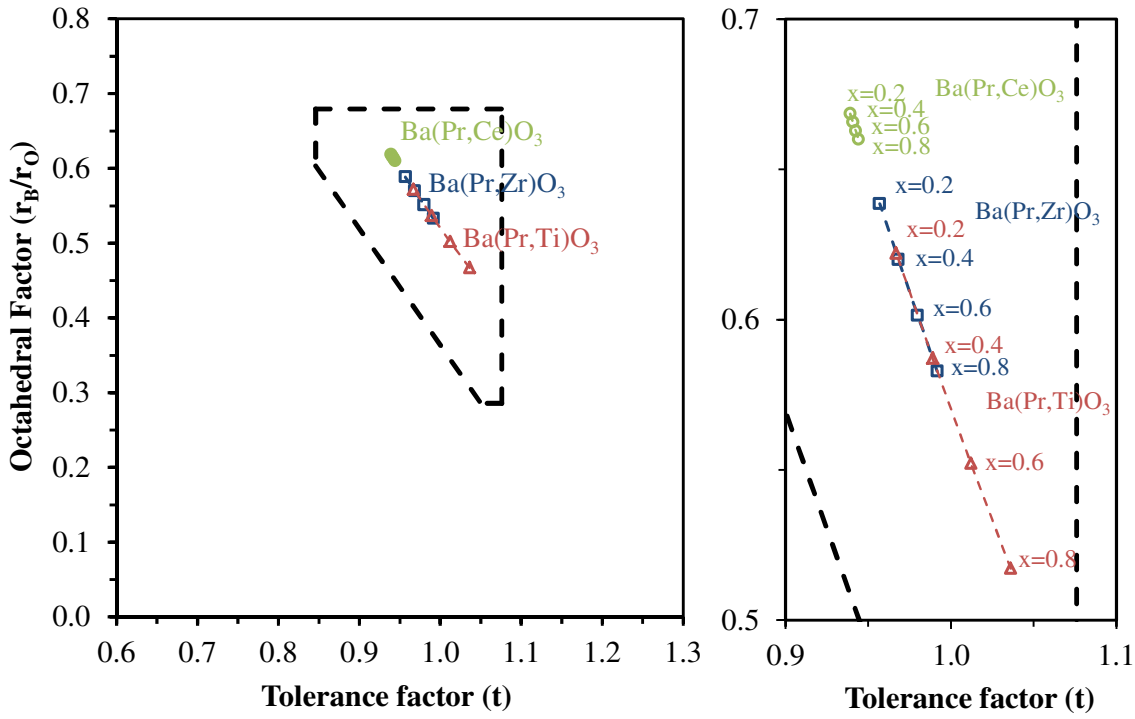

Fig. 8.2. Structure maps plotted by the tolerance and octahedral factors with data of $Ba(Pr,M)O_3$ compositions, with x = 0, 0.20, 0.40, 0.60 and 0.80, zoom image on the right.

In this context, preliminary results of phase formation by mechanochemical preparation and thermal stability of $BaPr_{1-x}M_xO_{3-\delta}$ (M = Zr, Ti, Ce) were performed.

The $BaPr_{1-x}Ti_xO_{3-\delta}$ system presents comparable behaviour during the milling process relative to the system $BaPr_{1-x}Zr_xO_{3-\delta}$, shown in the previous chapter (Fig.7.1 and Fig.7.2). Sequential XRD patterns during milling reveal a significant decrease in peak intensity of the precursors and the onset of perovskite phase formation with the additional appearance of a secondary phase of PrO_2. Further milling leads to an increased intensity of the perovskite reflections, more relevant for the composition with lower Pr content (x = 0.80), with no relevant additional crystallographic changes after 600 minutes of milling (Fig. 8.3). Fig. 8.4 compares the XRD patterns obtained after 600 minutes high energy milling for the $BaPr_{1-x}Ti_xO_{3-\delta}$ system ($0.20 \leq x \leq 0.80$), showing that only the x = 0.80 composition can attain a single perovskite phase by the mechanical method.

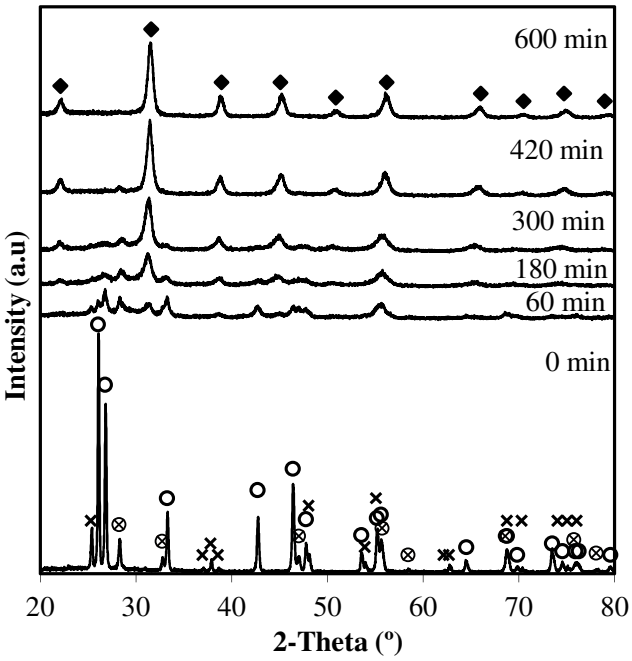

Fig. 8.3. Evolution of powder X-ray diffraction patterns with milling time for composition $BaPr_{0.20}Ti_{0.80}O_{3-\delta}$. The markers identify: (○) barium peroxide; (×) TiO_2; (⊗) Pr_6O_{11}; and (◆) perovskite phase.

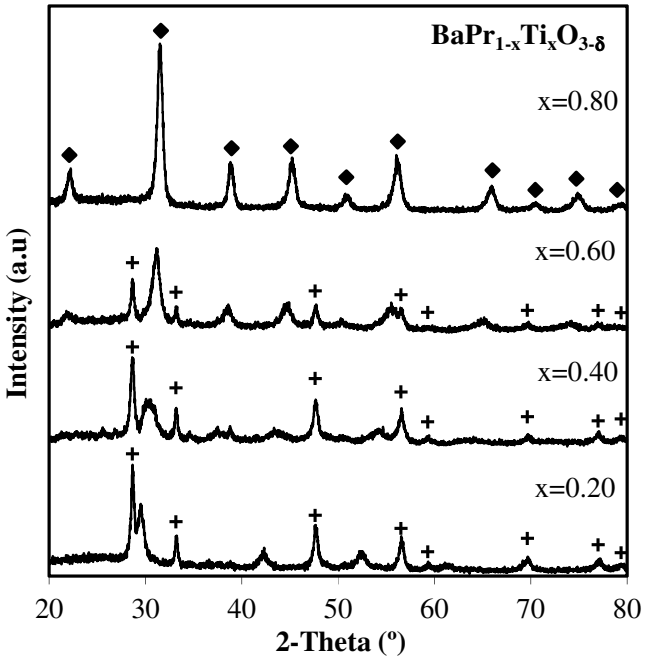

Fig. 8.4. X-ray diffraction pattern of the $BaPr_{1-x}Ti_xO_{3-\delta}$ ($0.20 \leq x \leq 0.80$) after high energy milling. The markers identify: (+) PrO_2; and (◆) perovskite phase.

In contrast, high energy milling of $BaPr_{1-x}Ce_xO_{3-\delta}$ system, leads an amorphisation of precursors, with formation of only small amount of crystalline perovskite phase, across all the tested range of Ce-content (Fig. 8.5).

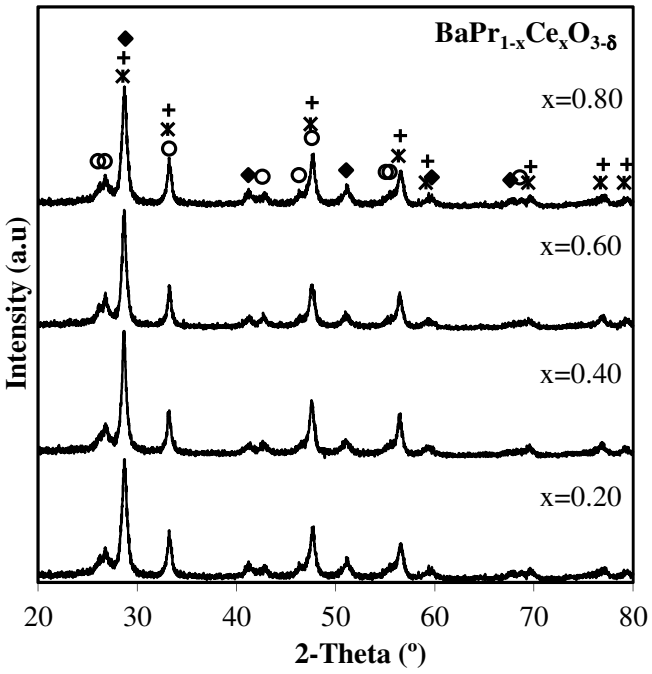

Fig. 8.5. X-ray diffraction patterns of the $BaPr_{1-x}Ce_xO_{3-\delta}$ ($0.20 \leq x \leq 0.80$) after high energy milling. The markers identify: (○) barium peroxide; (∗) cerium oxide; (+) PrO_2; and (◆) perovskite phase.

As stated, thermodynamic analysis can provide useful guidelines for predicting the success of mechanosynthesis at room temperature. In this respect, to estimate the likelihood for formability in the current systems, chemical-potential diagrams, Fig. 8.6, were calculated for the base systems TiO_2-BaO-O_2, ZrO_2-BaO-O_2 and CeO_2-BaO-O_2, according to the methodology described in the Appendix 1.

The chemical potential diagrams provide information on phase stability fields and on the thermodynamic driving force for synthesis. The chemical potential ratio shown in Fig.8.6 (a), for the system ZrO_2-BaO-O_2, combines the gradients of chemical potentials of both oxide components according to the relation:

$$RT\Delta\ln\left(\frac{a_{BaO}}{a_{ZrO_2}}\right) = RT\ \Delta\ln\left(a_{BaO}\right) - RT\ \Delta\ln\left(a_{ZrO_2}\right) \qquad (8.4)$$
$$= \Delta\mu_{\mathrm{BaO}} - \Delta\mu_{\mathrm{ZrO_2}}$$

where the chemical potential difference can be related to the thermodynamic driving force for synthesis. Similar relations can the established for the systems TiO_2-BaO-O_2 and CeO_2-BaO-O_2.

The chemical-potential diagrams of Fig. 8.6, predict the co-existence of perovskite phase with the precursor oxides, at high energy milling conditions. The magnitudes of the chemical-potential differences in the three systems, under such conditions, are shown to decrease in the order TiO_2-BaO-O_2 >> ZrO_2-BaO-O_2 > CeO_2-BaO-O_2. However, such decrease is noted to be only slight between the latter two systems. From a thermodynamic perspective one may, therefore, expect the formation of perovskite phase by high-energy milling for all systems, especially as Chapter 3 demonstrated that mechanosynthesis of $BaZrO_3$ was viable. One cannot, therefore, confidently relate the different behaviour of phase formation upon high energy milling of barium zirconate, barium titanate and barium cerate related systems in the current case, to the only slightly lower thermodynamic driving force for formation of barium cerate. In contrast, discussion must be extended to include further considerations.

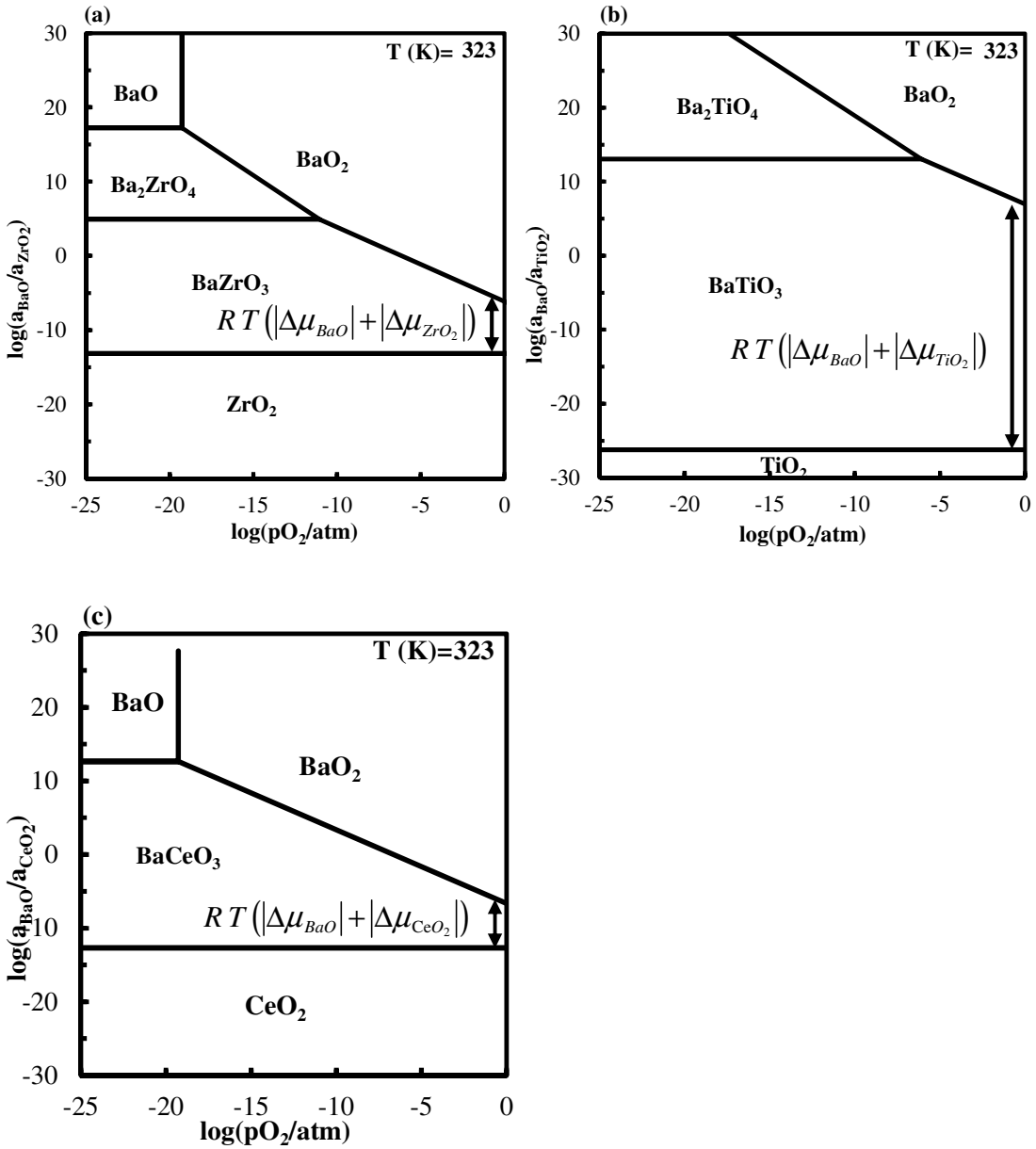

Fig. 8.6. Chemical potential diagrams describing conditions for synthesis of **(a)** barium zirconate; **(b)** barium titanate; and **(c)** barium cerate from precursors oxides BaO_2 and *m*-ZrO_2, TiO_2 (anatase) and CeO_2, respectively, at 323 K and versus oxygen partial pressure.

Another important factor may be the amorphisation of precursors. Rietveld analysis of the XRD patterns, shows the weight fraction of amorphous phase estimated in $BaPr_{0.20}Ti_{0.80}O_{3-\delta}$ to be high, 52 ± 2 % (w/w). TEM images of milled powders of $BaPr_{0.20}Ti_{0.80}O_{3-\delta}$ reinforce this conclusion, revealing the presence of crystalline phases dispersed in an amorphous matrix.

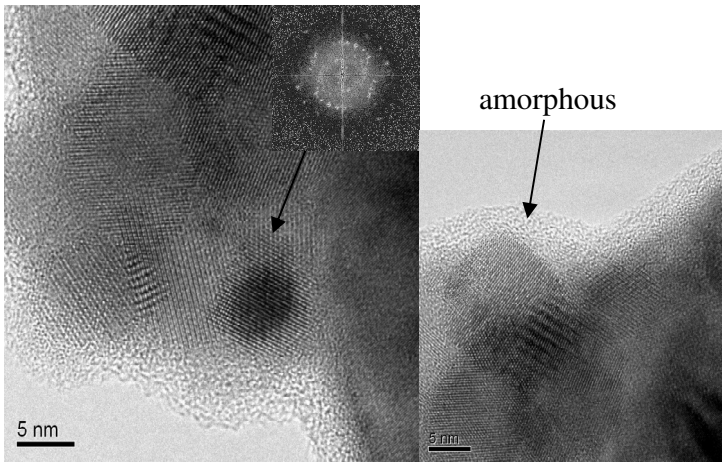

Fig. 8.7. TEM images collected for powder samples of $BaPr_{0.20}Ti_{0.80}O_{3-\delta}$ after high energy milling, revealing the presence of amorphous phase.

These observations suggest that the achievement of a pure perovskite phase by XRD after high energy milling may not reflect the expected chemical composition, as a significant quantity of amorphous phase may be present in the mechanochemically prepared powders. Hence, a heat treatment was performed on the mechanically prepared powders to assess the phase formation.

Similar to that reported for $BaPr_{1-x}Zr_xO_{3-\delta}$, formation, the perovskite phase was obtained for $BaPr_{1-x}Ce_xO_{3-\delta}$ for $x = 0.20$, 0.40, 0.60 and 0.80, after annealing the mechanochemical activated powders at 1250 ºC, in air (Fig. 8.8).

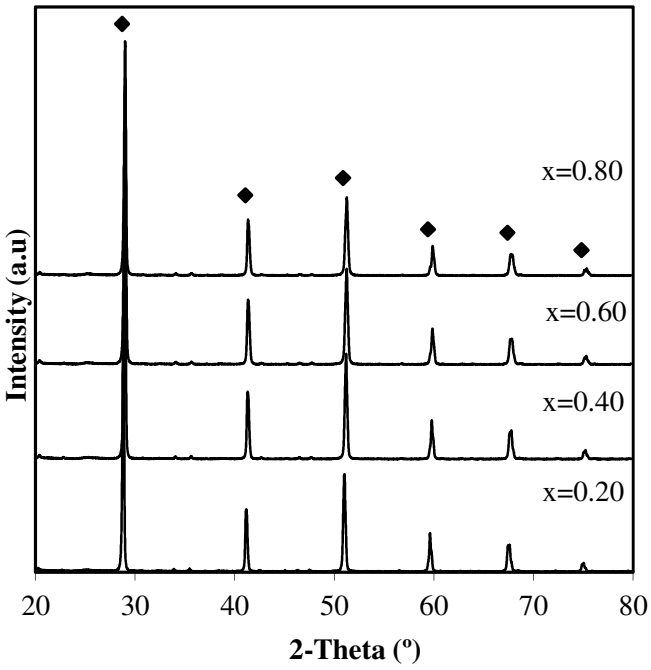

Fig. 8.8. X-ray diffractions patterns of $BaPr_{1-x}Ce_xO_{3-\delta}$, x = 0.20, 0.40, 0.60 and 0.80, prepared by high energy milling with further annealing in air at 1250 ºC,, and after annealing in air at 1250 ºC. The marker (◆) identify the main peaks of $BaCeO_3$.

On the contrary, the mechanically prepared powders of $BaPr_{1-x}Ti_xO_{3-\delta}$ exhibit the formation of secondary phases for all range of compositions upon similar annealing (Fig. 8.9). The presence of secondary phases is more pronounced for compositions $0.40 \leq x \leq 0.80$, while for $x = 0.20$ only small traces of Ba_2TiO_4 are observed after annealing.

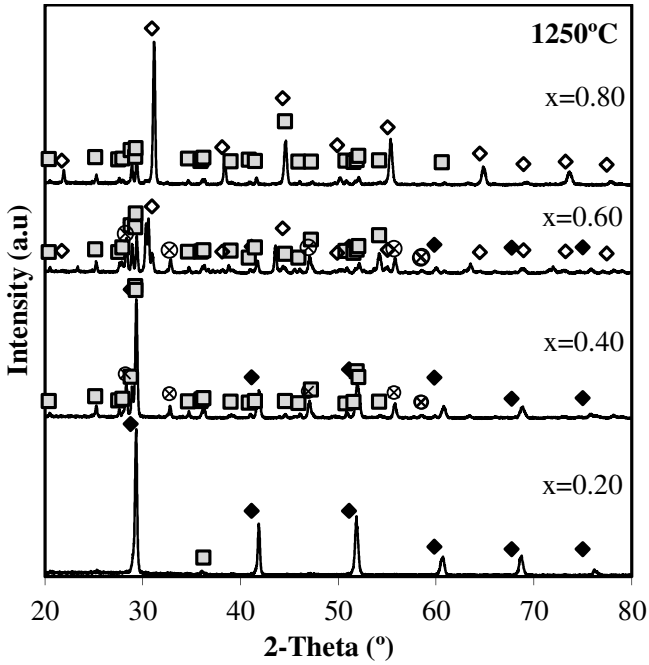

Fig. 8.9. X-ray diffraction patterns of high-milled powders corresponding to $BaPr_{1-x}Ti_xO_{3-\delta}$ compositions (x = 0.20, 0.40, 0.60 and 0.80), after annealing in air, at 1250 ºC. The markers identify: (⊗) Pr_6O_{11}; (▩) Ba_2TiO_4; (◇) $BaPrO_3$; and (◆) $BaTiO_3$.

The X-ray diffraction patterns after annealing at different temperatures (Fig. 8.10) of milled $BaPr_{0.20}Ti_{0.80}O_{3-\delta}$ reveal that further crystallisation of the perovskite phase on heating is accompanied by the formation of minor amounts of $BaCO_3$ at the lowest temperatures and a mixture of $BaCO_3$ and Ba_2TiO_4 at higher temperatures. These impurity phases may result from chemical reaction of amorphisised precursors with atmospheric CO2 or by partial decomposition of the perovskite phase.

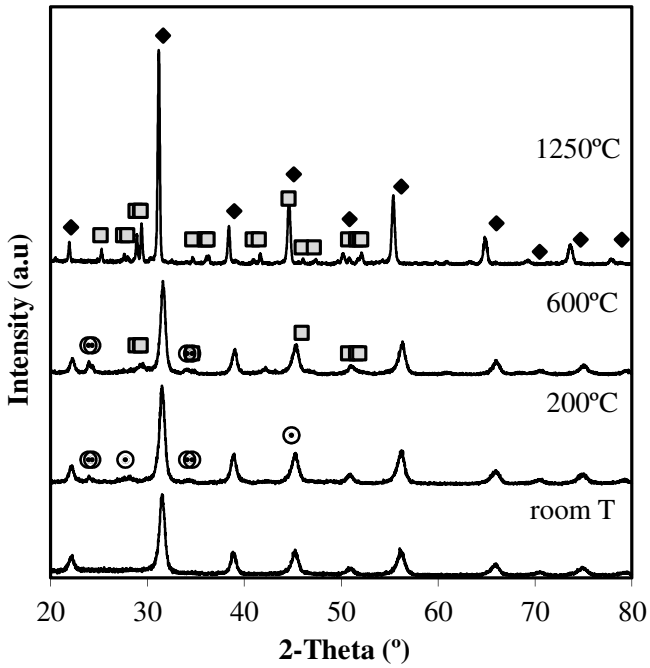

Fig. 8.10. X-ray diffraction powder patterns of $BaPr_{0.20}Ti_{0.80}O_{3-\delta}$ samples at room temperature and after annealing at 200, 600 and 1250 ºC, in air. The markers identify: (▫) Ba_2TiO_4; (⦿) $BaCO_3$; and (◆) perovskite phase.

These preliminary results, therefore, suggest that the prediction of formability of perovskite phase given by structural maps of $BaPr_{1-x}M_xO_{3-\delta}$ (M = Zr, Ti, Ce), coupled with consideration of thermodynamic factors, are tools that fail to allow accurate prediction of phase formation in these systems. For the annealed samples, formability is observed for compositions $0.20 \leq x \leq 0.80$, in the systems with M = Zr and Ce, while for M = Ti the perovskite phase is not formed across the whole composition range.

Besides the tolerance and octahedral factors and the thermodynamic predictions further factors can also be considered, such as, the size mismatch between cations that occupy the same lattice site. Note a possible reason for the different behaviour on phase formation in the different $BaPr_{1-x}M_xO_{3-\delta}$ systems reported could be due to the different size mismatch of the B-cations. In this respect, the high similarity of ionic radii of $_{VI}Ce^{3+}$ (1.01 Å) and $_{VI}Ce^{4+}$ (0.87 Å) with $_{VI}Pr^{3+}$ (0.99 Å) and $_{VI}Pr^{4+}$ (0.85 Å), in contrast with the extremely large size

difference between $_{VI}Ti^{4+}$ and (0.605 Å) and the Pr cation may dominate the potential for phase formation, especially under high temperature annealing where the average oxidation state of praseodymium may be reduced. Such variation of ionic size between site sharing cations can offer a possible explanation why the fact compositions $x = 0.20$ and $x = 0.40$ for $Ba(Pr,Ti)O_{3-\delta}$ and $Ba(Pr,Zr)O_{3-\delta}$, respectively, and for $x = 0.40$ and $x = 0.80$ for the same systems, are nearly coincident in the structural map, but present widely different behaviour with respect to the formability of the perovskite phase.

Table 8.1. Size mismatch, denoted as $(r_M - r_{Pr})/r_{Pr}$ between the dopant Pr and M cations in $BaPr_{1-x}M_xO_{3-\delta}$ sytems (M = Zr^{4+}, Ce^{4+} and Ti^{4+}).

M cation	$\frac{r_M - r_{Pr^{4+}}}{r_{Pr^{4+}}}(\%)$	$\frac{r_M - r_{Pr^{3+}}}{r_{Pr^{3+}}}(\%)$
Zr^{4+}	-15.3	-27.3
Ce^{4+}	2.4	-12.1
Ti^{4+}	-28.8	-38.9

Taking into account these preliminary results, the future work will focus on the combined adoption of these additional guidelines, with multiple variables, to successfully allow predictive design of novel perovskite-based materials.

9. REFERENCES

[1] M. Winter, R.J. Brodd, What are batteries, fuel cells, and supercapacitors?, Chem. Rev. 104 (2004) 4245–4269.

[2] A.B. Stambouli, E. Traversa, Solid oxide fuel cells (SOFCs): A review of an environmentally clean and efficient source of energy, Renew. Sustain. Energy Rev. 6 (2002) 433–455.

[3] L. Carrette, K.A. Friedrich, U. Stimming, Fuel Cells - Fundamentals and Applications, Fuel Cells. 1 (2001) 5–39.

[4] F. Barbir, PEM Fuel Cells, Elsevier, 2005.

[5] I. EG&G Technical Services, Fuel Cell Handbook, 7.ª ed., National Energy Technology Laboratory, Morgantown, 2004.

[6] G. Hoogers, A. Bauen, E. Chen, D. Hart, M. Hinsberger, M. Hogarth, et al., Fuel Cell Technology Handbook, CRC Press, 2003.

[7] J. St-Pierre, D.P. Wilkinson, Fuel cells: A new, efficient and cleaner power source, AIChE J. 47 (2001) 1482–1486.

[8] D. Hart, Sustainable energy conversion: Fuel cells - the competitive option?, J. Power Sources. 86 (2000) 23–27.

[9] S.P.S. Badwal, S. Giddey, C. Munnings, A. Kulkarni, Review of progress in high temperature solid oxide fuel cells, J. Aust. Ceram. Soc. 50 (2014) 23–37.

[10] S.M. Haile, Fuel cell materials and components, Acta Mater. 51 (2003) 5981–6000.

[11] N. Laosiripojana, W. Wiyaratn, W. Kiatkittipong, A. Arpornwichanop, A. Soottitantawat, S. Assabumrungrat, Reviews on solid oxide fuel cell technology, Eng. J. 13 (2009) 65–83.

[12] N. Minh, Solid oxide fuel cell technology - features and applications, Solid State Ionics.

174 (2004) 271–277.

[13] F. Lefebvre-Joud, G. Gauthier, J. Mougin, Current status of proton-conducting solid oxide fuel cells development, J. Appl. Electrochem. 39 (2009) 535–543.

[14] M. Lo Faro, D. La Rosa, V. Antonucci, A.S. Arico, Intermediate temperature solid oxide fuel cell electrolytes, J. Indian Inst. Sci. 89 (2012) 363–380.

[15] Brown, J T, 6. High-temperature solid-oxide fuel cells (SOFCs), Energy. 11 (1986) 209–229.

[16] S.C. Singhal, Recent Progress in Tubular Solid Oxide Fuel Cell Technology, em: Fifth Int. Symp. Solid Oxide Fuel Cells, 1997: p. 18.

[17] S.P.S. Badwal, K. Foger, Solid oxide electrolyte fuel cell review, Ceram. Int. 22 (1996) 257–265.

[18] L. Malavasi, C.A.J. Fisher, M.S. Islam, Oxide-ion and proton conducting electrolyte materials for clean energy applications: structural and mechanistic features., Chem. Soc. Rev. 39 (2010) 4370–4387.

[19] S.J. Skinner, J.A. Kilner, Oxygen ion conductors, Mater. Today. 6 (2003) 30–37.

[20] S.P.S. Badwal, F.T. Ciacchi, Oxygen-ion conducting electrolyte materials for solid oxide fuel cells, Ionics (Kiel). 6 (2000) 1–21.

[21] F. Goutenoire, O. Isnard, E. Suard, O. Bohnke, Y. Laligant, R. Retoux, et al., Structural and transport characteristics of the LAMOX family of fast oxide-ion conductors, based on lanthanum molybdenum oxide $La_2Mo_2O_9$, J. Mater. Chem. 11 (2001) 119–124.

[22] F. Goutenoire, O. Isnard, R. Retoux, P. Lacorre, Crystal structure of $La_2Mo_2O_9$, a new fast oxide-ion conductor, Chem. Mater. 12 (2000) 2575–2580.

[23] X. Wang, Effects of Ca doping on the oxygen ion diffusion and phase transition in oxide ion conductor $La_2Mo_2O_9$, Solid State Ionics. 146 (2002) 185–193.

[24] S. Tao, J.T.S. Irvine, Preparation and characterisation of apatite-type lanthanum silicates by a sol-gel process, Mater. Res. Bull. 36 (2001) 1245–1258.

[25] J.E.H. Sansom, L. Hildebrandt, P.R. Slater, An investigation of the synthesis and conductivities of La-Ge-O based systems, Ionics (2002) 155–160.

[26] J.R. Tolchard, M.S. Islam, P.R. Slater, Defect chemistry and oxygen ion migration in the apatite-type materials $La_{9.33}Si_6O_{26}$ and $La_8Sr_2Si_6O_{26}$, J. Mater. Chem. 13 (2003) 1956–1961.

[27] E.J. Abram, D.C. Sinclair, A.R. West, A novel enhancement of ionic conductivity in the cation-deficient apatite $La_{9.33}(SiO_4)_6O_2$, J. Mater. Chem. 11 (2001) 1978–1979.

[28] J. McFarlane, S. Barth, M. Swaffer, J.E.H. Sansom, P.R. Slater, Synthesis and conductivities of the apatite-type systems, $La_{9.33+x}Si_{6-y}M_yO_{26+z}$ (M = Co, Fe, Mn) and $La_8Mn_2Si_6O_{26}$. Ionics. 8 (2002) 49–154.

[29] S. Nakayama, T. Kageyama, H. Aono, Y. Sadaoka, Ionic conductivity of lanthanoid silicates, $Ln_{10}(SiO_4)_6O_3$ (Ln = La, Nd, Sm, Gd, Dy, Y, Ho, Er and Yb), J. Mater. Chem. 5 (1995) 1801–1805.

[30] E. Kendrick, J. Kendrick, K.S. Knight, M.S. Islam, P.R. Slater, Cooperative mechanisms of fast-ion conduction in gallium-based oxides with tetrahedral moieties. Nat. Mater. 6 (2007) 871–875.

[31] S. Li, F. Schönberger, P. Slater, $La_{1-x}Ba_{1+x}GaO_{4-x/2}$: A novel high temperature proton conductor, Chem. Commun. 9 (2003) 2694–2695.

[32] F. Schonberger, E. Kendrick, M. Islam, P. Slater, Investigation of proton conduction in $La_{1-x}Ba_{1+x}GaO_{4-x/2}$ and $La_{1-x}Sr_{2+x}GaO_{5-x/2}$, Solid State Ionics. 176 (2005) 2951–2953.

[33] X. Kuang, M.A. Green, H. Niu, P. Zajdel, C. Dickinson, J.B. Claridge, et al., Interstitial oxide ion conductivity in the layered tetrahedral network melilite structure., Nat. Mater. 7 (2008) 498–504.

[34] C.I. Thomas, X. Kuang, Z. Deng, H. Niu, J.B. Claridge, M.J. Rosseinsky, Phase stability control of interstitial oxide ion conductivity in the $La_{1+x}Sr_{1-x}Ga_3O_{7+x/2}$ Melilite Family, Chem. Mater. 22 (2010) 2510–2516.

[35] C. Tealdi, P. Mustarelli, M.S. Islam, Layered $LaSrGa_3O_7$-based oxide-ion conductors: cooperative transport mechanisms and flexible structures, Adv. Funct. Mater. 20 (2010) 3874–3880.

[36] M. Lacerda, J.T.S. Irvine, F.P. Glasser, A.R. West, High oxide ion conductivity in $Ca_{12}Al_4O_{33}$, Nature. 332 (1988) 525–526.

[37] F. Abraham, M.F. Debreuille-Gresse, G. Mairesse, G. Nowogrocki, Phase transitions and ionic conductivity in $Bi_4V_2O_{11}$ an oxide with a layered structure, Solid State Ionics. 28-30 (1988) 529–532.

[38] I. Abrahams, F. Krok, Defect chemistry of the BIMEVOXes, J. Mater. Chem. 12 (2002) 3351–3362.

[39] S.P.S. Badwal, F.T. Ciacchi, V. Zelizko, The effect of alumina addition on the conductivity, microstructure and mechanical strength of zirconia - yttria electrolytes, Ionics 4 (1998) 25–32.

[40] S. Badwal, Scandia–zirconia electrolytes for intermediate temperature solid oxide fuel cell operation, Solid State Ionics. 136-137 (2000) 91–99.

[41] T. Kudo, H. Obayashi, Oxygen Ion Conduction of the Fluorite-Type $Ce_{1-x}Ln_xO_{2-x/2}$ (Ln = Lanthanoid Element), J. Electrochem. Soc. 122 (1975) 142–147.

[42] J. Drennan, V. Zelizko, D. Hay, F.T. Ciacchi, S. Rajendran, S.P.S. Badwal, Characterisation, conductivity and mechanical properties of the oxygen-ion conductor $La_{0.9}Sr_{0.1}Ga_{0.8}Mg_{0.2}O_{3-x}$, J. Mater. Chem. 7 (1997) 79–83.

[43] K. Huang, R.S. Tichy, J.B. Goodenough, Superior perovskite oxide-ion conductor; Strontium- and magnesium-doped $LaGaO_3$: I, phase relationships and electrical properties, J. Am. Ceram. Soc. 81 (1998) 2565–2575.

[44] M.J. Verkerk, K. Keizer, A.J. Burggraaf, High oxygen ion conduction in sintered oxides of the Bi_2O_3-Er_2O_3 system, J. Appl. Electrochem. 10 (1980) 81–90.

[45] H. Iwahara, High temperature proton conducting oxides and their applications to solid electrolyte fuel cells and steam electrolyzer for hydrogen production, Solid State Ionics. 28-30 (1988) 573–578.

[46] T. Norby, Solid-state protonic conductors: principles, properties, progress and prospects, Solid State Ionics. 125 (1999) 1–11.

[47] K.D. Kreuer, Proton-conducting oxides, Annu. Rev. Mater. Res. 33 (2003) 333–359.

[48] Y. Yamazaki, R. Hernandez-Sanchez, S.M. Haile, High total proton conductivity in large-grained yttrium-doped barium zirconate, Chem. Mater. 21 (2009) 2755–2762.

[49] H. Iwahara, Prospect of hydrogen technology using proton-conducting ceramics, Solid State Ionics. 168 (2004) 299–310.

[50] A. Orera, P.R. Slater, New chemical systems for solid oxide fuel cells, Chem. Mater. 22 (2010) 675–690.

[51] H. Iwahara, T. Yajima, T. Hibino, K. Ozaki, H. Suzuki, Protonic conduction in calcium, strontium and barium zirconates, Solid State Ionics. 61 (1993) 65–69.

[52] H. Iwahara, Oxide-ionic and protonic conductors based on perovskite-type oxides and their possible applications, Solid State Ionics. 52 (1992) 99–104.

[53] H. Iwahara, Proton conducting ceramics and their applications, Solid State Ionics. 86-88 (1996) 9–15.

[54] K. Katahira, Y. Kohchi, T. Shimura, H. Iwahara, Protonic conduction in Zr-substituted $BaCeO_3$, Solid State Ionics. 138 (2000) 91–98.

[55] K.D. Kreuer, S. Adams, W. Münch, A. Fuchs, U. Klock, J. Maier, Proton conducting alkaline earth zirconates and titanates for high drain electrochemical applications, Solid State Ionics, 145 (2001) 295–306.

[56] K. Liang, Y. Du, A. Nowick, Fast high-temperature proton transport in nonstoichiometric mixed perovskites, Solid State Ionics. 69 (1994) 117–120.

[57] Y. Du, A.S. Nowick, Structural transitions and proton conduction in nonstoichiometric $A_3B'B''_2O_9$ perovskite-type oxides, J. Am. Ceram. Soc. 78 (1995) 3033–3039.

[58] D.J.D. Corcoran, J.T.S. Irvine, Investigations into $Sr_3CaZr_{0.5}Ta_{1.5}O_{8.75}$, a novel proton conducting perovskite oxide, Solid State Ionics. 145 (2001) 307–313.

[59] Zhang, Protonic conduction in $Ba_2In_2O_5$, Solid State Ionics. 82 (1995) 153–160.

[60] S. Noirault, S. Celerier, O. Joubert, M. Caldes, Y. Piffard, Water incorporation into the $(Ba_{1-x}La_x)_2In_2O_{5+x}\square_{1-x}$ ($0 \leq x < 0.6$) system, Solid State Ionics. 178 (2007) 1353–1359.

[61] J.F. Shin, L. Hussey, A. Orera, P.R. Slater, Enhancement of the conductivity of $Ba_2In_2O_5$ through phosphate doping., Chem. Commun. 46 (2010) 4613–5.

[62] C.A.J. Fisher, M.S. Islam, Defect, protons and conductivity in brownmillerite-structured $Ba_2In_2O_5$, Solid State Ionics. 118 (1999) 355–363.

[63] T. Schober, J. Friedrich, F. Krug, Phase transition in the oxygen and proton conductor $Ba_2In_2O_5$ in humid atmospheres below 300°C, Solid State Ionics. 99 (1997) 9–13.

[64] T. Schober, Protonic conduction in $BaIn_{0.5}Sn_{0.5}O_{2.75}$, Solid State Ionics. 109 (1998) 1-11.

[65] K. Kakinuma, A. Tomita, H. Yamamura, T. Atake, Water vapor absorption and proton conductivity of $(Ba_{1-x}La_x)_2In_2O_{5+x}$, J. Mater. Sci. 41 (2006) 6435–6440.

[66] E. Quarez, S. Noirault, M.T. Caldes, O. Joubert, Water incorporation and proton conductivity in titanium substituted barium indate, J. Power Sources. 195 (2010) 1136-1141.

[67] T. Norby, Proton conduction in Ca- and Sr-substituted $LaPO_4$, Solid State Ionics. 77 (1995) 240–243.

[68] K. Amezawa, S. Kjelstrup, T. Norby, Y. Ito, Protonic and native conduction in Sr-substituted $LaPO_4$ studied by thermoelectric power measurements, J. Electrochem. Soc. 145 (1998) 3313–3319.

[69] K. Amezawa, High-temperature protonic conduction in $La_7P_3O_{18}$, Solid State Ionics. 175 (2004) 569–573.

[70] K. Amezawa, Y. Kitajima, Y. Tomii, N. Yamamoto, M. Wideroe, T. Norby, Protonic conduction in acceptor-doped LaP_3O_9, Solid State Ionics. 176 (2005) 2867–2870.

[71] T. Norby, Y. Larring, Concentration and transport of protons in oxides, Curr. Opin. Solid State Mater. Sci. 2 (1997) 593–599.

[72] R. Haugsrud, T. Norby, Proton conduction in rare-earth ortho-niobates and ortho-tantalates, Nat. Mater. 5 (2006) 193–196.

[73] D. Fu, M. Itoh, Ferroelectricity in silver perovskite oxides, Ferroelectrics - material aspects, InTech, 2011.

[74] K.S. Knight, Structural phase transitions, oxygen vacancy ordering and protonation in doped $BaCeO_3$: Results from time-of-flight neutron powder diffraction investigations, Solid State Ionics, 145 (2001) 275–294.

[75] H.D. Megaw, Crystal Structures — A Working Approach, Phyladelphia, 1973.

[76] P.M. Woodward, Octahedral tilting in perovskites. II. Structure stabilizing forces, Acta Crystallogr. Sect. B Struct. Sci. 53 (1997) 44–66.

[77] A.M. Glazer, The classification of tilted octahedra in Perovskites, Acta Crystallogr. Sect. B Struct. Sci. 28 (1972) 3384–3392.

[78] Bonanos, N, Perovskite solid electrolytes: Structure, transport properties and fuel cell applications, Solid State Ionics. 79 (1995) 161–170.

[79] E. Fabbri, D. Pergolesi, E. Traversa, Materials challenges toward proton-conducting oxide fuel cells: a critical review, Chem. Soc. Rev. 39 (2010) 4355–4369.

[80] C.J. Howard, H.T. Stokes, Group-theoretical analysis of octahedral tilting in perovskites, Acta Crystallogr. Sect. B Struct. Sci. 54 (1998) 782–789.

[81] C.J. Howard, H.T. Stokes, Group-theoretical analysis of octahedral tilting in perovskites. Erratum, Acta Crystallogr. Sect. B Struct. Crystallogr. Cryst. Chem. 58 (2002) 564–565.

[82] V.M. Goldschmidt, Die gesetze der krystallochemie, Naturwissenschaften. 14 (1926) 477–485.

[83] W.T. Fu, D. Visser, D.J.W. IJdo, On the crystal structure of $BaTbO_3$, J. Solid State Chem. 165 (2002) 393–396.

[84] C.J. Howard, K.S. Knight, B.J. Kennedy, E.H. Kisi, The structural phase transitions in strontium zirconate revisited, J. Phys. Condens. Matter. 12 (2000) L677–L683.

[85] L. Li, J.R. Wu, M. Knight, S.M. Haile, Mixed proton and electron transport in doped $BaPrO_3$, Electrochem. Soc. Proc. 28 (2001) 58.

[86] C.S. Knee, A. Magrasó, T. Norby, R.I. Smith, Structural transitions and conductivity of $BaPrO_3$ and $BaPr_{0.9}Y_{0.1}O_{3-\delta}$, J. Mater. Chem. 19 (2009) 3238-3247.

[87] I.M. Reaney, E.L. Colla, N. Setter, Dielectric and structural characteristics of Ba- and Sr-based complex perovskites as a function of tolerance factor, Japanese J. Appl. Physics, Part 1 Regul. Pap. Short Notes Rev. Pap. 33 (1994) 3984–3990.

[88] D.I. Woodward, I.M. Reaney, Electron diffraction of tilted perovskites, Acta Crystallogr. Sect. B Struct. Sci. 61 (2005) 387–399.

[89] A. Navrotsky, Physics and Chemistry of Earth Materials, Cambridge University Press, 1994.

[90] Y. Yamazaki, P. Babilo, S.M. Haile, Defect chemistry of yttrium-doped barium zirconate: A thermodynamic analysis of water uptake, Chem. Mater. 20 (2008) 6352-6357.

[91] N. Bonanos, Oxide-based protonic conductors: Point defects and transport properties, Solid State Ionics. 145 (2001) 265–274.

[92] N. Bonanos, Transport properties and conduction mechanism in high-temperature protonic conductors, Solid State Ionics. 53-56 (1992) 967–974.

[93] T. He, K.D. Kreuer, Y.M. Baikov, J. Maier, Impedance spectroscopic study of thermodynamics and kinetics of a Gd-doped $BaCeO_3$ single crystal, Solid State Ionics. 95 (1997) 301–308.

[94] W. Münch, G. Seifert, K.D. Kreuer, J. Maier, A quantum molecular dynamics study of proton conduction phenomena in $BaCeO_3$, Solid State Ionics. 86-88 (1996) 647–652.

[95] Cherry, M, Computational studies of proton migration in perovskite oxides, Solid State Ionics. 77 (1995) 207–209.

[96] K.D. Kreuer, Aspects of the formation and mobility of protonic charge carriers and the stability of perovskite-type oxides, Solid State Ionics. 125 (1999) 285–302.

[97] R.D. Shannon, Revised effective ionic radii and systematic studies of interatomic distances in halides and chalcogenides, Acta Crystallogr. Sect. A. 32 (1976) 751–767.

[98] A.K. Azad, C. Savaniu, S. Tao, S. Duval, P. Holtappels, R.M. Ibberson, et al., Structural origins of the differing grain conductivity values in $BaZr_{0.9}Y_{0.1}O_{2.95}$ and indication of novel approach to counter defect association, J. Mater. Chem. 18 (2008) 3414-3418.

[99] S. Imashuku, T. Uda, Y. Awakura, Sintering Properties of Trivalent Cation-Doped Barium Zirconate at 1600°C, Electrochem. Solid-State Lett. 10 (2007) B175- B178.

[100] B. Guillaume, F. Boschini, I. Garcia-Cano, A. Rulmont, R. Cloots, M. Ausloos, Optimization of $BaZrO_3$ sintering by control of the initial powder size distribution; a factorial design statistical analysis, J. Eur. Ceram. Soc. 25 (2005) 3593–3604.

[101] P. Babilo, T. Uda, S.M. Haile, Processing of yttrium-doped barium zirconate for high

proton conductivity, J. Mater. Res. 22 (2007) 1322–1330.

[102] S.M. Haile, G. Staneff, K.H. Ryu, Non-stoichiometry, grain boundary transport and chemical stability of proton conducting perovskites, J. Mater. Sci. 36 (2001) 1149-1160.

[103] B. Robertz, F. Boschini, R. Cloots, A. Rulmont, Importance of soft solution processing for advanced $BaZrO_3$ materials, Int. J. Inorg. Mater. 3 (2001) 1185–1187.

[104] S.B. Reddy, K.P. Rao, M.S.R. Rao, Nanocrystalline barium zirconate titanate synthesized at low temperature by an aqueous co-precipitation technique, Scr. Mater. 57 (2007) 591–594.

[105] F. Boschini, A. Rulmont, R. Cloots, B. Vertruyen, Rapid synthesis of submicron crystalline barium zirconate $BaZrO_3$ by precipitation in aqueous basic solution below 100 °C, J. Eur. Ceram. Soc. 29 (2009) 1457–1462.

[106] Y. V. Kolen'ko, A.A. Burukhin, B.R. Churagulov, N.N. Oleinikov, A.S. Vanetsev, On the possibility of preparing fine-particle barium zirconate by hydrothermal synthesis, Inorg. Mater. 38 (2002) 252–255.

[107] P.P. Phulé, D.C. Grundy, Pathways for the low temperature synthesis of nano-sized crystalline barium zirconate, Mater. Sci. Eng. B. 23 (1994) 29–35.

[108] R.B. Cervera, Y. Oyama, S. Yamaguchi, Low temperature synthesis of nanocrystalline proton conducting $BaZr_{0.8}Y_{0.2}O_{3-\delta}$ by sol-gel method, Solid State Ionics. 178 (2007) 569–574.

[109] A. Magrez, T. Schober, Preparation, sintering, and water incorporation of proton conducting $Ba_{0.99}Zr_{0.8}Y_{0.2}O_{3-\delta}$: Comparison between three different synthesis techniques, Solid State Ionics. 175 (2004) 585–588.

[110] Z. Khani, M. Taillades-Jacquin, G. Taillades, M. Marrony, D.J. Jones, J. Rozière, New synthesis of nanopowders of proton conducting materials. A route to densified proton ceramics, J. Solid State Chem. 182 (2009) 790–798.

[111] A. Sin, B. El Montaser, P. Odier, F. Weiss, Synthesis and sintering of large batches of barium zirconate nanopowders, J. Am. Ceram. Soc. 85 (2002) 1928–1932.

[112] A.M. Azad, S. Subramaniam, Temperature dependence of the dielectric response of $BaZrO_3$ by immittance spectroscopy, Mater. Res. Bull. 37 (2002) 11–21.

[113] M.M. Bućko, J. Obłakowski, Preparation of $BaZrO_3$ nanopowders by spray pyrolysis method, J. Eur. Ceram. Soc. 27 (2007) 3625–3628.

[114] P.A. Stuart, T. Unno, R. Ayres-Rocha, E. Djurado, S.J. Skinner, The synthesis and sintering behaviour of $BaZr_{0.9}Y_{0.1}O_{3-\delta}$ powders prepared by spray pyrolysis, J. Eur. Ceram. Soc. 29 (2009) 697–702.

[115] G. Taglieri, M. Tersigni, P. Villa, C. Mondelli, Synthesis by the citrate route and characterisation of $BaZrO_3$, a high tech ceramic oxide: preliminary results, Int. J. Inorg. Mater. 1 (1999) 103–110.

[116] Z. Khani, M. Taillades-Jacquin, G. Taillades, M. Marrony, D.J. Jones, J. Rozière, New synthesis of nanopowders of proton conducting materials. A route to densified proton ceramics, J. Solid State Chem. 182 (2009) 790–798.

[117] V. V. Zyryanov, V.A. Sadykov, N.F. Uvarov, G.M. Alikina, A.I. Lukashevich, S. Neophytides, et al., Mechanosynthesis of complex oxides with fluorite and perovskite-related structures and their sintering into nanocomposites with mixed ionic-electronic conductivity, Solid State Ionics. 176 (2005) 2813–2818.

[118] P. Gonçalves, J. Canales-Vázquez, F.M. Figueiredo, Mecanosíntesis de polvos nanocristalinos de $CaTi_{1-x}Mn_xO_{3-\delta}$, Bol. la Soc. Esp. Ceram. y Vidr. 47 (2008) 233-237.

[119] A. Moure, A. Castro, J. Tartaj, C. Moure, Mechanosynthesis of perovskite $LaGaO_3$ and its effect on the sintering of ceramics, Ceram. Int. 35 (2009) 2659–2665.

[120] I. Antunes, A. Brandão, F.M. Figueiredo, J.R. Frade, J. Gracio, D.P. Fagg, Mechanosynthesis of nanopowders of the proton-conducting electrolyte material $Ba(Zr, Y)O_{3-\delta}$, J. Solid State Chem. 182 (2009) 2149–2156.

[121] M.J. Sayagués, J.M. Córdoba, F.J. Gotor, Room temperature mechanosynthesis of the $La_{1-x}Sr_xMnO_{3\pm\delta}$ ($0 \leq x \leq 1$) system and microstructural study, J. Solid State Chem. 188 (2012) 11–16.

[122] V. Šepelák, A. Düvel, M. Wilkening, K.-D. Becker, P. Heitjans, Mechanochemical reactions and syntheses of oxides, Chem. Soc. Rev. 42 (2013) 7507–7520.

[123] V. Šepelák, S. Bégin-Colin, G. Le Caër, Transformations in oxides induced by high-energy ball-milling, Dalt. Trans. 41 (2012) 11927.

[124] T. Friščić, I. Halasz, P.J. Beldon, A.M. Belenguer, F. Adams, S. a J. Kimber, et al., Real-time and in situ monitoring of mechanochemical milling reactions., Nat. Chem. 5 (2013) 66–73.

[125] P. Baláž, M. Achimovičová, M. Baláž, P. Billik, Z. Cherkezova-Zheleva, J.M. Criado, et al., Hallmarks of mechanochemistry: from nanoparticles to technology., Chem. Soc. Rev. 42 (2013) 7571–637.

[126] V. V. Boldyrev, K. Tkácová, Mechanochemistry of Solids: Past, Present, and Prospects, J. Mater. Synth. Process. 8 (2000) 121-132.

[127] P. Baláž, Mechanical activation in hydrometallurgy, Int. J. Miner. Process. 72 (2003) 341–354.

[128] L. Takacs, Quicksilver from cinnabar the first documented mechanochemical reaction?, JOM. 52 (2000) 12–13.

[129] L. Takacs, M. Carey Lea, the first mechanochemist, J. Mater. Sci. 39 (2004) 4987-4993.

[130] M.K. Beyer, H. Clausen-Schaumann, Mechanochemistry: the mechanical activation of covalent bonds, Chem. Rev. 105 (2005) 2921–2948.

[131] E. Ivanov, C. Suryanarayana, Materials and process design through mechanochemical routes, J. Mater. Synth. Process. 8 (2000) 235–244.

[132] V. V. Zyryanov, Ultrafast mechanochemical synthesis of mixed oxides, Inorg. Mater.41

(2005) 378–392.

[133] P. Balaz, Mechanochemistry in Nanoscience and Minerals Engineering, 1.ª ed., Springer-Verlag Berlin Heidelberg, 2008.

[134] J.M. Xue, Z.H. Zhou, J. Wang, Nanocrystalline Ceramics by Mechanical Activation, Encycl. Nanosci. Nanotechnol. (2004) 417–433.

[135] W. Stichert, F. Schüth, Influence of crystallite size on the properties of zirconia, Chem. Mater. 4756 (1998) 2020–2026.

[136] L.A. Pérez-Maqueda, E. Matijević, Preparation and characterization of nanosized zirconium (hydrous) oxide particles, J. Mater. Res. 12 (1997) 3286–3292.

[137] J.A. Navio, G. Colón, P.J. Sánchez-Soto, M. Macias, Effects of H_2O_2 and SO_4^{2-} species on the crystalline structure and surface properties of ZrO_2 processed by alkaline precipitation, Chem. Mater. 9 (1997) 1256–1261.

[138] J.I. Langford, Use of pattern decomposition or simulation to study microstructure: theoretical considerations, em: P. Snyder, F. Fiala, H. Bunge (Eds.), Defect Microstruct. Anal. by Diffr., IUCr, Oxford University Press, Oxford, 1999: p. 59.

[139] J.I. Langford, D. Louër, P. Scardi, Effect of a crystallite size distribution on X-ray diffraction line profiles and whole-powder-pattern fitting, J. Appl. Crystallogr. 33 (2000) 964–974.

[140] S. Krumm, An Interactive Windows Program for Profile Fitting and Size/Strain Analysis, Mater. Sci. Forum. 228-231 (1996) 183–190.

[141] J. Rodriguez-Carvajal, FULLPROF: A Program for Rietveld Refinement and pattern matching analysis, em: Abstr. Satell. Meet. Powder Diffr. XV Congr. IUCr, 1990.

[142] A. De Pablos-Martín, G.C. Mather, F. Muñoz, S. Bhattacharyya, T. Höche, J.R. Jinschek, et al., Design of oxy-fluoride glass-ceramics containing $NaLaF_4$ nano-crystals, J. Non. Cryst. Solids. 356 (2010) 3071–3079.

[143] E. Barsoukov, J.R. Macdonald, Impedance Spectroscopy: Theory, Experiment, and Applications, 2005.

[144] S.M. Haile, D.L. West, J. Campbell, The role of microstructure and processing on the proton conducting properties of gadolinium-doped barium cerate, J. Mater. Res. 13 (1998) 1576–1595.

[145] Y. Yamazaki, R. Hernandez-Sanchez, S.M. Haile, Cation non-stoichiometry in yttrium-doped barium zirconate: phase behavior, microstructure, and proton conductivity, J. Mater. Chem. 20 (2010) 8158-8166.

[146] M.C. Steil, F. Thevenot, M. Kleitz, Densification of yttria-stabilized zirconia: Impedance spectroscopy analysis, J. Electrochem. Soc. 144 (1997) 390–398.

[147] D. Pérez-Coll, E. Sánchez-López, G.C. Mather, Influence of porosity on the bulk and grain-boundary electrical properties of Gd-doped ceria, Solid State Ionics. 181 (2010) 1033–1042.

[148] G.E. Archie, The electrical resistivity log as an aid in determining some resevoir characteristics, Trans. AIME. 146 (1942) 54–62.

[149] J.E. Bauerle, Study of solid electrolyte polarization by a complex admittance method, J. Phys. Chem. Solids. 30 (1969) 2657–2670.

[150] T. Hungría, A. Castro, Synthesis and structural characterization of the new solid solution $Ba_{2-x}Sr_xTiO_4$ ($0 \leq x \leq 1$): Effect of the method of synthesis on the polymorphic phase isolated, J. Alloys Compd. 436 (2007) 266–271.

[151] S. Ohara, A. Kondo, H. Shimoda, K. Sato, H. Abe, M. Naito, Rapid mechanochemical synthesis of fine barium titanate nanoparticles, Mater. Lett. 62 (2008) 2957–2959.

[152] V.M. Marchev, G.G. Gospodinov, D.G. Stoyanov, Mechanochemical synthesis of calcium, strontium, and barium zirconates, Russ. J. Gen. Chem. 69 (1999) 360–362.

[153] C.W. Bale, P. Chartrand, S.A. Degterov, G. Eriksson, K. Hack, R. Ben Mahfoud, et al.,

FactSage thermochemical software and databases, Calphad. 26 (2002) 189–228.

[154] J.F. Monteiro, A.A.L. Ferreira, I. Antunes, D.P. Fagg, J.R. Frade, Thermodynamic restrictions on mechanosynthesis of strontium titanate, J. Solid State Chem. 185 (2012) 143–149.

[155] T. Hungría, M. Algueró, A.B. Hungría, A. Castro, Dense, Fine-Grained Ba 1 - x Sr x TiO 3 Ceramics Prepared by the Combination of Mechanosynthesized Nanopowders and Spark Plasma Sintering, Chem. Mater. 17 (2005) 6205–6212.

[156] E. Rodríguez-Reyna, A.F. Fuentes, M. Maczka, J. Hanuza, K. Boulahya, U. Amador, Structural, microstructural and vibrational characterization of apatite-type lanthanum silicates prepared by mechanical milling, J. Solid State Chem. 179 (2006) 522–531.

[157] P. Pasierb, S. Komornicki, M. Rokita, M. Rękas, Structural properties of Li_2CO_3-$BaCO_3$ system derived from IR and Raman spectroscopy, J. Mol. Struct. 596 (2001) 151–156.

[158] P. Colomban, F. Romain, A. Neiman, I. Animitsa, Double perovskites with oxygen structural vacancies: Raman spectra, conductivity and water uptake, Solid State Ionics. 145 (2001) 339–347.

[159] P.-L.-L. Chen, I.-W.-W. Chen, Role of defect interaction in boundary mobility and cation diffusivity of CeO_2, J. Am. Ceram. Soc. 77 (1994) 2289–2297.

[160] B. Groß, C. Beck, F. Meyer, T. Krajewski, R. Hempelmann, H. Altgeld, $BaZr_{0.85}Me_{0.15}O_{2.925}$ (Me = Y, In and Ga): crystal growth, high-resolution transmission electron microscopy, high-temperature X-ray diffraction and neutron scattering experiments, Solid State Ionics. 145 (2001) 325–331.

[161] R.B. Cervera, Y. Oyama, S. Miyoshi, K. Kobayashi, T. Yagi, S. Yamaguchi, Structural study and proton transport of bulk nanograined Y-doped $BaZrO_3$ oxide protonics materials, Solid State Ionics. 179 (2008) 236–242.

[162] G. Štefanić, S. Musić, A. Gajović, Structural and microstructural changes in monoclinic

ZrO_2 during the ball-milling with stainless steel assembly, Mater. Res. Bull. 41 (2006) 764–777.

[163] G. Štefanić, S. Musić, A. Gajović, A comparative study of the influence of milling media on the structural and microstructural changes in monoclinic ZrO_2, J. Eur. Ceram. Soc. 27 (2007) 1001–1016.

[164] G. Štefanić, S. Musić, Factors influencing the stability of low temperature tetragonal ZrO2, Croat. Chem. Acta. 75 (2002) 727–767.

[165] J.E. Bailey, D. Lewis, Z.M. Librant, L.J. Porter, Phase Transformations in Milled Zirconia, Trans. J. Brit. Ceram. Soc. 71 (1972) 25–30.

[166] A. V. Chadwick, M.J.. Pooley, K.E. Rammutla, S.L.P.. Savin, A. Rougier, A comparison of the extended X-ray absorption fine structure of nanocrystalline ZrO_2 prepared by high-energy ball milling and other methods, J. Phys. Condens. Matter. 15 (2003) 431.

[167] A.N. Scian, E.F. Aglietti, M.C. Caracoche, P.C. Rivas, A.F. Pasquevich, A.R. López García, Phase transformations in monoclinic zirconia caused by milling and subsequent annealing, J. Am. Ceram. Soc. 77 (1994) 1525–1530.

[168] J.-P. Brog, C.-L. Chanez, A. Crochet, K.M. Fromm, Polymorphism, what it is and how to identify it: a systematic review, RSC Adv. 3 (2013) 16905-16931.

[169] M. Chen, B. Hallstedt, L.J. Gauckler, Thermodynamic modeling of the ZrO_2-$YO_{1.5}$ system, Solid State Ionics. 170 (2004) 255–274.

[170] J.R. Kelly, I. Denry, Stabilized zirconia as a structural ceramic: An overview, Dent. Mater. 24 (2008) 289–298.

[171] A.F. Fuentes, K. Boulahya, M. MacZka, J. Hanuza, U. Amador, Synthesis of disordered pyrochlores, $A_2Ti_2O_7$ (A = Y, Gd and Dy), by mechanical milling of constituent oxides, Solid State Sci. 7 (2005) 343–353.

[172] V. V. Boldyrev, S. V. Pavlov, E.L. Goldberg, Interrelation between fine grinding and mechanical activation, Int. J. Miner. Process. 44-45 (1996) 181–185.

[173] I.J. Lin, Implications of fine grinding in mineral processing: Mechanochemical approach, J. Therm. Anal. Calorim. 52 (1998) 453–461.

[174] M.J. Tribelhorn, M.E. Brown, Thermal decomposition of barium and strontium peroxides, Thermochim. Acta. 255 (1995) 143–154.

[175] Y. Oyama, A. Kojima, X. Li, R.B. Cervera, K. Tanaka, S. Yamaguchi, Phase relation in the BaO-ZrO_2-$YO_{1.5}$ system: Presence of separate $BaZrO_3$ phases and complexity in phase formation, Solid State Ionics. 197 (2011) 1–12.

[176] S. Imashuku, T. Uda, Y. Nose, Y. Awakura, To journal of phase equilibria and diffusion phase relationship of the BaO-ZrO_2-$YO_{1.5}$ system at 1500 and 1600 °C, J. Phase Equilibria Diffus. 31 (2010) 348–356.

[177] K.-Y. Park, Y. Seo, K.B. Kim, S.-J. Song, B. Park, J.-Y. Park, Enhanced proton conductivity of yttrium-doped barium zirconate with sinterability in protonic ceramic fuel cells, J. Alloys Compd. 639 (2015) 435–444.

[178] S. Imashuku, T. Uda, Y. Nose, G. Taniguchi, Y. Ito, Y. Awakura, Dependence of dopant cations on microstructure and proton conductivity of barium zirconate, J. Electrochem. Soc. 156 (2009) B1-B8.

[179] E. Fabbri, D. Pergolesi, S. Licoccia, E. Traversa, Does the increase in Y-dopant concentration improve the proton conductivity of $BaZr_{1-x}Y_xO_{3-\delta}$ fuel cell electrolytes?, Solid State Ionics. 181 (2010) 1043–1051.

[180] F. Iguchi, N. Sata, T. Tsurui, H. Yugami, Microstructures and grain boundary conductivity of $BaZr_{1-x}Y_xO_3$ (x = 0.05, 0.10, 0.15) ceramics, Solid State Ionics. 178 (2007) 691–695.

[181] S. Imashuku, T. Uda, Y. Nose, K. Kishida, S. Harada, H. Inui, et al., Improvement of grain-boundary conductivity of trivalent cation-doped barium zirconate sintered at

1600°C by Co-doping scandium and yttrium, J. Electrochem. Soc. 155 (2008) B581-B586.

[182] E. Fabbri, A. D'Epifanio, E. Di Bartolomeo, S. Licoccia, E. Traversa, Tailoring the chemical stability of $Ba(Ce_{0.8-x}Zr_xY_{0.2}O_{3-\delta}$ protonic conductors for intermediate temperature solid oxide fuel cells (IT-SOFCs), Solid State Ionics. 179 (2008) 558–564.

[183] K. Nomura, H. Kageyama, Transport properties of $BaZr_{0.8}Y_{0.2}O_{3-\delta}$ perovskite, Solid State Ionics. 178 (2007) 661–665.

[184] Y. Liu, R. Ran, M.O. Tade, Z. Shao, Structure, sinterability, chemical stability and conductivity of proton-conducting $BaZr_{0.6}M_{0.2}Y_{0.2}O_{3-\delta}$ electrolyte membranes: The effect of the M dopant, J. Memb. Sci. 467 (2014) 100–108.

[185] D. Han, K. Kishida, H. Inui, T. Uda, Substantial appearance of origin of conductivity decrease in Y-doped $BaZrO_3$ due to Ba-deficiency, RSC Adv. 4 (2014) 31589-31593.

[186] F. Iguchi, T. Tsurui, N. Sata, Y. Nagao, H. Yugami, The relationship between chemical composition distributions and specific grain boundary conductivity in Y-doped $BaZrO_3$ proton conductors, Solid State Ionics. 180 (2009) 563–568.

[187] K.. Kreuer, Aspects of the formation and mobility of protonic charge carriers and the stability of perovskite-type oxides, Solid State Ionics. 125 (1999) 285–302.

[188] Y. Yamazaki, F. Blanc, Y. Okuyama, L. Buannic, J.C. Lucio-Vega, C.P. Grey, et al., Proton trapping in yttrium-doped barium zirconate., Nat. Mater. 12 (2013) 647–651.

[189] D.-K. Lim, C.-J. Park, M.-B. Choi, C.-N. Park, S.-J. Song, Partial conductivities of mixed conducting $BaCe_{0.65}Zr_{0.2}Y_{0.15}O_{3-\delta,}$ Int. J. Hydrogen Energy. 35 (2010) 10624-10629.

[190] H.-D. Baek, Modeling of electrical conductivity in high-temperature proton-conducting oxides, Solid State Ionics. 110 (1998) 255–262.

[191] K.D. Kreuer, S. Adams, W. Münch, A. Fuchs, U. Klock, J. Maier, Proton conducting

alkaline earth zirconates and titanates for high drain electrochemical applications, Solid State Ionics. 145 (2001) 295–306.

[192] A.K. Azad, C. Savaniu, S. Tao, S. Duval, P. Holtappels, R.M. Ibberson, et al., Structural origins of the differing grain conductivity values in $BaZr_{0.9}Y_{0.1}O_{2.95}$ and indication of novel approach to counter defect association, J. Mater. Chem. 18 (2008) 3414-3418.

[193] D. Han, K. Kishida, K. Shinoda, H. Inui, T. Uda, A comprehensive understanding of structure and site occupancy of Y in Y-doped $BaZrO_3$, J. Mater. Chem. A. 1 (2013) 3027-3033.

[194] S.M. Choi, J.-H. Lee, H. An, J. Hong, H. Kim, K.J. Yoon, et al., Fabrication of anode-supported protonic ceramic fuel cell with $BaZr_{0.85}Y_{0.15}O_{3-\delta}$–$Ba(Ce_{0.9}Y_{0.1})O_{3-\delta}$ dual-layer electrolyte, Int. J. Hydrogen Energy. 39 (2014) 12812–12818.

[195] D. Shima, S.M. Haile, The influence of cation non-stoichiometry on the properties of undoped and gadolinia-doped barium cerate, Solid State Ionics. 97 (1997) 443–455.

[196] G. Ma, H. Matsumoto, H. Iwahara, Ionic conduction and nonstoichiometry in non-doped $Ba_xCeO_{3-\delta}$, Solid State Ionics. 122 (1999) 237–247.

[197] G.C. Mather, S. García-Martín, D. Benne, C. Ritter, U. Amador, A-site-cation deficiency in the $SrCe_{0.9}Yb_{0.1}O_{3-\delta}$ perovskite: effects of charge-compensation mechanism on structure and proton conductivity, J. Mater. Chem. 21 (2011) 5764-5773.

[198] N. V Sharova, V.P. Gorelov, Effect of cation nonstoichiometry on the properties of solid electrolyte $Ba_xCe_{0.97}Nd_{0.03}O_{3-\delta}$ ($0.90 \leq x \leq 1.10$), Russ. J. Electrochem. 40 (2004) 639–645.

[199] G.C. Mather, M.S. Islam, Defect and dopant properties of the $SrCeO_3$-based proton conductor, Chem. Mater. 17 (2005) 1736–1744.

[200] G.C. Mather, S. García-Martín, D. Benne, C. Ritter, U. Amador, A-site-cation

deficiency in the $SrCe_{0.9}Yb_{0.1}O_{3-\delta}$ perovskite: effects of charge-compensation mechanism on structure and proton conductivity, J. Mater. Chem. 21 (2011) 5764-5733..

[201] R.A. Davies, M.S. Islam, J.D. Gale, Dopant and proton incorporation in perovskite-type zirconates, Solid State Ionics. 126 (1999) 323–335.

[202] C. Long, H. Fan, M. Li, High temperature Aurivillius piezoelectrics: the effect of (Li,Ln) modification on the structure and properties of $(Li,Ln)_{0.06}(Na,Bi)_{0.44}Bi_2Nb_2O_9$ (Ln = Ce, Nd, La and Y)., Dalton Trans. 42 (2013) 3561–3570.

[203] J.-H. Lee, Z. Gan, O.H. Han, Effect of Ba Nonstoichiometry in $Ba_xZr_{0.8}Y_{0.2}O_{3-\delta}$ on Population of 5-Coordinated Y, J. Am. Ceram. Soc. 97 (2014) 3749–3754.

[204] A. Kruth, G.C. Mather, J.R. Jurado, J.T.S. Irvine, Anomalous variations of unit cell parameters with composition in proton conducting, $ACeO_3$-type perovskite solid solutions, Solid State Ionics. 176 (2005) 703–712.

[205] Suk-Joong L.Kang, Sintering Densification,Grain Growth,and Microstructure, Elsevier Butterworth-Heinemann Linacre House. (2005) pp. 9–18.

[206] F. Iguchi, N. Sata, H. Yugami, Proton transport properties at the grain boundary of barium zirconate based proton conductors for intermediate temperature operating SOFC, J. Mater. Chem. 20 (2010) 6265-6270.

[207] S. Mimuro, S. Shibako, Y. Oyama, K. Kobayashi, T. Higuchi, S. Shin, et al., Proton incorporation and defect chemistry of Yb-doped $BaPrO_3$, Solid State Ionics. 178 (2007) 641–647.

[208] K.A. Furøy, R. Haugsrud, M. Hänsel, A. Magrasó, T. Norby, Role of protons in the electrical conductivity of acceptor-doped $BaPrO_3$, $BaTbO_3$, and $BaThO_3$, Solid State Ionics. 178 (2007) 461–467.

[209] A. Magrasó, F. Espiell, M. Segarra, J.T.S. Irvine, Chemical and electrical properties of $BaPr_{0.7}Gd_{0.3}O_{3-\delta}$, J. Power Sources. 169 (2007) 53–58.

[210] A. Magrasó, R. Haugsrud, M. Segarra, T. Norby, Defects and transport in Gd-doped $BaPrO_3$, J. Electroceramics. 23 (2009) 80–88.

[211] S. V. Bhide, A. V. Virkar, Stability of $AB'_{1/2}B''_{1/2}O3$-type mixed perovskite proton conductors, J. Electrochem. Soc. 146 (1999) 4386–4392.

[212] A. Magrasó, X. Solans, J.T.S. Irvine, M. Segarra, Preparation of stabilized Gd-doped $BaPrO_3$ materials by Zr substitution, Ceram. Int. 35 (2009) 1819–1827.

[213] N. Zakowsky, S. Williamson, J.T.S. Irvine, Elaboration of CO_2 tolerance limits of $BaCe_{0.9}Y_{0.1}O_{3-\delta}$ electrolytes for fuel cells and other applications, Solid State Ionics. 176 (2005) 3019–3026.

[214] K.. Kreuer, On the development of proton conducting materials for technological applications, Solid State Ionics. 97 (1997) 1–15.

[215] A. Brandão, J.F. Monteiro, A. V. Kovalevsky, D.P. Fagg, V. V. Kharton, J.R. Frade, Guidelines for improving resistance to CO_2 of materials for solid state electrochemical systems, Solid State Ionics, 192 (2011) 16–20.

[216] E. Fabbri, L. Bi, H. Tanaka, D. Pergolesi, E. Traversa, Chemically stable Pr and Y co-doped barium zirconate electrolytes with high proton conductivity for intermediate-temperature solid oxide fuel cells, Adv. Funct. Mater. 21 (2011) 158–166.

[217] E. Fabbri, L. Bi, D. Pergolesi, E. Traversa, High-performance composite cathodes with tailored mixed conductivity for intermediate temperature solid oxide fuel cells using proton conducting electrolytes, Energy Environ. Sci. 4 (2011) 4984-4993.

[218] E. Fabbri, I. Markus, L. Bi, D. Pergolesi, E. Traversa, Tailoring mixed proton-electronic conductivity of $BaZrO_3$ by Y and Pr co-doping for cathode application in protonic SOFCs, Solid State Ionics. 202 (2011) 30–35.

[219] F. Giannici, M. Shirpour, A. Longo, A. Martorana, R. Merkle, J. Maier, Long-Range and Short-Range Structure of Proton-Conducting Y:$BaZrO_3$, Chem. Mater. 23 (2011)

2994–3002.

[220] M. Havel, D. Baron, P. Colomban, 'Smart' Raman/Rayleigh imaging of nanosized SiC materials using the spatial correlation model, J. Mater. Sci. 39 (2004) 6183 – 6190.

[221] A. Slodczyk, P. Colomban, D. Lamago, M.-H. Limage, F. Romain, S. Willemin, et al., Phase transitions in the H^+-conducting perovskite ceramics by the quasi-elastic neutron and high-pressure Raman scattering, Ionics 14 (2007) 215–222.

[222] W. Kaabar, S. Bott, R. Devonshire, Raman spectroscopic study of mixed carbonate materials., Spectrochim. Acta. A. Mol. Biomol. Spectrosc. 78 (2011) 136–41.

[223] P. Colomban, A. Slodczyk, Raman intensity: An important tool in the study of nanomaterials and nanostructures, Acta Phys. Pol. A. 116 (2009) 7–12.

[224] M. V. Abrashev, J. Bäckström, L. Börjesson, V.N. Popov, R.A. Chakalov, N. Kolev, et al., Raman spectroscopy of $CaMnO_3$: Mode assignment and relationship between Raman line intensities and structural distortions, Phys. Rev. B - Condens. Matter Mater. Phys. 65 (2002) 1843011–1843019.

[225] C.J. Howard, K.S. Knight, B.J. Kennedy, E.H. Kisi, The structural phase transitions in strontium zirconate revisited The structural phase transitions in strontium zirconate revisited, J. Phys. Condens. Matter. 12 (2000) L677–L683.

[226] Z.L. Wang, Z.C. Kang, FUNCTIONAL AND SMART MATERIALS - Structural evolution and structure analysis, 1st ed., Plenum Publishing Corp., New York, 1998.

[227] C. Li, K.C.K. Soh, P. Wu, Formability of ABO_3 perovskites, J. Alloys Compd. 372 (2004) 40–48.

[228] L.M. Feng, L.Q. Jiang, M. Zhu, H.B. Liu, X. Zhou, C.H. Li, Formability of ABO_3 cubic perovskites, J. Phys. Chem. Solids. 69 (2008) 967–974.

[229] A. Kumar, A.S. Verma, S.R. Bhardwaj, Prediction of formability in perovskite-type oxides, Open Appl. Phys. J. 1 (2008) 11–19.

[230] H. Zhang, N. Li, K. Li, D. Xue, Structural stability and formability of ABO_3-type perovskite compounds, Acta Crystallogr. Sect. B Struct. Sci. 63 (2007) 812–818.

APPENDIX 1: CHEMICAL-POTENTIAL DIAGRAMS

Chemical-potential diagrams were plotted and used as thermodynamic guidelines for the ternary-systems ZrO_2-BaO-O_2, CeO_2-BaO-O_2 and TiO_2-BaO-O_2, to assess conditions required for reactivity.

Taking as example the ZrO_2-BaO-O_2 system, one identifies the single oxides phases BaO, BaO_2 and ZrO_2 and the zirconate phases, $BaZrO_3$ and Ba_2ZrO_4, interacting with a single reactive gas (O_2), in the atmosphere. In this case, equilibrium diagrams ZrO_2-BaO-O_2 at a given temperature, may be represented by plots of $\log(a_{BaO}/a_{ZrO_2})$ vs $\log(P_{O_2})$ and include three types of reactions, corresponding to:

a) Reactions that depend only of P_{O_2}, as the reaction:

$$BaO\,(s) + O_2\,(g) \rightleftarrows 2BaO_2\,(s) \qquad (1)$$

b) Reactions that depend exclusively on a_{BaO}/a_{ZrO_2}, such as the reaction:

$$BaO + 3BaZrO_3\,(s) \rightleftarrows ZrO_2 + 2Ba_2ZrO_4\,(s) \qquad (2)$$

c) Reactions that depend on the activity BaO/ZrO_2 ratio and P_{O_2}, such as:

$$Ba_2ZrO_4\,(s) + BaO + 1.5O_2\,(g) \rightleftarrows ZrO_2 + 3BaO_2\,(s) \qquad (3)$$

In the first case, reaction (1), the correspondent equilibrium constant, is given by:

$$K_1 = \frac{1}{P_{O_2}} = \exp\left(\frac{-\Delta G_1}{RT}\right) \qquad (4)$$

and thus,

$$\log\left(P_{O_2}\right) = \frac{\Delta G_1}{2.30\ RT} \tag{5}$$

This type of two-phase equilibrium are represented in chemical potential diagrams by vertical lines.

For the reaction (2), the equilibrium constant is expressed by:

$$K_2 = \frac{a_{ZrO}}{a_{BaO}} = \exp\left(\frac{-\Delta G_2}{RT}\right) \tag{6}$$

and,

$$\log\left(\frac{a_{BaO}}{a_{ZrO_2}}\right) = \frac{\Delta G_2}{2.30\ RT} \tag{7}$$

where such two phase equilibrium correspond to horizontal lines in the chemical-potential diagrams.

Finally, the equilibrium constant of reaction (A.3) can be written as:

$$K_3 = \frac{a_{ZrO_2}}{a_{BaO} \cdot \mathrm{P}_{O_2}^{1.5}} = \exp\left(\frac{-\Delta G_3}{RT}\right) \tag{8}$$

and the relation between activity ratio and partial pressure of the reactant gas, is given by:

$$\log\left(\frac{a_{BaO}}{a_{ZrO_2}}\right) = \left(\frac{\Delta G_3}{2.30\ RT}\right) - 1.5\log\left(P_{O_2}\right) \tag{9}$$

In chemical-potential diagram such equilibrium are represented by inclined lines.

The stoichiometry of type 1 reactions is written per mole of gaseous reactant for ready drawing of the corresponding vertical line in the activity diagrams. For type 2 and type 3 reactions the stoichiometry of individual oxides is unit and the stoichiometric coefficients of other reactants and products are derived by solving the elemental mass balances. Similar approaches were used to obtain the corresponding relations for other two-phase equilibria in the system ZrO_2-BaO-O_2 (Table A.1). A suitable database (FactSage, GTT Technologies) was used to extract thermodynamic properties required to calculate the Gibbs free energy changes for the reactions, and to obtain the dependence of chemical activity ration on partial pressure of oxygen.

A similar strategy was adopted to build the potential-chemical diagrams of the systems TiO_2-BaO-O_2 and CeO_2-BaO-O_2 considering the two-phase equilibria of these systems.

Table A.1. Two-phase equilibria in the ZrO_2-BaO-O_2 system.

Two-phase equilibria	Reaction
BaO(s)/BaO_2(s)	$\mathrm{BaO\,(s) + O_2\,(g) \rightleftarrows 2BaO_2\,(s)}$ $\log\left(P_{O_2}\right) = \dfrac{\Delta G_1}{2.30\,RT}$
$BaZrO_3$(s)/Ba_2ZrO_4(s)	$\mathrm{BaO + 3BaZrO_3\,(s) \rightleftarrows ZrO_2 + 2Ba_2ZrO_4\,(s)}$ $\log\left(\dfrac{a_{BaO}}{a_{ZrO_2}}\right) = \dfrac{\Delta G_2}{2.30\,RT}$
Ba_2ZrO_4(s)/BaO_2(s)	$\mathrm{Ba_2ZrO_4\,(s) + BaO + 1.5O_2\,(g) \rightleftarrows ZrO_2 + 3BaO_2\,(s)}$ $\log\left(\dfrac{a_{BaO}}{a_{ZrO_2}}\right) = \dfrac{\Delta G_3}{2.30\,RT} - 1.5\log\left(P_{O_2}\right)$
ZrO_2(s)/$BaZrO_3$(s)	$\mathrm{BaO + ZrO_2\,(s) \rightleftarrows BaZrO_3\,(s)}$ $\log\left(\dfrac{a_{BaO}}{a_{ZrO_2}}\right) = \dfrac{\Delta G_4}{2.30\,RT}$, with $a_{ZrO_2} = 1$
BaO(s)/Ba_2ZrO_4(s)	$\mathrm{2BaO + ZrO_2\,(s) \rightleftarrows Ba_2ZrO_4\,(s)}$ $\log\left(\dfrac{a_{BaO}}{a_{ZrO_2}}\right) = \dfrac{\Delta G_5}{2.30\,RT}$, with $a_{BaO} = 1$
$BaZrO_3$(s)/BaO_2(s)	$\mathrm{BaO + BaZrO_3\,(s) + O_2\,(g) \rightleftarrows ZrO_2 + 2BaO_2\,(s)}$ $\log\left(\dfrac{a_{BaO}}{a_{ZrO_2}}\right) = \dfrac{\Delta G_6}{2.30\,RT} - \log\left(P_{O_2}\right)$
BaO(s)/$BaZrO_3$(s)	$\mathrm{BaO\,(s) + ZrO_2 \rightleftarrows BaZrO_3\,(s)}$ $\log\left(\dfrac{a_{BaO}}{a_{ZrO_2}}\right) = \dfrac{\Delta G_7}{2.30\,RT}$, with $a_{BaO} = 1$
ZrO_2(s)/Ba_2ZrO_4(s)	$\mathrm{BaO\,(s) + 0.5ZrO_2 \rightleftarrows 0.5Ba_2ZrO_4\,(s)}$ $\log\left(\dfrac{a_{BaO}}{a_{ZrO_2}}\right) = \dfrac{\Delta G_8}{2.30\,RT}$, with $a_{ZrO_2} = 1$
ZrO_2(s)/BaO_2(s)	$\mathrm{BaO + 0.5O_2\,(g) \rightleftarrows BaO_2\,(s)}$ $\log\left(\dfrac{a_{BaO}}{a_{ZrO_2}}\right) = \dfrac{\Delta G_9}{2.30\,RT} - 0.5\log\left(P_{O_2}\right)$, with $a_{ZrO_2} = 1$